

Investigations of interactions between membrane and PEI/siRNA nanoparticles
and their implication for non-viral gene delivery

by

Yousef Nademi

A thesis submitted in partial fulfillment of the requirements for the degree of

Doctor of Philosophy

in

Chemical Engineering

University of Alberta

© Yousef Nademi, 2021

Abstract

Cell entry of polynucleotide-based therapeutic agents can be promoted by nanoparticle (NP) mediated delivery. This dissertation investigates membrane penetration of polynucleotide NPs, using mainly computational approaches, accompanied by some experiments. Major emphasis was placed on computational approaches to explore configurational changes and stability of polymer-polynucleotide NPs upon penetration into lipidic membranes at the all-atom level. The first part of our studies explored the stability and configurational changes of NPs formed by 6 polyethylenimine (PEI) and 2 siRNA molecules during penetration into the zwitterionic 2-oleoyl-1-palmitoyl-sn-glycero-3-phosphocholine (POPC) membrane. For the zwitterionic membrane, we found that hydrogen bond formation between the PEIs and the membrane did not lead to instability of the polymer-polynucleotide NPs during the internalization process. Instead, our results suggested adoption of a “self-protecting” configuration by the NP during membrane penetration, where the NP become more compact and polynucleotides become aligned, leading to more stable configurations while detaching from the membrane. The polymer-polynucleotide NP modified with linoleic acid (LA) showed the smallest structural change due to its strong intra-particle lipid associations and the resulting rigidity, while NP modified with caprylic acid showed the largest structural changes. Next, in addition of zwitterionic membrane of POPC, anionic membrane of 1-palmitoyl-2-oleoyl-sn-glycero-3-phospho-L-serine (POPS) were also utilized. For the anionic membrane, our experiments showed that POPS liposomes interacted strongly with NPs, which caused partial dissociation of the NPs. Consistent with the experiments, steered molecular dynamics simulations (SMD) showed a stronger interaction between the NPs and POPS membrane as compared to the POPC membrane. Lipid substitution on the PEIs enhanced the stability of the NPs during membrane crossing; lipid association between PEIs of the LA-bearing NPs as well as

parallel orientation of the siRNAs provided protection against their dissociation (unlike NPs from native PEI). Later on, deformation of lipid membranes and pore closure during a NP penetration process was studied. POPC, dipalmitoylphosphatidylcholine (DPPC) and dilauroylphosphatidylcholine (DLPC) lipidic membrane models were utilized. Our results showed that different membrane lipids could lead to differences in pore formation (symmetric vs. asymmetric), and could undergo different levels of pore-mediated flip-flops during the closure. DLPC showed the largest number of flip-flops among the three lipid membranes. In addition, introduction of hydrophobic LA substitution onto the PEIs was found to facilitate pore formation, since the long LA tails could insert themselves into the hydrophobic region of the membrane where the lipid tails were less aligned. Compared with DPPC, POPC and DLPC membranes had less alignment of lipid tails in the bilayer, which promoted the insertion of LA tails and hence NP entry into the cell. At the end, machine learning algorithms were employed on the basis of quantitative structure activity relationship (QSAR) method to predict the cellular uptake of hydrophobically modified PEI/siRNA nanoparticles (NPs) into various cancer cell lines. A dataset consisting of 197 datapoints along with 3 different regression models, namely random forest (RF), multi-layer perceptron (MLP) and linear regression (LR), were used. The results of this modeling showed that RF and MLP regression methods had a better performance than the LR method, suggesting that non-linear models were better estimators when predicting the cellular uptake of PEI/siRNA NPs. Additionally, critical descriptors that had major contributions to cellular uptake were found to be PEI-to-siRNA weight ratio, type of hydrophobic substitution, as well as total numbers of Cs, unsaturated C and thioester groups on substitutions in each PEI. This dissertation provides valuable insight into the various aspects of polymer-polynucleotide NPs as well as lipidic membranes which will help in the design of more effective carriers for nucleic acid delivery.

Preface

Part of this thesis have been previously published, as explained below. Therefore, their structures are mostly maintained so that each chapter has its own introduction, method, results, discussion, and references, and abbreviations are defined at their first appearance. Specific acknowledgments are embedded within each chapter. It worth noting that this thesis was funded by Alberta Innovates Technology Futures (AITF).

A version of **Chapter 2** of this thesis will be submitted. As the primary author, I was responsible for concept formatting, and writing the manuscript. Dr. Tian Tang and Dr. Hasan Uludağ were the supervisory authors who were involved in concept formation, and revision of the manuscript.

Chapter 3 of this thesis is adapted from a previously published paper of Nademi Y, Tang T, & Uludağ H (2018) Steered molecular dynamics simulations reveal a self-protecting configuration of nanoparticles during membrane penetration. *Nanoscale* 10 (37), 17671-17682. As the primary author, I was responsible for concept formatting, performing the molecular simulations, data analysis, and writing the manuscript. Dr. Tian Tang and Dr. Hasan Uludağ were the supervisory authors who were involved in concept formation, results validation, and revision of the manuscript.

A version of **chapter 4** of this thesis has been published as Nademi Y, Tang T, & Uludağ H (2020) Membrane lipids destabilize short interfering ribonucleic acid (siRNA)/polyethylenimine nanoparticles. *Nanoscale* 12 (2), 1032-1045. As the primary author, I was responsible for concept formatting, conducting the molecular simulations and experimental studies, analyzing the data, and writing the manuscript. Dr. Tian Tang and Dr. Hasan Uludağ were the supervisory authors who were involved in concept formation, results validation, and revision of the manuscript.

A version of **chapter 5** of will be submitted as Nademi Y, Tang T, & Uludağ H, Nature of bilayer lipids affects membranes deformation and pore resealing during nanoparticle penetration. I was

responsible for concept formatting, conducting the molecular simulations, data analysis, and writing the manuscript. Dr. Tian Tang and Dr. Hasan Uludağ were the supervisory authors who contributed in concept formation, results validation, and revision of the manuscript.

A version of **Chapter 6** of this thesis will be submitted as Nademi Y, Tang T, & Uludağ H modeling uptake of polyrthylenimine (PEI)/siRNA nanoparticles in breast cancer cells using machine learning. I was responsible for concept formatting, conducting the machine learning algorithms, data analysis, and writing the manuscript. Dr. Tian Tang and Dr. Hasan Uludağ were the supervisory authors who were involved in concept formation, results validation, and revision of the manuscript.

Chapter 7 includes future perspective and limitations on the basis of the research conducted in this dissertation.

Acknowledgments

During my PhD years, I have been given the privilege of working with some of the best researchers specialized in molecular modeling and biomedical engineering. I would like to express my gratitude to those people who assisted in my personal and professional development during my doctoral journey.

First and foremost, I would like to thank my supervisors, Dr. Tian Tang, and Dr. Hasan Uludağ, for their patience, unconditional support, ongoing encouragement, and expertise to guide me through challenging tasks. I also appreciate having weekly constructive discussions with them, thereby helping me grow as an independent researcher.

I would like to acknowledge the financial support from Alberta Innovates Technology Futures (AITF), Captain Thomas Farrell Greenhalgh Memorial Graduate Scholarship, and University of Alberta Doctoral Recruitment Scholarship.

I would want to express my gratitude to Dr. Deniz Meneksedag-Erol for passing on her knowledge and expertise in modeling studies, and Dr. Remant Bahadur KC for mentoring me in the experimental studies. Also, I would like to thank my colleagues and friends in Tang and Uludağ lab for sharing their knowledge and expertise with me, and making my graduate student life a delightful experience.

Last but not the least, I am thankful to my parents and girlfriend for their boundless love and support. Without their support and inspiration, none of this would have been possible.

Table of Contents

1. Introduction: Scope of the Dissertation.....	1
1.1. References.....	4
2. Interactions of Polynucleotide Nanoparticles with Cellular Membranes: Insights from Computational Studies	5
2.1. Introduction.....	6
2.2. Computational Modeling of Cell Membranes	11
2.3. CG Simulation of Cell Membrane-NP Interactions	12
2.3.1. Effect of NP Features.....	14
2.3.1.1. NP Size.....	14
2.3.1.2. NP Shape	16
2.3.1.3. NP Hydrophobicity and Surface Charge	18
2.3.1.4. Ligands.....	23
2.3.1.5. Protein Adsorption on NPs.....	26
2.3.1.6. Cooperative Effects of NPs	28
2.3.2. Effect of Membrane Properties	31
2.4. AA simulation of Cell Membrane-NP Interactions.....	34
2.5. Machine Learning of Cell Membrane-NP Interactions	37
2.6. Conclusion	37
2.7. Acknowledgments	38
2.8. References.....	38
3. Steered Molecular Dynamics Simulations Reveal Self-Protecting Configuration of Nanoparticles during Membrane Penetration	49
3.1. Introduction.....	50
3.2. Methods	54
3.2.1. Simulated Systems and Procedure.....	54
3.2.2. SMD method	56
3.2.3. Simulation Details	58
3.3. Results.....	59
3.3.1. Equilibrated Structure of Isolated NPs	59
3.3.2. Membrane Penetration Process	63
3.3.3. Configurational changes of NP during Membrane Penetration	67

3.4. Discussion	70
3.4.1. Self-protecting Configuration.....	70
3.4.2. Implications	74
3.5. Conclusions.....	76
3.6. Acknowledgements	77
3.7. References.....	77
4. Membrane Lipids Destabilize Short Interfering Ribonucleic Acid (siRNA)/Polyethylenimine Nanoparticles.	83
4.1. Introduction.....	84
4.2. Materials and Methods	87
4.2.1. Materials.....	87
4.2.2. Experimental Procedures	88
4.2.3. Simulated Systems and Procedure.....	89
4.2.4. Simulation Details	92
4.3. Results.....	93
4.3.1. Experimental Determination of PEI Binding to siRNA	93
4.3.2. Liposome Characterization and Dissociation Assay	94
4.3.3. Steered Molecular Dynamics Simulations	96
4.5. Conclusions.....	112
4.6. Acknowledgments	113
4.7. References.....	113
5. Nature of Bilayer Lipids Affects Membranes Deformation and Pore Resealing During Nanoparticle Penetration.	120
5.1. Introduction.....	121
5.2. Methods	125
5.2.1. Simulated systems and procedure.....	125
5.2.2. Simulation details	129
5.3. Results.....	130
5.3.1. Membrane deformations during penetration of PEI NP	130
5.3.2. Pore formation caused by PEI NP penetration.....	132
5.3.3. Interaction between membrane and PEI NP	137

5.3.4. Membrane recovery and pore closure	140
5.3.5. Effect of PEI-LA NP on membranes	144
5.4. Discussion	148
5.4.1. Implications	148
5.5. Conclusion	152
5.6. Acknowledgments	153
5.7. References	153
6. Modeling Uptake of Polyethylenimine/siRNA Nanoparticles in breast Cancer Cells: using machine learning	160
6.1. Introduction	161
6.2. Methods	164
6.2.1. Dataset	164
6.2.2. Descriptors	165
6.2.3. Modeling	166
6.2.4. Metrics of model performance	168
6.3. Results and discussion	168
6.3.1. Significant descriptors	168
6.3.2. Effect of most significant descriptors	170
6.3.3. Closed-form predictions	173
6.4. Limitation and future perspective	176
6.5. Conclusions	178
6.6. Acknowledgements	178
6.7. References	178
7. Overall conclusions, General Discussion and Future Perspectives	182
7.1. Overall conclusions	183
7.2. Limitation and future direction to study polynucleotide NP-membrane interactions	186
7.3. References	189
Unified Bibliography	191
APPENDIX A: Supplementary Information for Chapter 3	223
APPENDIX B: Supplementary Information for Chapter 4	237
APPENDIX C: Supplementary Information for Chapter 5	244

APPENDIX D: Supplementary Information for Chapter 6.....266

List of Tables

Table 2.1. Effect of NP size on its internalization into the membrane through simulation studies.	15
Table 2.2. Effect of NP shape on uptake.	18
Table 3.1. Information of the simulated systems.	59
Table 4.1. Details of simulated systems.	92
Table 4.2. Hydrodynamic diameter (dz), polydispersity index (PDI) and ζ -potential (ξ) of POPS and POPC liposomes.	95
Table 5.1. Detailed information of the simulated systems.	129
Table 6.1. Descriptors used to model cellular uptake of PEI/siRNA NPs.	166
Table 6.2. Correlation of cellular uptake with descriptors used in model type 2.	169
Table 6.3. Performance of different regression models.	170
Table 6.4. Coefficients generated from LR using the three model types.	175

List of Figures

Figure 2.1. Different endocytosis pathways of polynucleotide NPs including phagocytosis, macropinocytosis, caveolae- and clathrin-mediated endocytosis, and caveolae- and clathrin-independent endocytosis.....	9
Figure 2.2. Schematic representation of a typical glycerophospholipid along with different models to represent its structure.	12
Figure 2.3. PMF of hydrophobic (left) and semi-hydrophilic (right) NP vs. distance from the center of the DPPC bilayer.	20
Figure 2.4. Surface modification of hydrophobic NPs with architecturally different copolymers.	21
Figure 2.5. The cross-section view of wrapping and pinching off of lipid raft covered NP.	32
Figure 3.1. Molecular structure of the simulated molecules.	56
Figure 3.2. Initial and final conformations of the NPs in absence of the membrane.....	61
Figure 3.3. Compactness of NPs and COM distance between siRNA molecules.	62
Figure 3.4. Force and number of HB between NP and membrane as a function of COM position of the NP during SMD.	64
Figure 3.5. Side-view snapshots of the NP and membrane at different time of the SMD simulation:	65
Figure 3.6. Structural changes of NPs during the SMD simulation.....	69
Figure 3.7. Angle between (a) siRNA-1 (b) siRNA-2 of NPs with unperturbed membrane surface.	73
Figure 4.1. Molecular structure of the simulated molecules.	90
Figure 4.2. Physiochemical studies on PEI binding to siRNA.	94
Figure 4.3. Physiochemical studies exploring the effect of liposome addition on the integrity of PEI/siRNA NPs.....	96
Figure 4.4. Force vs. COM position of the NP during SMD.....	97
Figure 4.5. Side-view snapshots of the NP and membrane at different instants of the SMD simulations.....	98
Figure 4.6. Dynamics of PEI binding to siRNA while interacting with POPS membrane.	101
Figure 4.7. Dynamics of PEI binding to siRNA while interacting with POPC membrane.....	102
Figure 4.8. Structural changes of NPs during the SMD simulation.....	103
Figure 4.9. Gyration radius of the PEIs as a function of COM position of NP crossing the POPS (left panel) and POPC (right panel) membranes.....	105
Figure 4.10. Average number of Ns of bridging PEIs within 4 Å of siRNAs N/O atoms during the first and last 5 Å of the penetration.	111
Figure 5.1. Molecular structure of the simulated molecules.	128
Figure 5.2. Positions of P atoms in the (blue) upper and (red) lower leaflets of membranes	131
Figure 5.3. Distribution of P atoms around the COM of PEI NP, within the x-y plane,	135

Figure 5.4. Probability distribution of the angle between Sn1 and Sn2.....	136
Figure 5.5. Structural changes of NPs during the SMD simulation.....	138
Figure 5.6. Schematic of two types of pores:	141
Figure 5.7. Position of P atoms in the (blue) upper and (red) lower leaflets of membrane	142
Figure 5.8. Process of pore resealing	143
Figure 5.9. Side-view snapshots of PEI-LA NP crossing the membranes	146
Figure 5.10. Side view snapshots at 34 ns of the SMD.....	147
Figure 6.1. Molecular structure of hydrophobic substitutions used in this chapter.....	165
Figure 6.2. Visualization of dataset.	172

List of Abbreviations

AA	All-atom
aLA	Alpha-linoleic acid
AI	Artificial intelligent
ATR-FTIR	Attenuated total-internal reflection Fourier Transform Infrared Spetctroscopy
bPEIs	Branched PEIs
CA	Caprylic acid
CvME	Caveolae-mediated endocytosis
COM	Center of mass
Chol	Cholesterol
CS	Chondroitin sulfate
CME	Clathrin-mediated endocytosis
CG	Coarse-grained
DNA	Deoxyribonucleic acid
DS	Dermatan sulfate
DLPC	Dilauroylphosphatidylcholine
DMSO	Dimethylsulfoxide
DOPA	Dioleoylglycerophosphoric acid
DOPC	Dioleoylsnglycerophosphocholine
DPPG	Dipalmitoylphosphatidylglycerol
DPPC	Dipalmitoylphosphatidylcholine
DPD	Dissipative particle dynamics
DSPC	Distearoylphosphatidylcholine
EMSA	Electrophoretic Mobility Shift Assay
GAGs	Glycosaminoglycans

HS	Heparin sulfate
HSPG	Heparan sulfate proteoglycans
HMW	High molecular weight
HA	Hyaluronic acid
HB	Hydrogen bonds
KS	Keratin sulfate
Lau	Lauric acid
LR	Linear regression
IPEI	Linear PEI
LA	Linoleic acid
LMW	Low molecular weight
mRNAs	Messenger RNAs
MD	Molecular dynamics
MLP	Multi-layer perceptron
NP	Nanoparticle
OA	Oleic acid
POPC	2-oleoyl-1-palmitoyl-sn-glycero-3-phosphocholine
POPS	1-palmitoyl-2-oleoyl-sn-glycero-3-phospho-L-serine
POPG	1-palmitoyl-2-oleoyl-sn-glycero-3-phosphoglycerol
POPE	1-palmitoyl-2-oleoyl-sn-glycero-3-phosphoethanolamine
PA	Palmitic acid
PME	Particle Mesh Ewald
PBC	Periodic boundary conditions
PE	Phosphatidylethanolamine
PS	Phosphatidylserine

PI	Phosphatidylinositol
PA	Phosphatidic acid
PDI	Polydispersity index
PAMAM	polyamidoamine
PEI	Polyethyleneimine
PLL	Poly-L-Lysine
PMF	Potential of mean force
PKC	Protein kinase C
QSAR/QSPR	Quantitative activity/property relationship
RGD	Arginylglycylaspartic acid
RF	Random forest
RMSE	Root mean square error
StA	Stearic acid
SMD	Steered molecular dynamics simulations
SFG	Sum frequency generation
tLA	Thioester linkage linoleic acid
Tfn	Transferrin
vdW	Van der Waals
VLPs	Virus like NPs

1. Introduction: Scope of the Dissertation

Gene therapy has excited the scientific field due to its applicability for a wide range of therapeutic applications. However, genetic material (short interfering RNA (siRNA) and DNA) because of their anionic nature cannot cross the anionic phospholipid cell membranes [1]. Therefore, many techniques have been utilized to design carriers to protect genetic materials from degradation and facilitate their cellular entry. Among non-viral vectors cationic polymers form the dominant strategy for delivery of genetic materials. The major advantages of polymers are their structural characteristics, which allowing convenient manipulation of the physiochemical characteristics of the delivery vector [1]. This dissertation aims at exploring the interaction between polymer/siRNA nanoparticles (NPs) with the cell membranes through a series of atomistic simulations, machine learning, and experimental techniques, where the major emphasis was on computational aspect. The thesis provides insights into structural changes of NPs during membrane penetration as well as the effect of membrane properties on penetration of NPs. Experiments were executed using liposomes to mimic surface properties of cell membranes and to test their ability to dissociate NPs.

The work described in this dissertation starts with **chapter 2**, which includes an in-depth literature review on molecular dynamics simulations studies performed on NPs-membrane interactions. Specifically, the studies investigating the effect of NP's physical properties on its direct penetration using dissipative particle dynamics (DPD) simulations was reviewed. The explored physical properties of NPs include size, shape, surface charge and hydrophobicity of NPs, and presence of ligands on their surface. The current progress in the field focused on coarse grained (CG) methods to investigate NP-membrane interactions, while mechanistic details on polymer/siRNA nanoparticle penetration into cell membrane remain to be explored. Following chapters have been conducted to address this knowledge gap.

Chapter 3 was the first all-atom study that systematically investigate the conformational changes of polymer/siRNA NPs during their penetration into a cell membrane. The non-functional low molecular weight PEI was modified with two different hydrophobic substitutions, which were experimentally proven to enhance the delivery performance of polymer. The all-atom steered molecular dynamics simulation (SMD) was employed to expedite the penetration process, which allowed us to provide mechanistic insight for design of better NP carrier for nucleic acid delivery.

Chapter 4 investigate the integrity of polymer/siRNA NPs during penetration into membranes with different surface molecules. The goal was exploring the role of membrane's surface molecule on integrity and conformational changes of polymer/siRNA NPs. Two membrane lipids namely 2-oleoyl-1-palmitoyl-sn-glycero-3-phosphocholine (POPC) and 1-palmitoyl-2-oleoyl-sn-glycero-3-phospho-L-serine (POPS) have been utilized. The integrity of polymer/siRNA NPs were first explored using *in vitro* dissociation assay, followed by all-atom SMD simulations. The experimental result presented in this chapter revealed the capability of anionic POPS liposomes to dissociate polymer/siRNA nanoparticles, while zwitterionic POPC liposomes lack such ability. Our SMD simulations provide molecular level insight on the penetration of polymer/siRNA nanoparticles into POPC and POPS membrane, and explained why dissociation happened when NP interacted with POPS liposomes.

Cell membranes are formed from various lipid molecules that exhibit different levels of saturation, chain length, and hydrophobicity. In **chapter 5**, the role of membrane's lipid tails molecules on membrane's deformation and its pore closure upon interaction with polymer/siRNA molecules were investigated. Membrane models with varying lipid tail length and level of saturation were selected. Afterward, both all-atom molecular dynamics (MD) and SMD simulations were executed to provide an atomistic detail on membranes deformation. The work

presented in this chapter showed that depending on types of membrane lipids, different types of pore (symmetric vs. asymmetric) as well as different level of pore mediated flip-flops occurred.

Machine learning is a statistical approach that can provide valuable information from existing data generated through various experimental studies. In recent years, chemoinformatics methods such as quantitative activity/property relationship (QSAR/QSPR) have been utilized. The core assumption of this method is that the biological activities of a NP and changes in its molecular structure are correlated. In **chapter 6**, QSAR approach were utilized to generate a predictive model for cellular uptake of polymer/siRNA NPs into breast cancer cell lines. To this end, a dataset consisting of cellular uptake various polymer/siRNA NPs were constructed, and upon applying machine learning algorithms, a predictive model for cellular uptake of polymer/siRNA NPs was generated. The model can provide valuable structural insights into parameters that affect cellular uptake the most, and help designing better polymer for gene delivery applications.

The results presented in this dissertation enhanced our understanding on the interplay between polymer/siRNA NPs and cell membranes, which can be applied to design better polymeric carriers to protect the polynucleotide and have a higher delivery performance. Our study highlighted future direction and remaining challenges with the emphasis on all-atom simulations approaches. Overall conclusions and future direction for each chapter will be discussed in **chapter 7**.

1.1. References

[1] H. M. Aliabadi, B. Landry, C. Sun, T. Tang, and H. Uludağ, “Supramolecular assemblies in functional siRNA delivery: where do we stand?,” *Biomaterials*, vol. 33, no. 8, pp. 2546–2569, 2012.

2. Interactions of Polynucleotide Nanoparticles with Cellular Membranes: Insights from Computational Studies

2.1. Introduction

Genetic therapy based on the deployment of ribonucleic acid (RNA) and deoxyribonucleic acid (DNA) agents is an exciting approach that can impact treatment of many diseases and in particular cancer. In the traditional treatment of cancer, drugs derived from small organic compounds are utilized to eradicate malignant cells by a variety of mechanisms. These drugs display broad activities to create a toxic environment inside malignant cells, killing the healthy cells to a significant degree as well. DNA delivery has been undertaken to induce expression of a variety of proteins with direct anti-cancer and immune stimulation activities, while RNA delivery has been undertaken to inhibit protein expression and interfere with endogenous messenger RNAs (mRNAs), thereby silencing the drivers of malignancy. However, DNA and RNA agents are highly polyanionic and cannot cross the anionic lipid bilayers of intact cell membranes. They need a carrier to form cationic nanoparticles (NPs) for cellular entry. Cellular entry of NPs usually occurs through direct penetration and/or active endocytosis[1]. In direct penetration, a NP crosses the cell membrane without being confined by endocytosis vesicles, and this can occur through diffusion, permeation and pore formation. Passive diffusion do not induce distinct pores in the membrane, and are usually adopted by small (< 1 nm) to intermediate sized NPs. Direct translocation can also be enabled by inducing transient pores using electroporation, mechanical stress, shock waves (sonoporation), surface-active molecules, and small cationic peptides or polymers[2]. Most of the NPs internalized by direct penetration are <50 nm in diameter[3], although internalization of NPs as large as 100 nm have also been reported[3].

Endocytosis, in which vesicular uptake of NPs or solutes is induced by invagination of plasma membrane[4], relies on several different pathways such as phagocytosis, macropinocytosis, caveolae- and clathrin-mediated endocytosis, and caveolae- and clathrin-independent endocytosis

(see **Figure 2.1**). Depending on the size and surface features of NPs, it is typical to utilize more than one specific pathways[5]. Phagocytosis is common to immune cells such as monocytes and macrophages, and can transport NPs with size ranging from a few hundred nms to dozens of μm [6]. NPs that will undergo phagocytosis need to first bind to opsonins, such as immunoglobulin IgG and IgM, serum proteins, and complement components (C3, C4, and C5) to make them prone to binding to receptors on the surface of cell membrane[7]. Internalized NPs end up in lysosomes, which will eventually get degraded by acidification and enzymolysis within the lysosomes[8], [9]. Therefore, the cargo of the NPs need to escape before reaching to lysosomes to avoid degradation. Macropinocytosis is the signal-dependent pathway that involves an actin-mediated internalization process[10]. It differs from other endocytosis pathways by a lack of ‘coat’ structure on the macropinosome, which is generally considered to have a vesicular size of $0.2 \mu\text{m}$ but can be as large as $5 \mu\text{m}$ [10]. NP uptake through macropinocytosis generally begins with external stimulations that activate the receptor tyrosine kinases[7]. Intracellular fate of the internalized NP depends on the cell type, and in most cases, NP moves through the cytosol and fuses with lysosomes[7], [9], [11]. Taking A431 cells as an example, the macropinosomes return to cell membrane and release their content to the extracellular space[12]. Macropinocytosis, along with phagocytotic pathway, facilitates non-selective internalization of a large volume of fluid, solutes and membrane material[10]. Clathrin-mediated endocytosis (CME) exists in all mammalian cells, and enable uptake of essential nutrients, such as the cholesterol laden low-density lipoprotein (LDL) particles that bind to the LDL receptor, and iron-laden transferrin (Tfn) that binds to Tfn receptors[13]. CME is receptor-dependent, clathrin-mediated, and GTPase dynamin required[9], [14]. Receptor-ligand binding stimulates formation of clathrin-coated vesicles on the cytosolic side of the plasma membrane[5]. NPs with diameter $<200 \text{ nm}$ can be internalized through the CME[15].

Caveolae-mediated endocytosis (CvME), on the other hand, involves formation of a flask-shaped structures with a size range of 60 to 80 nm due to the assembly of hairpin-like caveolin coats[6]. Caveolin family proteins play an important role in the CvME. Enriched with cholesterol and sphingolipids[9], [16], they are abundant in endothelial cells, where they form 10-20% of the surface of cell membrane[13], [16], [17]. Folic acid, albumin, and cholesterol are known ligands that are internalized through CvME[17]. Compared to CME, CvME pathway displays a longer internalization[7], [16]; however, NPs that utilizes CvME pathway may avoid lysosomal route, and get transported to the Golgi and/or endoplasmic reticulum[9]. Finally, the caveolae- and clathrin-independent endocytosis pathways rely on cholesterol, and therefore are dependent on specific lipid compositions of the membrane. Many molecules including SV40 virions, CTxB, GPI-linked proteins, receptors for growth hormone, and endothelin have been internalized through these pathways[18].

Various non-viral vectors including lipids, polymers, and peptides have been developed to package the polynucleotides and deliver them into the cytoplasm[19]. Typical examples of polymeric delivery systems include synthetic polyethyleneimine (PEI), poly-L-Lysine (PLL), dendrimeric polyamidoamine (PAMAM), and naturally-derived chitosan. The endocytosis pathway(s) undertaken vary with chemical structure of the NP and molecular composition of target cell surface [20]. For instance, anionic heparan sulfate proteoglycans (HSPG) are key molecules affecting internalization of cationic NPs [21]. They are present on membrane surfaces associated with the Syndecan protein family members, CD44-transmembrane proteins, as well as the Glypican family that are bound to membranes with the glycosylphosphatidylinositol anchor [22]. *Kopatz et al.* [21] proposed that syndecans with anionic HSPG facilitate extracellular matrix binding and interaction with large cationic PEI/DNA NPs. Specifically, PEI/DNA NP binds to syndecans by gradual

electrostatic zipping of the plasma membrane around the NP, followed by lateral diffusion of syndecans that cluster into cholesterol-rich rafts. Clustering of the syndecans triggers protein kinase C (PKC) activation and linker protein-mediated actin binding to the cytoplasmic tails of syndecans. The well-developed tension fibers and a growing network of cortical actin will then pull the NP into the cell.

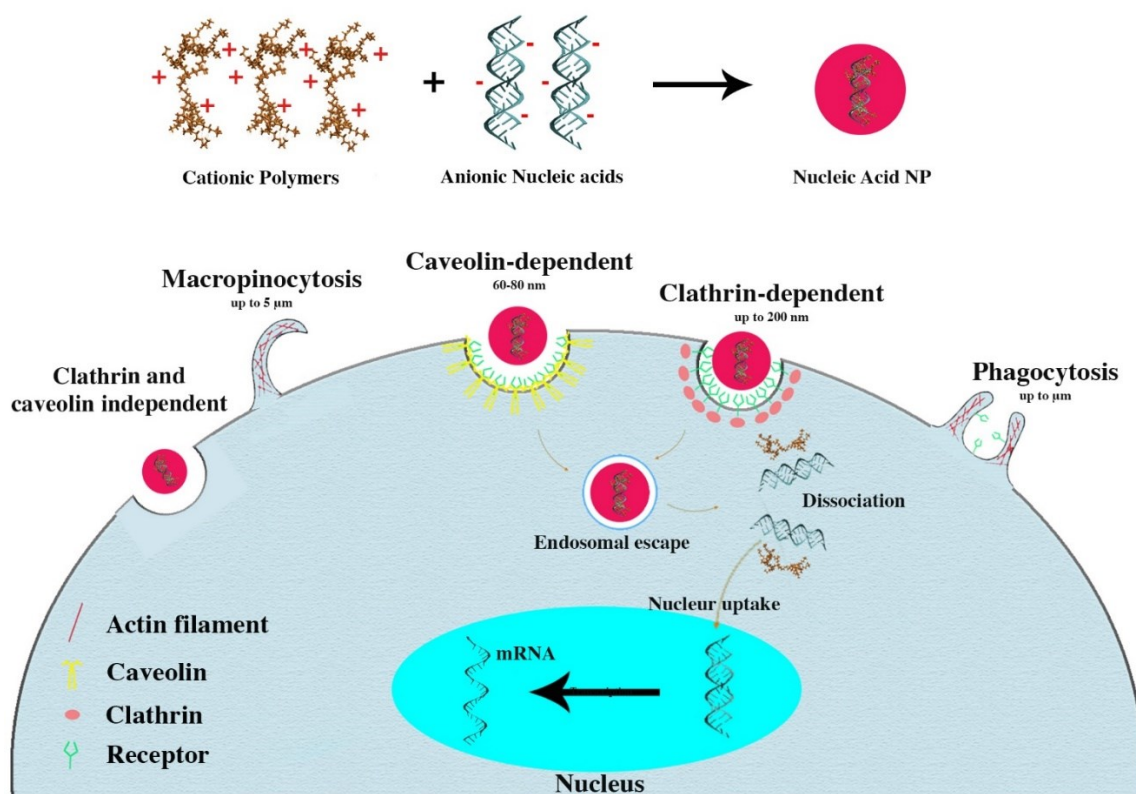


Figure 2.1. Different endocytosis pathways of polynucleotide NPs including phagocytosis, macropinocytosis, caveolae- and clathrin-mediated endocytosis, and caveolae- and clathrin-independent endocytosis.

Although experimental studies have provided significant understanding on the operation of various polymeric vectors, it is challenging to obtain mechanistic details of their beneficial effect(s) at atomistic level from experiments. In addition, it is rather difficult to systematically investigate the

entire delivery process of NPs under various conditions, due to presence of many participating factors. Cellular uptake, one the most important steps in NP delivery, is initiated through interaction of NPs with cell membrane [5]. Theoretical calculations and computer simulations may help illuminate the underlying mechanism(s) of NP-cell membrane interactions, especially on aspects that cannot be directly addressed through experiments. MD simulation is a useful technique for computing the equilibrium and transport properties of a classical many-body system [23], and it has been used to study NP-cell membrane interaction in order to facilitate the design of effective carriers for both conventional drugs and polynucleotides [1], [5], [24]–[26]. All-atom (AA) MD treats all participating atoms explicitly and are computationally costly. A typical AA MD simulation involves $<10^6$ atoms and is shorter than one μs , much smaller than real experimental systems [27]. Another commonly used approach is united-atom MD, where each aliphatic carbon and associated hydrogens are combined into a single bead. This leads to a small decrease in the degrees of freedom, and a 20-30% increase in computational efficiency [28]. One approach to overcome the computational limit is to use Coarse-Grained (CG) approaches. CG models can be categorized into two types: the specific type (e.g. the MARTINI force field [29]) that retain detailed information of specific residues, and the generic type such as dissipative particle dynamic (DPD). DPD is a CG method first introduced by *Hoogerbrugge* and *Koelman* to simulate hydrodynamic behavior, and was later extended to simulation of polymers[30], [31]. In DPD, a cluster of atoms is treated as one soft spherical bead, whose motion is governed by the interactions among beads and certain collision rules [31]. Use of beads allows us to simulate events over a longer period due to both decreased degrees of freedom and use of larger time steps enabled by the removal of high frequency motions. As a result, computational efficiency increases significantly in CG simulations[31].

Due to the high demand of computing capability by AA MD simulations, previous simulations on NP-membrane interactions are almost exclusively done at the CG level using DPD, while AA approaches are just beginning to be explored. Below, we will first review the computational modeling of cell membranes and NP-membrane interactions simulated by DPD, and discuss factors influencing cellular uptake. Afterwards, we will examine the few investigations using AA approach.

2.2. Computational Modeling of Cell Membranes

Cell membranes are laterally heterogeneous structures composed of various lipids (cholesterol, phospholipids (glycerol-, sphingo-, glycol-)), and functional proteins such as ion channels, pumps, receptors, etc.[32]. Lipid rafts are a significant source of membrane heterogeneity; semi-stable interactions among various lipids in the plane of the membrane lead to formation of relatively-ordered, large scale membrane domains as a result of liquid-liquid phase separation[33], [34]. The role of lipid rafts on membrane organization and its functioning [35] and the experimental membrane models to study NP-membrane interactions have been recently reviewed [36]. Glycerophospholipid are the major structural lipids in eukaryotic membranes, which consist of glycerol group to which a hydrophilic head group and two hydrocarbon chains are connected as shown in Figure 2.2 [37]. The head group is composed of a phosphate group and an alcohol group. A polar alcohol specifies the name and total charge of phosphoglycerides, for example phosphatidylcholine (abbreviation: PC, head group name: choline, charge at physiological pH: 0), phosphatidylethanolamine (PE, ethanolamine, 0), phosphatidylserine (PS, serine, -1), phosphatidylinositol (PI, inositol, -1) and phosphatidic acid (PA, no head group, -1) [38]. PC accounts for >50% of the phospholipids in most eukaryotic membranes[38]. The hydrocarbon chains may vary in length (typically 12 to 20 carbon groups) and may be saturated or unsaturated.

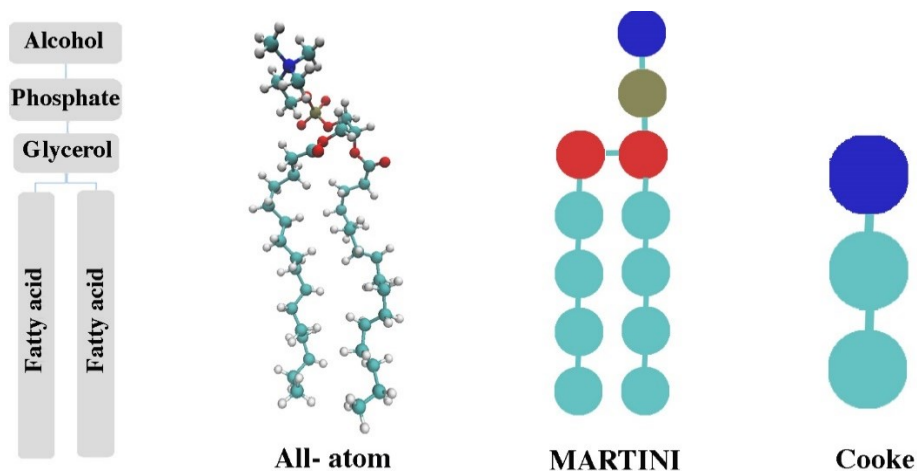


Figure 2.2. Schematic representation of a typical glycerophospholipid along with different models to represent its structure.

Since the neighboring lipids in a bilayer are not covalently bonded, non-bonded interactions play a critical role in dynamical properties of a bilayer. In order to reproduce these properties, non-bonded parameters need to capture two opposing tendencies, namely, the affinity of the hydrophobic tails to minimize the exposure to water and the tendency of the hydrophilic head groups to maximize it [39]. AA models of lipid bilayers exist in force fields such as GROMOS [40], [41] and CHARMM[42], with the former using a united-atom approach. The number of beads in a CG bilayer model can also vary. As an example, Figure 2.2 shows AA and CG representations of dipalmitoylphosphatidylcholine (DPPC) bilayer, where the AA model contains 130 atoms while the Martini[43] and Cooke[44] CG models include 12 and 3 beads respectively.

2.3. CG Simulation of Cell Membrane-NP Interactions

When a NP is bound to a cell membrane, its wrapping by the membrane and subsequent engulfment is determined by interactions[45] that can be divided into 2 broad categories. One is the adhesive force between the NP and membrane, manifested in different forms including non-

specific interactions such as hydrophobic, electrostatic and van der Waals (vdW), and specific interactions such as receptor-ligand binding. The other is the mechanical stiffness of the membrane during its deformation, which resists the wrapping and engulfment[5].

The energy associated with membrane deformation consists of bending and stretching components [5], [46], [47]. In the modeling of NP-membrane interaction, it is common to assume that the membrane is tensionless and therefore the stretching energy is zero. The elastic bending energy is given by[5]:

$$E = \frac{1}{2} B (\bar{c} - c_0)^2 \quad (1)$$

where E is the local bending energy per unit area, B is the bending modulus, and $\bar{c} = \frac{1}{2} \left(\frac{1}{R_1} + \frac{1}{R_2} \right)$ is mean curvature of the membrane in contact with the NP, in which R_1 and R_2 are the two principal curvatures of the NP. The value of B for typical phospholipid bilayers is around $20 k_B T$ [48], k_B being the Boltzmann constant and T the absolute temperature. In Eqn. (1), c_0 is the intrinsic curvature of the membrane, which arises from the asymmetry of the lipid bilayers and/or presence of asymmetrically shaped trans-membrane proteins [5]. Using the seminal Helfrich theory of membrane elasticity[49], [50], *Bahrami et al.*[51] demonstrated the significant effect of intrinsic curvature on the wrapping of a vesicle membrane around a rigid NP. Specifically, if initially the membrane bulged away from the NP ($c_0 > 0$), the NP was able to form stable partially-wrapped states. Whereas there was a large energetic barrier if the membrane initially bulged toward the NP ($c_0 < 0$). The intrinsic curvature is considered to be small if the corresponding radius of curvature is much larger in value than the membrane thickness (d), i.e., $1/c_0 \gg d$. In many of the CG simulations reviewed below, only a section of the membrane was considered and it was constructed with a flat initial configuration that has zero intrinsic

curvature. In addition, most simulations have assumed the membrane to be tensionless. *Deserno et al.* [46] derived an expression for the critical NP radius λ below which membrane tension can be neglected compared to bending:

$$\lambda = \left(\frac{2B}{\sigma}\right)^{1/2} \quad (2)$$

where σ is the lateral tension of the membrane. For typical values of $B = 20 k_B T$ and $\sigma = 0.05 \text{ mN/m}$ [5], $\lambda \approx 58 \text{ nm}$ is obtained. Above this critical radius, membrane tension will have a profound effect on cellular uptake of NP [5].

Past CG studies have revealed many factors that impact the interaction of NP with cell membrane, such as size, shape, hydrophobicity and ligands on the surface of the NP, which will be described in detail.

2.3.1. Effect of NP Features

2.3.1.1. NP Size

The size of NP is important for specific uptake pathway(s) undertaken. NPs $< 1 \text{ nm}$ may use passive diffusion, while the NPs $> 50 \text{ nm}$ mainly utilizes endocytosis. Past simulations[52]–[58] addressing the size effect are summarized in **Table 2.1** for spherical NPs. *Vácha et al.* [52] found that increasing the size of spherical NP is beneficial for endocytosis, which was explained by the fact that as the NP size increases, the energy required to bend the membrane decreases (see Equation 1). Two other studies[53], [54] also confirmed that at an optimal density of functional groups (i.e., ligands) on the NP, increase in NP size is beneficial for endocytosis or penetration of the NP. The trend, however, can vary as the areal density of the ligands changes. *Yue et al.* [55] used NPs with diameters ranging from 10 to 20 nm and introduced rotation of the NPs. Experimentally, rotation of magnetic NPs can be induced by a dynamic magnetic field [59], which

can subsequently cause apoptosis in cells via mechanical forces exerted on the cell membrane. The results of Yue et al.[55] showed that rotation of larger NPs caused more disruption of cell membrane and larger pore formation, and NPs with diameter ≥ 15 nm led to mechanical rupture of the membrane. Small NPs especially hydrophobic ones can enter the cell through direct penetration. Some simulation studies[56], [57] suggested that increase in size of hydrophobic NP is beneficial for penetration, while others[60], [61] stated the opposite by arguing that the energy for a hydrophobic NP to penetrate through (and not just bend) the membrane increases with NP size.

Table 2.1. Effect of NP size on its internalization into the membrane through simulation studies.

Reference	Size	NP property	Key findings
Vácha et al.[52]	5.7,8.6, and 14.3 nm	Hydrophilic	Increase in NP size is beneficial for endocytosis.
Yue et al.[53]	3-6.5 nm	Not specified	Size effect varies depending on the areal density of functional groups. At an optimal density increase in size is beneficial for endocytosis.
Ding et al.[54]	2.1, 3.0, 3.9, and 4.8 nm	Hydrophilic	For a fixed number of functional groups, increase in NP size decreases penetration efficiency.
Yue et al.[55]	10, 12.5, 15, and 20 nm	Hydrophilic	NPs ≥ 15 nm cause mechanical rupture of membrane
Lin et al.[56]	1.284, 2.098, and 2.912 nm	Hydrophobic	No significant energy barrier observed; translocation time decreases with increase in NP size.
Curtis et al.[57]	1-25 nm	Hydrophilic	Hydrophilic NP > 2 nm become wrapped by the DPPC membrane; hydrophobic NP directly penetrate the membrane and embed themselves within the inner hydrophobic core of the bilayers.
	1-4 nm	hydrophobic	
Chen et al.[58]	1.5-10.5 nm	Not specified	NP < 4.5 nm uses penetration and NP > 4.5 uses endocytosis (note: this simulation involves multiple NPs).

The above studies suggest that there may exist optimal NP sizes that best facilitate uptake, resulting from the competition between forces that favors internalization and those resisting it. For example, in the case of NP modified with functional groups, interaction between functional groups and membrane receptors drive NP wrapping[62], while resisting forces include receptor diffusion

that carries translational entropy[5], [63], [64] and membrane bending. In fact, experimentally optimal NP sizes of 40-50 nm has been reported[65], although such sizes are still difficult to simulate even at the CG level. The simulations in **Table 2.1** all involved NPs less than 25 nm in diameter. When the radius of the NP is larger than the critical value of 58 nm (Equation 2), one also needs to consider the presence of membrane tension, which may alter the influence of NP size.

2.3.1.2. NP Shape

NP shape has direct impact on the bending energy of the membrane. In an experimental uptake study using HeLa cell and NPs with size >100 nm, cubic NP showed the lowest uptake, with increasing order of uptake demonstrated by cylindrical, spherical, and rod shaped NPs[66]. In contrast, in the size range of <100 nm, uptake of the spherical Au NP was higher than the rod shape Au NP[67]. Many simulations have been conducted with different NP shapes including rod, capsid, icosahedral, cylindrical, spherical, ellipsoid, discs, spherocylindrical and pushpin particles[52], [68], [69], which are summarized in **Table 2.2**. In both direct penetration and endocytosis, simulations showed that initial orientation and shape anisotropy of NPs have great effects on their interaction with lipid bilayers[60], [70]. Also, NP translocation is often accompanied by rotation within lipid bilayer as reported in several studies[52], [60], [68], [71], [72]. The rotation is proposed to help the NP to adapt its configuration for a facilitated internalization process [71], [72]. In case of direct penetration,[60], [70] a sharp shape can be beneficial as the NP rotates so that its sharp edge penetrates the membrane. *Li et al.* [73] utilized DPD simulations to investigate the interaction between virus like NPs (VLPs) and lipid bilayer. The force profile analysis of NP penetration into lipid bilayer showed that VLPs with relatively longer and sparser spikes had better penetrability, because the spikes perturbed the bilayer

structure after VLPs adhered to it. As a result, there was an increase in the lateral defects as well as a decrease in the vertical deformation of the bilayer [73]. In the case of endocytosis, additional factors such as membrane surface tension, strength of ligand-receptor interaction, receptor diffusion and ligand density) need to be considered beyond the simple shape. Simulation elucidated some of these effects. For example, with a similar length scale, spherocylindrical NPs were shown to have higher endocytosis efficiency compared to spherical, and cylindrical NPs [52], [70]. This was attributed to the smaller mean curvature of spherocylindrical NPs compared to the others. In another study, *Huang et al.* [74], using a membrane model with small number of diffusive receptors that bound strongly to functional groups on the NP, observed that spherocylindrical NP first rotated to a parallel orientation when attaching to the membrane, and then rotated to a perpendicular orientation during the endocytosis process. The NP rotation can be understood from energetic point of view. Binding of NP ligands to cell surface receptor reduces the total energy and favors endocytosis. As a result, the NP first rotates to maximize the binding. On the other hand, the rotation leads to increase of lateral dimension of the NP in contact with the membrane, which increases the bending energy. Consequently, the NP rotates back to an orientation perpendicular to the membrane during endocytosis. Besides natural rotation of NPs, actively rotating NPs (i.e., by applying magnetic field) might lead to membrane rupture. *Zhang et al.* [75] using DPD simulations explored how the rotation of hydrophobic NPs coated with hydrophilic functional groups affected their interaction with the membrane and triggered membrane rupture. Spherical, cylindrical and L-shaped NPs with the same volume were simulated. It was observed that under high shear force, both cylindrical and L-shaped NP broke the integrity of membrane at shorter time compared with spherical NPs, and the breaking time was shortest for L-shaped NP.

Table 2.2. Effect of NP shape on uptake.

Indices (x,y,z) in the membrane models are the number of beads in the head (x) and tail groups (y in the case of single chain; y and z in the case of two chains).

Reference	NP property	Shape	Membrane	Key findings
Vácha et al.[52]	Hydrophilic with ligand	Sphere, spherocylinder, cylinder	(1,2) bead model	Spherocylinder showed the highest uptake followed by sphere. No uptake for cylinder within their simulation time.
Ding et al.[54]	Hydrophilic with ligand	Sphere, bullet, ellipse	(3,4,4) bead model	Initial orientation influenced the penetration ability of NP; shape anisotropy hindered NP penetration.
Yue et al.[55]	Hydrophilic with ligand	Sphere, cylinder	(1,3) bead model	Shear force on the membrane is maximized when the longest edge of the NP was parallel to the membrane.
Yang et al.[60]	Hydrophilic without ligand	Sphere, ellipsoid, rod, disc, pushpin	(2,5) bead model	Shape anisotropy and initial orientation of NP was crucial to the nature of the interaction; penetration capability of NP was dependent on the local NP curvature at contact point.
Liu et al.[68]	Hydrophilic and hydrophobic	Sphere, rod	(3,5,5) bead model	Membrane binding time was shorter for rod than for spherical NP.
Nangia et al.[70]	Gold NP with ligand	Cone, rice, cube, pyramid, rod, sphere	3:1 ratio of DSPC:DSPE	At similar sizes, rice-shaped NP had the fastest membrane internalization followed by sphere-, pyramid-, cone-, rod-, and cube-shaped NP.
Li et al.[72]	Hydrophilic With ligand	Sphere, rod, disk	(3,5,5) DMPC	NP rotation was important for endocytosis of anisotropy NP; spherical NP had the fastest endocytosis followed by rod- and disk-shaped NP.

2.3.1.3. NP Hydrophobicity and Surface Charge

Another important NP feature investigated in simulations is the surface hydrophobicity [76]–[79]. Potential of mean force (PMF) evaluated from CG simulations for the translocation of charge neutral hydrophobic (apolar beads) and semi-hydrophilic (nonpolar beads with four subtypes reflecting different hydrogen bonding capability) NPs through DPPC bilayer showed inclusion tendency of hydrophobic NP into the bilayer, whereas a semi-hydrophilic NP preferred to remain at the surface (**Figure 2.3**)[76]. It was hypothesized that internalization of a hydrophobic NP involves 3 steps. The NP first expels lipid molecules and enter the hydrophobic core of the bilayer.

This step requires significant energy to overcome the barrier set by the hydrophilic head groups of the lipid bilayer, which is compensated by the hydrophobic interactions between the tails of the lipid bilayer and the NP[76]. In the second step, because of the favorable interaction between the inserted NP and surrounding lipids, the membrane adjusts itself to the shape of inclusion (**Figure 2.3-Left, B**). In the third step, both the top and bottom of the NP are exposed to the water (**Figure 2.3-Left, C**)[76]. On the contrary, the PMF profile of semihydrophilic NP shows that NP needs to overcome a substantial energy barrier to penetrate through the membrane, which makes endocytosis a more plausible uptake mechanism [76]. Similar observations were also made by other studies,[77], [78] so that for non-penetrating NPs, the critical issue could be stable anchoring of NP to lipid membrane rather than the ability to penetrate the lipid bilayer.

Wang et al.[80] using DPD simulations investigated the direct penetration of core-shell soft hydrophilic and hydrophobic NPs with different elasticity into cell membrane. Their free energy calculations showed that rigid hydrophilic NPs and soft hydrophobic NPs encountered lower energy barriers during penetration. The reason was caused by different deformation modes. Soft hydrophilic NPs spread out at the upper surface of the membrane due to attraction between the NP and the lipid heads, while rigid hydrophilic NP did not spread out at the membrane surface. The NP spreading on membrane surface increased energy required to bend the membrane. For the soft hydrophobic NP, elongated configuration and lower contact areas with the membrane caused NP to diffuse more readily into the membrane, thereby reducing the energy required to penetrate into the membrane. However, it had difficulty detaching from the membrane because of attraction between the NP and the lipid tail.

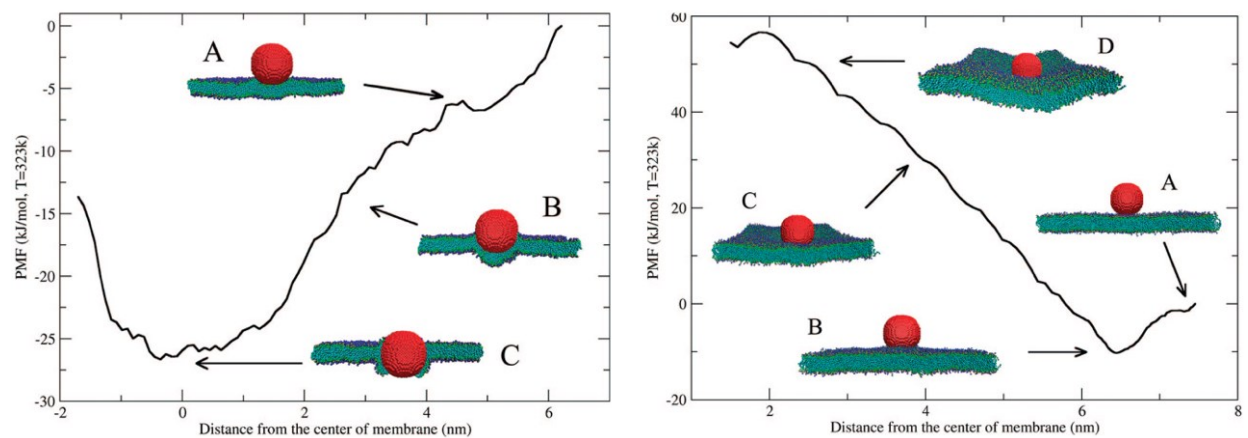


Figure 2.3. PMF of hydrophobic (left) and semi-hydrophilic (right) NP vs. distance from the center of the DPPC bilayer.

Inset images are snapshots corresponding to sampling positions[74]. The comparison of left and right panel suggest it is much easier for hydrophobic NP to enter the DPPC bilayer.

The membrane interaction of Janus NPs composed of both hydrophilic and hydrophobic surface characteristics were simulated.[61], [81] It was found that when a pore was induced in the membrane by external stress or change in temperature or pH, Janus NP diffused to the edge of the hole and stabilized the pore,[82], [83] with their hydrophobic part interacting with the lipid tails. The presence of Janus NP at the edge of the pore causes redistribution of lipids around the NP, which has a smaller curvature compared with the curvature of the pore. This lowers the free energy of the system, and makes the pore resealable: it opens under a set of conditions (i.e., pH), but can close with a change in the surroundings.

Cellular entry of NPs coated with mixed hydrophilic/hydrophobic groups is sensitive to the surface pattern of these groups. Hydrophobic NPs were surface-modified with hydrophilic-hydrophobic (AB), hydrophobic-hydrophilic (BA), hydrophobic-hydrophilic-hydrophobic-hydrophilic (BABA) and random copolymers[79], [84] (**Figure 2.4**). AB and random copolymers required higher force for NP internalization and also left a non-repairable pore in the membrane

upon its translocation, which was attributed to the hydrophilic beads on the NP surface that interacted with the membrane even after penetration. In the cases of BA and BABA copolymer patterns, the unfavorable interactions of hydrophobic beads with the membrane did not lead to permanent pores. The BA configuration required the lowest force for internalization, but the NP tended to remain in the center of the lipid bilayer due to the strong hydrophobic interaction with lipid tails. Based on these results, BABA was suggested to be the most suitable structure for the uptake of NPs[84], although experimental validation remains to be demonstrated.

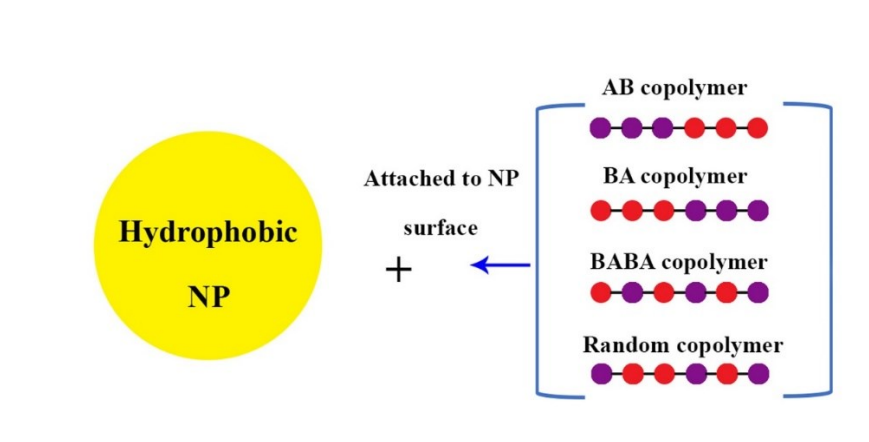


Figure 2.4. Surface modification of hydrophobic NPs with architecturally different copolymers.

(purple: hydrophobic units, red: hydrophilic units).

Attaching hydrophobic moieties to hydrophilic NPs is a widely practiced approach to enhance uptake of hydrophilic NPs. *Ding et al.* designed a non-covalent approach to anchor functional groups (each composed of 4 beads, 1 hydrophilic and 3 hydrophobic) on hydrophilic NPs. The NPs were able to internalize into lipid bilayer more easily and, after internalization, the functional groups tended to detach from the hydrophilic NP as a result of interactions with the hydrophobic region of lipid tails. The NP had higher probability to exit the lipid bilayer instead of

being trapped within[54]. Such ‘dynamic’ structures might be operational in supramolecular systems capable of shedding some of the components within membranes.

Liu et al. [85] using DPD simulations investigated the interactions between hydrophilic NP (3, 5, and 10 nm in size) uniformly modified with 114 amphiphilic functional group (12 hydrophilic and 4 hydrophobic beads) and lipidic membrane. They observed that amphiphilic groups first curled in solvent (water) to reduce the surface hydrophobicity. As NP attached to the membrane, the curled groups extended and hydrophobic functional group rearranged and started interacting with lipid tails, dragging NP into the membrane. Afterwards, three states of NP-membrane interactions were observed, namely penetration (a pore was formed and NP was likely to enter cells), adhesion (NP interacted with the outer leaflet of the membrane but failed to reach the inner leaflet), and engulfment (NP entered the core of the lipid bilayer and remained entrapped by swollen membrane), depending on the NP size and the membrane surface tension.

Ding et al. [86] investigated the interaction between a lipid bilayer and a cationic NP with adsorbed pH-sensitive polymers. 12 hydrophilic beads representing the polymer displayed varying degree of ionization depending on the pH value. At both low (number of ionized beads, $N \leq 3$) and high pH ($N \geq 9$), the polymers were found to detach from the NP, which was due to the weak polymer-NP interaction in the former case and strong repulsion among the ionized beads in the latter case. The poor polymer adsorption allowed stronger attraction between membrane receptors and NP surface, and complete wrapping of NP by the membrane. Whereas at intermediate pH ($4 \leq N \leq 8$), the polymers remained adsorbed on the NP surface, which prevented wrapping and internalization of the NP.

2.3.1.4. Ligands

To simulate ligand-receptor interaction at the CG level, receptor beads on the surface of lipid bilayers are introduced with defined interactions with ligand beads on the NP. Different studies explored the influence of strength of ligand-receptor interactions, hydrophilic/hydrophobic nature of the ligand, ligand density, and ligand length on NP interactions with cell membrane and uptake[52], [68], [69], [87]–[89].

Vácha et al. studied the effect of ligand-receptor attraction on the internalization of hydrophilic NPs with different shapes. Attraction energies of 2, 5, and 8 kT were applied to each NP. Increase in the ligand-receptor interaction led to higher endocytosis speed for spherical and spherocylindrical NPs. For the cylindrical NP, endocytosis did not happen even at the highest attraction energy (8 kT), which was attributed to the sharp edges of the cylinder where large curvatures were present[52].

In the study of *Liu et al.* [68], hydrophobic and hydrophilic NPs were coated with hydrophobic or hydrophilic ligands containing functional ends that can interact with membrane receptors. Binding and uptake of NPs were evaluated based on the engulfment percentage, defined as the fraction of the NP surface covered by the membrane. Hydrophilic NP coated with hydrophilic ligands gradually attached to the membrane surface due to the receptor-ligand interactions, and after attachment, receptors rearranged themselves to interact with more functional ends. However, during the simulation time (0.51 μ s) there was no internalization, which may have originated from the use of small NP size (3.2 nm) and hence large bending energy. In the case of hydrophobic NP coated with hydrophobic ligands without any functional ends, complete engulfment occurred while for the same NP with functional ends, two different regimes were observed. Below 70% functional ends, the engulfment percentage decreased with increasing

functional ends, which was attributed to the increased binding of functional end to membrane receptors that prevented the contact of NP with the inner hydrophobic part of the membrane. However, when the functional ends was >70%, more ligands could attach to membrane due to the enhanced interaction of functional ends with receptors, which led to partial wrapping of the NP.

To investigate the role of ligand distribution on NP internalization[25], icosahedral hydrophilic NP, a typical shape of viruses, was shown to undergo successful endocytosis with only 10% ligand coverage when its distribution on NP surface was uniform. On the other hand, no endocytosis was observed for 20% asymmetric distribution in the form of patches[69]. After the first ligand-receptor contacts are formed, subsequent NP wrapping is driven by energy decrease associated with further formation of ligand-receptor contacts. However, for asymmetric distribution of ligands on the NP surface, the wrapping process incurs a large penalty in bending energy before it can gain an energy decrease by new ligand-receptor contacts. In another study, Xue et al.[90] studied 3 ligand distributions (helical, abacus-like and smooth) on a rod-shaped NP (length/diameter = 5.5). Their result showed that helical NPs exhibited the best endocytosis efficiency, followed by smooth and abaus like NPs. The lowest efficiency of abacus-like NP was attributed to the its tip entry that caused large membrane curvature, while the other two NP underwent rotation during their endocytosis.

Shen et al. [91] investigated receptor mediated endocytosis of elastic NP covered by uniformly distributed ligand, with various NP's stiffness (0.1, 1, 10, and 100 ϵ , ϵ being basic unit of energy in their simulations) and size (8.8, 13.2, 17.6, and 22 nm). They found that membrane wrapping of the soft NPs was faster than that of the stiff NPs at the early stage. This was due to deformation of NP, which induced large contact area between the NPs and the membrane. However during late stage of membrane wrapping process , the wrapping speed of soft NPs slowed

down because of the large energy penalties induced by NP deformation. For large NP size (22 nm), difference in membrane wrapping efficiencies between soft and stiff NPs were insignificant, which was due to the stronger ligand-receptor binding force and smaller difference in the stiffness of elastic NPs (based on their virtual nano-indentation test on their simulated NPs).

One approach to enhance cellular uptake of NP is dual-ligand targeting, where NP is decorated with two different ligands that can interact with their receptors on membrane surface. Xia et al.[89] studied the influence of dual ligands on NP surface by using 2 type of receptors (beads with different affinity toward ligand beads), each covering 25% of the membrane surface. Two types of hydrophilic ligands, with length range of 1-5 beads, were covalently decorated on the NP surface at a 50:50 ratio. Their results showed higher engulfment efficiency compared to the use of single ligand when NPs were decorated with long ligands (3 to 5 beads), which was not the case for short ligand coated NPs (1 or 2 bead). The beneficial effect of long ligands was attributed to spontaneous rearrangement of dual ligands on the NP surface, which was limited for short ligands. Additionally, length mismatch between dual ligands had a negative effects on cellular uptake as longer ligands hindered the interaction of shorter ligands with their receptors.

A different application of ligand modified NPs is for the detection of circulating tumor cells (CTCs). Effective early detection of CTCs in the blood facilitated a means to detect metastatic potential before the formation of secondary tumors[92]. *Huang et al.*[93] using DPD simulations designed a new type of polymeric substrate containing NPs for detecting cancer cells from normal cells. They utilized 16 hydrophilic NPs (2.8 nm) with ligand density of 9.0 nm^{-2} (surface beads), and vesicles (11 nm) composed of receptors/lipid ratio of 1:1 as a representative of cancer cells and receptor/lipid ratio of 1:9 as a representative of normal cells. Their substrate was comprised of 3 layers of hydrophilic beads and polymers (15 hydrophilic beads) grafted to the substrate. They

observed that when the non-specific NP-polymer interaction was around $5 k_B T/r_c$, upon addition of shear flow the uptake number of NPs on the polymer layer representing cancer cells could be high, while it was nearly zero on the layer representing normal cells. However, when the non-specific NP-polymer interaction became weaker or stronger, uptake by cancer and normal cells could not be distinguished. Additionally, for better cancer cell detection, they suggested optimal values for the strength of the specific ligand-receptor interaction and the polymer density to be 5-7.5 kJ mol⁻¹ and 1.56 nm⁻², respectively. Xia et al.[94] based on their DPD simulations proposed non-covalent coating of protective copolymers onto NP surface to promote active targeting of NPs to the cancer cells. Two membrane models with receptor/lipid ratio of 6:4 and 1:9 were utilized to mimic cancer and normal cells. Hydrophilic NP (3 nm) covalently covered with hydrophilic ligands (1 functional head bead + 4 hydrophilic tail beads) was first interacted with non-covalently coated copolymer (6 non-specific beads and 3 specific beads that can weakly interact with the ligand). Afterwards, NP coated with protective copolymer was exposed to the substrate. This set up led to small probability of NP adsorption onto the normal cells while NP was totally engulfed by the cancer cell membrane along with detachments of most protective copolymers. Such methodology can be utilized to design NPs to maximize their different sensitive to normal and cancer cells.

2.3.1.5. Protein Adsorption on NPs

NPs typically encounter different proteins that adsorb on their surface. Some of the proteins could act as specific ligands for cell binding, such as Arginylglycylaspartic acid (RGD) sequence that can interact with integrin receptors. Plasma proteins can form a protein corona on NPs with 3-15 nm thickness.[95]·[96] ‘Hard’ corona is composed of proteins strongly bound on the surface, whereas the soft corona layer interacts weakly with hard corona.[65] vdW interactions, H-bonding,

electrostatic interactions, hydrophobic forces, and $\pi - \pi$ stacking all contribute to protein adsorption on NPs[97], with vdW interactions being the major contributor. Studies on protein coronas have been reviewed in detail before [95], [96], [98], [99]. As a representative study, silica NPs with and without pre-adsorbed proteins showed different internalization efficiencies, as well as differences in NP location after internalization (cytoplasm and lysosome in the case of silica NPs in serum-free medium vs. lysosome in the case of silica NP in protein-rich complete medium) [100].

Ding et al. [101] conducted a DPD study on the ability of two polymer coatings to resist protein adsorption on NP. Human serum albumin (HSA) was used as the adsorbing protein. A hydrophobic and a cationic NPs were coated with hydrophilic or zwitterionic polymers with different surface density and polymer length. Regardless of the type of polymer decoration, for the hydrophobic NP protein adsorption was mainly influenced by the surface density of polymers, while the polymer length controlled protein adsorption on cationic NP. Moderately long polymers inhibited protein adsorption by screening the long-range electrostatic interaction, while increasing the polymer length beyond a threshold did not affect protein adsorption. In a similar study[102], the adsorption of HSA on hydrophobic, hydrophilic, anionic and cationic NPs was investigated. The HSA only adsorbed onto charged and hydrophobic NPs, and the adsorption lowered the cellular uptake efficiency of NPs. It must be emphasized that while HSA is abundant in the plasma, various other proteins can adsorb onto NPs and change the nature of NP-cell membrane interaction.

2.3.1.6. Cooperative Effects of NPs

Unlike previous simulations on single NPs, delivery systems in reality are composed of many NPs that interact with cell membrane simultaneously, and among themselves. Yue et al.[103] simulated multiple hydrophobic NPs, coated with small ligands, on the surface of a lipid bilayer. Depending on the inter-particle distance and NP size, four different internalization pathways were observed: synchronous, where NPs were internalized simultaneously in an aggregated form; asynchronous, where larger NPs were internalized first followed by smaller NPs; independent, where each NP were wrapped by the membrane independently and the wrapping was from all sides of the NP; and pinocytosis-like, where the membrane protruded from one side to wrap a NP due to the hindrance from another nearby NP. Small (2.5 nm in diameter) NPs formed a cluster and were internalized as a whole. Intermediate (4 nm in diameter) NPs formed a pearl chain-like arrangement during internalization, while larger NPs were internalized individually. These observations can be attributed to the membrane mediated interaction among multiple NPs, which was highly sensitive to NP size. Direct internalization of small NP is associated with large energy penalty due to membrane bending, so they tend to aggregate as a remedy. Bending is reduced for larger NPs and exceeded by stronger receptor-ligand interaction; consequently internalization of larger NPs tend to be independent[103].

Yue et al. additionally investigated rod-like hydrophilic NPs with diameter of 4.52 nm and length 9.7 nm[104]. Weak adhesion (86 ligands/NP) led to slow membrane wrapping during which the NPs rearranged themselves, changing from the initial configuration of a parallel bundle to the final configuration where the NPs connected end-to-end to form a line. This observation was attributed to the shape anisotropy of NPs, which resulted in the heterogeneous distribution of NP-induced membrane deformations, with more severe membrane deformations at the NP ends.

Therefore, NPs tended to rotate and connect their ends to minimize local membrane perturbation induced by their ends. In the case of strong NP-membrane adhesion (174 ligands/NP), the wrapping process was in two stages, rapid wrapping and asymmetric wrapping (an unusual pathway different from endocytosis). In rapid wrapping, upon the initiation of NP rotation, the membrane prevented linear rearrangement. In the second stage, because of the strong NP-membrane attraction, the upper leaflet of the membrane started to protrude between two rod-like NPs, eventually leading to NPs embedded within the bilayer with the formation of inverted micelles around them where the hydrophilic lipid head groups were attached to the NPs and tail groups pointed outward. The asymmetrical wrapping also led to orientation-dependent interaction of these embedded NPs: the protrusion on the upper leaflet induced a short-range repulsion and intermediate-range attraction between two rod-shape NPs, and as the inter-NP distance was further increased, asymmetrical wrapping disappeared and the NPs departed from each other indicating a long-range repulsion between them.

Xiong et al.[105] conducted CGMD simulations to study wrapping of multiple NPs as a function of size, shape (spherical, prolate and oblate) and adhesion strength between NPs and cell membrane. They found that wrapping fraction increased with increasing adhesion strength, consistent with previous studies. Two approaches were used for adding multiple NPs: adding one NP at a time, and adding NPs simultaneously. In the first scenario for spherical NPs, depending on the size of NP, different wrapping structures were observed: from complete wrapping for large NPs, to partial wrapping with tubular vesicle for intermediate NPs, and partial wrapping with pocket-like vesicle for small NPs. During the formation of pocket-like vesicle, the lipid membranes surrounding the NPs hemifused together to increase the wrapping fraction of NPs. For the case in which spherical NPs were added simultaneously, two large NPs may be cooperatively or

individually wrapped by the lipid bilayer depending on their interparticle distance. For intermediate NP sizes, the membrane formed tubular structures to wrap multiple NPs, and sometimes detachment of tubular vesicle occurred. For small NPs, two vesicle structures, pocket-like (enclosing 4 NPs) and handle-like (enclosing 6 or 9 NPs), were observed. For prolate NP, a single large NP could not be completely wrapped by the lipid membrane due its large curvature. Intermediate prolate NPs were wrapped in a handle-like structure, while small prolate NPs were internalized by pocket-like structure. Large oblate NPs could be completely wrapped, while intermediate and small NPs induced tubular and pocket like membrane structures, respectively.

Direction of membrane bending can affect NP-membrane interaction. For example, NPs bound to the outer side of a cell membrane can induce endocytosis while those bound to the inner side can lead to exocytosis [106]. *Yan et al.* [107] performed systematic simulations to investigate the cooperative effects in the wrapping of multiple hydrophilic NPs at the same or opposite sides of a membrane. Studied spherical NPs had sizes of 3.5 nm and 6.5 nm, and half of their surface beads were set as ligands. For the NPs placed on the same side of the membrane, similar results as the ones discussed above were obtained. (1) Membrane wrapping and NP aggregation states were occurred. (2) The curvature-mediated interactions were either attractive or repulsive, depending on factors such as the initial NP distance and the competition between the membrane bending, NP binding and membrane protrusion. While for the NPs placed at opposite sides of a membrane, the interaction between two NPs was always attractive and cooperative wrapping of NPs was promoted, as the curved regions induced by the NPs were shared in a way that the NP-membrane contact was enhanced and the penalty of membrane bending was reduced.

Ni et al. [108] proposed a polymeric tether method to link two NPs in order to enhance or reduce the wrapping of NPs. Two NPs (6 nm) covered with hydrophilic ligands (surface density

of 4.5 nm^2) were covalently connected through a hydrophilic polymeric tether (3, 7, and 15 bead lengths). Upon attachment to the membrane (50% ligand coverage), the surface distance between two NPs significantly decreased to about 0.8 nm. The membrane lipids between the two NPs can be efficiently deformed which promoted the wrapping of NPs. The observation was due to reduction in total bending energy of membrane. With increase in polymer rigidity, the wrapping of two NPs decreased due to increase in energy to deform the tether, which could hinder the approaching of the NPs and weaken the cooperative wrapping. Additionally, for short and moderate polymer length (3 and 7 beads), both NPs were fully wrapped, while for the long length (15 beads), the wrapping of NP showed a decrease, suggesting that long polymer hindered the cooperative wrapping. When the NPs were linked using two polymer tethers, the cooperative wrapping decreased (lower wrapping percentage than single NP) due to the increased bond energy and the greater steric effect of two polymers [108].

2.3.2. Effect of Membrane Properties

Smith et al. [109] modeled interactions between a hydrophilic NP and two types of membranes: one uniformly adhesive and the other containing adhesive rafts (phase separated lipid islands)[110]. For the uniformly adhesive membrane, depending on the adhesion energy between NP and membrane, two possibilities emerged. Below an adhesion energy of $2044.8 k_B T / R_p^2$, R_p being the radius of the NP, the NP was partially wrapped by the membrane and remained attached to the bulk membrane through a stable, long-lasting neck. For the adhesion energy $> 2044.8 k_B T / R_p^2$, the NP was completely wrapped but remains trapped in the membrane. For the membrane containing adhesive rafts, NP was able to cross the lipid membrane. In this case, when

the NP was nearly fully wrapped, the rafts drove a fission process at the membrane neck, freeing the wrapped NP from the flat membrane.

Yang et al. [71] introduced a lipid raft in a lipidic vesicle. Spherical hydrophilic NP came close to the lipid raft, initiating the wrapping of the lipid bilayer around the NP. After complete wrapping, the shape of the lipid raft changed significantly, which led to an unstable lipid raft domain. Due to the small size of the vesicle, no adequate space was available to accommodate the lipid raft domain and the wrapped NP, leading to pinch-off of the NP rather than internalization (Figure 2.5).

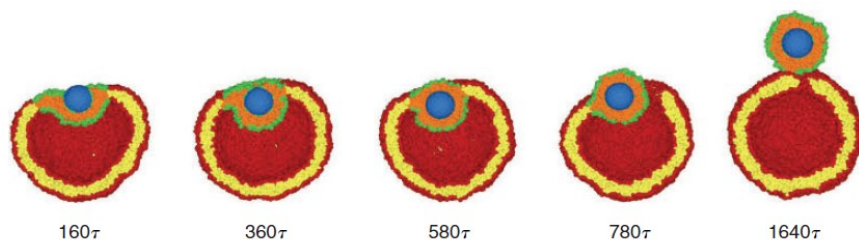


Figure 2.5. The cross-section view of wrapping and pinching off of lipid raft covered NP.

Green: heads of lipid raft, orange: tails of lipid raft, red: heads of membrane lipids, yellow: tails of membrane lipids, blue: NP[71]

Lin et al. [111] explored the interaction of a ligand modified hydrophobic spherical NP (~2.2 nm) with a lipid bilayer containing raft domains. The membrane was modeled using Martini CG model of saturated DPPC, unsaturated dinoleoylphosphatidylcholine (DUPC) and cholesterol(CHOL) with molar ratio of 5:3:2. Three ligand densities of 30, 60, and 100% were used to cover the NP surface, which had different ligand length varying from 1 to 5 beads, as well as two different hydrophobicities (high hydrophobic ligand vs. low hydrophobic ligand). More hydrophobic NPs (high density, high hydrophobicity, and high ligand length) tended to interact with

the raft domain, while less hydrophobic NPs preferred the non-raft domain. *Yang et al.* [112] using a similar set up investigated the interplay between hydrophilic NP (1 and 3 nm size) and a three-component lipid bilayer with composition ratio of DPPC/DUPC/CHOL = 0.35/0.35/0.3. They found that NPs were able to preferentially locate at the liquid disordered (Ld) phase domains. The preferential partitioning behaviour of NPs was associated with physical properties of membrane (e.g., the membrane stiffness) and NPs (e.g., size and quantity). Additionally, the preferred partitioning of NPs promoted the growth of Ld domain. It worth noting that due to hydrophilic characteristics of the NP simulated, it remained at the surface of lipidic membrane and no internalization was observed.

Membranes may experience oxidative stress, which has paramount importance on cell aging, cancer, and neurodegenerative diseases [113]. It is known that unsaturated bonds of lipids react with singlet oxygen, causing the addition of peroxide group to the carbon chain, along with a shift of the double bond and its cis to trans conversion[114]. *Su et al.* [114] using MARTINI CG model investigated the effect of peroxidation of lipid bilayer on the passive translocation of small NPs (~ 1 nm) of varying hydrophobicity. Oxidation of membrane caused an expansion of the area per lipid, accompanied by the decrease of membrane thickness and a significant drop of the stretching modulus of membrane. Similar results was also observed in CG simulations of Aceves-Luna et al.[115]. Additionally, the membrane permeability for solvent increased upon peroxidation. These changes led to significant increase in the translocation rate of NPs (at optimum hydrophobicity) compared to non-oxidized bilayers.

Membrane curvatures generated from embedded proteins also lead to a wide range of cell shapes[116] that can affect the interaction with NPs. Reynwar et al.[48] conducted one of the earliest CGMD simulation on the impact of curvature-inducing proteins on the wrapping of

external particles. Their simplified curvature-inducing proteins included 2 curved caps of different sizes and a capsid. These protein models were placed on the surface of a membrane. The outer surface of the proteins attracts hydrophilic lipid beads, thus locally curving the membrane. Sufficiently large membrane curvature drove protein clustering and subsequent transformation of the lipid membrane into internalizing vesicles around the proteins.

2.4. AA simulation of Cell Membrane-NP Interactions

The literature reviewed above are all at CG level which, although allowed longer simulations for larger systems compared with AA simulations, were incapable of capturing the molecular details such as the difference between different cell receptors and NP carriers. CG simulations also cannot capture the role of H-bonding, which may dictate the interaction of NP with cell surfaces. AA simulations will be better in illuminating the actual interaction of NPs with the membranes, but have higher computing requirements. Because of this, AA simulations targeting NP-membrane interaction are almost non-existent. Prior to our recent AA work[117], there were only three AA studies[118]–[120] that considered carrier-membrane and DNA-membrane interactions.

Choudhury et al.[118] used AA MD simulations to investigate the effect of surface charge (completely protonated vs. unprotonated Ns) of linear PEI (IPEI), in absence of any polynucleotides, on its interactions with a dioleoylsnglycerophosphocholine (DOPC) membrane. Fully protonated IPEI chain induced water/ion channels through the membrane, and formed elongated conformations due to the electrostatic repulsion among the protonated amine groups. During the internalization, the IPEI formed contact with head groups of both leaflets of the membrane, which was accommodated by the re-orientation of the lipid molecules around the PEI

chain. On the other hand, the unprotonated IPEI formed a highly coiled configuration that predominantly resided at the bilayer-water interface.

In a recent AA study by Kwolek et al.[119], zwitterionic and anionic membranes were constructed from palmitoyloleoylphosphatidylcholine (POPC) and POPC/dioleoylglycerophosphoric acid (DOPA) mixtures, respectively. 30% protonated branched PEI (bPEI) and IPEI were placed at the surface or inside the membrane. For polymers placed at the surface of zwitterionic membrane, both bPEI and IPEI showed no tendency to bind, remaining in the bulk solution. In the case of anionic membrane, both polymers showed high affinity to the lipid membrane, but no full internalization occurred during the 200 ns simulation. The interaction between the lipids and PEIs are mainly through the H-bond formation between the PEI amines and Os in the phosphate or ester groups of the lipids, which is negligible in the case of zwitterionic membrane but significant in the case of anionic membrane. PEIs pre-embedded in the membrane did not leave the membrane and caused some phosphate groups to rearrange themselves toward the hydrophobic core of the bilayer to shield the polar polymer amines from the hydrophobic part of the membrane. This observation was consistent with that of Choudhury et al.[118], and was more pronounced in the anionic membrane where the reorientation led to pore formation that allowed water to cross the membrane[119]. The PEI-induced perturbation in cell membrane by altering the distribution of anionic lipids may imply cytotoxicity of the PEIs, which cannot be captured by CG simulations.

To better understand DNA uptake, which is not expected to occur in the absence of carriers, Antipina et al[120] recently utilized umbrella sampling to generate the free energy profile of a bare 22 bp DNA across two zwitterionic POPC bilayers, with and without pre-adsorbed Ca^{2+} ions. As the DNA approached and crossed the zwitterionic bilayer, the free energy monotonically

increased, indicating a lack of attraction. On the other hand, a free energy minimum was found in the presence of Ca^{2+} , which was attributed to electrostatic attraction between the anionic DNA and Ca^{2+} ions on the surface of the bilayer, leading to a stable configuration of the DNA near the lipid bilayer.

While AA simulations on NP-membrane interaction have been limited, many AA simulations have been performed on the complexation of polynucleotides with carriers. These simulations have prepared NPs that can be adopted in NP-membrane simulations. As a representative of cationic polymers, PEI is one of the most promising polymers with the advantage of being easily modified with functional groups and have been widely studied in gene delivery applications. AA simulations significantly enhanced our understanding on the complexation and decomplexation of PEI with polynucleotides[27]. Factors that have been considered by AA simulations include protonation state[121], polymer structure[122], lipidic and hydrophobic modifications of PEI [123], [124], and effect of destabilizing compounds such as heparin on the formed complexes[125]. However, the entire process of polynucleotide delivery is vastly understudied.

Based on these AA models, recently our group made the first step towards simulating NP-membrane interaction at the AA level. Specifically, the membrane penetration process of a NP formed by 2 siRNA and 6 PEI molecules was simulated using Steered Molecular Dynamics [117]. Three types of PEIs were considered, a native one (without any modification), one modified with caprylic acid and the third modified with linoleic acid. During the internalization, H-bond formation between PEI and the membrane did not cause instability of the NPs. Instead, the NP adopted “self-protecting” configurations with a more compact structure and more aligned siRNAs while detaching from the membrane. NP modified with linoleic acid exhibited the smallest

structural change due to its strong intra-particle lipid association, while largest changes was observed for NP modified with caprylic acid. These observations provided unique insight into structural changes of siRNA/PEI NPs during penetration that are pertinent to the design of new carriers for effective polynucleotide delivery.

2.5. Machine Learning of Cell Membrane-NP Interactions

Artificial intelligent (AI) can significantly help us to understand NP uptake through a set of existing experimental data to train and test the model generated by machine learning techniques such as neural networks. The use of nano-quantitative structure activity relationship (QSAR) methods in this area could be very useful especially due to significant development cost of novel NPs with the desired properties. The core assumption in these methods is that variation in the biological activities of a compound is correlated with changes in its molecular structure. In such method, many descriptors can be considered simultaneously by the AI and each descriptor will be attributed a weight to represent its relative importance. The literature using machine learning to predict cellular uptake of NPs is emerging [128]. However, there are no systematic investigation on cellular uptake prediction of NPs using easy to interpret descriptor. These descriptors will help design of more potent gene delivery vehicle.

2.6. Conclusion

This chapter highlights recent progress on NP-cell membrane interaction studied by molecular simulations. Several parameters were found to be critical in NP- membrane interaction and subsequent internalization . While these parameters do not independently affect the cellular uptake and intracellular pathway, molecular simulations were able to provide some insights regarding the influence of each parameter, which points to directions in which experiments can be done to design, synthesis and test potent NPs as gene delivery systems. For example, one approach to

enhance cellular uptake of NPs is dual-ligand targeting, where each NP is decorated with two different ligands that can interact with their complementary receptors on the membrane surface. Simulation showed that this method is effective when the two ligands are both long, of similar length and have a uniform distribution on the NP surface. Based on this result, a set of experiments can be designed to modify the NPs and monitor their uptake by different cell lines. While past molecular simulations have shed light on the interaction of polynucleotide NP with cell membrane, much remains to be explored especially atomistic level details on the intracellular events of the delivery process of NP. This is important since it may facilitate the design of better delivery vectors.

2.7. Acknowledgments

Compute Canada and Westgrid are gratefully acknowledged for providing the computing resources and technical support. This work was funded by the Natural Sciences and Engineering Research Council of Canada (NSERC), Canadian Institutes of Health Research (CIHR) and Alberta Innovates Technology Futures (AITF).

2.8. References

- [1] H. Ding and Y. Ma, “Theoretical and Computational Investigations of Nanoparticle-Biomembrane Interactions in Cellular Delivery,” *Small*, vol. 11, no. 9–10, pp. 1055–1071, Mar. 2015, doi: 10.1002/sml.201401943.
- [2] A. A. Gurtovenko, J. Anwar, and I. Vattulainen, “Defect-mediated trafficking across cell membranes: insights from in silico modeling,” *Chem. Rev.*, vol. 110, no. 10, pp. 6077–6103, 2010.
- [3] H. Nakamura and S. Watano, “Direct Permeation of Nanoparticles across Cell Membrane: A Review,” *KONA Powder Part. J.*, vol. 35, no. 35, pp. 49–65, 2018, doi: 10.14356/kona.2018011.
- [4] I. a Khalil, K. Kogure, H. Akita, and H. Harashima, “Uptake pathways and subsequent intracellular trafficking in nonviral gene delivery,” *Pharmacol. Rev.*, vol. 58, no. 1, pp. 32–45, Mar. 2006, doi: 10.1124/pr.58.1.8.

- [5] S. Zhang, H. Gao, and G. Bao, “Physical Principles of Nanoparticle Cellular Endocytosis,” *ACS Nano*, vol. 9, no. 9, pp. 8655–8671, Sep. 2015, doi: 10.1021/acsnano.5b03184.
- [6] G. Sahay, D. Y. Alakhova, and A. V. Kabanov, “Endocytosis of nanomedicines,” *J. Control. Release*, vol. 145, no. 3, pp. 182–195, Aug. 2010, doi: 10.1016/j.jconrel.2010.01.036.
- [7] L. Kou, J. Sun, Y. Zhai, and Z. He, “The endocytosis and intracellular fate of nanomedicines: Implication for rational design,” *Asian J. Pharm. Sci.*, vol. 8, no. 1, pp. 1–8, 2013, doi: 10.1016/j.ajps.2013.07.001.
- [8] A. Aderem and D. M. Underhill, “MECHANISMS OF PHAGOCYTOSIS IN MACROPHAGES,” *Annu. Rev. Immunol.*, vol. 17, no. 1, pp. 593–623, Apr. 1999, doi: 10.1146/annurev.immunol.17.1.593.
- [9] S. Xiang *et al.*, “Uptake mechanisms of non-viral gene delivery,” *J. Control. Release*, vol. 158, no. 3, pp. 371–378, Mar. 2012, doi: 10.1016/j.jconrel.2011.09.093.
- [10] J. P. Lim and P. A. Gleeson, “Macropinocytosis: an endocytic pathway for internalising large gulps,” *Immunol. Cell Biol.*, vol. 89, no. 8, pp. 836–843, Nov. 2011, doi: 10.1038/icb.2011.20.
- [11] S. Falcone, E. Cocucci, P. Podini, T. Kirchhausen, E. Clementi, and J. Meldolesi, “Macropinocytosis: regulated coordination of endocytic and exocytic membrane traffic events,” *J. Cell Sci.*, vol. 119, no. 22, pp. 4758–4769, 2006, doi: 10.1242/jcs.03238.
- [12] M. Hamasaki, N. Araki, and T. Hatae, “Association of early endosomal autoantigen 1 with macropinocytosis in EGF-stimulated a431 cells,” *Anat. Rec.*, vol. 277A, no. 2, pp. 298–306, Apr. 2004, doi: 10.1002/ar.a.20027.
- [13] S. D. Conner and S. L. Schmid, “Regulated portals of entry into the cell,” *Nature*, vol. 422, no. 6927, pp. 37–44, Mar. 2003, doi: 10.1038/nature01451.
- [14] J. Z. Rappoport, “Focusing on clathrin-mediated endocytosis,” *Biochem. J.*, vol. 412, no. 3, pp. 415–423, Jun. 2008, doi: 10.1042/BJ20080474.
- [15] J. REJMAN, V. OBERLE, I. S. ZUHORN, and D. HOEKSTRA, “Size-dependent internalization of particles via the pathways of clathrin- and caveolae-mediated endocytosis,” *Biochem. J.*, vol. 377, no. 1, pp. 159–169, Jan. 2004, doi: 10.1042/bj20031253.
- [16] H. Hillaireau and P. Couvreur, “Nanocarriers’ entry into the cell: relevance to drug delivery,” *Cell. Mol. Life Sci.*, vol. 66, no. 17, pp. 2873–2896, Sep. 2009, doi: 10.1007/s00018-009-0053-z.
- [17] L. BAREFORD and P. SWAAN, “Endocytic mechanisms for targeted drug delivery☆,” *Adv. Drug Deliv. Rev.*, vol. 59, no. 8, pp. 748–758, Aug. 2007, doi: 10.1016/j.addr.2007.06.008.
- [18] G. J. Doherty and H. T. McMahon, “Mechanisms of Endocytosis,” *Annu. Rev. Biochem.*,

- vol. 78, no. 1, pp. 857–902, Jun. 2009, doi: 10.1146/annurev.biochem.78.081307.110540.
- [19] S. Y. Wong, J. M. Pelet, and D. Putnam, “Polymer systems for gene delivery—Past, present, and future,” *Prog. Polym. Sci.*, vol. 32, no. 8–9, pp. 799–837, Aug. 2007, doi: 10.1016/j.progpolymsci.2007.05.007.
- [20] C. Pichon, L. Billiet, and P. Midoux, “Chemical vectors for gene delivery: uptake and intracellular trafficking,” *Curr. Opin. Biotechnol.*, vol. 21, no. 5, pp. 640–645, Oct. 2010, doi: 10.1016/j.copbio.2010.07.003.
- [21] I. Kopatz, J.-S. Remy, and J.-P. Behr, “A model for non-viral gene delivery: through syndecan adhesion molecules and powered by actin,” *J. Gene Med.*, vol. 6, no. 7, pp. 769–776, Jul. 2004, doi: 10.1002/jgm.558.
- [22] J. L. Dreyfuss, C. V. Regatieri, T. R. Jarrouge, R. P. Cavalheiro, L. O. Sampaio, and H. B. Nader, “Heparan sulfate proteoglycans: structure, protein interactions and cell signaling,” *An. Acad. Bras. Cienc.*, vol. 81, no. 3, pp. 409–429, Sep. 2009, doi: 10.1590/S0001-37652009000300007.
- [23] D. Frenkel, B. Smit, and M. A. Ratner, “Understanding Molecular Simulation: From Algorithms to Applications,” *Phys. Today*, vol. 50, no. 7, pp. 66–66, Jul. 1997, doi: 10.1063/1.881812.
- [24] F. Tian, T. Yue, Y. Li, and X. Zhang, “Computer simulation studies on the interactions between nanoparticles and cell membrane,” *Sci. China Chem.*, vol. 57, no. 12, pp. 1662–1671, Dec. 2014, doi: 10.1007/s11426-014-5231-7.
- [25] G. Rossi and L. Monticelli, “Simulating the interaction of lipid membranes with polymer and ligand-coated nanoparticles,” *Adv. Phys. X*, vol. 1, no. 2, pp. 276–296, Mar. 2016, doi: 10.1080/23746149.2016.1177468.
- [26] C. M. Beddoes, C. P. Case, and W. H. Briscoe, “Understanding nanoparticle cellular entry: A physicochemical perspective,” *Adv. Colloid Interface Sci.*, vol. 218, pp. 48–68, Apr. 2015, doi: 10.1016/j.cis.2015.01.007.
- [27] D. Meneksedag-Erol, T. Tang, and H. Uludağ, “Molecular modeling of polynucleotide complexes,” *Biomaterials*, vol. 35, no. 25, pp. 7068–7076, Aug. 2014, doi: 10.1016/j.biomaterials.2014.04.103.
- [28] S. J. Marrink, A. H. de Vries, and D. P. Tieleman, “Lipids on the move: Simulations of membrane pores, domains, stalks and curves,” *Biochim. Biophys. Acta - Biomembr.*, vol. 1788, no. 1, pp. 149–168, Jan. 2009, doi: 10.1016/j.bbamem.2008.10.006.
- [29] S. J. Marrink, H. J. Risselada, S. Yefimov, D. P. Tieleman, and A. H. De Vries, “The MARTINI force field: coarse grained model for biomolecular simulations,” *J. Phys. Chem. B*, vol. 111, no. 27, pp. 7812–7824, 2007.
- [30] P. J. Hoogerbrugge and J. M. V. A. Koelman, “Simulating Microscopic Hydrodynamic Phenomena with Dissipative Particle Dynamics,” *Europhys. Lett.*, vol. 19, no. 3, pp. 155–160, Jun. 1992, doi: 10.1209/0295-5075/19/3/001.

- [31] R. D. Groot and P. B. Warren, “Dissipative particle dynamics: Bridging the gap between atomistic and mesoscopic simulation,” *J. Chem. Phys.*, vol. 107, no. 11, pp. 4423–4435, Sep. 1997, doi: 10.1063/1.474784.
- [32] P. L. Yeagle, *The structure of biological membranes*. CRC press, 2011.
- [33] K. Simons and E. Ikonen, “Functional rafts in cell membranes,” *Nature*, vol. 387, no. 6633, p. 569, 1997.
- [34] K. Simons and W. L. C. Vaz, “Model systems, lipid rafts, and cell membranes,” *Annu. Rev. Biophys. Biomol. Struct.*, vol. 33, pp. 269–295, 2004.
- [35] E. Sezgin, I. Levental, S. Mayor, and C. Eggeling, “The mystery of membrane organization: composition, regulation and roles of lipid rafts,” *Nat. Rev. Mol. Cell Biol.*, vol. 18, no. 6, pp. 361–374, Mar. 2017, doi: 10.1038/nrm.2017.16.
- [36] E. Rascol, J.-M. Devoisselle, and J. Chopineau, “The relevance of membrane models to understand nanoparticles–cell membrane interactions,” *Nanoscale*, vol. 8, no. 9, pp. 4780–4798, 2016, doi: 10.1039/C5NR07954C.
- [37] M. VENTUROLI, M. MADDALENASPEROTTO, M. KRANENBURG, and B. SMIT, “Mesoscopic models of biological membranes,” *Phys. Rep.*, vol. 437, no. 1–2, pp. 1–54, Dec. 2006, doi: 10.1016/j.physrep.2006.07.006.
- [38] G. Van Meer, D. R. Voelker, and G. W. Feigenson, “Membrane lipids: Where they are and how they behave,” *Nat. Rev. Mol. Cell Biol.*, vol. 9, no. 2, pp. 112–124, 2008, doi: 10.1038/nrm2330.
- [39] J. A. McCammon and Y. Wang, “Lipid Bilayers: Structure, Dynamics, and Interactions with Antimicrobial Peptides,” in *Molecular Modeling at the Atomic Scale*, CRC Press, 2014, pp. 210–233.
- [40] I. Chandrasekhar *et al.*, “A consistent potential energy parameter set for lipids: dipalmitoylphosphatidylcholine as a benchmark of the GROMOS96 45A3 force field,” *Eur. Biophys. J.*, vol. 32, no. 1, pp. 67–77, 2003.
- [41] L. D. Schuler, X. Daura, and W. F. Van Gunsteren, “An improved GROMOS96 force field for aliphatic hydrocarbons in the condensed phase,” *J. Comput. Chem.*, vol. 22, no. 11, pp. 1205–1218, 2001.
- [42] J. B. Klauda *et al.*, “Update of the CHARMM all-atom additive force field for lipids: validation on six lipid types,” *J. Phys. Chem. B*, vol. 114, no. 23, pp. 7830–7843, Jun. 2010, doi: 10.1021/jp101759q.
- [43] S. J. Marrink, A. H. De Vries, and A. E. Mark, “Coarse grained model for semiquantitative lipid simulations,” *J. Phys. Chem. B*, vol. 108, no. 2, pp. 750–760, 2004.
- [44] I. R. Cooke, K. Kremer, and M. Deserno, “Tunable generic model for fluid bilayer membranes,” *Phys. Rev. E*, vol. 72, no. 1, p. 11506, 2005.

- [45] A. E. Nel *et al.*, “Understanding biophysicochemical interactions at the nano–bio interface,” *Nat. Mater.*, vol. 8, no. 7, pp. 543–557, Jul. 2009, doi: 10.1038/nmat2442.
- [46] M. Deserno and T. Bickel, “Wrapping of a spherical colloid by a fluid membrane,” *Europhys. Lett.*, vol. 62, no. 5, pp. 767–774, Jun. 2003, doi: 10.1209/epl/i2003-00438-4.
- [47] M. Deserno, “Elastic deformation of a fluid membrane upon colloid binding,” *Phys. Rev. E*, vol. 69, no. 3, pp. 1–14, 2004, doi: 10.1103/PhysRevE.69.031903.
- [48] B. J. Reynwar, G. Illya, V. A. Harmandaris, M. M. Müller, K. Kremer, and M. Deserno, “Aggregation and vesiculation of membrane proteins by curvature-mediated interactions,” *Nature*, vol. 447, no. 7143, pp. 461–464, May 2007, doi: 10.1038/nature05840.
- [49] W. Helfrich, J. Charvolin, J. F. Joanny, and J. Zinn-Justin, “Liquids at interfaces,” *Les Houches Sess. XLVIII*, 1990.
- [50] W. Helfrich, “Elastic properties of lipid membranes: theory and possible experiments,” *Zeitschrift für Naturforsch. C*, vol. 28, p. 693703, 1973.
- [51] A. H. Bahrami, R. Lipowsky, and T. R. Weigl, “The role of membrane curvature for the wrapping of nanoparticles,” *Soft Matter*, vol. 12, no. 2, pp. 581–587, 2016, doi: 10.1039/C5SM01793A.
- [52] R. Vácha, F. J. Martinez-Veracoechea, and D. Frenkel, “Receptor-Mediated Endocytosis of Nanoparticles of Various Shapes,” *Nano Lett.*, vol. 11, no. 12, pp. 5391–5395, Dec. 2011, doi: 10.1021/nl2030213.
- [53] T. Yue and X. Zhang, “Molecular understanding of receptor-mediated membrane responses to ligand-coated nanoparticles,” *Soft Matter*, vol. 7, no. 19, p. 9104, 2011, doi: 10.1039/c1sm05398a.
- [54] H. Ding, W. Tian, and Y. Ma, “Designing Nanoparticle Translocation through Membranes by Computer Simulations,” *ACS Nano*, vol. 6, no. 2, pp. 1230–1238, Feb. 2012, doi: 10.1021/nn2038862.
- [55] T. Yue, X. Zhang, and F. Huang, “Molecular modeling of membrane responses to the adsorption of rotating nanoparticles: promoted cell uptake and mechanical membrane rupture,” *Soft Matter*, vol. 11, no. 3, pp. 456–465, 2015, doi: 10.1039/C4SM01760A.
- [56] X. Lin, Y. Li, and N. Gu, “Nanoparticle’s Size Effect on Its Translocation Across a Lipid Bilayer: A Molecular Dynamics Simulation,” *J. Comput. Theor. Nanosci.*, vol. 7, no. 1, pp. 269–276, Jan. 2010, doi: 10.1166/jctn.2010.1358.
- [57] E. M. Curtis, A. H. Bahrami, T. R. Weigl, and C. K. Hall, “Modeling nanoparticle wrapping or translocation in bilayer membranes,” *Nanoscale*, vol. 7, no. 34, pp. 14505–14514, 2015, doi: 10.1039/C5NR02255J.
- [58] X. Chen, F. Tian, X. Zhang, and W. Wang, “Internalization pathways of nanoparticles and their interaction with a vesicle,” *Soft Matter*, vol. 9, no. 31, p. 7592, 2013, doi: 10.1039/c3sm50931a.

- [59] E. Zhang, M. F. Kircher, M. Koch, L. Eliasson, S. N. Goldberg, and E. Renström, “Dynamic Magnetic Fields Remote-Control Apoptosis via Nanoparticle Rotation,” *ACS Nano*, vol. 8, no. 4, pp. 3192–3201, Apr. 2014, doi: 10.1021/nn406302j.
- [60] K. Yang and Y.-Q. Ma, “Computer simulation of the translocation of nanoparticles with different shapes across a lipid bilayer,” *Nat. Nanotechnol.*, vol. 5, no. 8, pp. 579–583, Aug. 2010, doi: 10.1038/nnano.2010.141.
- [61] H. Ding and Y. Ma, “Interactions between Janus particles and membranes,” *Nanoscale*, vol. 4, no. 4, pp. 1116–1122, 2012, doi: 10.1039/C1NR11425E.
- [62] H. Gao, W. Shi, and L. B. Freund, “Mechanics of receptor-mediated endocytosis,” *Proc. Natl. Acad. Sci.*, vol. 102, no. 27, pp. 9469–9474, Jul. 2005, doi: 10.1073/pnas.0503879102.
- [63] V. B. Shenoy and L. B. Freund, “Growth and shape stability of a biological membrane adhesion complex in the diffusion-mediated regime,” *Proc. Natl. Acad. Sci.*, vol. 102, no. 9, pp. 3213–3218, Mar. 2005, doi: 10.1073/pnas.0500368102.
- [64] S. Tzllil, M. Deserno, W. M. Gelbart, and A. Ben-Shaul, “A Statistical-Thermodynamic Model of Viral Budding,” *Biophys. J.*, vol. 86, no. 4, pp. 2037–2048, Apr. 2004, doi: 10.1016/S0006-3495(04)74265-4.
- [65] A. Albanese, P. S. Tang, and W. C. W. Chan, “The Effect of Nanoparticle Size, Shape, and Surface Chemistry on Biological Systems,” *Annu. Rev. Biomed. Eng.*, vol. 14, no. 1, pp. 1–16, Aug. 2012, doi: 10.1146/annurev-bioeng-071811-150124.
- [66] S. E. A. Gratton *et al.*, “The effect of particle design on cellular internalization pathways,” *Proc. Natl. Acad. Sci.*, vol. 105, no. 33, pp. 11613–11618, Aug. 2008, doi: 10.1073/pnas.0801763105.
- [67] B. D. Chithrani, A. A. Ghazani, and W. C. W. Chan, “Determining the Size and Shape Dependence of Gold Nanoparticle Uptake into Mammalian Cells,” *Nano Lett.*, vol. 6, no. 4, pp. 662–668, Apr. 2006, doi: 10.1021/nl052396o.
- [68] Y. Liu, B. Peng, S. Sohrabi, and Y. Liu, “The Configuration of Copolymer Ligands on Nanoparticles Affects Adhesion and Uptake,” *Langmuir*, vol. 32, no. 39, pp. 10136–10143, Oct. 2016, doi: 10.1021/acs.langmuir.6b02371.
- [69] V. Schubertová, F. J. Martinez-Veracoechea, and R. Vácha, “Influence of ligand distribution on uptake efficiency,” *Soft Matter*, vol. 11, no. 14, pp. 2726–2730, 2015, doi: 10.1039/C4SM02815E.
- [70] S. Nangia and R. Sureshkumar, “Effects of Nanoparticle Charge and Shape Anisotropy on Translocation through Cell Membranes,” *Langmuir*, vol. 28, no. 51, pp. 17666–17671, Dec. 2012, doi: 10.1021/la303449d.
- [71] K. Yang and Y. Ma, “Wrapping and Internalization of Nanoparticles by Lipid Bilayers: a Computer Simulation Study,” *Aust. J. Chem.*, vol. 64, no. 7, p. 894, 2011, doi: 10.1071/CH11053.

- [72] Y. Li, T. Yue, K. Yang, and X. Zhang, "Molecular modeling of the relationship between nanoparticle shape anisotropy and endocytosis kinetics," *Biomaterials*, vol. 33, no. 19, pp. 4965–4973, Jun. 2012, doi: 10.1016/j.biomaterials.2012.03.044.
- [73] J. Li *et al.*, "Why synthetic virus-like nanoparticles can achieve higher cellular uptake efficiency?," *Nanoscale*, vol. 12, no. 27, pp. 14911–14918, 2020.
- [74] C. Huang, Y. Zhang, H. Yuan, H. Gao, and S. Zhang, "Role of Nanoparticle Geometry in Endocytosis: Laying Down to Stand Up," *Nano Lett.*, vol. 13, no. 9, pp. 4546–4550, Sep. 2013, doi: 10.1021/nl402628n.
- [75] L. Zhang, Y. Zhao, and X. Wang, "Nanoparticle-mediated mechanical destruction of cell membranes: A coarse-grained molecular dynamics study," *ACS Appl. Mater. Interfaces*, vol. 9, no. 32, pp. 26665–26673, 2017.
- [76] Y. Li, X. Chen, and N. Gu, "Computational Investigation of Interaction between Nanoparticles and Membranes: Hydrophobic/Hydrophilic Effect," *J. Phys. Chem. B*, vol. 112, no. 51, pp. 16647–16653, Dec. 2008, doi: 10.1021/jp8051906.
- [77] A. Verma and F. Stellacci, "Effect of Surface Properties on Nanoparticle Cell Interactions," *Small*, vol. 6, no. 1, pp. 12–21, Jan. 2010, doi: 10.1002/smll.200901158.
- [78] M. Werner, J.-U. U. Sommer, and V. A. Baulin, "Homo-polymers with balanced hydrophobicity translocate through lipid bilayers and enhance local solvent permeability," *Soft Matter*, vol. 8, no. 46, p. 11714, 2012, doi: 10.1039/c2sm26008e.
- [79] Y. Li, X. Li, Z. Li, and H. Gao, "Surface-structure-regulated penetration of nanoparticles across a cell membrane," *Nanoscale*, vol. 4, no. 12, pp. 3768–3775, 2012, doi: 10.1039/c2nr30379e.
- [80] S. Wang, H. Guo, Y. Li, and X. Li, "Penetration of nanoparticles across a lipid bilayer: effects of particle stiffness and surface hydrophobicity," *Nanoscale*, vol. 11, no. 9, pp. 4025–4034, 2019.
- [81] N. Arai, K. Yasuoka, and X. C. Zeng, "A vesicle cell under collision with a Janus or homogeneous nanoparticle: translocation dynamics and late-stage morphology," *Nanoscale*, vol. 5, no. 19, pp. 9089–9100, 2013.
- [82] A. C. Balazs, O. Kuksenok, and A. Alexeev, "Modeling the Interactions between Membranes and Inclusions: Designing Self-Cleaning Films and Resealing Pores," *Macromol. Theory Simulations*, vol. 18, no. 1, pp. 11–24, 2009.
- [83] A. Alexeev, W. E. Uspal, and A. C. Balazs, "Harnessing Janus nanoparticles to create controllable pores in membranes," *ACS Nano*, vol. 2, no. 6, pp. 1117–1122, 2008.
- [84] L. Zhang, M. Becton, and X. Wang, "Designing Nanoparticle Translocation through Cell Membranes by Varying Amphiphilic Polymer Coatings," *J. Phys. Chem. B*, vol. 119, no. 9, pp. 3786–3794, Mar. 2015, doi: 10.1021/acs.jpcc.5b00825.
- [85] Y. Liu *et al.*, "Design of small nanoparticles decorated with amphiphilic ligands: self-

- preservation effect and translocation into a plasma membrane,” *ACS Appl. Mater. Interfaces*, vol. 11, no. 27, pp. 23822–23831, 2019.
- [86] H. Ding and Y. Ma, “Controlling Cellular Uptake of Nanoparticles with pH-Sensitive Polymers,” *Sci. Rep.*, vol. 3, no. 1, p. 2804, Dec. 2013, doi: 10.1038/srep02804.
- [87] H. Ding and Y. Ma, “Role of physicochemical properties of coating ligands in receptor-mediated endocytosis of nanoparticles,” *Biomaterials*, vol. 33, no. 23, pp. 5798–5802, Aug. 2012, doi: 10.1016/j.biomaterials.2012.04.055.
- [88] H. Yuan and S. Zhang, “Effects of particle size and ligand density on the kinetics of receptor-mediated endocytosis of nanoparticles,” *Appl. Phys. Lett.*, vol. 96, no. 3, p. 033704, Jan. 2010, doi: 10.1063/1.3293303.
- [89] Q. Xia, H. Ding, and Y. Ma, “Can dual-ligand targeting enhance cellular uptake of nanoparticles?,” *Nanoscale*, vol. 9, no. 26, pp. 8982–8989, 2017, doi: 10.1039/C7NR01020F.
- [90] J. Xue, Z. Guan, J. Lin, C. Cai, W. Zhang, and X. Jiang, “Cellular Internalization of Rod-Like Nanoparticles with Various Surface Patterns: Novel Entry Pathway and Controllable Uptake Capacity,” *small*, vol. 13, no. 24, p. 1604214, 2017.
- [91] Z. Shen, H. Ye, and Y. Li, “Understanding receptor-mediated endocytosis of elastic nanoparticles through coarse grained molecular dynamic simulation,” *Phys. Chem. Chem. Phys.*, vol. 20, no. 24, pp. 16372–16385, 2018.
- [92] D. F. Hayes *et al.*, “Circulating tumor cells at each follow-up time point during therapy of metastatic breast cancer patients predict progression-free and overall survival,” *Clin. Cancer Res.*, vol. 12, no. 14, pp. 4218–4224, 2006.
- [93] L. Huang, Y. Yu, X. Lu, H. Ding, and Y. Ma, “Designing a nanoparticle-containing polymeric substrate for detecting cancer cells by computer simulations,” *Nanoscale*, vol. 11, no. 5, pp. 2170–2178, 2019.
- [94] Q. Xia, T. Zhu, Z. Jiang, H. Ding, and Y. Ma, “Enhancing the targeting ability of nanoparticles via protected copolymers,” *Nanoscale*, vol. 12, no. 14, pp. 7804–7813, 2020.
- [95] B. Kharazian, N. L. Hadipour, and M. R. Ejtehadi, “Understanding the nanoparticle–protein corona complexes using computational and experimental methods,” *Int. J. Biochem. Cell Biol.*, vol. 75, pp. 162–174, Jun. 2016, doi: 10.1016/j.biocel.2016.02.008.
- [96] C. C. Fleischer and C. K. Payne, “Nanoparticle–Cell Interactions: Molecular Structure of the Protein Corona and Cellular Outcomes,” *Acc. Chem. Res.*, vol. 47, no. 8, pp. 2651–2659, Aug. 2014, doi: 10.1021/ar500190q.
- [97] S.-T. Yang, Y. Liu, Y.-W. Wang, and A. Cao, “Biosafety and Bioapplication of Nanomaterials by Designing Protein-Nanoparticle Interactions,” *Small*, vol. 9, no. 9–10, pp. 1635–1653, May 2013, doi: 10.1002/smll.201201492.
- [98] S. Behzadi *et al.*, “Protein corona change the drug release profile of nanocarriers: The

- 'overlooked' factor at the nanobio interface," *Colloids Surfaces B Biointerfaces*, vol. 123, pp. 143–149, Nov. 2014, doi: 10.1016/j.colsurfb.2014.09.009.
- [99] M. Mahmoudi *et al.*, "Temperature: The 'Ignored' Factor at the NanoBio Interface," *ACS Nano*, vol. 7, no. 8, pp. 6555–6562, Aug. 2013, doi: 10.1021/nn305337c.
- [100] A. Lesniak, F. Fenaroli, M. P. Monopoli, C. Åberg, K. A. Dawson, and A. Salvati, "Effects of the Presence or Absence of a Protein Corona on Silica Nanoparticle Uptake and Impact on Cells," *ACS Nano*, vol. 6, no. 7, pp. 5845–5857, Jul. 2012, doi: 10.1021/nn300223w.
- [101] H. Ding and Y. Ma, "Design strategy of surface decoration for efficient delivery of nanoparticles by computer simulation," *Sci. Rep.*, vol. 6, no. May, p. 26783, May 2016, doi: 10.1038/srep26783.
- [102] H. Ding and Y. Ma, "Computer simulation of the role of protein corona in cellular delivery of nanoparticles," *Biomaterials*, vol. 35, no. 30, pp. 8703–8710, Oct. 2014, doi: 10.1016/j.biomaterials.2014.06.033.
- [103] T. Yue and X. Zhang, "Cooperative Effect in Receptor-Mediated Endocytosis of Multiple Nanoparticles," *ACS Nano*, vol. 6, no. 4, pp. 3196–3205, Apr. 2012, doi: 10.1021/nn205125e.
- [104] T. Yue, X. Wang, F. Huang, and X. Zhang, "An unusual pathway for the membrane wrapping of rodlike nanoparticles and the orientation- and membrane wrapping-dependent nanoparticle interaction," *Nanoscale*, vol. 5, no. 20, p. 9888, 2013, doi: 10.1039/c3nr02683c.
- [105] K. Xiong, J. Zhao, D. Yang, Q. Cheng, J. Wang, and H. Ji, "Cooperative wrapping of nanoparticles of various sizes and shapes by lipid membranes," *Soft Matter*, vol. 13, no. 26, pp. 4644–4652, 2017, doi: 10.1039/C7SM00345E.
- [106] A. H. Bahrami, R. Lipowsky, and T. R. Weigl, "Tubulation and Aggregation of Spherical Nanoparticles Adsorbed on Vesicles," *Phys. Rev. Lett.*, vol. 109, no. 18, p. 188102, Oct. 2012, doi: 10.1103/PhysRevLett.109.188102.
- [107] Z. Yan, Z. Wu, S. Li, X. Zhang, X. Yi, and T. Yue, "Curvature-mediated cooperative wrapping of multiple nanoparticles at the same and opposite membrane sides," *Nanoscale*, vol. 11, no. 42, pp. 19751–19762, 2019.
- [108] S. Ni, Y. Yin, X. Li, H. Ding, and Y. Ma, "Controlling the Interaction of Nanoparticles with Cell Membranes by the Polymeric Tether," *Langmuir*, vol. 35, no. 39, pp. 12851–12857, 2019.
- [109] K. A. Smith, D. Jasnow, and A. C. Balazs, "Designing synthetic vesicles that engulf nanoscopic particles," *J. Chem. Phys.*, vol. 127, no. 8, p. 084703, Aug. 2007, doi: 10.1063/1.2766953.
- [110] S. L. Veatch and S. L. Keller, "Separation of Liquid Phases in Giant Vesicles of Ternary Mixtures of Phospholipids and Cholesterol," *Biophys. J.*, vol. 85, no. 5, pp. 3074–3083, Nov. 2003, doi: 10.1016/S0006-3495(03)74726-2.

- [111] X. Lin, X. Lin, and N. Gu, “Optimization of hydrophobic nanoparticles to better target lipid rafts with molecular dynamics simulations,” *Nanoscale*, vol. 12, no. 6, pp. 4101–4109, 2020.
- [112] K. Yang *et al.*, “Partitioning of nanoscale particles on a heterogeneous multicomponent lipid bilayer,” *Phys. Chem. Chem. Phys.*, vol. 20, no. 44, pp. 28241–28248, 2018.
- [113] D. Allan Butterfield, “Amyloid β -peptide (1-42)-induced oxidative stress and neurotoxicity: implications for neurodegeneration in Alzheimer’s disease brain. A review,” *Free Radic. Res.*, vol. 36, no. 12, pp. 1307–1313, 2002.
- [114] C.-F. Su, H. Merlitz, F. Thalmann, C. Marques, and J.-U. Sommer, “Coarse-Grained Model of Oxidized Membranes and Their Interactions with Nanoparticles of Various Degrees of Hydrophobicity,” *J. Phys. Chem. C*, vol. 123, no. 11, pp. 6839–6848, 2019.
- [115] H. Aceves-Luna, D. Glossman-Mitnik, and N. Flores-Holguín, “Oxidation degree of a cell membrane model and its response to structural changes, a coarse-grained molecular dynamics approach,” *J. Biomol. Struct. Dyn.*, vol. 0, no. 0, pp. 1–12, 2020, doi: 10.1080/07391102.2020.1833759.
- [116] J. Zimmerberg and M. M. Kozlov, “How proteins produce cellular membrane curvature,” *Nat. Rev. Mol. Cell Biol.*, vol. 7, no. 1, pp. 9–19, Jan. 2006, doi: 10.1038/nrm1784.
- [117] Y. Nademi, T. Tang, and H. Uludağ, “Steered molecular dynamics simulations reveal a self-protecting configuration of nanoparticles during membrane penetration,” *Nanoscale*, vol. 10, no. 37, pp. 17671–17682, 2018, doi: 10.1039/C8NR04287J.
- [118] C. K. Choudhury, A. Kumar, and S. Roy, “Characterization of Conformation and Interaction of Gene Delivery Vector Polyethylenimine with Phospholipid Bilayer at Different Protonation State,” *Biomacromolecules*, vol. 14, no. 10, pp. 3759–3768, Oct. 2013, doi: 10.1021/bm4011408.
- [119] U. Kwolek, D. Jamr??z, M. Janiczek, M. Nowakowska, P. Wydro, and M. Kepczynski, “Interactions of Polyethylenimines with Zwitterionic and Anionic Lipid Membranes,” *Langmuir*, vol. 32, no. 19, pp. 5004–5018, May 2016, doi: 10.1021/acs.langmuir.6b00490.
- [120] A. Y. Antipina and A. A. Gurtovenko, “Molecular-level insight into the interactions of DNA with phospholipid bilayers: barriers and triggers,” *RSC Adv.*, vol. 6, no. 43, pp. 36425–36432, 2016, doi: 10.1039/C6RA05607E.
- [121] C. Sun, T. Tang, H. Uludağ, and J. E. Cuervo, “Molecular dynamics simulations of DNA/PEI complexes: Effect of PEI branching and protonation state,” *Biophys. J.*, vol. 100, no. 11, pp. 2754–2763, 2011, doi: 10.1016/j.bpj.2011.04.045.
- [122] C. Sun, T. Tang, and H. Uludağ, “Molecular Dynamics Simulations for Complexation of DNA with 2 kDa PEI Reveal Profound Effect of PEI Architecture on Complexation,” *J. Phys. Chem. B*, vol. 116, no. 8, pp. 2405–2413, Mar. 2012, doi: 10.1021/jp211716v.
- [123] D. Meneksedag-Erol, R. B. KC, T. Tang, and H. Uludağ, “A Delicate Balance When Substituting a Small Hydrophobe onto Low Molecular Weight Polyethylenimine to

- Improve Its Nucleic Acid Delivery Efficiency,” *ACS Appl. Mater. Interfaces*, vol. 7, no. 44, pp. 24822–24832, Nov. 2015, doi: 10.1021/acsami.5b07929.
- [124] C. Sun, T. Tang, and H. Uludag, “A molecular dynamics simulation study on the effect of lipid substitution on polyethylenimine mediated siRNA complexation,” *Biomaterials*, vol. 34, no. 11, pp. 2822–2833, Apr. 2013, doi: 10.1016/j.biomaterials.2013.01.011.
- [125] D. Meneksedag-Erol, T. Tang, and H. Uludağ, “Mechanistic insights into the role of glycosaminoglycans in delivery of polymeric nucleic acid nanoparticles by molecular dynamics simulations,” *Biomaterials*, vol. 156, pp. 107–120, Feb. 2018, doi: 10.1016/j.biomaterials.2017.11.037.
- [126] D. P. Tieleman, H. Leontiadou, A. E. Mark, and S.-J. Marrink, “Simulation of Pore Formation in Lipid Bilayers by Mechanical Stress and Electric Fields,” *J. Am. Chem. Soc.*, vol. 125, no. 21, pp. 6382–6383, May 2003, doi: 10.1021/ja029504i.
- [127] M. Sud *et al.*, “LMSD: LIPID MAPS structure database,” *Nucleic Acids Res.*, vol. 35, no. suppl_1, pp. D527–D532, Nov. 2006, doi: 10.1093/nar/gkl838.
- [128] D. A. Winkler *et al.*, “Modelling and predicting the biological effects of nanomaterials,” *SAR QSAR Environ. Res.*, vol. 25, no. 2, pp. 161–172, 2014.

3. Steered Molecular Dynamics Simulations Reveal Self-Protecting Configuration of Nanoparticles during Membrane Penetration^x

^x A version of this chapter has been published. Adapted with permission from Nademi Y, Tang T, & Uludağ H (2018) Steered molecular dynamics simulations reveal a self-protecting configuration of nanoparticles during membrane penetration. *Nanoscale* 10 (37), 17671-17682. Copyright (2018) Royal Society of Chemistry

3.1. Introduction

Gene therapy using polynucleotide-based therapeutic agents is a promising strategy that have attracted immense attention during the past decade[1]–[3]. For functional delivery, carriers are needed in order to facilitate translocation of polynucleotides through the plasma membrane as well as protection of polynucleotides from degradation[4]. Synthetic cationic polymers due to their safety and versatility are the commonly utilized carriers for gene delivery[5]. For a therapeutic benefit, administered nucleotide/polymer nanoparticles (NPs) must be internalized by the targeted cells while retaining its integrity, and then polynucleotides need to disassemble from the polymeric carrier for transport to the appropriate sub-cellular compartment. Among synthetic carriers, polyethylenimines (PEI) have gained a central role for gene delivery with the advantage of being easily modified with functional groups, which makes it possible to tailor their properties for various applications[6]. High molecular weight (HMW) PEI (~25kDa) is often considered as ‘gold standard’ in non-viral gene delivery, however, it manifests considerable toxicity by damaging the plasma membrane of the cells[7]. Low molecular weight (LMW) PEI (< 2kDa) display acceptable level of toxicity, but it has a low efficiency for gene delivery. Modification of LMW PEI with hydrophobic groups significantly increase cellular uptake and facilitate the entry to cells by promoting hydrophobic interactions with membrane lipids[8], [9]. The beneficial effect of the hydrophobic modifications depends on the nature of the substituted lipids and the level of substitution[9].

The first stage of NP delivery into the cells is the cellular uptake, which usually occurs through two pathways: active endocytosis and direct penetration [10]. Direct penetration is a non-endocytic translocation pathway, where a NP crosses the cell membrane without the need to be confined by the endocytosis vesicles. Compared with endocytosis, direct penetration is a less frequent event,

but it can occur through diffusion, permeation and pore formation. Small NPs (< 1 nm) may cross cell membranes by passive diffusion through specialized transport protein channels existing on the cell membrane[11]. Intermediate sized NPs can permeate across cell membranes without inducing distinct pore in the membrane structure. Such a mechanism was proposed for polymeric NPs with appropriate hydrophobicity [12], [13] such that the NP experienced repulsion from both the solvent and the membrane tail. In this case, frequent exchange occurred between the polymer adsorption onto the membrane and desorption back into the solvent, which increased fluctuations in the lipid bilayer and eventually enhanced NP permeability.

Translocation by transiently induced pores is another direct penetration method, where pores are induced by various approaches including electroporation, mechanical stress, shock waves (sonoporation), surface-active molecules, small cationic peptides, and cationic polymers[14]. In electroporation, pores are induced by applying an external electric fields. *Tieleman et al.* [15], using molecular dynamics (MD) simulation, found that the external electric field interacted with water dipoles, increased the probability of forming water defects in the membrane interior, and stabilized the formed defects. Pore mediated translocation can also be enabled by the application of shock waves such as high pressure waves that propagate at a supersonic speed and pass the cell membranes within several picoseconds [16]. While the process of pore formation due to shock waves is still not fully understood, *Koshiyama et al.* [17] proposed that shock wave caused structural changes in the lipid bilayer such as bilayer thinning and disordering of lipid chains, which led to penetration of a considerable amount of water molecules into the hydrophobic core of the bilayer and eventually formation of a hydrophilic pore. Some surface-active molecules with covalently bonded hydrophilic and hydrophobic groups may also induce pore in the membrane structure[14]. For example, MD simulations[18] revealed that dimethylsulfoxide (DMSO),

containing a hydrophilic sulfoxide group and two hydrophobic methyl groups, could readily penetrate into lipid/water interface, which led to bilayer expansion and loss of lateral interactions between the lipid head groups. Consequently, thermal fluctuations at the lipid/water interface caused structural defects and eventually a pore in the membrane. Small cationic peptides can also induce pores in membranes via different mechanisms. As an example, *Leontiadou et al.* [19] through their MD simulations proposed a cooperative pore formation mechanism for the cationic (+3) magainin MG-H2 peptide which is an antimicrobial peptide. Upon binding to the membrane surface, the peptide molecules aggregated and oriented themselves in a way such that their hydrophobic side chains interacted with the membrane lipid tails while their charged lysine residues remained bonded with the membrane head groups. As a result, the fluctuation in the lipid/water interface increased, triggering the contact between peptide lysine residues and water molecules on the other side of the lipid bilayer, and finally leading to the formation of a hydrophilic pore. Some cationic polymers such as polyamidoamine (PAMAM) dendrimers were also shown to induce pore into membrane structure[20]. It was observed[20] that after initial binding to membrane surface, the charged moieties of the dendrimer penetrated into the lipid/water interface, and made contact with lipid head groups of the opposite leaflet, causing pore formation.

These simulations have focused on pore formation by external fields or small polymeric molecules. Although direct penetration is most efficient for NPs of <50 nm in diameter[21], NPs as large as 100 nm have also been internalized using this method[21]. It is therefore of interest to investigate the membrane penetration of polynucleotide/polymer NPs employed in gene delivery. While previous MD simulations have provided critical insights into the nucleic acid complexation with the carriers[6], [22]–[24], simulations on NP penetration across membranes were performed almost exclusively at the coarse-grained (CG) level[25]–[29], which are incapable

of revealing atomistic details behind effective carriers. To the best of our knowledge, no studies at all-atom level have simulated the membrane penetration of polynucleotide NPs. However, we found three all-atom studies that investigated the interaction of either PEI or deoxyribonucleic acid (DNA) alone with a lipidic bilayer[30]–[32]. *Antipina et al.* [31] utilized umbrella sampling method to study free energy profile of a bare 22 b.p. DNA across the palmitoyl-oleoylphosphatidylcholine (POPC) lipid bilayer. They observed that as the DNA approached and crossed the zwitterionic lipid bilayer, the free energy monotonically increased, which indicated the lack of attraction between the DNA and the zwitterionic lipid bilayer. This study confirmed that the anionic DNA requires a cationic vector to facilitate its interaction with the membrane. *Kwolek et al.* [30] simulated the interaction of a PEI with POPC and POPC/1,2-dioleoyl-sn-glycero-3-phosphoric acid (DOPA) lipid bilayers. It was observed that the PEI interacted with the lipid bilayers mainly by the hydrogen bond (HB) formation between the PEI amine groups and Os in the phosphate or ester groups of the lipids. *Choudhury et al.* [32] utilized MD simulation to assess how linear PEI (IPEI) in different protonation states (complete vs. partially protonated N atoms) interacts with dioleoylphosphatidylcholine (DOPC) lipid bilayers. Their simulation showed that at low pH, IPEI chains formed an elongated conformation due to the electrostatic repulsion between the protonated N atoms, and induced a water/ion channels through the membrane. Unprotonated IPEI, on the other hand, was highly coiled and predominantly remained at the bilayer-water interface.

While these studies on the individual constituents of polynucleotide NPs may be beneficial, it is evident that further studies are required to provide atomistic insight into the membrane penetration of polynucleotides NPs. In this work, we applied steered molecular dynamics (SMD) simulation to examine the membrane penetration of a polynucleotide NP formed by small

interfering ribonucleic acid (siRNA) and PEI molecules. Zwitterionic POPC lipid membrane was used as a model of cellular membranes. The siRNA/PEI NPs were steered by applying a moving constraint to cross the membrane structure. The SMD simulation serves not only to accelerate the penetration process, which is difficult to observe under standard MD simulation for such large and complex NP, but also to mimic the situation where the NP is pulled by external or biophysical forces towards the interior of the cell membrane. Our focus in this chapter is not to reveal the specific forces that drive NP internalization, but rather to investigate the: (i) stability and structural changes of siRNA/PEI NPs, (ii) pore formation across membrane and its stability, and (iii) effect of lipid groups on PEI during the penetration. A native and two additional PEIs modified with caprylic acid (CA) and linoleic acid (LA) were adopted here as the polynucleotide carriers.

3.2. Methods

3.2.1. Simulated Systems and Procedure

Three NPs are simulated each composed of 2 siRNA molecules and 6 branched PEIs (bPEIs). The simulated siRNA had the following sequence: sense: 5'-CAGAAAGCUUAGUACCAAATT-3', antisense: 5'-UUUGGUACUAAGCUUUCUGTC-3' which was used to silence P-glycoprotein[9], [33], [34]. It is composed of 42 nucleotides that carry a total charge of -40 in its fully deprotonated state. The simulated bPEI, in its native form, has a MW of 1874 Da[23] and consists of 43 amino groups, 20 of which are protonated corresponding to the protonation ratio of 47% at pH=6 as reported by Utsuno and Uludağ[35]. The selected pH is due to the fact that siRNA based therapeutic are utilized to target cancer cells, and the extracellular pH of human tumors is known to be slightly on the acidic side[36], [37]. The chemical structures and protonation sites of the simulated bPEI, as well as structures of lipid substitutions (LA and CA) are shown in Figure 3.1. The simulated NPs are referred to as LA-NP, where each PEI was modified with 3 LA

substitutions; CA-NP, where each PEI was modified with 3 CA substitutions; and native NP, where the PEIs were not modified. These substitutions are in the line with practical range in which functional differences were seen from the native PEI in siRNA delivery[9].

The initial structures of NPs were adopted from a previous study[22] after 200 ns production run. The original systems each included 4 siRNAs and 18 PEI molecules, from which we selected 2 siRNAs and 6 PEIs. Then, to equilibrate the structures, each NP was solvated with TIP3P[38] water molecules and ions (150 mM KCL) and subjected to 5 ns (restrained) + 45 ns (free) simulation with MD package of NAMD[39]. The NP atoms were restrained in order to first equilibrate the solvent and ions around the NP. The structure of each NP at the end of the simulation was adopted as the initial configuration of NPs for SMD simulations of membrane penetration.

The zwitterionic bilayer of 920 POPC molecules were constructed using VMD[40] Membrane Builder plugin. The chemical structure of the POPC lipid bilayer is shown in Figure 3.1. Upon solvation with proper amount of ions (150 mM KCl) and TIP3P[38] water molecules, the structure of POPC lipid bilayer were equilibrated for 50 ns until the area per lipid of $63.06 \pm 0.53 \text{ \AA}^2$ (data collected from last 20 ns) was obtained which is in agreement with experimental values ($63 - 68.3 \text{ \AA}^2$ per lipid) [41]–[43]. The final configuration of the POPC lipid bilayer was then adopted as input structure for SMD simulation with NPs. To facilitate the discussion, we will refer to the POPC lipid bilayer as the membrane. To prepare the membrane-NP systems for SMD simulation, each NP was placed above the membrane so that the center of mass (COM) distance between the membrane and the NP was 8 nm. Next, upon solvation with proper amount of ions (150 mM KCl) and TIP3P[38] water molecules, the three membrane-NP systems were equilibrated

for 10 ns with harmonic restraint of 10 kcal/mol.Å² exerted on the non-H atoms of the NP. The equilibrated systems were then used for SMD simulations.

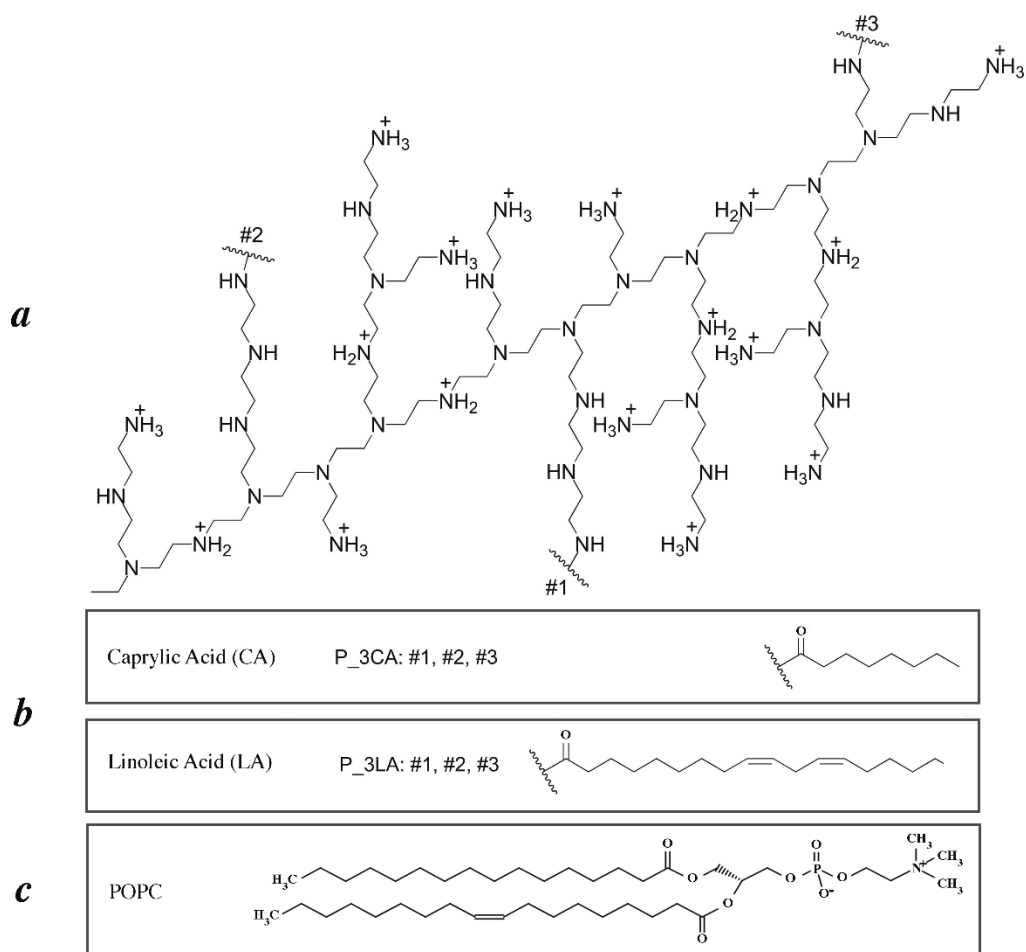


Figure 3.1. Molecular structure of the simulated molecules.

(a) Molecular structure, protonation sites and lipid substitution sites of the simulated PEIs, (b) Structures of the 2 substituted lipids, and (c) Structure of the POPC molecule.

3.2.2. SMD method

MD simulations are limited to the time scale of nanosecond which is not long enough to observe relevant processes [44]. SMD simulations can overcome such limitation that applies

external steering forces in the right direction to accelerate processes that due to energy barrier limitation are too slow[45]. This method has been extensively used to study mechanical functions of proteins such as extraction of lipid molecules out of lipidic membrane [44]. SMD simulations is a nonequilibrium process that can be connected to equilibrium properties through a theory. Such a theory has been proposed in nonequilibrium statistical mechanics, especially through the discovery of Jarzynski's equality theorem[46]. The theorem connects the equilibrium free energy difference ΔF to the statistics of work W carried out on a system that is initially in contact with a heat reservoir at some inverse temperature β ($\beta = \frac{1}{k_B T}$) and then subject to a nonequilibrium transformation $e^{-\overline{\beta W}} = e^{-\beta \Delta F}$ [46]. Here the overbar indicates an average over many realizations of the transformation process which is driven by switching an external parameter from an initial to a final value. In a typical SMD simulation, the system is pulled along a certain direction by imposing a constant force or velocity on the simulated structure[47]. Here we used the constant velocity approach, where COM of the NP was attached to a dummy atom via a virtual spring. The dummy atom was moved with a constant velocity in the z direction perpendicular to the membrane surface, and the force between the COM of NP and the dummy atom is calculated by the following equations:

$$U = \frac{1}{2}k[v t - (\mathbf{r} - \mathbf{r}_0) \cdot \mathbf{n}]^2 \quad (1)$$

$$F = -\nabla U \quad (2)$$

where U is the potential energy, k is the spring force constant, v is the speed of pulling, t is the current time, \mathbf{r} is the current position vector of the COM of NP, \mathbf{r}_0 is the initial position vector of the COM of NP, and \mathbf{n} is the unit vector indicating the direction in which the dummy atom is pulled. Pulling speed in the range of 0.1 to 100 Å/ns have been reported in the literature for constant

velocity SMD simulation, while lower values of v have been used to estimate the potential of mean force (PMF) from SMD trajectories[45], [48]–[50]. Results reported in this work are based on the value of $v = 2.5 \text{ \AA/ns}$, while the influence of v value is briefly discussed later. The spring force constant k was set to be 5 kcal/mol.\AA^2 according to the “stiff-spring approximation”[45]. This value for k was chosen large enough to ensure small deviation of the reaction coordinate from the constraint position. Each SMD simulation took 64 ns to complete. All computations were performed using Compute Canada servers, where 32 CPU along with 2 GPU were utilized. Detailed information of simulated systems in this chapter is given in Table 3.1.

3.2.3. Simulation Details

The force field for the PEI molecules was adopted from a previous study[22] in our group which was generated based on the CHARMM General Force Field and validated with *ab initio* calculations. CHARMM 36[51], [52] Force Field was used for all other molecules. CHARMM Force Field is one of the most successful Force Fields in the study of biomolecules. Especially, CHARMM 36 Force Field was optimized to reproduce a zero-surface tension as well as reproduce experimental quantification of lipidic membranes including deuterium order parameters. TIP3P[38] model was used for water molecules that were placed at above and below of the membrane. Appropriate amount of K^+ and Cl^- ions were added to reach the salt concentration of 150 mM at physiological levels. The NAMD[39] molecular dynamic package was used to perform all simulations in the NPT ensemble using a 2 fs time step, and with periodic boundary conditions (PBC) in x , y , and z directions. Long-ranged electrostatic interactions were calculated with Particle Mesh Ewald[53] (PME), and the cut-off distance of 12 \AA was used for van der Waals and short-ranged electrostatic interactions. In the PME method, short ranged electrostatic interactions were

calculated in real space while long ranged electrostatics were calculated in Fourier space. The SHAKE[54] algorithm was used to constrain bonds involving H atoms. In the NPT simulations, temperature was controlled at 310 K using Langevin dynamics thermostat, and pressure was controlled at 1 bar using Nose-Hoover-Langevin barostat with damping time scale of 100 fs and Langevin piston oscillation period of 200 fs [55], [56]. VMD[40] was used for visualization and trajectories analysis.

Table 3.1. Information of the simulated systems.

Number	System	Number of atoms	Size of simulation box (\AA^3)	Lipid no./type on each PEI	Charge ratio PEI/siRNA	Simulation time (ns)
1	POPC	242756	170×172×81	-	-	50
2	2siRNA-6PEIs (native NP)	106042	109×100×104	None	1.5	50
3	2siRNA-6LA-PEIs (LA-NP)	112598	93×118×109	3 LA	1.27	50
4	2siRNA-6CA-PEIs (CA-NP)	106921	94×101×120	3 CA	1.27	50
5	(native NP)-POPC	782077	170×172×268	None	1.5	64
6	(LA-NP)-POPC	778742	170×172×270	3 LA	1.27	64
7	(CA-NP)-POPC	778859	170×172×270	3 CA	1.27	64

3.3. Results

3.3.1. Equilibrated Structure of Isolated NPs

Figure 3.2. shows the initial (left panel) and final equilibrated (right panel) configurations of the NPs in absence of the membrane. For each system, the final equilibrated structure shows the 2 siRNAs stably bound together by 2 to 4 PEIs located in between (“bridging PEIs”) while the rest

of the PEIs are attached to the periphery of the NP (“peripheral PEIs”). Gyration radius (R_g) of the NP and COM distance between the 2 siRNAs, which represent the compactness of NP, are shown in Figure 3.3. The horizontal time axis starts at 5 ns since the NP is subjected to restrained simulations with little structural changes during the first 5 ns. R_g for all three systems shows a decreasing trend, ultimately reached stable values of 24.07 ± 0.17 , 25.44 ± 0.40 and 26.08 ± 0.31 Å (data collected from the last 20 ns) for native NP, LA-NP and CA-NP, respectively. The COM distance also shows similar decreasing trend for LA-NP and CA-NP, indicating the siRNA molecules moving closer compared to their starting configurations. The 2 siRNAs in the native NP system, on the other hand, remain more stable, with the COM distance deviating little from its starting value. The final COM distances, averaged over the last 20 ns, are 25.07 ± 0.38 , 24.11 ± 0.79 and 29.14 ± 1.37 Å for native NP, LA-NP and CA-NP, respectively.

Based on Figure 3.3., it can be concluded that CA-NP has the loosest equilibrium structure among the 3 systems. Compared with native NP, LA-NP has a larger R_g while its COM distance is slightly smaller. Via additional simulations, we have confirmed that the observed phenomena are not caused by the chosen initial configurations (see details in Appendix A, Section A.1). Rather, these observations can be understood by examining the two competing factors brought by the lipids grafted on the PEI: steric hindrance that prevents the formation of a compact structure and lipid association that favors compactness[22], [24], [57]. The final configuration of CA-NP in Figure 3.2c shows that there is limited association between the CA lipids due to their short chain length. Therefore, compared with the native PEIs, the steric hindrance of the bridging PEIs has caused larger separation of the siRNAs and consequently larger R_g . In the case of LA-NP, the association of the long-chained LAs is significant (see Figure 3.2b), surpassing the influence of steric hindrance and leading to the COM distance even smaller than the native NP. The larger R_g

of LA-NP as compared to native NP is due to the peripheral PEIs in which the long LA substitutions also show high degree of association. The large amount of lipid association in LA-NP leads to a more rigid structure compared with native NP and CA-NP, which is expected to influence the configurational changes of the NP during membrane penetration.

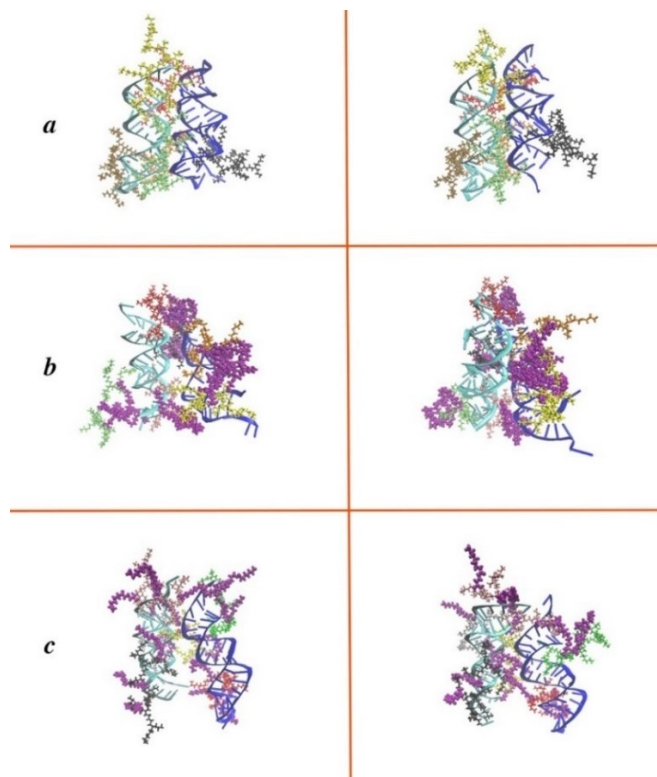


Figure 3.2. Initial and final conformations of the NPs in absence of the membrane.

Initial (left panel) and final (right panel) conformations of the NPs in absence of the membrane. **(a)** native NP, **(b)** LA-NP, **(c)** CA-NP. Different PEIs and siRNAs are represented by different colors; the lipid moieties on the PEIs are highlighted by color purple; water and ions are removed for clarity.

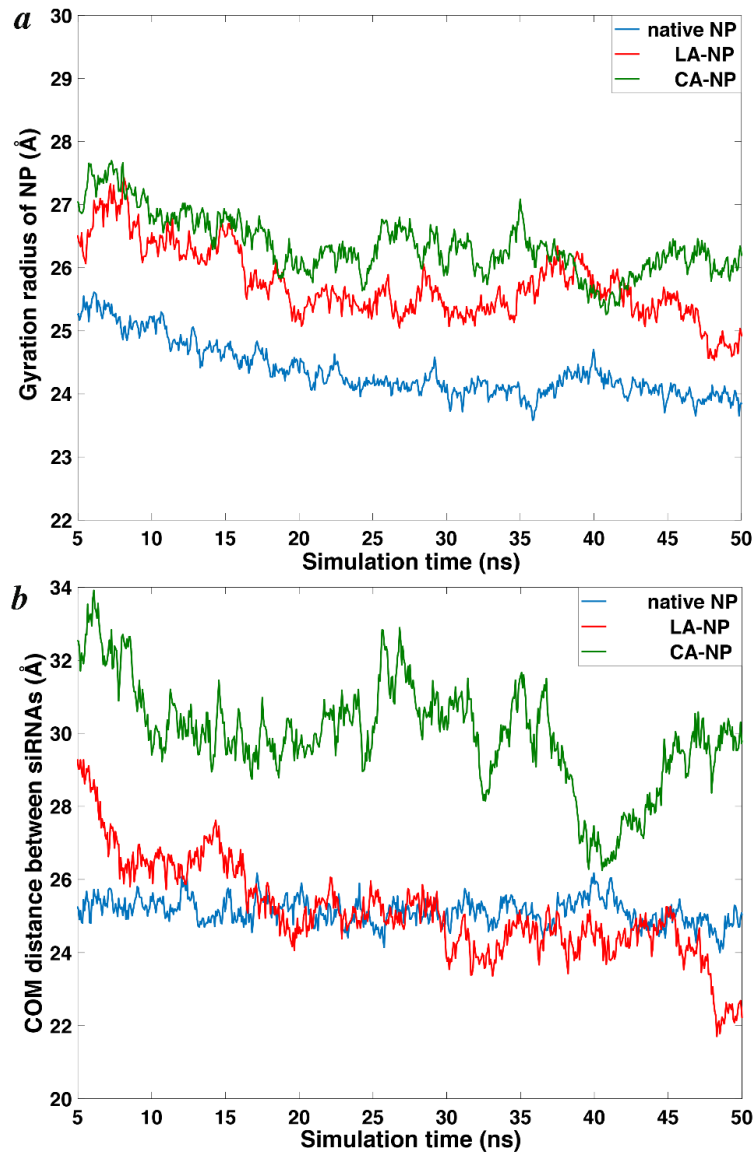


Figure 3.3. Compactness of NPs and COM distance between siRNA molecules.

(a) Radii of gyration of NPs and **(b)** COM distance between the siRNA molecules as functions of simulation time.

3.3.2. Membrane Penetration Process

Figure 3.4a. shows the force profiles during the SMD simulations, plotted against the COM position of the NP. The two dashed lines mark the two surfaces of the original undeformed membrane. The membrane-crossing process in this figure can be divided into four stages: approach (-80 to -60 Å), attachment (-60 to 0 Å), embedment (0 to 50 Å), and detachment (50 to 80 Å). Figure 3.5 shows side-view snapshots of the NPs and the membrane representative of each of these four stages. The corresponding COM positions of the NP are marked in Figure 3.4a. Overall, the force profiles of the three systems show a similar trend. During approach stage, the applied force is small and almost constant, which shows that the only resistance against the movement of NP is due to dissipative force caused by its friction with the solvent. In the attachment stage, the NP experiences additional resistance due to the presence of membrane and the applied force rises. Physically, this resistance originates from the necessity of deforming the membrane to allow for NP entry. The bi-layer structure of the membrane is maintained by the hydrogen bonds between the phosphate and amino groups on the two leaflets, as well as by the hydrophobic-hydrophobic interaction between the lipid tails located in the center. Attachment of the NP to the membrane causes bending of the membrane (Figure 3.5.) and disruption of those interactions. During the embedment stage, the rising trend of the applied force continues until a critical COM position is reached where the force is maximal. The magnitude of the peak force is only slightly different for the three NPs and the small difference is comparable to the fluctuations in the force profiles. This suggests that the maximum membrane resistance is insensitive to the lipid modification of the PEI carriers. After the peak value, the force decreases due to the visible formation of a pore in the membrane that facilitates further NP penetration (Figure 3.5.). The force continues to decrease in the detachment stage as the NP leaves the lower leaflet of the membrane. However, even at the

end of the simulation ($z = 80 \text{ \AA}$), the force did not reduce to the levels seen in the attachment stage, indicating attractive interactions of the NP with the membrane (Figure 3.5).

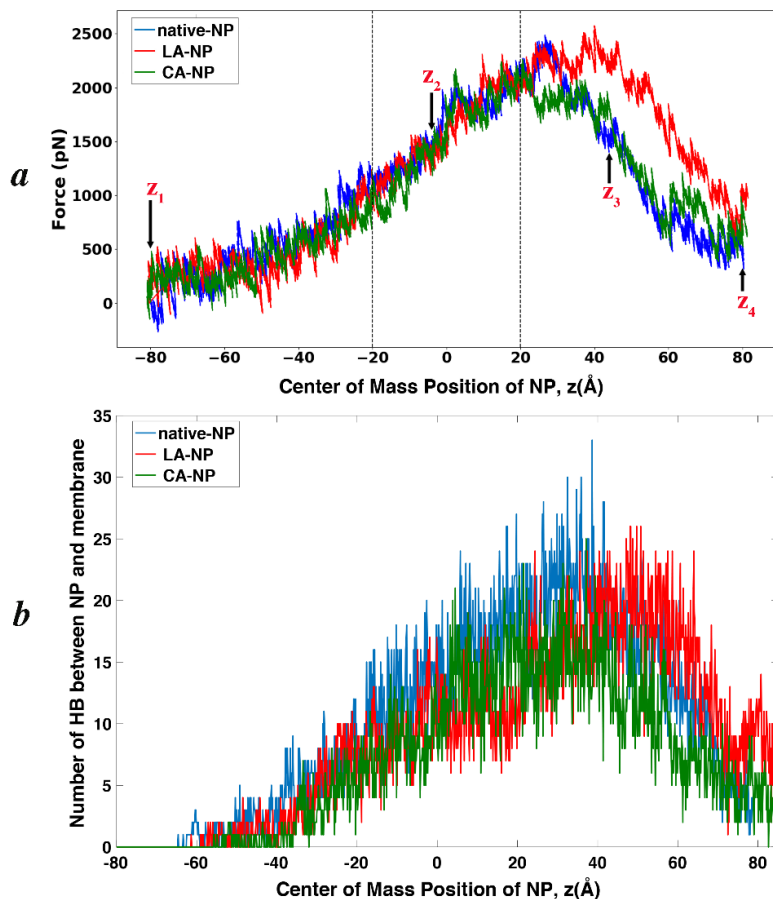


Figure 3.4. Force and number of HB between NP and membrane as a function of COM position of the NP during SMD.

(a) Force vs. COM position of the NP during SMD. The two dashed lines mark the surfaces of the initial undeformed membrane. Black arrows indicate the four locations where the snapshots in Fig. 5 are taken. (b) Number of HB between NP and the membrane as a function of COM position of NP.

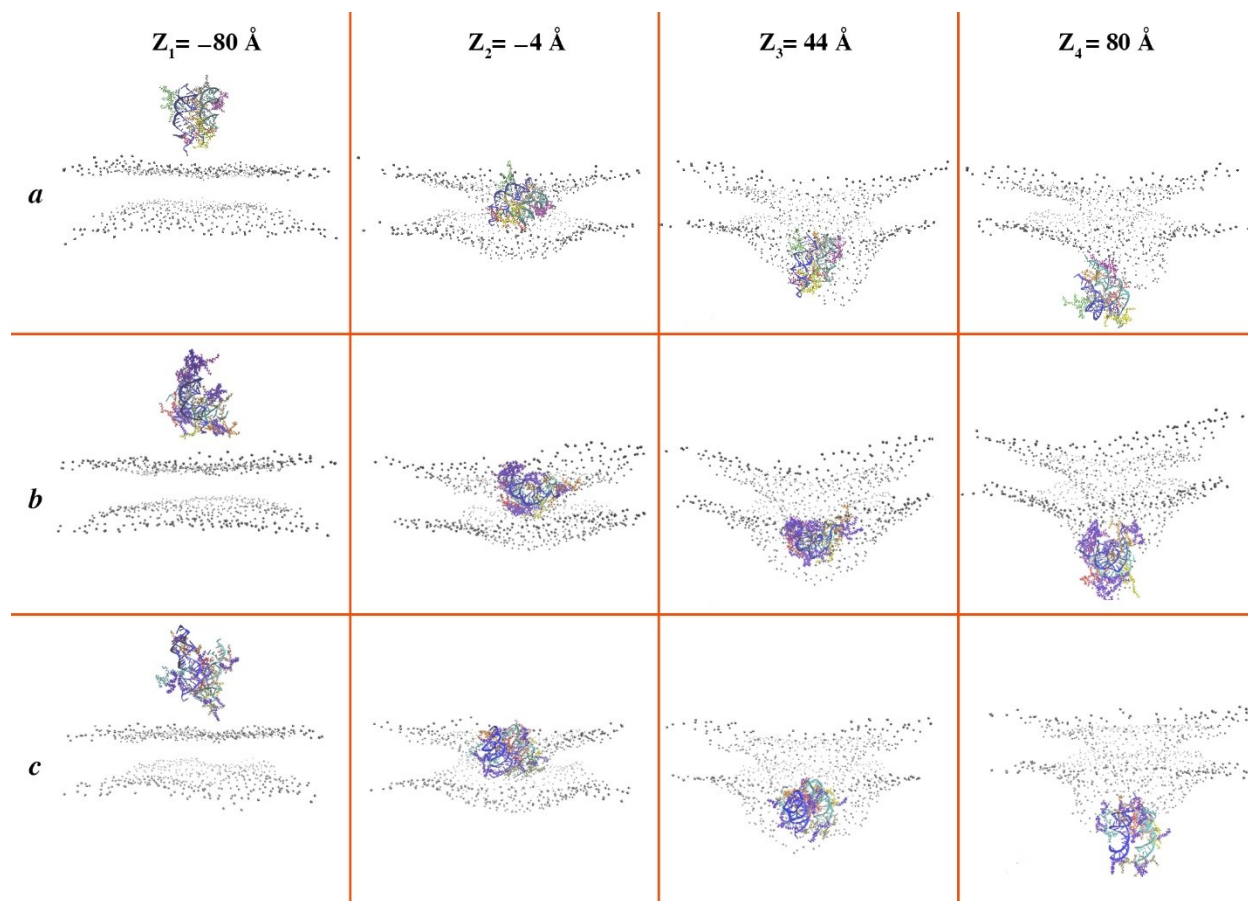


Figure 3.5. Side-view snapshots of the NP and membrane at different time of the SMD simulation:

(a) Native NP (b) LA-NP, (c) CA-NP. Different PEIs and siRNAs are represented by different colors; lipid moieties on the PEIs are highlighted by color purple; for clarity, water and ions are removed and only the phosphate (P) atoms of the membrane are shown (by color gray). The four snapshots, from left to right, correspond to simulation time of 0 ns, 30 ns, 50 ns and 64 ns, respectively. The corresponding positions of the NP COM are indicated on the top, and also marked in Figure 3.4a.

During the membrane-crossing process, as the NP establishes contact with the membrane, its exposure to water can be reduced. Such contact can be quantified by calculating the number of

hydrogen bonds (HB) between the NP and the membrane, as shown in Figure 3.4b. To calculate HB, the donor-acceptor distance of 3 Å and cut off angle of 20° were utilized. The HB between water and the membrane, and between water and the NP are shown in Figure A.2 of the Appendix A. Comparison between Figures 3.4a. and 3.4b. shows a positive correlation between the force and the NP-membrane HB. During the approach stage, the number of HB is zero, indicating the lack of interaction between NP and the membrane, consistent with the constant force in this stage. As the NP makes contact with the membrane during attachment and embedment, the number of HB between NP and the membrane rises, along with the increase in force. Ultimately during detachment, the number of HB shows a decreasing trend due to the separation of NP from the membrane. At the end of the simulations, the HB counts are nonzero, indicating that the NPs are still in contact with the membrane.

Although the force and HB profiles in Figure 3.4 are qualitatively similar among the three systems, the COM position at which the force reaches its maximum and begin to decrease is noticeably larger for the LA-NP system (around 40 Å as compared to 20 to 30 Å in the native NP and CA-NP systems). Consistently, the COM position at which the HB reaches maximum is also larger in the LA-NP system (around 50 Å as compared to 30 to 40 Å in the native NP and CA-NP systems). This indicates that pore formation, the occurrence of water translocation from one side of the leaflet to the other, induced by LA-NP occurs at a much deeper location within the membrane compared with native NP and CA-NP, and as a result its detachment stage is delayed. At the end of the simulation, both the force and HB counts are higher in the LA-NP system than in the other two systems, suggesting stronger contact between LA substituted PEIs and the membrane during detachment. The stronger contact is also evidenced by the extraction of some

lipid molecules out of the membrane, which can be seen from the presence of lipid molecules at deep locations along the z-axis at the end of the penetration process (Figure A.3, Appendix A).

It is of interest to point out that in Figure 3.4b., the increase in the number of HB at the beginning of the embedment stage indicates that when the NP entered the interior of the membrane, it did not get surrounded by the hydrophobic tails of the bi-layer membrane. Otherwise, we would have seen the shielding of the interactions between the polar groups on the NP and the hydrophilic head groups of the membrane, which would have limited the HB formation. The membrane has bent during the embedment and the lipid molecules have re-oriented themselves to expose their head groups to the NP in order to facilitate the interaction. Kwolek et al.[30] studied the interaction of PEI alone (in the absence of siRNA) with a membrane. They also observed that phosphate groups of the membrane rearranged themselves to interact with the polar amine groups of the polymer, and this reorientation led to pore formation that allowed water to cross the membrane.

From the representative snapshots in Figure 3.5., it is clear that while the NPs have experienced some deformation during membrane penetration, they have all maintained their overall integrity in this process. NP integrity during its membrane transport is critical to ensure full internalization of siRNAs. The configurational changes of the simulated NPs are assessed next by examining several parameters that describe the structural characteristics of the NPs during the penetration process.

3.3.3. Configurational changes of NP during Membrane Penetration

To gauge the NP compactness, we plotted R_g of the NP as a function of its COM position in each system (Figure 3.6a.). For all the three systems, the R_g curve starts from a relatively stable

value in the approach stage ($\sim 24, 25$ and 26 \AA respectively for native NP, LA-NP and CA-NP), follows a decreasing trend in the attachment and embedment stages until reaching a minimum value, and ultimately finds an increasing trend in the detachment stage. This suggests that each NP undergoes some extent of compaction during attachment and embedment, and “recovers” from its compacted structure as it separates from the membrane. The most compact structures correspond to R_g being around 22.5 \AA for native NP and CA-NP, and around 23.5 \AA for LA-NP. The relative compaction is smallest for LA-NP ($\sim 6 \%$), followed by $\sim 7\%$ for native NP and $\sim 17\%$ for CA-NP.

Additional evidence for NP compaction during penetration can be seen from Figure 3.6*b*., which shows COM distance between the 2 siRNAs as a function of COM position of the NP. The trend of CA-NP is similar to its corresponding R_g curve in Figure 3.6*a*, indicating significant compaction of the NP. For native NP, the COM distance is almost constant except for the detachment stage where it experiences a small increase. Together with the decrease in R_g during attachment and embedment, the result suggests that the compaction of native NP is through the peripheral PEIs. For LA-NP, its COM separation exhibits some extent of increase during attachment; it then stays almost constant until the detachment stage. Interestingly, despite the very different initial COM separations, the three NPs attain similar COM separation when embedded in the membrane ($\sim 23.5 \text{ \AA}$).

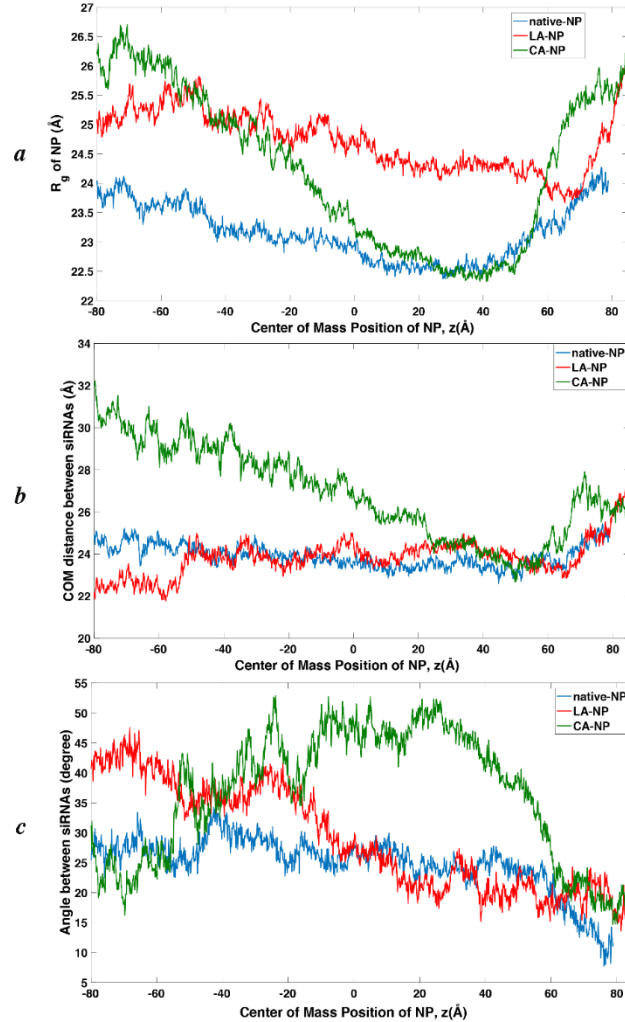


Figure 3.6. Structural changes of NPs during the SMD simulation.

(a) Gyration radius of the NP, (b) COM distance between the two siRNA molecules, and (c) Relative angle between the two siRNA molecules, each as a function of COM position of the NP.

Visual examination of simulation trajectories also revealed rotation of the NPs while crossing the membrane. Misalignment of principal axes of the two siRNA molecules may impact the NP stability by influencing (i) the bridging PEIs, and (ii) the area between two siRNAs accessible to destabilizing compounds such as heparin.[5] Relative orientation of the 2 siRNAs was monitored by measuring the angle (θ) between two vectors each defined in one siRNA (see

section S4, Supporting Information for detail). $\theta = 0^\circ$ corresponds to the siRNAs being parallel, whereas $\theta = 90^\circ$ represents two siRNAs perpendicular to each other. Figure 3.6c. shows θ as a function of COM position of the NP. For native NP, θ starts from $\sim 28^\circ$ and gradually decreases to $\sim 15^\circ$ at the end of the simulation. LAs-NP shows a similar trend: while its initial θ is much larger (above 40°), the decrease in θ is also more significant, and the ultimate θ value is also $\sim 15^\circ$. A different trend is observed for the CA-NP system: θ starts from $\sim 25^\circ$, experiences an initial increase, reaches a maximum value of $\sim 50^\circ$ and ultimately decreases sharply to $\sim 15^\circ$. Similar to the COM separation, while the NPs start from different angles between the 2 siRNAs, the final angles after crossing the membrane are similar, which corresponds to a relatively parallel orientation.

3.4. Discussion

3.4.1. Self-protecting Configuration

Using SMD simulations, this chapter investigated configurational changes of siRNA/PEI NPs during membrane penetration for the first time at all-atom scale. We focused on a comparison of NPs derived from lipid-substituted PEIs, given the importance of these carriers in delivering siRNAs across cellular membranes [8]. We found that HB formation between PEI and the membrane molecules did not lead to instability of NPs during the internalization process. In contrast, each NP was observed to undergo some degree of compaction during attachment and embedment stages. As the NP crosses the membrane, it introduces disruptions to the interactions among the lipid molecules of the membrane, causing the membrane to bend and inducing a pore in the membrane structure. Internalization of the NP therefore involves overcoming an energy barrier inherently dependent on the size of the NP. To minimize this energy barrier, the NP alters

its stiffness and compacts during the embedment process. *Yi et al.* [58] previously noted that many viruses utilize their stiffness to facilitate the infectious process, where they soften (expand) before uptake while harden (compact) before budding out of the host cells. The structure compaction is expected to protect the NP from being disintegrated by its interaction with the membrane molecules. In particular, it limits the interaction between the bridging PEIs and the membrane, stabilizing the siRNA/PEI NP while present in the membrane. Another way of promoting the stability of the NP, which has been observed from our simulations, is the re-orientation of the siRNA. In the case of two siRNAs simulated here, they were found to form a nearly parallel configuration at the end of the membrane-penetration process, which leads to a reduction in the area between the siRNAs accessible to destabilizing compounds, beneficial to enhancing the NP stability. Our results suggest the adoption of a “self-protecting strategy” by the NPs: during membrane penetration, they become more compact and the siRNAs are more parallel leading to more stable configuration while detaching from the membrane.

Depending on the lipid substitutions on the PEI, different NPs showed different degrees of internal restructuring (compaction and re-orientation) during membrane crossing. The restructuring in native NP was mild: there was less than 10% reduction in R_g , no reduction in the siRNA COM separation, and insignificant change in the angle between the two siRNAs. LA-NP also showed little change in the siRNA COM separation, while there was a small degree of compaction of peripheral PEIs reducing R_g . The low capacity of LA-NP for compaction is likely due to its high rigidity caused by significant association of the long-chained LA substitutions, especially among the bridging PEIs. Nevertheless, the LA-NP was able to enhance the NP stability by changing the relative orientation of the 2 siRNAs, which underwent a large change and became almost parallel. The CA-NP showed the largest changes in the compactness: it started with a much

looser structure in the initial configuration due to non-associating CAs; both R_g and COM separation of the siRNAs decreased significantly to the level similar to native NP and LA-NP, which were originally much more compact. The angle between the two siRNAs increased during the compaction, but decreased to the same value as the other two NPs. The initial increase in angle is likely due to the steric hindrance caused by the short CA substitution. In order to form a more compact structure, COM separation of the siRNAs need to decrease, which is resisted by the steric hindrance. To compensate for this, the angle between the 2 siRNAs has increased to accommodate a more compact structure. Interestingly, while the 3 NPs start from very different values of initial COM distance and relative angle between the 2 siRNAs, they converge to similar values after crossing the membrane.

One important observation made in the past with CG simulations is the rotation of the NP as a whole, relative to the lipid bilayer, during its translocation[59]–[63]. *Huang et al.* [64] simulated the wrapping of spherocylindrical NPs with different aspect ratios by lipidic membrane. For aspect ratio of 2, the NP rotated from its initial upright docking position until it completely laid down with its long axis parallel to the membrane surface. The NP then stood up and was ultimately endocytosed with a nearly 90° entry angle. Here, although we simulated direct penetration instead of endocytosis, we also observed the rotation of the NP components in a similar manner (Figure A5, Appendix A). Figure 3.8. shows the angle between each siRNA and the unperturbed membrane surface at the four NP locations where the snapshots in Figure 3.5. are taken.

During attachment, the NP rotates to a more parallel configuration to allow for more HB formation between its peripheral PEIs and the membrane surface. This continues in the embedment stage accompanied by NP compaction and mutual re-orientation of the siRNAs. At the end, the NP

rotates to a more perpendicular (standup) configuration to reduce the pore size in the detachment stage. The standup orientation is more evident in native NP and CA-NP than in LA-NP.

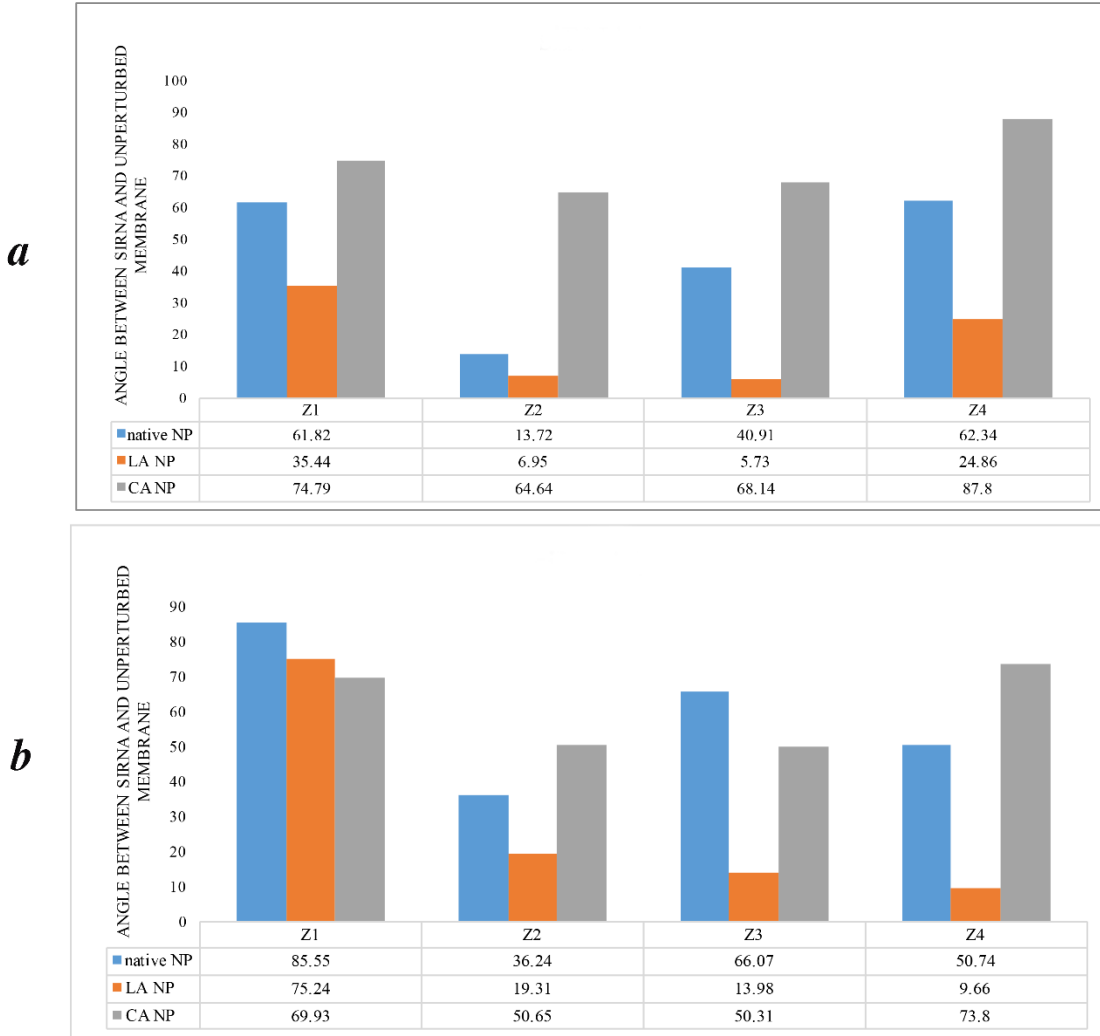


Figure 3.7. Angle between (a) siRNA-1 (b) siRNA-2 of NPs with unperturbed membrane surface.

Z₁, Z₂, Z₃, and Z₄ indicate the four locations where the snapshots in Figure 3.5. are taken.

3.4.2. Implications

Our simulations revealed the configuration changes of siRNA/PEI NPs during penetration through a model membrane, which is inaccessible in experiments. Various experimental studies on cellular uptake of LA and CA modified PEI have showed improved efficiency of siRNA delivery with lipid substitutions as compared to native PEI[9], [65], [66]. In an experimental study by *Neamnark et al.*,[67] the effect of different lipid substitutions on the transfection efficiency of PEI-mediated gene delivery was investigated. CA substitution was found to be less effective in transfection compared to other lipids including LA substitutions. While the mechanism of cellular uptake in those studies might be different from the direct penetration simulated in our study (i.e., endocytosis), our results still provide insights for NPs that can undergo direct penetration, as well as for endosomal escape stage of polynucleotide NPs, in which the encapsulating lipid bilayer around the NP needs to be broken and the polynucleotides need to disassemble from the polymeric carrier to be transported to the appropriate sub-cellular compartment. Our simulation shows that LA-NP is very stable during the penetration process due to the strong intra-particle lipid association. Another origin of the stability of the LA-NP is the close-to-parallel orientation of its siRNAs that makes it difficult for the binding of destabilizing compounds such as heparin to the bridging PEIs. Higher uptake and transfection ability of LA-NPs may be partially attributed to this enhanced stability. In the case of CA-NP, the observed increase in the relative angle between siRNAs may make the CA-NP more prone to dissociation during penetration. Usually cell membrane surface contains destabilizing compounds such as heparin. Meneksedag-Erol et al.[5] proposed the following 5 stages for heparin mediated disassembly: (i) heparin binding to NP, (ii) detachment of surface PEIs, (iii) disengagement of bridging PEIs, (iv) torsional change of siRNA and subsequent relaxation of NP, and (v) separation of siRNAs. The destabilizing compounds are

more probable to attach to the bridging PEIs of CA-NP due to creation of accessible area between 2 siRNAs resulting from the increase in relative angle between siRNAs, which could have contributed to the observed lower transfection efficiency of CA-NP compared to LA-NP in the experiments.

In the simulations performed here, the COM of the NP is restrained by SMD to mimic the process where the NP is pulled by certain external (e.g. electroporation) or biophysical forces towards the interior of the cell membrane. From Figure 3.4a., the required force for pulling the NP is positive throughout the process, indicating resistance from membrane against NP penetration. Previous studies on polymer penetration through membrane[14], [20], [68] have suggested that polymer with higher surface charge density and hydrophobic component are more likely to induce pore into the membrane. The hydrophobic groups interact with the lipid tails and increase the fluctuations in the membrane, while the charged moieties make contact with the lipid head groups on the opposite leaflet. Such cooperative efforts lead to pore formation. For the three NPs investigated in this work, the native NP does not have any hydrophobic components, while the long LA lipids in LA-NP form strong association with themselves, which prevent them from interacting with the lipid tails in the membrane. In the case of CA-NP, the short CA lipids do not associate with themselves, but they are too short to establish sufficient contacts with the lipid tails. Consequently, the membrane resisted the NP penetration and we did not observe attractive forces during attachment and embedment that could cause spontaneous pore formation. This analysis implies that the NP would not be able to move towards the interior of the membrane should the external restraint be removed. To confirm this, we performed a series of MD simulations in absence of the pulling force (see details in Appendix A, Section A.6). In particular, a NP configuration obtained from the SMD simulation was first selected. Then, the restraint on the COM

of NP was removed and the system was simulated for 20 ns. Each NP was observed to move backwards (in the -z direction in Figure 3.4.), away from the membrane. The tendency of the membrane to recover from its deformation, and the more favorable interaction of the NP with water compared with the membrane will eventually cause the previously induced pore to reseal.

To further strengthen the mechanistic understanding of NP performance, future MD simulations should be conducted for NPs with different charge ratios and different levels of substitutions, to examine whether proper assignments of those parameters might lead to forces driving the NP internalization. Simulations can also be done to assess the NP integrity and relative angle between siRNAs in the presence of destabilizing compounds, thus helping to better interpret the experimental results on silencing and transfection efficiency and eventually helping to screen more effective carriers.

3.5. Conclusions

The configurational changes of siRNA/PEI NPs during membrane penetration into are studied from a series of SMD simulations for the first time at all-atom scale. We developed an approach to study the effect of lipid substitutions (LA and CA) on the behavior of the NP. We found that, within the time scale of our SMD simulations, HB formation between PEI and the membrane molecules did not lead to NP instability during the penetration. Additionally, our results suggested the adoption of a “self-protecting” configuration by NPs during membrane penetration: the NPs become more compact and siRNAs more parallel leading to more stable configuration while detaching from the membrane. Depending on the lipid substitutions, different NPs showed different degrees of internal restructuring (compaction and re-orientation). LA-NP showed the lowest change in compactness due to its high rigidity caused by the significant lipid associations among the long-chained LA substitutions. CA-NP showed the largest changes: it started with a

much looser structure due to steric hindrance of non-associating CA substitutions, but underwent significant compaction accompanied by large changes in the relative orientation of the siRNAs to overcome the steric hindrance. These mechanistic observations provide unique insight into the internalization of siRNA/PEI NPs, and facilitate the design of new carriers for gene delivery.

3.6. Acknowledgements

Compute Canada and Westgrid were gratefully acknowledged for providing the computing resources and technical support. This work is funded by Natural Sciences and Engineering Research Council of Canada (NSERC), Canadian Institutes of Health Research (CIHR) and Alberta Innovates-Technology Futures (AITF).

3.7. References

- [1] S. M. Elbashir, J. Harborth, W. Lendeckel, A. Yalcin, K. Weber, and T. Tuschl, “Duplexes of 21-nucleotide RNAs mediate RNA interference in cultured mammalian cells,” *Nature*, vol. 411, no. 6836, p. 494, 2001.
- [2] D. Castanotto and J. J. Rossi, “The promises and pitfalls of RNA-interference-based therapeutics,” *Nature*, vol. 457, no. 7228, p. 426, 2009.
- [3] M. Zheng *et al.*, “Targeting the Blind Spot of Polycationic Nanocarrier-Based siRNA Delivery,” *ACS Nano*, vol. 6, no. 11, pp. 9447–9454, Nov. 2012, doi: 10.1021/nn301966r.
- [4] A. S. Ansari, P. J. Santerre, and H. Uludağ, “Biomaterials for polynucleotide delivery to anchorage-independent cells,” *J. Mater. Chem. B*, vol. 5, no. 35, pp. 7238–7261, 2017, doi: 10.1039/C7TB01833A.
- [5] D. Meneksedag-Erol, T. Tang, and H. Uludağ, “Mechanistic insights into the role of glycosaminoglycans in delivery of polymeric nucleic acid nanoparticles by molecular dynamics simulations,” *Biomaterials*, vol. 156, pp. 107–120, Feb. 2018, doi: 10.1016/j.biomaterials.2017.11.037.
- [6] D. Meneksedag-Erol, R. B. KC, T. Tang, and H. Uludağ, “A Delicate Balance When Substituting a Small Hydrophobe onto Low Molecular Weight Polyethylenimine to Improve Its Nucleic Acid Delivery Efficiency,” *ACS Appl. Mater. Interfaces*, vol. 7, no. 44, pp. 24822–24832, Nov. 2015, doi: 10.1021/acsami.5b07929.
- [7] D. Fischer, Y. Li, B. Ahlemeyer, J. Kriegelstein, and T. Kissel, “In vitro cytotoxicity testing of polycations: influence of polymer structure on cell viability and hemolysis,” *Biomaterials*, vol. 24, pp. 1121–31, 2003, doi: S0142961202004453 [pii].

- [8] V. Incani, A. Lavasanifar, and H. Uludağ, “Lipid and hydrophobic modification of cationic carriers on route to superior gene vectors,” *Soft Matter*, vol. 6, no. 10, p. 2124, 2010, doi: 10.1039/b916362j.
- [9] H. M. Aliabadi, B. Landry, R. K. Bahadur, A. Neamark, O. Suwantong, and H. Uludağ, “Impact of Lipid Substitution on Assembly and Delivery of siRNA by Cationic Polymers,” *Macromol. Biosci.*, vol. 11, no. 5, pp. 662–672, May 2011, doi: 10.1002/mabi.201000402.
- [10] H. Ding and Y. Ma, “Theoretical and Computational Investigations of Nanoparticle-Biomembrane Interactions in Cellular Delivery,” *Small*, vol. 11, no. 9–10, pp. 1055–1071, Mar. 2015, doi: 10.1002/smll.201401943.
- [11] S. Zhang, H. Gao, and G. Bao, “Physical Principles of Nanoparticle Cellular Endocytosis,” *ACS Nano*, vol. 9, no. 9, pp. 8655–8671, Sep. 2015, doi: 10.1021/acsnano.5b03184.
- [12] J.-U. Sommer, M. Werner, and V. A. Baulin, “Critical adsorption controls translocation of polymer chains through lipid bilayers and permeation of solvent,” *EPL (Europhysics Lett.)*, vol. 98, no. 1, p. 18003, Apr. 2012, doi: 10.1209/0295-5075/98/18003.
- [13] M. Werner, J.-U. Sommer, and V. A. Baulin, “Homo-polymers with balanced hydrophobicity translocate through lipid bilayers and enhance local solvent permeability,” *Soft Matter*, vol. 8, no. 46, p. 11714, 2012, doi: 10.1039/c2sm26008e.
- [14] A. A. Gurtovenko, J. Anwar, and I. Vattulainen, “Defect-mediated trafficking across cell membranes: insights from in silico modeling,” *Chem. Rev.*, vol. 110, no. 10, pp. 6077–6103, 2010.
- [15] D. P. Tieleman, “The molecular basis of electroporation,” *BMC Biochem.*, vol. 5, no. 1, p. 10, 2004.
- [16] T. Kodama, A. G. Doukas, and M. R. Hamblin, “Shock wave-mediated molecular delivery into cells,” *Biochim. Biophys. Acta (BBA)-Molecular Cell Res.*, vol. 1542, no. 1–3, pp. 186–194, 2002.
- [17] K. Koshiyama, T. Kodama, T. Yano, and S. Fujikawa, “Structural change in lipid bilayers and water penetration induced by shock waves: molecular dynamics simulations,” *Biophys. J.*, vol. 91, no. 6, pp. 2198–2205, 2006.
- [18] A. A. Gurtovenko and J. Anwar, “Modulating the structure and properties of cell membranes: the molecular mechanism of action of dimethyl sulfoxide,” *J. Phys. Chem. B*, vol. 111, no. 35, pp. 10453–10460, 2007.
- [19] H. Leontiadou, A. E. Mark, and S. J. Marrink, “Antimicrobial peptides in action,” *J. Am. Chem. Soc.*, vol. 128, no. 37, pp. 12156–12161, 2006.
- [20] H. Lee and R. G. Larson, “Molecular dynamics simulations of PAMAM dendrimer-induced pore formation in DPPC bilayers with a coarse-grained model,” *J. Phys. Chem. B*, vol. 110, no. 37, pp. 18204–18211, 2006.

- [21] H. Nakamura and S. Watano, "Direct Permeation of Nanoparticles across Cell Membrane: A Review," *KONA Powder Part. J.*, vol. 35, no. 35, pp. 49–65, 2018, doi: 10.14356/kona.2018011.
- [22] C. Sun, T. Tang, and H. Uludag, "A molecular dynamics simulation study on the effect of lipid substitution on polyethylenimine mediated siRNA complexation," *Biomaterials*, vol. 34, no. 11, pp. 2822–2833, Apr. 2013, doi: 10.1016/j.biomaterials.2013.01.011.
- [23] C. Sun, T. Tang, and H. Uludağ, "Molecular Dynamics Simulations for Complexation of DNA with 2 kDa PEI Reveal Profound Effect of PEI Architecture on Complexation," *J. Phys. Chem. B*, vol. 116, no. 8, pp. 2405–2413, Mar. 2012, doi: 10.1021/jp211716v.
- [24] C. Sun, T. Tang, and H. Uludağ, "Probing the Effects of Lipid Substitution on Polycation Mediated DNA Aggregation: A Molecular Dynamics Simulations Study," *Biomacromolecules*, vol. 13, no. 9, pp. 2982–2988, Sep. 2012, doi: 10.1021/bm301045b.
- [25] Y. Li, X. Li, Z. Li, and H. Gao, "Surface-structure-regulated penetration of nanoparticles across a cell membrane," *Nanoscale*, vol. 4, no. 12, pp. 3768–3775, 2012, doi: 10.1039/c2nr30379e.
- [26] Q. Xia, H. Ding, and Y. Ma, "Can dual-ligand targeting enhance cellular uptake of nanoparticles?," *Nanoscale*, vol. 9, no. 26, pp. 8982–8989, 2017, doi: 10.1039/C7NR01020F.
- [27] T. Yue, X. Wang, F. Huang, and X. Zhang, "An unusual pathway for the membrane wrapping of rodlike nanoparticles and the orientation- and membrane wrapping-dependent nanoparticle interaction," *Nanoscale*, vol. 5, no. 20, p. 9888, 2013, doi: 10.1039/c3nr02683c.
- [28] X. Chen, D. P. Tieleman, and Q. Liang, "Modulating interactions between ligand-coated nanoparticles and phase-separated lipid bilayers by varying the ligand density and the surface charge," *Nanoscale*, vol. 10, no. 5, pp. 2481–2491, 2018, doi: 10.1039/C7NR06494B.
- [29] K. Shimizu, H. Nakamura, and S. Watano, "MD simulation study of direct permeation of a nanoparticle across the cell membrane under an external electric field," *Nanoscale*, vol. 8, no. 23, pp. 11897–11906, 2016, doi: 10.1039/C6NR02051H.
- [30] U. Kwolek, D. Jamr??z, M. Janiczek, M. Nowakowska, P. Wydro, and M. Kepczynski, "Interactions of Polyethylenimines with Zwitterionic and Anionic Lipid Membranes," *Langmuir*, vol. 32, no. 19, pp. 5004–5018, May 2016, doi: 10.1021/acs.langmuir.6b00490.
- [31] A. Y. Antipina and A. A. Gurtovenko, "Molecular-level insight into the interactions of DNA with phospholipid bilayers: barriers and triggers," *RSC Adv.*, vol. 6, no. 43, pp. 36425–36432, 2016, doi: 10.1039/C6RA05607E.
- [32] C. K. Choudhury, A. Kumar, and S. Roy, "Characterization of Conformation and Interaction of Gene Delivery Vector Polyethylenimine with Phospholipid Bilayer at Different Protonation State," *Biomacromolecules*, vol. 14, no. 10, pp. 3759–3768, Oct. 2013, doi: 10.1021/bm4011408.

- [33] M. Abbasi *et al.*, “siRNA-Mediated Down-Regulation of P-glycoprotein in a Xenograft Tumor Model in NOD-SCID Mice,” *Pharm. Res.*, vol. 28, no. 10, pp. 2516–2529, Oct. 2011, doi: 10.1007/s11095-011-0480-z.
- [34] M. Abbasi, A. Lavasanifar, L. G. Berthiaume, M. Weinfeld, and H. Uludağ, “Cationic polymer-mediated small interfering RNA delivery for P-glycoprotein down-regulation in tumor cells,” *Cancer*, vol. 116, no. 23, pp. 5544–5554, Dec. 2010, doi: 10.1002/cncr.25321.
- [35] K. Utsuno and H. Uludağ, “Thermodynamics of Polyethylenimine-DNA Binding and DNA Condensation,” *Biophys. J.*, vol. 99, no. 1, pp. 201–207, Jul. 2010, doi: 10.1016/j.bpj.2010.04.016.
- [36] L. E. Gerweck, “Tumor pH controls the in vivo efficacy of weak acid and base chemotherapeutics,” *Mol. Cancer Ther.*, vol. 5, no. 5, pp. 1275–1279, 2006, doi: 10.1158/1535-7163.MCT-06-0024.
- [37] Y. Kato *et al.*, “Acidic extracellular microenvironment and cancer,” *Cancer Cell Int.*, vol. 13, no. 1, p. 89, 2013, doi: 10.1186/1475-2867-13-89.
- [38] W. L. Jorgensen, “Quantum and statistical mechanical studies of liquids. 10. Transferable intermolecular potential functions for water, alcohols, and ethers. Application to liquid water,” *J. Am. Chem. Soc.*, vol. 103, no. 2, pp. 335–340, Jan. 1981, doi: 10.1021/ja00392a016.
- [39] J. C. Phillips *et al.*, “Scalable molecular dynamics with NAMD,” *J. Comput. Chem.*, vol. 26, no. 16, pp. 1781–1802, Dec. 2005, doi: 10.1002/jcc.20289.
- [40] W. Humphrey, A. Dalke, and K. Schulten, “VMD: Visual molecular dynamics,” *J. Mol. Graph.*, vol. 14, no. 1, pp. 33–38, Feb. 1996, doi: 10.1016/0263-7855(96)00018-5.
- [41] R. D. Hills and N. McGlinchey, “Model parameters for simulation of physiological lipids,” *J. Comput. Chem.*, vol. 37, no. 12, pp. 1112–1118, May 2016, doi: 10.1002/jcc.24324.
- [42] N. Kučerka, S. Tristram-Nagle, and J. F. Nagle, “Structure of Fully Hydrated Fluid Phase Lipid Bilayers with Monounsaturated Chains,” *J. Membr. Biol.*, vol. 208, no. 3, pp. 193–202, Jan. 2006, doi: 10.1007/s00232-005-7006-8.
- [43] J. M. Smaby, M. M. Momsen, H. L. Brockman, and R. E. Brown, “Phosphatidylcholine acyl unsaturation modulates the decrease in interfacial elasticity induced by cholesterol,” *Biophys. J.*, vol. 73, no. 3, pp. 1492–1505, 1997, doi: 10.1016/S0006-3495(97)78181-5.
- [44] S. Park and K. Schulten, “Calculating potentials of mean force from steered molecular dynamics simulations,” *J. Chem. Phys.*, vol. 120, no. 13, pp. 5946–5961, Apr. 2004, doi: 10.1063/1.1651473.
- [45] S. Park, F. Khalili-Araghi, E. Tajkhorshid, and K. Schulten, “Free energy calculation from steered molecular dynamics simulations using Jarzynski’s equality,” *J. Chem. Phys.*, vol. 119, no. 6, pp. 3559–3566, Aug. 2003, doi: 10.1063/1.1590311.

- [46] E. Schöll-Paschinger and C. Dellago, “A proof of Jarzynski’s nonequilibrium work theorem for dynamical systems that conserve the canonical distribution,” *J. Chem. Phys.*, vol. 125, no. 5, p. 054105, Aug. 2006, doi: 10.1063/1.2227025.
- [47] B. Isralewitz, J. Baudry, J. Gullingsrud, D. Kosztin, and K. Schulten, “Steered molecular dynamics investigations of protein function,” *J. Mol. Graph. Model.*, vol. 19, no. 1, pp. 13–25, 2001.
- [48] S. Z. Mousavi, S. Amjad-Iranagh, Y. Nademi, and H. Modarress, “Carbon Nanotube-Encapsulated Drug Penetration Through the Cell Membrane: An Investigation Based on Steered Molecular Dynamics Simulation,” *J. Membr. Biol.*, vol. 246, no. 9, pp. 697–704, Sep. 2013, doi: 10.1007/s00232-013-9587-y.
- [49] Q. Wei, W. Zhao, Y. Yang, B. Cui, Z. Xu, and X. Yang, “Method Evaluations for Adsorption Free Energy Calculations at the Solid/Water Interface through Metadynamics, Umbrella Sampling, and Jarzynski’s Equality,” *ChemPhysChem*, vol. 210009, pp. 1–14, Feb. 2018, doi: 10.1002/cphc.201701241.
- [50] H. Nguyen, N. Do, T. Phan, and T. Pham, “Steered Molecular Dynamics for Investigating the Interactions Between Insulin Receptor Tyrosine Kinase (IRK) and Variants of Protein Tyrosine Phosphatase 1B (PTP1B),” *Appl. Biochem. Biotechnol.*, vol. 184, no. 2, pp. 401–413, Feb. 2018, doi: 10.1007/s12010-017-2549-6.
- [51] E. J. Denning, U. D. Priyakumar, L. Nilsson, and A. D. Mackerell, “Impact of 2'-hydroxyl sampling on the conformational properties of RNA: Update of the CHARMM all-atom additive force field for RNA,” *J. Comput. Chem.*, vol. 32, no. 9, pp. 1929–1943, Jul. 2011, doi: 10.1002/jcc.21777.
- [52] J. B. Klauda *et al.*, “Update of the CHARMM all-atom additive force field for lipids: validation on six lipid types,” *J. Phys. Chem. B*, vol. 114, no. 23, pp. 7830–7843, Jun. 2010, doi: 10.1021/jp101759q.
- [53] T. Darden, D. York, and L. Pedersen, “Particle mesh Ewald: An $N \cdot \log(N)$ method for Ewald sums in large systems,” *J. Chem. Phys.*, vol. 98, no. 12, pp. 10089–10092, Jun. 1993, doi: 10.1063/1.464397.
- [54] J.-P. Ryckaert, G. Ciccotti, and H. J. . Berendsen, “Numerical integration of the cartesian equations of motion of a system with constraints: molecular dynamics of n-alkanes,” *J. Comput. Phys.*, vol. 23, no. 3, pp. 327–341, Mar. 1977, doi: 10.1016/0021-9991(77)90098-5.
- [55] G. J. Martyna, D. J. Tobias, and M. L. Klein, “Constant pressure molecular dynamics algorithms,” *J. Chem. Phys.*, vol. 101, no. 5, pp. 4177–4189, 1994.
- [56] S. E. Feller, Y. Zhang, R. W. Pastor, and B. R. Brooks, “Constant pressure molecular dynamics simulation: the Langevin piston method,” *J. Chem. Phys.*, vol. 103, no. 11, pp. 4613–4621, 1995.
- [57] S. Bagai, C. Sun, and T. Tang, “Lipid-modified polyethylenimine-mediated DNA

attraction evaluated by molecular dynamics simulations,” *J. Phys. Chem. B*, vol. 118, no. 25, pp. 7070–7076, 2014, doi: 10.1021/jp503381r.

[58] X. Yi, X. Shi, and H. Gao, “Cellular Uptake of Elastic Nanoparticles,” *Phys. Rev. Lett.*, vol. 107, no. 9, p. 098101, Aug. 2011, doi: 10.1103/PhysRevLett.107.098101.

[59] R. Vácha, F. J. Martinez-Veracoechea, and D. Frenkel, “Receptor-Mediated Endocytosis of Nanoparticles of Various Shapes,” *Nano Lett.*, vol. 11, no. 12, pp. 5391–5395, Dec. 2011, doi: 10.1021/nl2030213.

[60] Y. Liu, B. Peng, S. Sohrabi, and Y. Liu, “The Configuration of Copolymer Ligands on Nanoparticles Affects Adhesion and Uptake,” *Langmuir*, vol. 32, no. 39, pp. 10136–10143, Oct. 2016, doi: 10.1021/acs.langmuir.6b02371.

[61] K. Yang and Y.-Q. Ma, “Computer simulation of the translocation of nanoparticles with different shapes across a lipid bilayer,” *Nat. Nanotechnol.*, vol. 5, no. 8, pp. 579–583, Aug. 2010, doi: 10.1038/nnano.2010.141.

[62] K. Yang and Y. Ma, “Wrapping and Internalization of Nanoparticles by Lipid Bilayers: a Computer Simulation Study,” *Aust. J. Chem.*, vol. 64, no. 7, p. 894, 2011, doi: 10.1071/CH11053.

[63] Y. Li, T. Yue, K. Yang, and X. Zhang, “Molecular modeling of the relationship between nanoparticle shape anisotropy and endocytosis kinetics,” *Biomaterials*, vol. 33, no. 19, pp. 4965–4973, Jun. 2012, doi: 10.1016/j.biomaterials.2012.03.044.

[64] C. Huang, Y. Zhang, H. Yuan, H. Gao, and S. Zhang, “Role of Nanoparticle Geometry in Endocytosis: Laying Down to Stand Up,” *Nano Lett.*, vol. 13, no. 9, pp. 4546–4550, Sep. 2013, doi: 10.1021/nl402628n.

[65] H. M. Aliabadi, B. Landry, P. Mahdipoor, C. Y. M. Hsu, and H. Uludağ, “Effective down-regulation of Breast Cancer Resistance Protein (BCRP) by siRNA delivery using lipid-substituted aliphatic polymers,” *Eur. J. Pharm. Biopharm.*, vol. 81, no. 1, pp. 33–42, May 2012, doi: 10.1016/j.ejpb.2012.01.011.

[66] H. Montazeri Aliabadi, B. Landry, P. Mahdipoor, and H. Uludağ, “Induction of Apoptosis by Survivin Silencing through siRNA Delivery in a Human Breast Cancer Cell Line,” *Mol. Pharm.*, vol. 8, no. 5, pp. 1821–1830, Oct. 2011, doi: 10.1021/mp200176v.

[67] A. Neamark, O. Suwantong, R. B. K. C., C. Y. M. Hsu, P. Supaphol, and H. Uludağ, “Aliphatic Lipid Substitution on 2 kDa Polyethylenimine Improves Plasmid Delivery and Transgene Expression,” *Mol. Pharm.*, vol. 6, no. 6, pp. 1798–1815, Dec. 2009, doi: 10.1021/mp900074d.

[68] S. Pogodin, M. Werner, J.-U. Sommer, and V. A. Baulin, “Nanoparticle-induced permeability of lipid membranes,” *ACS Nano*, vol. 6, no. 12, pp. 10555–10561, 2012.

4. Membrane Lipids Destabilize Short Interfering Ribonucleic Acid (siRNA)/Polyethylenimine Nanoparticles.^x

^x A version of this chapter has been published. Adapted with permission from Nademi Y, Tang T, & Uludağ H (2020) Membrane Lipids Destabilize Short Interfering Ribonucleic Acid (siRNA)/Polyethylenimine Nanoparticles. *Nanoscale* 12 (2), 1032-1045. Copyright (2020) Royal Society of Chemistry

4.1. Introduction

Gene therapy involves delivery of nucleic acids (NAs) deoxyribonucleic acid (DNA) and ribonucleic acid (RNA) into cells with the purpose of modifying protein expression profile in order to alter disease progression[1]. However, effective delivery of NAs to cells is a challenging task. Various viral and non-viral vectors have been devised to enable NA delivery. Among the non-viral carriers, cationic polymers are commonly used due to their ability to form ‘nano’-sized polyelectrolyte complexes with the NAs that are ideal for cell uptake. The cationic polymers protect NAs from enzymatic degradation, and facilitate their cellular uptake and endosomal escape[2]. The cationic polymer polyethylenimine (PEI) is a versatile cationic carrier that has been used since 1995 for NA delivery *in vivo* and *in vitro*[3]. PEIs form a nanoparticle (NP) with NAs *via* electrostatic interaction between the positively charged amine groups of PEIs and the negatively charged phosphate groups in the NA backbone[4]. The PEI/NA NPs enter the cells through a process that involves interaction with cell membrane molecules[5]. Cell membranes consist of a wide variety of components, but their major constituent is the lipid bilayer that acts as a physical barrier against foreign components and maintains the integrity of intracellular milieu[6].

Some PEIs in PEI/NA NP systems can exist in free form (not bound to NAs), which might destabilize membrane structures, thus contributing to the uptake of PEI/NA NPs[7]. Because of this, many experimental and simulation studies focused on the interaction of free PEIs with phospholipid bilayer of cell membrane. Among those, some studies have focused on investigating the stability of liposomes in the presence of free PEI molecules. *Zhang et al.* [8], using sum frequency generation (SFG) vibrational spectroscopy and attenuated total-internal reflection

Fourier Transform Infrared Spectroscopy (ATR-FTIR), found that both linear PEI (lPEI) and branched PEI (bPEI) induced lipid translocation, also known as lipid “flip-flop”, in anionic dipalmitoylphosphatidylglycerol (DPPG) and zwitterionic distearoylphosphatidylcholine (DSPC) lipid bilayers, while lipid translocation was higher with bPEI. *Yasuhara et al.* [9] proposed that PEI–lipid interactions depended on the molecular weight (MW) and stoichiometry of the PEI. Both high MW PEI (1.8 and 10 kg mol⁻¹), and low MW PEI (0.6 kg mol⁻¹) were able to induce membrane fusion [10], however, latter induce membrane fusion at wider range of free PEI concentration. Other experimental studies proposed that PEI-lipid interactions could cause deformation and permeabilization of the lipid membrane, thus leading to enhanced exchange of material across the cell membrane [11], [12].

Details of membrane deformations caused by free PEI molecules were investigated by *Kwolek et al.* [13] and *Choudhury et al.* [14] using molecular dynamics (MD) simulations. *Kwolek et al.* [13] found that PEIs adsorbed only partially on the surface of the zwitterionic 2-oleoyl-1-palmitoyl-sn-glycero-3-phosphocholine (POPC) membrane, while they readily adhered to the anionic membrane of POPC/1,2-dioleoyl-sn-glycero-3-phosphoric acid (DOPA). Due to the electrostatic interactions and hydrogen bonding between PEIs and anionic lipid molecules, significant reorganization of the bilayer occurred in the vicinity of the polymers, which could facilitate their translocation. *Choudhury et al.*[14] observed that the PEI-lipid bilayer interactions were pH dependent. At low pH, PEIs were in an elongated configuration, caused by electrostatic repulsion between the protonated sites. This geometry induced formation of water/ion channels through the zwitterionic membrane of 1,2-dioleoyl-snglycero-3-phosphocholine (DOPC). No such channel was formed in the presence of unprotonated PEIs (at high pH), which possessed coil shape and remained at the bilayer-water interface.

To probe the stability of PEI/NA NPs in contact with cell membranes, experimental studies have focused mainly on the role of cell-surface glycosaminoglycans (GAGs). GAGs carry high anionic charge density, and are present on the surface of most cells[15]. Sulfated GAG species such as chondroitin sulfate (CS), heparin sulfate (HS), dermatan sulfate (DS) and keratin sulfate (KS) carry higher negative charges that vary in density and position[16]. Hyaluronic acid (HA), on the other hand, is not sulfated and bears the least net negative charge among GAGs[16]. It has been suggested that GAGs compete with the NAs in binding to PEIs, and disrupt the integrity of PEI/NA NPs intended for cell uptake [17], [18]. *Meneksedag-Erol et al.* [5] based on MD simulations proposed a 5-stage mechanism for heparin mediated dissociation of PEI/siRNA (short interfering RNA) NPs: (i) binding of heparin to the NP, (ii) separation of surface PEIs, (iii) detachment of bridging PEIs, (iv) misalignment between constituent siRNAs, and (v) disintegration of the NP. Ernst et al [19] studied the efficiency of transfection of various polymer/DNA NPs including the PEI/DNA NPs in presence of various liposomal surfactants (DPPG, 1-palmitoyl-2-oleoyl-sn-glycero-3-phosphoglycerol (POPG), 1,2-dipalmitoyl-sn-glycero-3-phosphocholine (DPPC), POPC, and 1-palmitoyl-2-oleoyl-sn-glycero-3-phosphoethanolamine (POPE)) using different cell lines including cultured human airway epithelial cells (16HBE14O-), COS7 cells and porcine primary airway epithelial cells. Lipids with PC head groups showed some inhibitory effect on the transfection of PEI/DNA NPs, while those with PE head groups had little or no effect. Lipids with negatively charged PG head groups, on the other hand, strongly inhibited the transfection, which was attributed to possible conformational changes of the NPs leading to different NP sizes unsuitable for transfection.

While some studies probed the integrity of lipid membrane exposed to free PEIs, whether the lipid membrane components might affect the integrity of PEI/NA NPs and alter their

configuration has been not explored. Others simulated PEI/NA NP interactions with lipidic membranes, but not NP stability as it is passing through the membrane[20]. Coarse-grained simulations were reported on the interaction of NP with membrane, in addition to a review paper that addressed strategies to tailor the spatial distribution and ordering of the NP at the interfaces of various systems [21]–[23]. To the best of our knowledge, this is the first atomistic-level study that focuses on the stability of PEI/siRNA NPs in contact with representative lipidic membranes. Experiments and steered molecular dynamics (SMD) simulations were combined to examine the role of lipid molecules on the integrity of NPs formed by siRNA and PEI. Zwitterionic POPC and anionic 1-palmitoyl-2-oleoyl-sn-glycero-3-phospho-L-serine (POPS) membranes were used as model cell membranes. A native (unmodified) PEI and a PEI substituted with linoleic acid (LA) were adopted to investigate the effect of lipid modification, since such lipid modification on PEI has shown beneficial effects in siRNA delivery [24], [25].

4.2. Materials and Methods

4.2.1. Materials

POPC and POPS lipids were purchased from Avanti Polar Lipids. Heparin sodium from porcine intestinal was purchased from Sigma-Aldrich (St. Louis, MO). The negative control siRNA was purchased from Ambion (Austin, TX). SYBR Green II RNA gel stain (10 000X concentrate in DMSO) was purchased from Cambrex Bio Science (Rockland, ME). Two kDa PEI and PEI-LA polymers were developed in our group, and the synthesis procedure was previously described [26].

4.2.2. Experimental Procedures

Binding Assay. The binding ability of native PEI and LA-modified PEI with siRNA was investigated using SYBR Green II dye binding assay in triplicates. Briefly, 0.42 μg of siRNA (in ddH₂O) was incubated with various concentrations of the indicated polymers (in ddH₂O) for 30 min. Then, 100 μl of SYBR Green II solution (1:10000 dilution in TAE buffer) was added to the mixture. The fluorescence intensity was measured using a Fluoroskan Ascent Microplate Fluorometer with $\lambda_{\text{ex}} = 485 \text{ nm}$ and $\lambda_{\text{em}} = 527 \text{ nm}$. The percentage of bound siRNA was estimated on the basis of the fluorescence intensity relative to the siRNA sample in the absence of polymer (fluorescence values taken as 0% binding).

Preparation of Liposomes. POPS and POPC liposomes were prepared using extrusion technique. First, lipids were weighted to the desired amounts and dissolved in chloroform to obtain 4 mg/mL solutions. Then, the solvent was evaporated under reduced pressure by a rotary evaporator. The lipid film so formed was re-suspended in nuclease free water and vortexed with a final lipid concentration of $\sim 1 \text{ mg/mL}$. The resulting liposomes were extruded ten times through membrane syringe filters with 220 nm pores.

Light Scattering and Zeta Potential Measurements. Mean hydrodynamic diameter, polydispersity (PDI), and ζ -potential of liposomes were measured using dynamic light and electrophoretic light scattering methods with a Zetasizer (Nano ZS; Malverin instruments, UK), and the measurements were performed in triplicates.

Electrophoretic Mobility Shift Assay (EMSA). EMSA was performed to assess the stability of PEI/siRNA NPs in the presence of POPS and POPC liposomes. The samples were prepared by mixing 0.28 μg of siRNA (in ddH₂O, pH = 7) with unmodified and LA-modified PEI at PEI:siRNA weight ratios of 0.3 and 1, respectively, for 30 min at room temperature. The selected weight ratios corresponded to 100% binding between siRNA and polymers (based on SYBR Green II binding assay above). Then, various concentrations of liposomes were added to the samples and incubated for one additional hour, after which 5 μL of 40% glycerol was added to the samples, and the samples were run on a 0.4% agarose gel containing SYBR Green II using 100 V for 30 min. The resulting gels were visualized under UV-illumination. As a control for complete dissociation, heparin was added to samples where no liposome was present, and it was analyzed by EMSA as above. A band in which siRNA without any polymers added was also used as a reference. The dissociation percentage was estimated on the basis of the fluorescence intensity of the identified bands relative to the free siRNA band. Gels were run in at least 2 independent assays.

4.2.3. Simulated Systems and Procedure

Two types of NPs were simulated, each consisting of 2 siRNA molecules and 6 bPEIs. The siRNA in the simulations had sense strand of 5'-CAGAAAGCUUAGUACCAAATT-3' with an antisense strand of 5'-UUUGGUACUAAGCUUUCUGTC-3'. This siRNA sequence was specific for P-glycoprotein silencing [27] and it was used in our previous simulation studies. It consists of 42 nucleotides with a total charge of -40 in its fully deprotonated state. The simulated native bPEI has a molecular weight of 1874 Da and is composed of 43 amine group. Twenty of them are protonated, corresponding to the protonation ratio of 47%, which is within the reported

range (10 to 50% [28]–[32]) of protonation ratio for PEI at physiological pH . Hereafter the NP formed by the 2 siRNA and 6 native PEIs is referred to as PEI NP. The other simulated NP is referred to as PEI-LA NP, where each PEI is modified with 3 LA substitutions. The substitution level is in the practical range used for siRNA delivery[24]. The chemical structures of simulated polymers as well as model membrane lipids are shown in Figure 4.1.

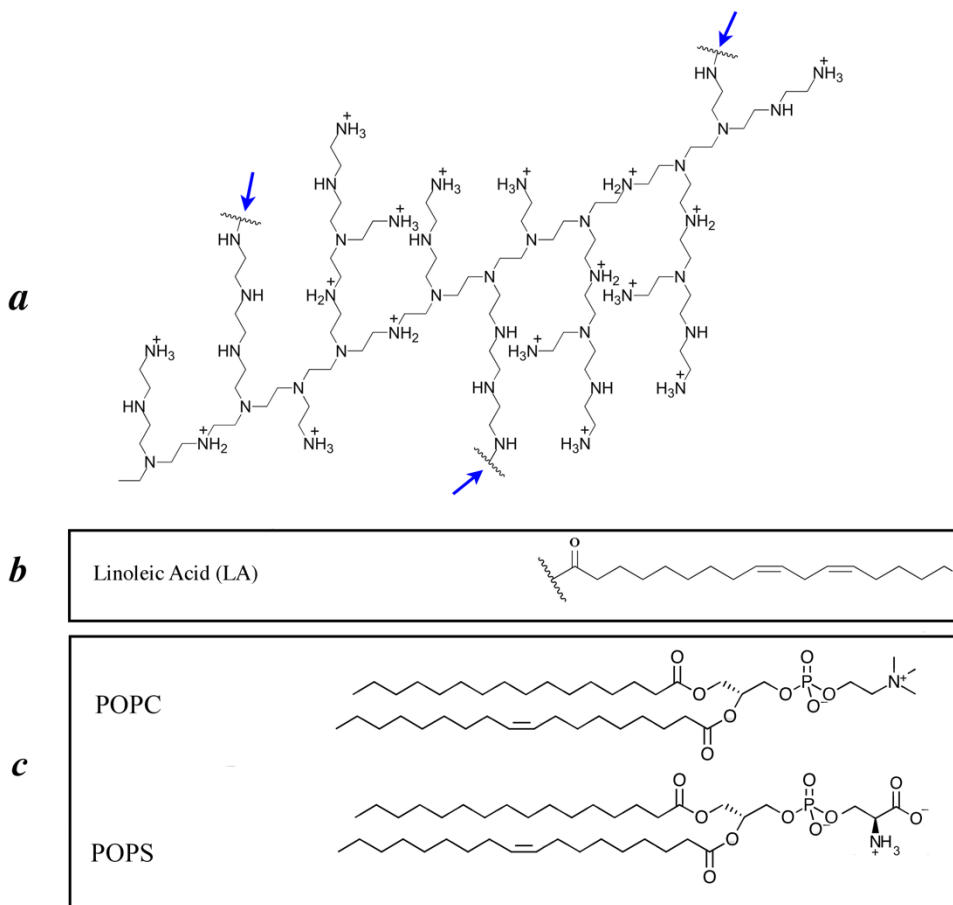


Figure 4.1. Molecular structure of the simulated molecules.

Molecular structure of (a) native PEI, where lipid substitution sites are shown with blue arrows, (b) LA to be substituted to native PEI, and (c) POPC and POPS molecules.

The initial structures of NPs as well as POPC membrane were adopted from our previous study [33]. Specifically, each NP was subjected to 50 ns of MD simulation, and the equilibrated structure was adopted as the initial configuration for subsequent SMD simulations in this work. The anionic bilayer of 1016 POPS molecules were constructed using Membrane Builder [34] in CHARMM-GUI [35], [36]. To equilibrate the membrane structure, the POPS lipids were solvated with TIP3P [37] water molecules and 150 mM KCl, and then subjected to 50 ns MD simulation until the area per lipid reached $57.26 \pm 0.43 \text{ \AA}^2$ (data collected from last 20 ns), which is in agreement with the values reported in literature [38]. The final configuration of the POPS lipid bilayer was used as the input structure for SMD simulation of the NPs. SMD systems were prepared by placing each NP above the membrane so that the center of mass (COM) distance between the membrane and the NP was 8 nm. Initial orientation of each NP was selected in a way that the axes of its siRNAs were almost perpendicular to the membrane surface. Following solvation with TIP3P [37] water and 150 mM KCl, each of the four membrane-NP systems was equilibrated for 6 ns with a harmonic restraint of $10 \text{ kcal mol}^{-1} \text{ \AA}^{-2}$ exerted on the non-H atoms of the NP. Water molecules were placed at above and below of the membranes. The equilibrated membrane-NP systems were then used for SMD simulations. Specifically, COM of the NP was attached to a dummy atom *via* a virtual spring, which was pulled with a constant velocity along z direction (perpendicular to the membrane surface), and the force between the COM of the NP and the dummy atom was calculated. Results reported in this work are on the basis of pulling speed $v = 5 \text{ \AA ns}^{-1}$ and spring constant $k = 5 \text{ kcal mol}^{-1} \text{ \AA}^{-2}$ according to the “stiff-spring approximation” [39]. Although pulling speeds as low as 0.1 \AA ns^{-1} have been used in the literature to determine the potential of mean force [39]–[41], much larger pulling speeds (as high as 100 \AA ns^{-1}) have also been used for qualitative assessment and for making comparisons among different system[42]–

[45]. In a previous work [33], we investigated the effect of pulling speed and demonstrated the suitability of using $v = 5 \text{ \AA ns}^{-1}$ for studying structural changes of NPs during membrane penetration. The length of each SMD simulation is 34 ns for the NP to travel a total distance of 170 \AA . Detailed information on the simulated systems is provided in Table 4.1.

Table 4.1. Details of simulated systems.

System	Number of atoms	Size of simulation box (\AA^3)	Lipid no./type on each PEI	PEI/siRNA charge ratio	Simulation time (ns)
PEI NP-POPS	988688	$170 \times 171 \times 340$	None	1.5	34
PEI-LA NP- POPS	988662	$170 \times 171 \times 340$	3 LA	1.27	34
PEI NP-POPC	782077	$170 \times 172 \times 270$	None	1.5	34
PEI-LA NP- POPC	778742	$170 \times 172 \times 270$	3 LA	1.27	34

4.2.4. Simulation Details

Force field parameters for the PEIs were previously generated and validated by our group [25] based on the CHARMM General Force Field. For other molecules, CHARMM 36 [46], [47] force field was used. Molecular simulation package NAMD [48] was used to perform the simulations in NPT ensemble. Time steps of 2 fs, periodic boundary conditions, and Particle Mesh Ewald [49] (PME) to calculate long-ranged electrostatic interactions were used for all simulations. The cut off distance was 12 \AA for van der Waals and short-ranged electrostatic interactions, and the SHAKE [50] algorithm was employed to constrain bonds involving H atoms. The temperature (310 K) was controlled using Langevin dynamic thermostat. To maintain the pressure (1 bar), Nose-Hoover Langevin barostat with a damping time scale of 100 fs and a Langevin piston

oscillation period of 200 fs were used [51], [52]. Visualization and analysis of simulations trajectories were performed using VMD [53].

4.3. Results

4.3.1. Experimental Determination of PEI Binding to siRNA

The percentage of bound siRNA as a function of PEI:siRNA weight ratio is shown in Figure 4.2. For both polymers, with increase in PEI:siRNA ratio, the fraction of bound siRNA was increased. However, 100% binding was achieved at different PEI:siRNA weight ratios, 0.3 for native PEI and 1.0 for PEI-LA. The results showed that LA substitution impeded siRNA binding to the cationic PEI. Similar observation was previously reported by Aliabadi et al [24]. It is worth noting that as lipid substitutions were introduced, the fraction of ‘protonable’ Ns was reduced so that PEI-LA was less charged as compared with its native counterpart. For the PEI structure shown in Fig. 1a where 3 LA substitutions were introduced to each PEI, to obtain the same cationic:anionic charge ratio, the PEI:siRNA weight ratio would have to be 1.45 times higher for PEI-LA. Since binding between siRNA and PEI strongly relies on their electrostatic interactions, it is not surprising to see a larger weight ratio required for PEI-LA to achieve 100% binding. For this reason, the dissociation assays were carried out using PEI:siRNA weight ratios that corresponded to 100% binding (0.3 and 1 respectively for PEI and PEI-LA), instead of using the same weight ratio.

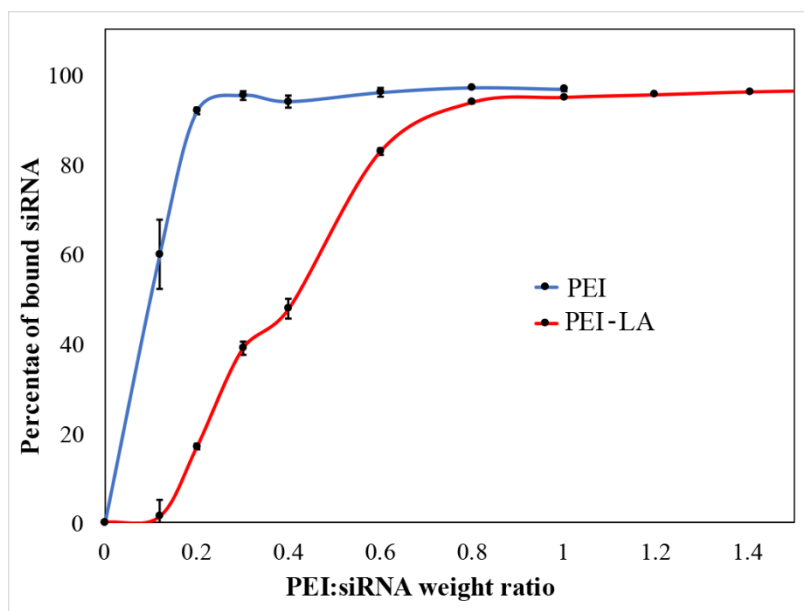


Figure 4.2. Physicochemical studies on PEI binding to siRNA.

Percentage of bound siRNA as a function of the PEI:siRNA weight ratio from SYBR Green II binding assay for PEI (blue) and PEI-LA (red).

4.3.2. Liposome Characterization and Dissociation Assay

The hydrodynamic diameter, polydispersity index and ζ -potential of the liposomes are shown in Table 4.2. The size of POPC liposomes was smaller than the POPS liposomes. As expected, the ζ -potential of the POPS liposomes was noticeably lower than the POPC liposomes due to the presence of the additional carboxyl group in POPS. Because of lower ζ -potential and presence of -COOH in the POPS liposomes, stronger interaction is expected between cationic PEI/siRNA NPs and POPS liposomes than between PEI/siRNA NPs and POPC liposomes. The size and ζ -potential of PEI/siRNA NPs were not determined in this chapter, since our group previously reported them to be ~ 200 nm and ~ 8 mV, respectively [24], [54].

Table 4.2. Hydrodynamic diameter (dz), polydispersity index (PDI) and ζ -potential (ξ) of POPS and POPC liposomes.

Liposome	d_z (nm)	PDI	ξ (mV)
anionic POPS	202.3 ± 4.0	0.262 ± 0.01	-32.53 ± 2.22
zwitterionic POPC	163.6 ± 8.0	0.240 ± 0.03	-18.73 ± 1.71

To investigate the effect of membrane lipids on the integrity of PEI/siRNA NPs, EMSA was performed by adding liposomes to fully bound PEI/siRNA NPs. The amount of liposome was gradually increased, and the dissociation percentage was measured (Figure 4.3.). With the addition of POPS liposomes, the NPs showed some level of dissociation: e.g., with 4 μ g of POPS liposomes, ~87% and ~47% dissociation was obtained with PEI and PEI-LA NPs, respectively. However, complete dissociation was not observed with further addition of POPS liposomes. The dissociation of PEI-LA NPs with POPS liposomes was consistently lower than the PEI NPs. The addition of POPC liposomes did not lead to significant dissociation as the percentage of unbound siRNA remained low (~10 and ~6% for PEI and PEI-LA NPs, respectively), indicating clear differences between the abilities of POPS and POPC liposomes to cause NP dissociation. To find an atomistic insight on configurational changes caused by liposomes – NP interactions, SMD simulations were utilized and the results are presented in the following section.

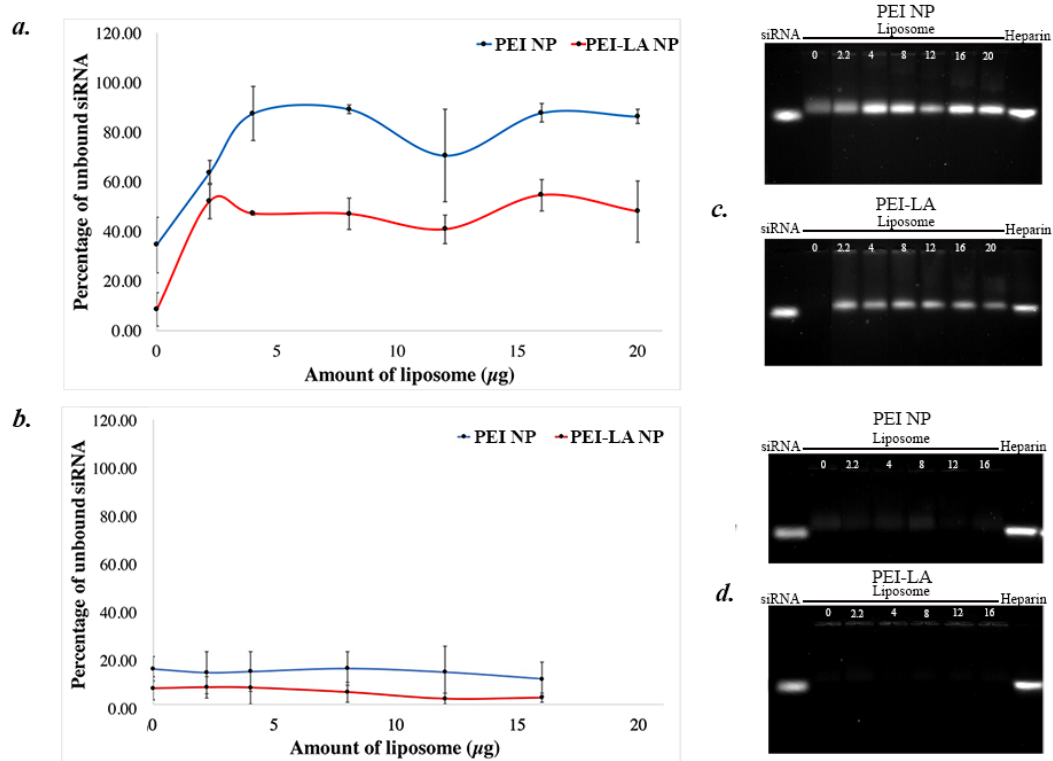


Figure 4.3. Physicochemical studies exploring the effect of liposome addition on the integrity of PEI/siRNA NPs.

Percentage of unbound siRNA as a function of amount of (a) POPS (b) POPC liposomes. EMSA images of siRNA release from NPs in presence of (c) POPS and (d) POPC liposomes.

4.3.3. Steered Molecular Dynamics Simulations

Figure 4.4 shows the force profiles during SMD simulations, as a function of COM position of the NP. The original locations of undeformed membrane surfaces are marked with the dashed lines. Depending on the distance of the NP from the membrane, the crossing process was divided into 4 stages: approach (-80 to -60 Å), attachment (-60 to 0 Å), embedment (0 to 50 Å), and detachment (50 to 90 Å). Side-view snapshots of the NPs and the membrane representative of

each of these four stages are shown in Figure 4.5. During the approach stage, the applied force was relatively constant and low, corresponding to the dissipative force from the solvent that resists the movement of the NP. In the attachment stage, the membrane applied an additional force against the NP movement, which continued to increase during the embedment stage until it reached a maximum value. Afterward a pore is formed in the membrane structure, and the force decreased during detachment. For both types of NPs, the magnitude of the force was higher for the POPS membrane during attachment stage and afterwards, suggesting its stronger interaction with the NPs. For the same membrane, the force profiles for the PEI NP and PEI-LA NP were overlapping during the approach, attachment and most of the embedment (up to ~ 40 Å) stages. However, during the detachment stage, the force was higher for PEI-LA NP, indicating stronger interaction between the PEI-LA NP and the membrane.

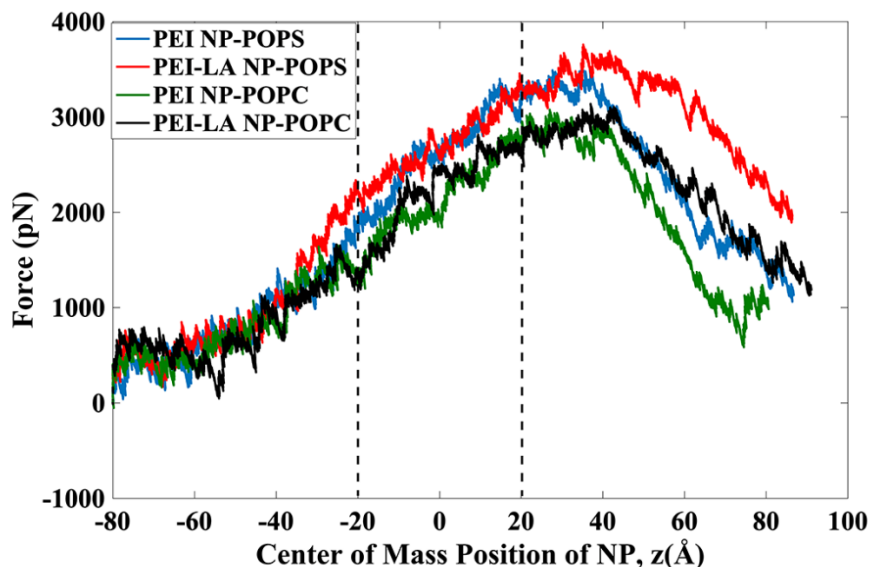


Figure 4.4. Force vs. COM position of the NP during SMD.

The two dashed lines denotes the surfaces of the initial undeformed membrane.

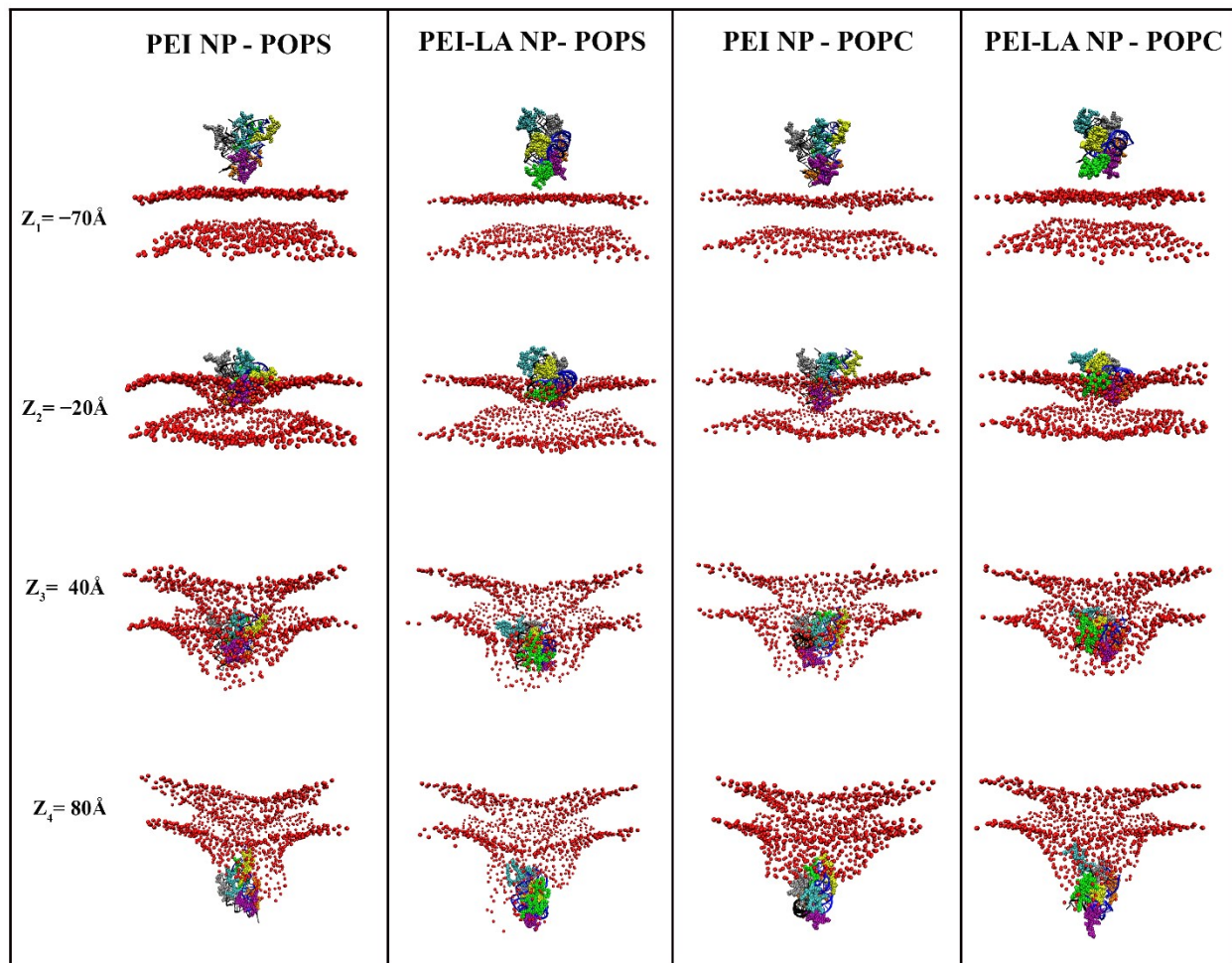


Figure 4.5. Side-view snapshots of the NP and membrane at different instants of the SMD simulations.

Different PEIs and siRNAs are represented by different colors. For clarity, water and ions are removed and only the phosphate (P) atoms of the membrane are shown (in red). The four snapshots, from top to bottom, correspond to the four stages of NP penetration, namely approach, attachment, embedding, and detachment.

The integrity of PEI/NA NPs highly depends on the binding between siRNAs and PEI molecules. Figure 4.6. and Figure 4.7. show the number of PEI N atoms within 4 \AA of any N/O atoms of siRNA as a function of COM position of NP for POPS and POPC membranes,

respectively. The use of 4 Å as a criterion is based on the distance in which a direct hydrogen bond between PEI amines and siRNA N/O could be formed [55], [56]. The number of hydrogen bonds (HBs) between PEIs and siRNA molecules were shown in Figure B.1 and Figure B.2 (see plots in Appendix B), which show the same trends. The results in Figure 4.6. and Figure 4.7. (one subplot for each PEI) thus represent the number of contacts the PEIs make with the siRNAs. Each subplot has two curves corresponding to the two siRNA molecules. A PEI is defined as 'bridging' if it has at least one N atom within 4 Å of any N/O atoms of both siRNA molecules, i.e., it is simultaneously attached to both siRNAs. Other PEI molecules are considered peripheral, as they are attached to only one of the siRNAs without forming polyion bridges between the two. In all systems, four PEIs were bridging (labeled as PEI-1, PEI-2, PEI-3 and PEI-4) and two PEIs were peripheral (labeled as PEI-5 and PEI-6). For the POPS membrane and PEI NP (Figure 4.6a.), interactions of bridging PEIs with siRNAs showed little changes during approach, attachment and embedment. However, during detachment, bridging performance of 3 PEIs (PEI-1, PEI-2, and PEI-3) were weakened, demonstrated by their reduced number of contacts with one or both of the siRNAs. By the end of the detachment process, PEI-2 and PEI-3 had almost completely lost their interactions with siRNA-2, starting to change from bridging to peripheral. Peripheral PEIs (PEI-5 and PEI-6) behaved similarly, where their interactions with siRNAs were increased during attachment and embedment and decreased during detachment. However, the decrease was more profound for PEI-6. For the POPS membrane and PEI-LA NP (Figure 4.6b.), interactions of 2 bridging PEIs (PEI-1 and PEI-2) with siNRAs barely changed during all stages, while the other 2 bridging PEIs (PEI-3 and PEI-4) displayed a dynamic trend. For PEI-3, number of contacts it had with both siRNAs increased during penetration. PEI-4 also showed increased interaction with siRNA-2; its interaction with siRNA-1 first decreased during attachment and embedment, but recovered during

detachment. Interactions of the peripheral PEIs (PEI-5 and PEI-6) with siRNAs were stable and showed little changes.

For the POPC membrane and PEI NP (Figure 4.7a.), bridging PEIs showed a fluctuating trend, however, no sign of weakened interaction was observed compared with the initial number of contacts. Peripheral PEI-5 showed an overall increasing interaction with siRNA-1, while the interaction of peripheral PEI-6 with siRNA-2 had a decreasing trend during detachment. For the POPC membrane and PEI-LA NP (Fig. 4.7b.), bridging PEIs maintained their interaction with siRNAs (PEI-4 temporarily lost contact with siRNA-1 during embedment but the interaction was recovered during detachment). Peripheral PEI-5 had a stable interaction with siRNA-1 while there was slight decrease in the interaction between PEI-6 and siRNA 2.

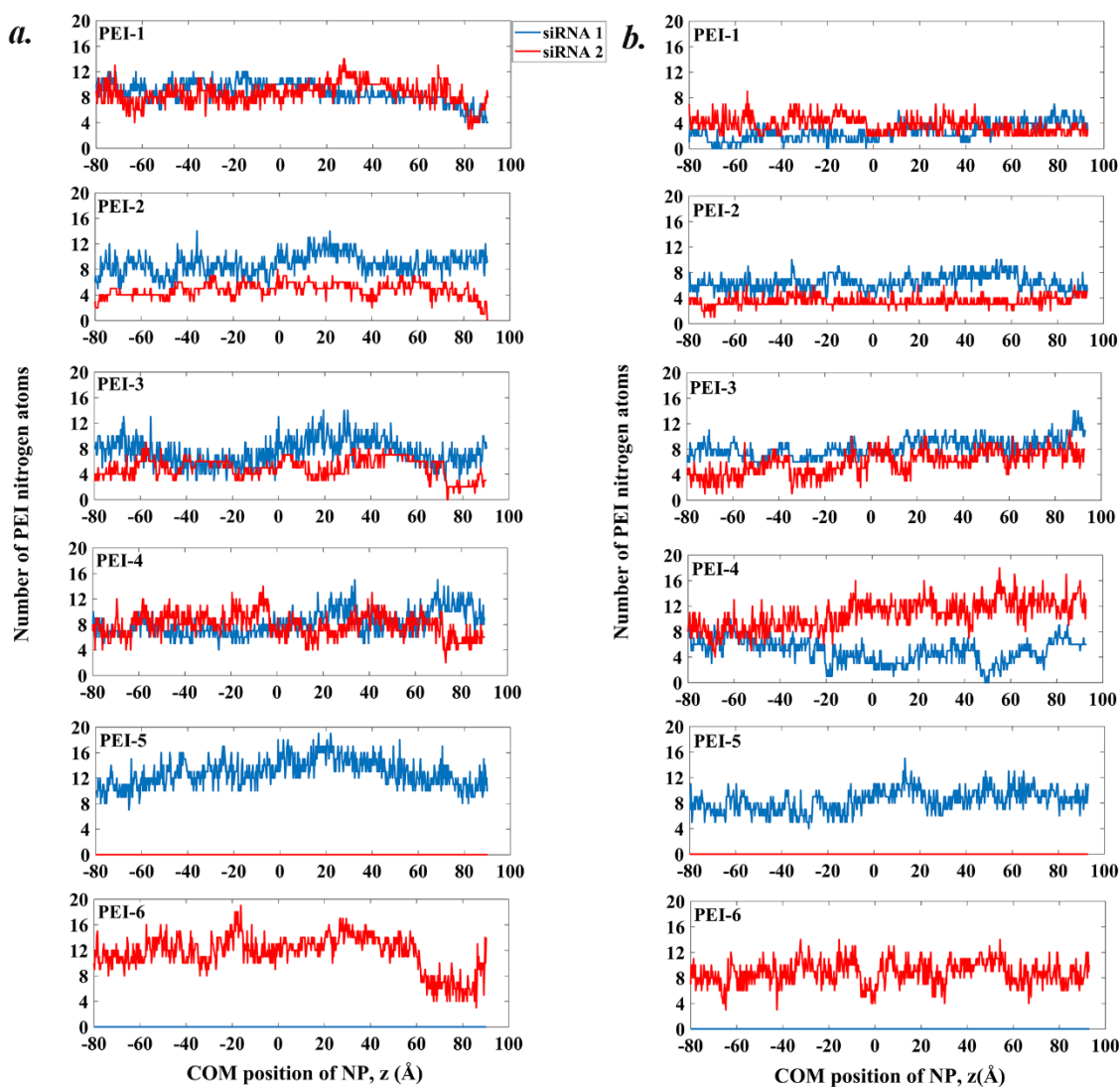


Figure 4.6. Dynamics of PEI binding to siRNA while interacting with POPS membrane.

Number of PEI Ns within 4 Å of any siRNAs N/O atoms as a function of COM position of NP while crossing the POPS membrane, (a) PEI NP and (b) PEI-LA NP.

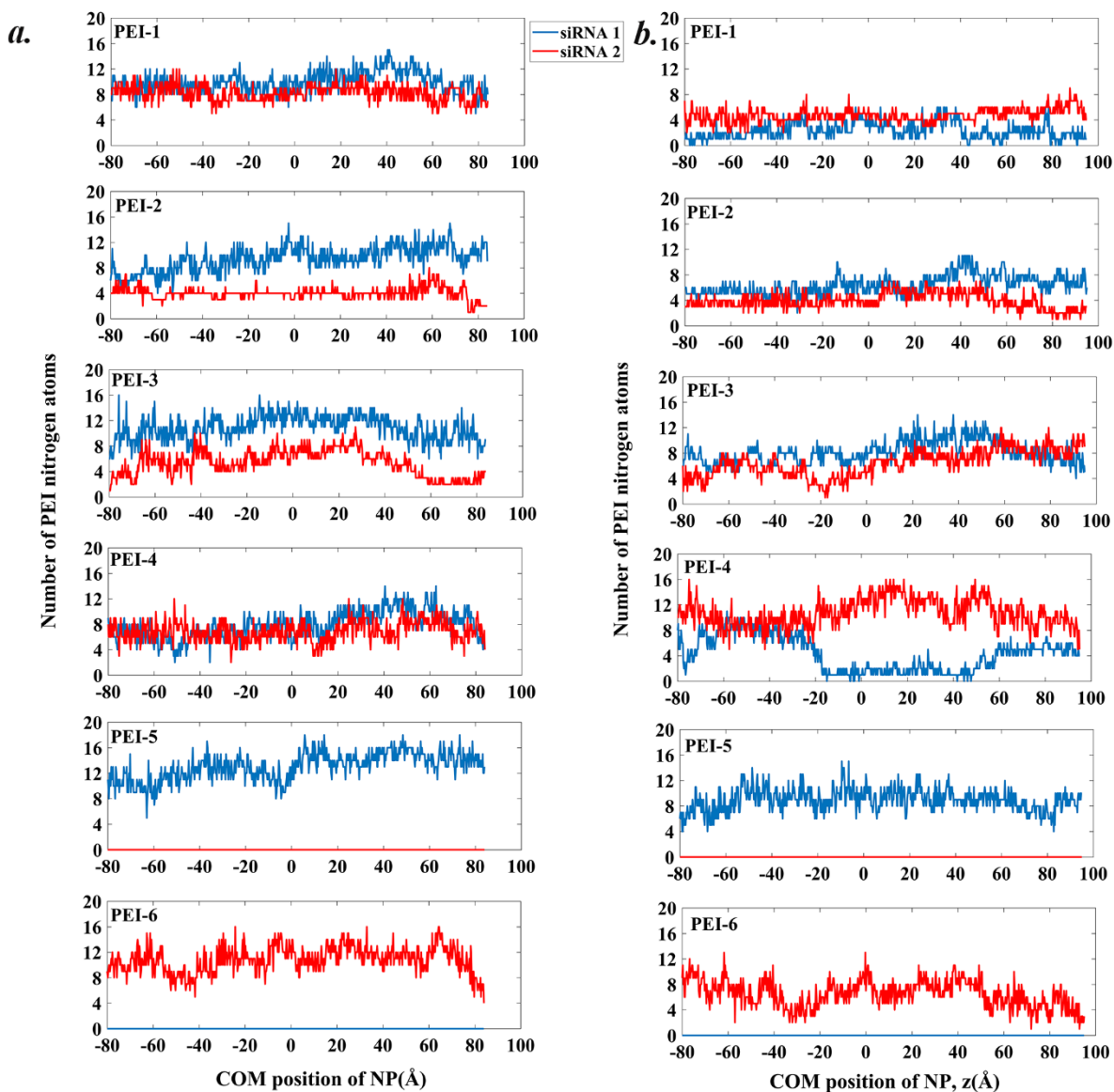


Figure 4.7. Dynamics of PEI binding to siRNA while interacting with POPC membrane.

Number of PEI Ns within 4 Å of any siRNAs N/O atoms as a function of COM position of NP while crossing the POPC membrane, (a) PEI NP and (b) PEI-LA NP.

These changes in PEI configurations could lead to structural changes in NP, thereby affecting the integrity of NP during penetration. Hence, configurational changes in NPs were quantified by calculating the gyration radius (R_g) of the NPs, and the COM distance and relative angle between the two siRNAs. Results are shown in Fig. 8 for the POPS (left panel) and POPC

(right panel) membranes. With POPS membrane, R_g (Figure 4.8a) was relatively constant for both NPs during the approach stage, decreased during attachment and embedment, and increased during detachment. This suggests that each NP experiences some level of compaction during attachment and embedment, while “recovering” from their compacted structure during detachment.

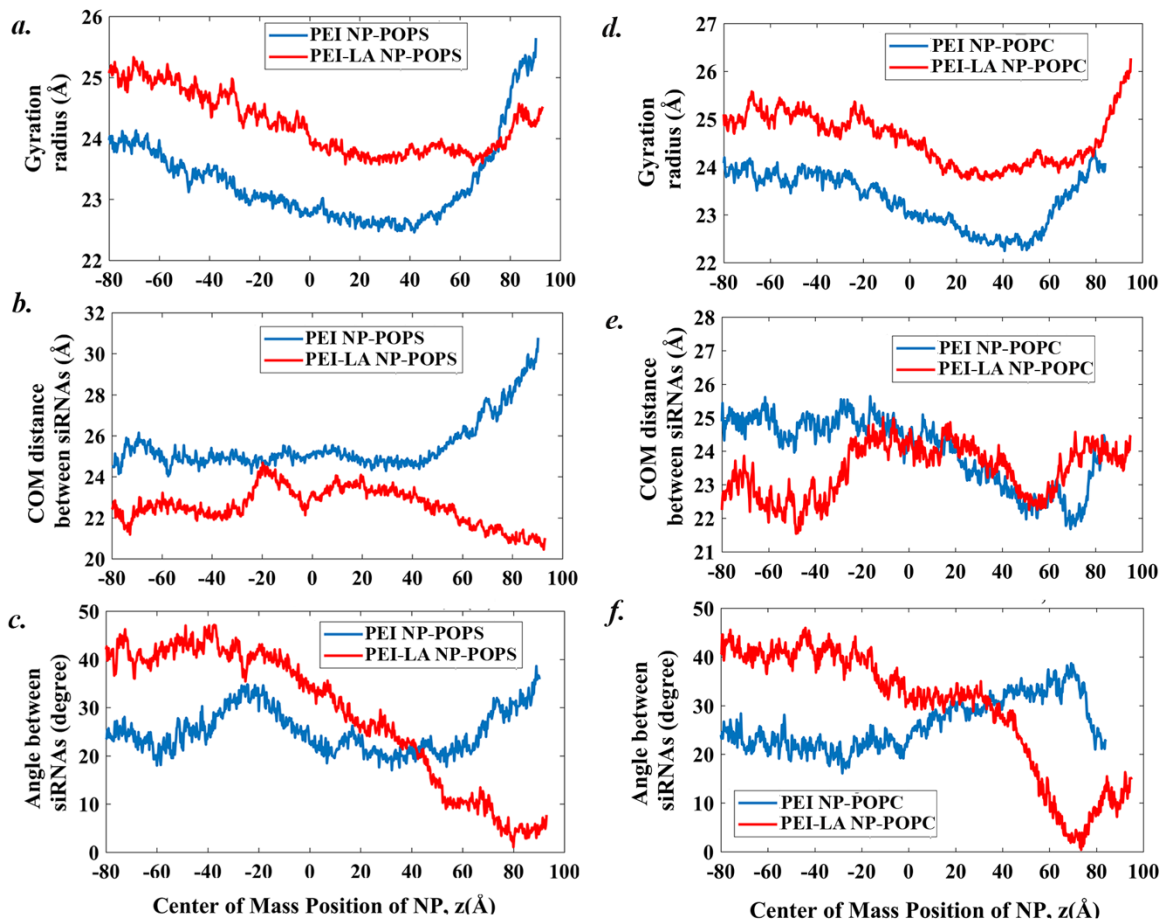


Figure 4.8. Structural changes of NPs during the SMD simulation.

Structural parameters for NPs crossing the POPS (left panel) and POPC (right panel) membranes: (a, d) Gyration radius of the NP, (b, e) COM distance between the two siRNAs, and (c, f) the relative angle between the two siRNAs, each as a function of the COM position of the NP.

The compaction of NP could occur in two ways, first through the reduction in COM distance between the two siRNAs, and second through the contraction of the PEIs. The COM distance

between the 2 siRNAs is plotted in Figure 4.8b. For both types of NPs, the COM distance hardly changed during the approach, attachment and embedment. During detachment, distinct behaviors were observed for the two NPs: while the COM distance increased significantly for PEI NP, it decreased for PEI-LA NP. To quantify the role of PEIs on the observed NP compaction and recovery, R_g of each NP are plotted for the POPS (left panel) and POPC (right panel) membranes (Figure 4.9.). For POPS membrane and PEI NP, R_g of all PEIs were constant during the approach stage. During attachment and embedment, R_g of 2 bridging PEIs (PEI-2 and PEI-4) and 1 peripheral PEI (PEI-6) remained constant while that of the other 2 bridging PEIs (PEI-1 and PEI-3) and 1 peripheral PEI (PEI-5) decreased. Together with the stable COM distance between the two siRNAs, it can be concluded that the compaction of the PEIs gave rise to the overall reduction in the R_g of the NP. During detachment, R_g of 3 PEIs (PEI-2, PEI-4, and PEI-5) were almost constant whereas R_g of the other 3 PEIs experienced slight increase. The increase, compared with the change in COM distance between the siRNAs, is small, and the increase in R_g of the NP was primarily due to the increased separation of the siRNA. For POPS and PEI-LA NP, similarly, R_g of all PEIs were constant during the approach stage. During attachment and embedment, R_g of 3 PEIs (PEI-2, PEI-3 and PEI-5) showed a decrease, while R_g of 1 PEI (PEI-4) displayed a slight increase. R_g of PEI-6 showed a fluctuating trend, where it first decreased up to the COM position of 0 Å, and then increased afterward. Considering the insignificant changes in COM distance between the siRNAs, the compaction of NP is again through the contraction of PEIs. During detachment, R_g of 4 PEIs (PEI-1, PEI-3, PEI-5, PEI-6) show an increase, while changes in R_g of the other PEIs was small. Considering a slight decrease in the COM distance between siRNAs, the recovery of the compacted NPs was mostly caused by the relaxation of the PEIs.

Figure 4.8c. shows the relative angle between the two siRNAs for POPS, as a way to quantify changes in siRNA alignment during membrane penetration. Previous studies suggested that misalignment may impact NP integrity by increasing the accessible area between the two siRNAs, which allows destabilizing compounds to interact with the NP core [5]. The relative angle (θ) was defined and calculated based on two vectors, one in each siRNA. $\theta = 0^\circ$ indicates parallel orientation, whereas $\theta = 90^\circ$ corresponds to perpendicular orientation of the siRNAs. For PEI NP, θ underwent some initial fluctuations but showed an increasing trend during detachment, corresponding to increased misalignment between the two siRNAs. For PEI-LA NP, θ was stable during approach but gradually decreased throughout the attachment, embedment and detachment stages. Eventually the two siRNAs formed an almost parallel orientation ($\theta \sim 4^\circ$). Such an alignment limits the interaction between membrane molecules and the PEIs at the center of the NP serving as polyion bridges, thereby protecting the PEI-LA NP from dissociation.

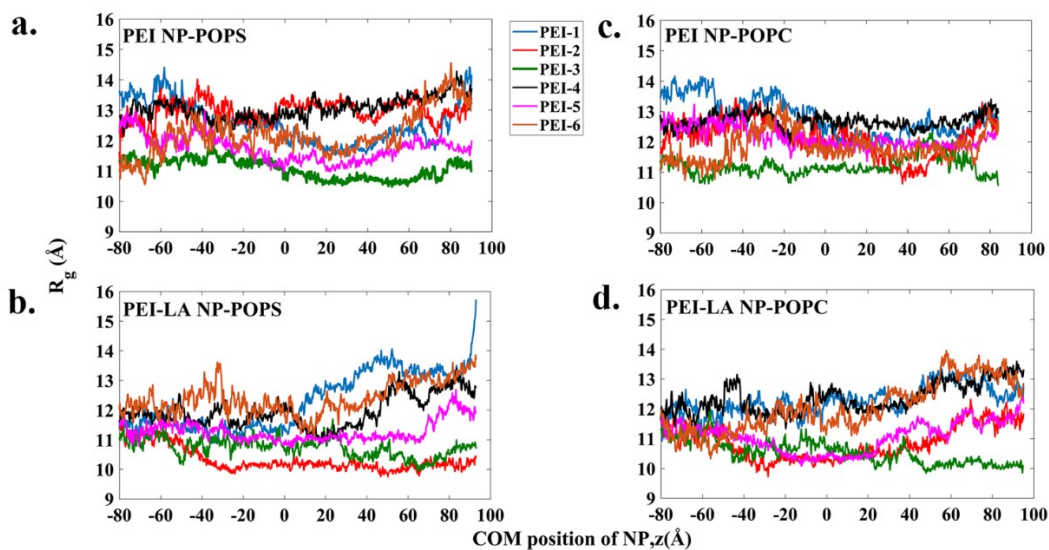


Figure 4.9. Gyration radius of the PEIs as a function of COM position of NP crossing the POPS (left panel) and POPC (right panel) membranes.

Corresponding results for the POPC membrane are shown in Figure 4.8d, e, f and Figure 4.9c, d. Table B.1. summarizes the changes in the structural parameters for the two types of NPs and two membranes. The key differences between POPC and POPS membranes are shown in red color, which mainly occur during detachment. For POPC in this stage, R_g of PEI NP increased to about the initial value, while it increased to 1 Å more than the initial value for the PEI-LA NP. The COM distance between siRNAs of both NPs exhibited no significant increase, indicating NPs retained their integrity. No noticeable change in θ was observed for PEI NP, while PEI-LA NP again formed an almost parallel orientation. Comparing the results in the right panels of Figure 4.8. and Figure 4.9., for PEI NP there was a clear correlation between R_g of the NP and the COM distance between the siRNAs, while R_g of individual PEIs were almost constant. This suggests that the compaction and recovery of the PEI NP while crossing the POPC membrane were both due to changes in the siRNA separation. On the other hand, the compaction and recover of PEI-LA NP depended more strongly on the configurational changes of the PEIs.

4.4. Discussion

The stability of PEI/siRNA NPs en-route to cells is crucial for an effective therapeutic outcome [57]. If the NP integrity is disrupted before uptake, the siRNAs will get exposed to surrounding environment prematurely, and the efficacy of delivery will reduce significantly [5]. Approximately 50% of cell surface is composed of lipids including anionic and zwitterionic species [58]. NPs during their cellular uptake are bound to interact with the charged lipidic groups[59]–[64]. It has been suggested that DNA is released from lipoplexes through electrostatic neutralization of cationic membranes by anionic lipids [61]. To assess NP integrity in the presence of membranes' lipids, representative anionic (POPS) and zwitterionic (POPC) liposomes have

been employed in this study. The results from ζ -potential measurements confirmed that POPS liposomes had higher negative charge than the POPC liposomes, which provide stronger electrostatic interaction with cationic NPs. Experiments of Kwolek et al.[13] on interaction between bare PEIs and liposomes showed that cationic PEIs did not interact strongly with zwitterionic POPC liposomes, and that the change in the ζ -potential of POPC liposomes treated with PEIs was insignificant. On the contrary, ζ -potential of the anionic liposomes of DOPA/POPC became positive after the addition of PEIs, indicating adsorption of the PEIs on the liposome surface. Recently, Gurtovenko[20] using MD simulations investigated the interactions between DNA/PEI NP and POPC membrane. In line with experimental observations, their simulations showed that the free energy gradually increased as the NP approached the surface of POPC membrane, indicating lack of attractive NP/membrane interactions. In our work, because of stronger interaction between anionic liposome and cationic NPs, POPS liposomes caused partial dissociation of both types of NPs in the EMSA experiments, while no dissociation was observed with the zwitterionic POPC liposomes. Our SMD simulations showed that both membranes induced configurational changes in both NPs. However, in line with the experiments, the structural changes caused by POPC was small while the POPS membrane significantly disturbed the structure of simulated NPs, evidenced by substantial increase in their siRNAs separation distance.

Besides lipids, the cell membrane contains other molecules that can interact with polymeric NPs to affect their dissociation. An example of such molecules is GAGs, among which heparin is known for its ability to destabilize polymeric NPs [54]. Liposome-induced dissociation may follow a different process than dissociation caused by the GAGs such as heparin. With increasing concentration of GAGs, complete disintegration of the NA cargo is common [18], [54].

On the contrary, even at highest concentrations of liposomes used here, complete dissociation was not observed in our work.

The presence of different membrane lipids can affect the resistive forces against the NP penetration. From atomistic point of view, these resistive forces originate from several types of interactions that stabilize the lipidic membranes. Interfacial tension caused by hydrophobic effect, steric repulsion between aliphatic chains, van der Waals interactions, HBs and electrostatics in the lipids' head group region, to name a few [65]. Here, since POPS and POPC membranes are difference from each other only by a -COOH group on POPS, stronger intermolecular interactions caused by formation of more HBs between POPS lipids is expected, consistent with the difference in the phase transition temperature of 13[66] and -3 °C[67] for POPS and POPC, respectively. The extra HBs can be formed between O of -COOH and hydrogen of -NH₂ on the adjacent lipid. Consistently, our simulations showed that resistive force for NP penetration into the POPS membrane was higher than the POPC membrane. Additionally, the presence of -COOH on POPS facilitates formation of more HBs between its surface and NP as quantified in Fig. B2, which provided additional resistance against the NP penetration. The HB curves mostly correlate with the force profiles, with higher number of HB leading to larger force. An exception to this was the PEI NP-POPS and PEI-LA NP-POPC systems. While the number of HBs is higher for the former system, their associated force profiles were comparable during the detachment stage. During detachment, R_g of the NPs in the PEI NP-POPS and PEI-LA NP-POPC systems were ~25.5 and ~26.5 Å (Figure 4.8a, d.), respectively. Considering stronger membrane deformation caused by the larger size of PEI-LA NP penetrating into the POPC membrane, the results suggest that more lipid-lipid interaction between POPC lipids needs to be broken, thereby increasing the force in the PEI-LA NP-POPC system.

Lipid substitution on PEIs can affect the stability of NPs and their ability to resist dissociation. We and others unequivocally demonstrated that binding of bare PEI to NAs in solution is superior to lipid substituted PEIs at the same PEI:siRNA ratio. However, dissociation of the NPs by POPS liposomes was easier for the PEI NP compared to the PEI-LA NP. It has been suggested that integrity of PEI/NA NPs are highly dependent on polyion bridging and its strength, where PEIs establish contact with multiple NA[68]. Figure 4.10. shows, for each bridging PEI in each simulated system, changes in its average number of N atoms within 4 Å of any N/O atoms of the siRNAs, based on calculations for the first and last 5 Å of the penetration process. For both membranes, bridging PEI Ns of PEI-LA NP either maintained or increased their interactions with siRNAs, while bridging PEI Ns of PEI NP behaved differently for the two membranes. For the POPS membrane, interaction of PEI-1 Ns of PEI NP with siRNAs was weakened considerably, while the total number of N of PEI-2 and PEI-3 in close contact with siRNAs remained relatively constant. However, the bridging performance of these two PEIs were weakened, as shown in Figure 4.6a., and they showed trend of becoming peripheral rather than remaining bridging. For the POPC membrane, on the other hand, bridging PEI Ns of PEI NP retained their interaction with both siRNAs. Our SMD simulations of NP penetration through the POPS membrane also showed insignificant changes in the angle between the two siRNAs in the PEI NP, accompanied by a large increase (up to 20%) in siRNA COM distance during detachment. On the other hand, PEI-LA NP showed a slight decrease in siRNA COM distance and a significant alignment of the two siRNAs, forming almost parallel orientation as the NP detached from the membrane. The results indicate that PEI-LA NP was able to better retain its integrity compared with native PEI NP, consistent with observations from EMSA experiments.

Sun et al.[25] previously explored the complexation mechanism for NPs derived from lipid-substituted PEIs using MD simulations, and found a high degree of correlation between the length of lipid chain and stability of the NPs; long-chained LA led to a more compact structure as compared to short-chain caprylic acid. Figure B.4. shows lipid associations between PEIs of PEI-LA NPs during penetration into the membranes. Lipid associations was quantified based on the number of pairs of lipid Cs that are closer than 5 Å between each pair of PEIs. Here, lipid association was formed only between the bridging PEI-2 and peripheral PEI-5. The associations follow a decreasing trend, where during detachment, associations were completely lost in the POPC membrane, while it was strongly weakened in the POPS membrane. Since in practical application excessive polymer will be used to form the NP with siRNA, associations are expected to occur between more pairs of PEI-LAs. To disintegrate the PEI-LA NP, these extra lipid associations need to be weakened and broken first, which requires stronger force and larger energy. These lipid associations therefore provide an additional protection mechanism against dissociation of PEI-LA NP, while PEI NP lacks this extra protection.

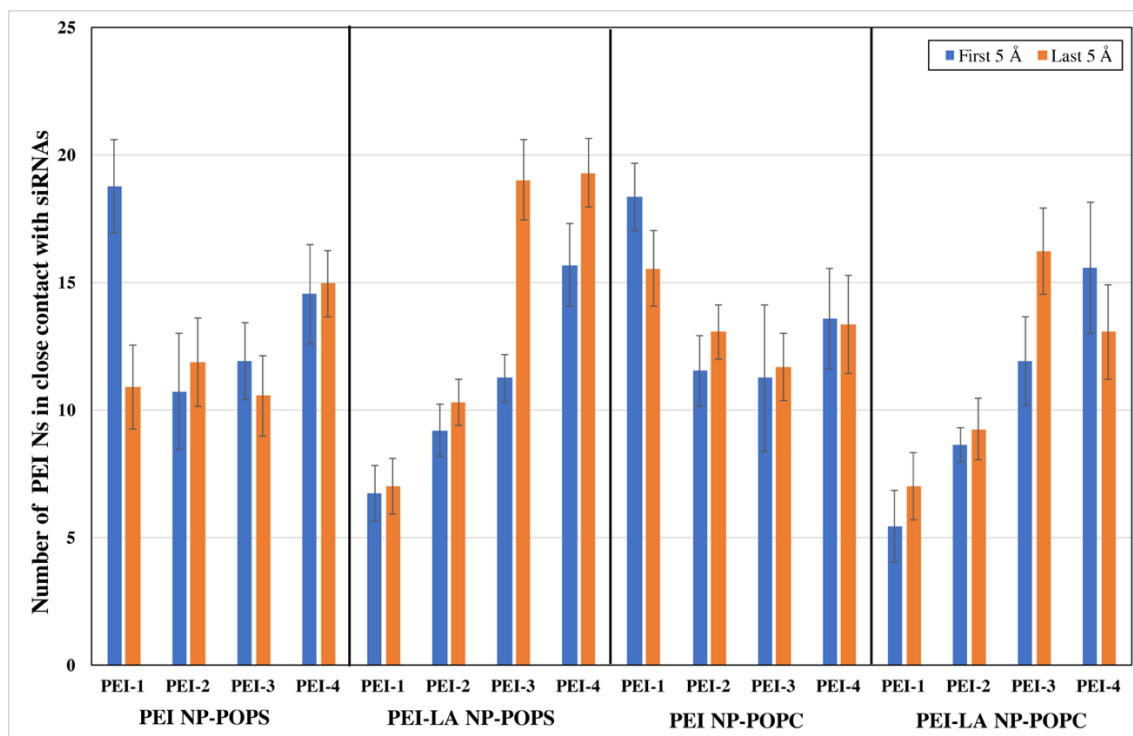


Figure 4.10. Average number of Ns of bridging PEIs within 4 Å of siRNAs N/O atoms during the first and last 5 Å of the penetration.

The anionic lipid molecules abundant in cell membranes may also contribute to dissociation of NPs within the cytoplasm, given that when NPs undergo endocytosis, a layer of encapsulating lipid bilayer will be formed around them [69]. Some NPs may also employ direct penetration to enter the cells through various methods involving diffusion, permeation and pore formation [33]. Upon NP entry into cells, siRNAs need to be released from their carriers for the Argonaute proteins and guide strand of siRNA to form RNA-induced silencing complex (RISC)[70]. Presence of POPS lipids might contribute to disintegration of NPs during endosomal escape. It has been reported that the percentage of PS lipids varies from being ~8.5% in the early endosome to 2.5-3.9% in the late endosome[71]. Unlike dissociation during cell entry, NP dissociation during endosomal escape can be beneficial to release the NAs for transport to appropriate sub-cellular sites. Our SMD simulations showed that anionic POPS membrane substantially disturbs the

integrity of siRNA/PEI NPs especially at the end of its membrane crossing and this methodology may help to understand lipids that contribute to release of siRNA in cytoplasm.

Liposomes are often utilized as a model for membrane interactions, but an important factor that may affect such interactions might be the size of liposomes used in the experimental systems. In our case, it is possible that the integrity of PEI/siRNA NPs might be differentially affected by the size of the liposomes. This issue was not explored in this chapter. With increase in liposome size, other effects such as wrapping of NPs, aggregation, pore formation, and deformation of liposomes might occur that need to be systematically evaluated [3], [72]–[74]. Here, we have used liposomes with relatively similar sizes to that of our PEI/siRNA NPs to avoid the aforementioned effects. It is of interest to evaluate the effect of liposome size on the stability of both PEI/siRNA NPs and liposomes. As pointed out by the anonymous reviewer, large liposomes or vesicles might be more representative of effects occurring at relatively flat cell membranes.

4.5. Conclusions

Using a combination of experiments and SMD simulations, integrity and configurational changes of siRNA/PEI NPs were assessed during their interaction with model membranes derived from POPC and POPS. We investigated two polymeric carriers for siRNA delivery, unmodified and LA-substituted PEIs. Binding experiments showed that at the same PEI/siRNA weight ratio, siRNA bound better with the PEI compared with PEI-LA, and higher polymer:NA ratio was required for LA-modified PEIs to provide full siRNA binding. POPS liposomes induced partial dissociation of both types of NPs whereas POPC liposomes lacked such an ability. SMD simulations showed that the NPs had stronger interactions with the POPS than with POPC membrane, evidenced by the formation of more HBs with the POPS membrane. Consequently, larger structural changes were experienced by the PEI NP penetrating the POPS membrane,

showing signs of NP destabilization. In addition, we found that lipid substitution on PEIs enhanced the stability of the NPs during membrane discharge. Lipid association among PEIs of PEI-LA NP as well as parallel orientation between its siRNAs provide an additional protection against the NP disintegration. Our complementary experimental and simulations data provide a unique insight into integrity and configurational changes of siRNA/PEI NPs during membrane crossing, which can facilitate the design of more efficient carrier for NA delivery.

4.6. Acknowledgments

Compute Canada and Westgrid are gratefully acknowledged for providing the computing resources and technical support. This work is funded by Natural Sciences and Engineering Research Council of Canada (NSERC), Canadian Institutes of Health Research (CIHR) and Alberta Innovates-Technology Futures (AITF). We thank Dr. A. Lavasanifar (Faculty of Pharmacy & Pharmaceutical Sciences, Univ. of Alberta) for access to the Zetasizer.

4.7. References

- [1] D. Pezzoli, E. K. Tsekoura, K. C. R. Bahadur, G. Candiani, D. Mantovani, and H. Uludağ, “Hydrophobe-substituted bPEI derivatives: boosting transfection on primary vascular cells,” *Sci. China Mater.*, vol. 60, no. 6, pp. 529–542, 2017.
- [2] S. K. Samal *et al.*, “Cationic polymers and their therapeutic potential,” *Chem. Soc. Rev.*, vol. 41, no. 21, pp. 7147–7194, 2012.
- [3] J. Sabín, C. Vázquez-Vázquez, G. Prieto, F. Bordini, and F. Sarmiento, “Double charge inversion in polyethylenimine-decorated liposomes,” *Langmuir*, vol. 28, no. 28, pp. 10534–10542, 2012.
- [4] K. Utsuno, H. Kono, E. Tanaka, N. Jouna, Y. Kojima, and H. Uludağ, “Low molecular weight branched PEI binding to linear DNA,” *Chem. Pharm. Bull.*, vol. 64, no. 10, pp. 1484–1491, 2016.
- [5] D. Meneksedag-Erol, T. Tang, and H. Uludağ, “Mechanistic insights into the role of glycosaminoglycans in delivery of polymeric nucleic acid nanoparticles by molecular dynamics simulations,” *Biomaterials*, vol. 156, pp. 107–120, Feb. 2018, doi: 10.1016/j.biomaterials.2017.11.037.
- [6] M. Laurencin, T. Georgelin, B. Malezieux, J.-M. Siaugue, and C. Ménager, “Interactions between giant unilamellar vesicles and charged core–shell magnetic nanoparticles,”

- Langmuir*, vol. 26, no. 20, pp. 16025–16030, 2010.
- [7] M. Boeckle, S. , von Gersdorff, K. , van der Piepen, S. , Culmsee, C. , Wagner, E. and Ogris, “Purification of polyethylenimine polyplexes highlights the role of free polycations in gene transfer,” *J. Gene Med.*, vol. 6, pp. 1102–1111, 2004, doi: 10.1002/jgm.598.
- [8] C. Zhang, F.-G. Wu, P. Hu, and Z. Chen, “Interaction of polyethylenimine with model cell membranes studied by linear and nonlinear spectroscopic techniques,” *J. Phys. Chem. C*, vol. 118, no. 23, pp. 12195–12205, 2014.
- [9] K. Yasuhara, M. Tsukamoto, Y. Tsuji, and J. Kikuchi, “Unique concentration dependence on the fusion of anionic liposomes induced by polyethyleneimine,” *Colloids Surfaces A Physicochem. Eng. Asp.*, vol. 415, pp. 461–467, 2012, doi: <https://doi.org/10.1016/j.colsurfa.2012.01.024>.
- [10] R. Jahn, T. Lang, and T. C. Südhof, “Membrane fusion,” *Cell*, vol. 112, no. 4, pp. 519–533, 2003.
- [11] S. R. Clark *et al.*, “Determining the effects of PEI adsorption on the permeability of 1,2-dipalmitoylphosphatidylcholine/bis(monoacylglycerol)phosphate membranes under osmotic stress,” *Acta Biomater.*, vol. 65, pp. 317–326, 2018, doi: <https://doi.org/10.1016/j.actbio.2017.10.027>.
- [12] S. Hong *et al.*, “Interaction of Polycationic Polymers with Supported Lipid Bilayers and Cells: Nanoscale Hole Formation and Enhanced Membrane Permeability,” *Bioconjug. Chem.*, vol. 17, no. 3, pp. 728–734, May 2006, doi: 10.1021/bc060077y.
- [13] U. Kwolek, D. Jamroz, M. Janiczek, M. Nowakowska, P. Wydro, and M. Kepczynski, “Interactions of Polyethylenimines with Zwitterionic and Anionic Lipid Membranes,” *Langmuir*, vol. 32, no. 19, pp. 5004–5018, May 2016, doi: 10.1021/acs.langmuir.6b00490.
- [14] C. K. Choudhury, A. Kumar, and S. Roy, “Characterization of Conformation and Interaction of Gene Delivery Vector Polyethylenimine with Phospholipid Bilayer at Different Protonation State,” *Biomacromolecules*, vol. 14, no. 10, pp. 3759–3768, Oct. 2013, doi: 10.1021/bm4011408.
- [15] L. Kjellen and U. Lindahl, “Proteoglycans: structures and interactions,” *Annu. Rev. Biochem.*, vol. 60, no. 1, pp. 443–475, 1991.
- [16] T. Miller, M. C. Goude, T. C. McDevitt, and J. S. Temenoff, “Molecular engineering of glycosaminoglycan chemistry for biomolecule delivery,” *Acta Biomater.*, vol. 10, no. 4, pp. 1705–1719, 2014.
- [17] I. Moret *et al.*, “Stability of PEI–DNA and DOTAP–DNA complexes: effect of alkaline pH, heparin and serum,” *J. Control. Release*, vol. 76, no. 1–2, pp. 169–181, 2001.
- [18] A. Kwok and S. L. Hart, “Comparative structural and functional studies of nanoparticle formulations for DNA and siRNA delivery,” *Nanomedicine Nanotechnology, Biol. Med.*, vol. 7, no. 2, pp. 210–219, 2011.

- [19] N. Ernst *et al.*, “Interaction of liposomal and polycationic transfection complexes with pulmonary surfactant,” *J. Gene Med. A cross-disciplinary J. Res. Sci. gene Transf. its Clin. Appl.*, vol. 1, no. 5, pp. 331–340, 1999.
- [20] A. A. Gurtovenko, “Molecular-Level Insight into the Interactions of DNA-Polycation Complexes with Model Cell Membranes,” *J. Phys. Chem. B*, vol. 123, no. 30, pp. 6505–6514, 2019, doi: <https://doi.org/10.1021/acs.jpccb.9b05110>.
- [21] P. Chen *et al.*, “Diffusion and directionality of charged nanoparticles on lipid bilayer membrane,” *ACS Nano*, vol. 10, no. 12, pp. 11541–11547, 2016.
- [22] G. Zhu, Z. Huang, Z. Xu, and L.-T. Yan, “Tailoring interfacial nanoparticle organization through entropy,” *Acc. Chem. Res.*, vol. 51, no. 4, pp. 900–909, 2018.
- [23] P. Chen *et al.*, “Transport of a graphene nanosheet sandwiched inside cell membranes,” *Sci. Adv.*, vol. 5, no. 6, p. eaaw3192, 2019.
- [24] H. M. Aliabadi, B. Landry, R. K. Bahadur, A. Neamark, O. Suwantong, and H. Uludağ, “Impact of Lipid Substitution on Assembly and Delivery of siRNA by Cationic Polymers,” *Macromol. Biosci.*, vol. 11, no. 5, pp. 662–672, May 2011, doi: 10.1002/mabi.201000402.
- [25] C. Sun, T. Tang, and H. Uludag, “A molecular dynamics simulation study on the effect of lipid substitution on polyethylenimine mediated siRNA complexation,” *Biomaterials*, vol. 34, no. 11, pp. 2822–2833, Apr. 2013, doi: 10.1016/j.biomaterials.2013.01.011.
- [26] A. Neamark, O. Suwantong, R. B. K. C., C. Y. M. Hsu, P. Supaphol, and H. Uludağ, “Aliphatic Lipid Substitution on 2 kDa Polyethylenimine Improves Plasmid Delivery and Transgene Expression,” *Mol. Pharm.*, vol. 6, no. 6, pp. 1798–1815, Dec. 2009, doi: 10.1021/mp900074d.
- [27] M. Abbasi *et al.*, “siRNA-Mediated Down-Regulation of P-glycoprotein in a Xenograft Tumor Model in NOD-SCID Mice,” *Pharm. Res.*, vol. 28, no. 10, pp. 2516–2529, Oct. 2011, doi: 10.1007/s11095-011-0480-z.
- [28] K. Utsuno and H. Uludağ, “Thermodynamics of Polyethylenimine-DNA Binding and DNA Condensation,” *Biophys. J.*, vol. 99, no. 1, pp. 201–207, Jul. 2010, doi: 10.1016/j.bpj.2010.04.016.
- [29] A. von Harpe, H. Petersen, Y. Li, and T. Kissel, “Characterization of commercially available and synthesized polyethylenimines for gene delivery,” *J. Control. Release*, vol. 69, no. 2, pp. 309–322, 2000.
- [30] J. Suh, H. Paik, and B. K. Hwang, “Ionization of Poly (ethylenimine) and Poly (allylamine) at Various pH’ s,” *Bioorg. Chem.*, vol. 22, no. 3, pp. 318–327, 1994.
- [31] J. Nagaya, M. Homma, A. Tanioka, and A. Minakata, “Relationship between protonation and ion condensation for branched poly (ethylenimine),” *Biophys. Chem.*, vol. 60, no. 1–2, pp. 45–51, 1996.
- [32] G. J. M. Koper, R. C. van Duijvenbode, D. D. P. W. Stam, U. Steuerle, and M. Borkovec,

- “Synthesis and protonation behavior of comblike poly (ethylimine),” *Macromolecules*, vol. 36, no. 7, pp. 2500–2507, 2003.
- [33] Y. Nademi, T. Tang, and H. Uludağ, “Steered molecular dynamics simulations reveal a self-protecting configuration of nanoparticles during membrane penetration,” *Nanoscale*, vol. 10, no. 37, pp. 17671–17682, 2018, doi: 10.1039/C8NR04287J.
- [34] E. L. Wu *et al.*, “CHARMM-GUI membrane builder toward realistic biological membrane simulations,” *J. Comput. Chem.*, vol. 35, no. 27, pp. 1997–2004, 2014.
- [35] B. R. Brooks *et al.*, “CHARMM: the biomolecular simulation program,” *J. Comput. Chem.*, vol. 30, no. 10, pp. 1545–1614, 2009.
- [36] S. Jo, T. Kim, V. G. Iyer, and W. Im, “CHARMM-GUI: a web-based graphical user interface for CHARMM,” *J. Comput. Chem.*, vol. 29, no. 11, pp. 1859–1865, 2008.
- [37] W. L. Jorgensen, “Quantum and statistical mechanical studies of liquids. 10. Transferable intermolecular potential functions for water, alcohols, and ethers. Application to liquid water,” *J. Am. Chem. Soc.*, vol. 103, no. 2, pp. 335–340, Jan. 1981, doi: 10.1021/ja00392a016.
- [38] J. Lee *et al.*, “CHARMM-GUI input generator for NAMD, GROMACS, AMBER, OpenMM, and CHARMM/OpenMM simulations using the CHARMM36 additive force field,” *J. Chem. Theory Comput.*, vol. 12, no. 1, pp. 405–413, 2015.
- [39] S. Park, F. Khalili-Araghi, E. Tajkhorshid, and K. Schulten, “Free energy calculation from steered molecular dynamics simulations using Jarzynski’s equality,” *J. Chem. Phys.*, vol. 119, no. 6, pp. 3559–3566, Aug. 2003, doi: 10.1063/1.1590311.
- [40] Q. Wei, W. Zhao, Y. Yang, B. Cui, Z. Xu, and X. Yang, “Method Evaluations for Adsorption Free Energy Calculations at the Solid/Water Interface through Metadynamics, Umbrella Sampling, and Jarzynski’s Equality,” *ChemPhysChem*, vol. 210009, pp. 1–14, Feb. 2018, doi: 10.1002/cphc.201701241.
- [41] H. Nguyen, N. Do, T. Phan, and T. Pham, “Steered Molecular Dynamics for Investigating the Interactions Between Insulin Receptor Tyrosine Kinase (IRK) and Variants of Protein Tyrosine Phosphatase 1B (PTP1B),” *Appl. Biochem. Biotechnol.*, vol. 184, no. 2, pp. 401–413, Feb. 2018, doi: 10.1007/s12010-017-2549-6.
- [42] Y. Xu *et al.*, “How does huperzine A enter and leave the binding gorge of acetylcholinesterase? Steered molecular dynamics simulations,” *J. Am. Chem. Soc.*, vol. 125, no. 37, pp. 11340–11349, 2003.
- [43] D. J. Brockwell *et al.*, “Pulling geometry defines the mechanical resistance of a β -sheet protein,” *Nat. Struct. Mol. Biol.*, vol. 10, no. 9, p. 731, 2003.
- [44] S. Azadi, M. Tafazzoli-Shadpour, and R. Omidvar, “Steered Molecular Dynamics Simulation Study of Quantified Effects of Point Mutation Induced by Breast Cancer on Mechanical Behavior of E-Cadherin,” *Mol. Biol.*, vol. 52, no. 5, pp. 723–731, 2018.

- [45] H. Lu and K. Schulten, “Steered molecular dynamics simulations of force-induced protein domain unfolding,” *Proteins Struct. Funct. Bioinforma.*, vol. 35, no. 4, pp. 453–463, 1999.
- [46] E. J. Denning, U. D. Priyakumar, L. Nilsson, and A. D. Mackerell, “Impact of 2'-hydroxyl sampling on the conformational properties of RNA: Update of the CHARMM all-atom additive force field for RNA,” *J. Comput. Chem.*, vol. 32, no. 9, pp. 1929–1943, Jul. 2011, doi: 10.1002/jcc.21777.
- [47] J. B. Klauda *et al.*, “Update of the CHARMM all-atom additive force field for lipids: validation on six lipid types,” *J. Phys. Chem. B*, vol. 114, no. 23, pp. 7830–7843, Jun. 2010, doi: 10.1021/jp101759q.
- [48] J. C. Phillips *et al.*, “Scalable molecular dynamics with NAMD,” *J. Comput. Chem.*, vol. 26, no. 16, pp. 1781–1802, Dec. 2005, doi: 10.1002/jcc.20289.
- [49] T. Darden, D. York, and L. Pedersen, “Particle mesh Ewald: An $N \cdot \log(N)$ method for Ewald sums in large systems,” *J. Chem. Phys.*, vol. 98, no. 12, pp. 10089–10092, Jun. 1993, doi: 10.1063/1.464397.
- [50] J.-P. Ryckaert, G. Ciccotti, and H. J. Berendsen, “Numerical integration of the cartesian equations of motion of a system with constraints: molecular dynamics of n-alkanes,” *J. Comput. Phys.*, vol. 23, no. 3, pp. 327–341, Mar. 1977, doi: 10.1016/0021-9991(77)90098-5.
- [51] G. J. Martyna, D. J. Tobias, and M. L. Klein, “Constant pressure molecular dynamics algorithms,” *J. Chem. Phys.*, vol. 101, no. 5, pp. 4177–4189, 1994.
- [52] S. E. Feller, Y. Zhang, R. W. Pastor, and B. R. Brooks, “Constant pressure molecular dynamics simulation: the Langevin piston method,” *J. Chem. Phys.*, vol. 103, no. 11, pp. 4613–4621, 1995.
- [53] W. Humphrey, A. Dalke, and K. Schulten, “VMD: Visual molecular dynamics,” *J. Mol. Graph.*, vol. 14, no. 1, pp. 33–38, Feb. 1996, doi: 10.1016/0263-7855(96)00018-5.
- [54] D. Meneksedag-Erol, T. Tang, and H. Uludağ, “Probing the effect of miRNA on siRNA–PEI polyplexes,” *J. Phys. Chem. B*, vol. 119, no. 17, pp. 5475–5486, 2015.
- [55] J. Ziebarth and Y. Wang, “Molecular dynamics simulations of DNA-polycation complex formation,” *Biophys. J.*, vol. 97, no. 7, pp. 1971–1983, 2009.
- [56] C. Sun, T. Tang, H. Uludağ, and J. E. Cuervo, “Molecular dynamics simulations of DNA/PEI complexes: Effect of PEI branching and protonation state,” *Biophys. J.*, vol. 100, no. 11, pp. 2754–2763, 2011, doi: 10.1016/j.bpj.2011.04.045.
- [57] H. M. Aliabadi, B. Landry, C. Sun, T. Tang, and H. Uludağ, “Supramolecular assemblies in functional siRNA delivery: where do we stand?,” *Biomaterials*, vol. 33, no. 8, pp. 2546–2569, 2012.
- [58] M. Sud *et al.*, “LMSD: LIPID MAPS structure database,” *Nucleic Acids Res.*, vol. 35, no. suppl_1, pp. D527–D532, Nov. 2006, doi: 10.1093/nar/gkl838.

- [59] G. Caracciolo and H. Amenitsch, "Cationic liposome/DNA complexes: from structure to interactions with cellular membranes," *Eur. Biophys. J.*, vol. 41, no. 10, pp. 815–829, 2012.
- [60] R. Dias, M. Rosa, A. C. Pais, M. Miguel, and B. Lindman, "DNA-Surfactant Interactions. Compaction, Condensation, Decompaction and Phase Separation," *J. Chinese Chem. Soc.*, vol. 51, no. 3, pp. 447–469, 2004.
- [61] G. Caracciolo, D. Pozzi, H. Amenitsch, and R. Caminiti, "Interaction of lipoplexes with anionic lipids resulting in DNA release is a two-stage process," *Langmuir*, vol. 23, no. 17, pp. 8713–8717, 2007.
- [62] Y. Xu and F. C. Szoka, "Mechanism of DNA release from cationic liposome/DNA complexes used in cell transfection," *Biochemistry*, vol. 35, no. 18, pp. 5616–5623, 1996.
- [63] G. Caracciolo *et al.*, "On the correlation between phase evolution of lipoplexes/anionic lipid mixtures and DNA release," *Appl. Phys. Lett.*, vol. 91, no. 14, p. 143903, 2007.
- [64] G. Caracciolo *et al.*, "Structural stability against disintegration by anionic lipids rationalizes the efficiency of cationic liposome/DNA complexes," *Langmuir*, vol. 23, no. 8, pp. 4498–4508, 2007.
- [65] M. Langner and K. Kubica, "The electrostatics of lipid surfaces," *Chem. Phys. Lipids*, vol. 101, no. 1, pp. 3–35, 1999.
- [66] D. Bach, E. Wachtel, N. Borochoy, G. Senisterra, and R. M. Epand, "Phase behaviour of heteroacid phosphatidylserines and cholesterol," *Chem. Phys. Lipids*, vol. 63, no. 1–2, pp. 105–113, 1992.
- [67] K. L. Koster, M. S. Webb, G. Bryant, and D. V Lynch, "Interactions between soluble sugars and POPC (1-palmitoyl-2-oleoylphosphatidylcholine) during dehydration: vitrification of sugars alters the phase behavior of the phospholipid," *Biochim. Biophys. Acta (BBA)-Biomembranes*, vol. 1193, no. 1, pp. 143–150, 1994.
- [68] D. Meneksedag-Erol, T. Tang, and H. Uludağ, "Molecular modeling of polynucleotide complexes," *Biomaterials*, vol. 35, no. 25, pp. 7068–7076, Aug. 2014, doi: 10.1016/j.biomaterials.2014.04.103.
- [69] S. Zhang, H. Gao, and G. Bao, "Physical Principles of Nanoparticle Cellular Endocytosis," *ACS Nano*, vol. 9, no. 9, pp. 8655–8671, Sep. 2015, doi: 10.1021/acsnano.5b03184.
- [70] B. Czech and G. J. Hannon, "Small RNA sorting: matchmaking for Argonautes," *Nat. Rev. Genet.*, vol. 12, no. 1, p. 19, 2011.
- [71] P. A. Leventis and S. Grinstein, "The Distribution and Function of Phosphatidylserine in Cellular Membranes," *Annu. Rev. Biophys.*, vol. 39, pp. 407–427, 2010, doi: 10.1146/annurev.biophys.093008.131234.
- [72] M. Sikor *et al.*, "Interaction of a charged polymer with zwitterionic lipid vesicles," *Langmuir*, vol. 26, no. 6, pp. 4095–4102, 2010.

- [73] N. Wilkosz *et al.*, “Effect of polycation structure on interaction with lipid membranes,” *J. Phys. Chem. B*, vol. 121, no. 30, pp. 7318–7326, 2017.
- [74] L. Wang and N. Malmstadt, “Interactions between charged nanoparticles and giant vesicles fabricated from inverted-headgroup lipids,” *J. Phys. D. Appl. Phys.*, vol. 50, no. 41, p. 415402, 2017.

5. Nature of Bilayer Lipids Affects Membranes Deformation and Pore Resealing During Nanoparticle Penetration.

5.1. Introduction

Delivery of genetic material, either deoxyribonucleic acid (DNA) or ribonucleic acid (RNA), into cells has proven to be an effective strategy in treating genetic disorders and cancers [1]. For effective therapy, genetic materials need a carrier to protect them against nucleases and facilitate their cellular entry. In this context, non-viral carriers acquired substantial attention due to their easy-to-engineer and relatively safe nature in comparison to their viral compartments [2]. Among non-viral carriers, the synthetic cationic polymer polyethylenimine (PEI) has received special attention due to the possibility of being easily modified with various functional groups. Its gene delivery performance has been tested extensively in a number of cell models [3]. PEI based nanoparticles (NPs) must enter the cells through a process that involves interaction with cell membrane molecules, where the NPs are expected to preserve their integrity while delivering their cargo into the cytoplasm [4]. Cytoplasmic membranes are vital components of every cell, which may contain hundreds of different lipids distributed between the two bilayer leaflets and crowded with proteins covering ~30% of membrane area [5]. The types of lipids and their spatial configurations define the biophysical properties of the membrane [6]. As an example, the length and degree of saturation of lipid acyl chains govern the thickness and ordering of the hydrophobic region of membranes [6]. Presence of double bonds in the fatty acyl chains of lipids can cause bending of the hydrocarbon chains, thereby affecting the structural and dynamical properties of the membrane[7].

There has been considerable interest in simulative and experimental studies to reveal interaction of NPs with membranes [8]–[10], especially to understand pore formation and resealing during NP penetration. Membrane pores can be intentionally induced for therapeutic applications, to momentarily enhance membrane permeability and allow therapeutic agents to diffuse into cells

[11]. Presence of defects or pores across membranes could lead to unregulated ionic flux and facilitate passive transport of polar molecules [12]. Also, pores can act as initiation sites for structural defects associated with phase transitions, cell fusion, and lysis [12]. *Kwolek et al.*[13], using experiments and molecular dynamics (MD) simulations, studied the role of free PEI molecules on membrane deformation. They found that the electrostatic interactions and hydrogen bonding between PEI and anionic membrane of 2-oleoyl-1-palmitoyl-sn-glycero-3-phosphocholine (POPC)/1,2-dioleoyl-sn-glycero-3-phosphoric acid (DOPA) induced reorganization of the bilayer in the vicinity of the polymers. This caused pulling of lipid head groups toward the membrane center and the formation of a pore within the membrane structure. *Zhang et al.* [14] using sum frequency generation (SFG) vibrational spectroscopy and attenuated total internal reflection Fourier Transform Infrared Spectroscopy (ATR-FTIR), observed that both linear PEI (lPEI) and branched PEI (bPEI) induced lipid translocations, also known as lipid “flip-flop”, in anionic dipalmitoylphosphatidylglycerol (DPPG) as well as zwitterionic distearoylphosphatidylcholine (DSPC) lipid bilayers. *Awasthi et al.* [15] based on their experiments and MD simulations proposed a molecular mechanism for polycation-induced pore formation in membranes. Changes in the membrane structure was attributed to difference in electrostatic potential between the two leaflets of the membrane, induced by polycations. Membrane pores can also be formed through electroporation as a result of applying external electrical fields. MD simulations of *Tieleman et al.*[16] showed that the external electric field interacted with water dipoles, amplified the probability of creating water defects in the membrane interior, and stabilized the formed defects. Experimental and simulation studies showed that pore formation caused by electroporation was highly dependent on the nature of the membrane, where a stronger electric field was required to induce a pore in more ordered membranes that had a larger

number of intermolecular hydrogen bonds [17]–[20]. As a representative example, *Ziegler et al.*[21] using MD simulations found that the minimal threshold of electric field to induce pore formation varied with lipid properties including the chain length and type of acyl chains (i.e., saturated or unsaturated). Specifically, there was a positive correlation between the minimum electric field required to induce the pore and the membrane's thickness as well as the unsaturation level of its acyl chains. Increase in the number of Cs and unsaturated bonds in the acyl chains amplified the required external electric field. Once a transmembrane pore is formed, its fate may be different depending on its size. Below a critical radius, spontaneous resealing occurs [12] whereas above the threshold the pore might lead to irreversible membrane rupture. This emphasizes the need to investigate not only pore formation, but also pore resealing after external stimuli were removed.

Many studies have investigated different membranes in terms of head groups, acyl chains length, and saturation level of lipid chains. *Hyvonen et al.*[7] using MD simulations studied lipid bilayers of dipalmitoylphosphatidylcholine (DPPC) and its mono-, di-, and tetraunsaturated counterparts in the Sn2 position. They found that presence of double bonds substantially reduced the order parameters of CH bonds. Additionally, the double bonds of tetraunsaturated chains were shown to be located in the region spanning from the head group to the bilayer center. On a similar topic, *Zhuang et al.*[22] studied a number of different membrane lipids, including lipids with various head groups (phosphatidic acid (PA), phosphocholine (PC), phosphoethanolamine (PE), phosphoglycerol (PG), and phosphoserine (PS)). It was found that PS had the highest inter-lipid hydrogen bonds, while PG had the most intra-lipid hydrogen bonds. This caused PS and PG bilayers to have the lowest surface area per lipid and the smallest thickness, respectively. In

addition, PS, PE and PA lipids had larger contact clusters (5-8 lipids per cluster) than the PC and PG, a size that characterizes the local packing behavior of lipid head groups.

While these studies provided valuable insights into the effect of lipid molecules on membrane features, and mechanism(s) of pore formation caused by small molecules such as free PEIs, it is evident that further studies are required to provide atomistic insight into more complex systems such as the NP interactions with membranes. Previously, our group performed steered MD (SMD) simulations and investigated the stability and configurational changes of NPs formed by PEI and short interfering RNA (siRNA) during penetration into the zwitterionic POPC membrane [23]. Three types of PEI molecules, namely unmodified PEI and PEIs modified with caprylic (CA) and linoleic acids (LA), were employed. The structural changes in the PEI-LA/siRNA NP were minimal, while the PEI-CA/siRNA NP showed the largest structural changes. In a more recent study [24], we investigated the effect of membrane surface molecules on the integrity and configurational changes of NPs, using a combined simulation and experimental approach. We found that anionic POPS lipids can dissociate the NPs, while zwitterionic POPC lipids did not induce dissociation. Additionally, LA substitution was found to enhance the stability of PEI/siRNA NPs. While those studies were beneficial for the understanding of structural changes in NPs, the effect of NP penetration on the integrity of membranes has not been explored. To the best of our knowledge, the present work is the first all-atom study that investigated the interplay between PEI NPs and various lipidic membrane models where the acyl chain lengths and saturation levels were altered. SMD and MD simulations were employed for zwitterionic POPC, DPPC, and dilauroylphosphatidylcholine (DLPC) membranes in this chapter. These membranes have the same surface properties, but possess different acyl chain properties. Native and LA-modified PEIs were adopted as polynucleotide carriers, since LA-modified PEIs have proven to be an

exceptionally effective carrier for gene delivery in our experimental studies [25], [26]. Our focus in this study was to investigate (i) pore formation and resealing mechanism during NP penetration, and (ii) the effects of acyl chain features of the membrane lipids, and carrier properties on pore formation.

5.2. Methods

5.2.1. Simulated systems and procedure

Two types of NPs were simulated, each comprised of 2 siRNA molecules and 6 branched PEIs (bPEIs). The model siRNA has the sense strand of 5'- CAGAAAGCUUAGUACCAAATT-3' and antisense strand of 5'-UUUGGUACUAAGCUUUCUGTC-3'. It is used to silence P-glycoprotein [27] and consists of 42 nucleotides with a total charge of -40 in its fully deprotonated state. The chemical structure of simulated PEI is shown in Figure 5.1a. The PEI in its native form has a molecular weight of 1874 Da and is composed of 43 amino groups. Twenty of these amino groups were protonated, equivalent to the protonation ratio of 47%, which was in the range of reported protonation ratio (10 to 50% [28]–[31]) for PEI at physiological pH. For simplicity, the NP formed by 2 siRNAs and 6 native PEIs was referred to as PEI NP (see Table 5.1). The other simulated NP was denoted as PEI-LA NP in Table 5.1, where each PEI was modified with 3 hydrophobic substitutions of LA. The chosen substitution level was in line with the practical range of modification used for siRNA delivery [32]. The initial structures of NPs were adopted from our previous study where they were equilibrated at 310K. Then, to equilibrate the NPs at 323K that was above the phase transition temperature of our simulated membrane lipids, each NP was solvated with TIP3P [33] water molecules and ions (150 mM KCL) and subjected to 7 ns (restrained) + 33 ns (free) simulation. The final equilibrated structure of each NP was adopted as

the initial configuration of the NP for SMD simulations of membrane penetration (see Appendix C, Figures C1 and C2).

Three membrane lipids, POPC, DPPC and DLPC, were used, and their chemical structures are shown in Figure 5.1b. Among these lipids, DLPC has the shortest lipid tails (12:0, 12:0), where the first indices represent the number of C atoms in Sn1 and Sn2 chains (12 and 12 here), and the second indices specify the number of unsaturated carbons in each chain (0 and 0 here). The tails of DPPC (16:0, 16:0) and POPC (16:0, 18:1) are of similar length, but differ in terms of saturation, where POPC has one unsaturated carbon on its Sn2 chain. The initial structure of POPC bilayer was adopted from our previous study [23]. DPPC and DLPC bilayers were constructed using Membrane Builder [34] in CHARMM-GUI [35], [36]. Similar to the NPs, the membranes were equilibrated by 50 ns MD simulations until the area per lipid reached $60.45 \pm 0.34 \text{ \AA}^2$ and $63.21 \pm 0.53 \text{ \AA}^2$ (data collected from the last 20 ns), respectively for DPPC and DLPC, which agreed with the values reported in the literature [37], [38]. The final equilibrated configurations were adopted as the input structures for SMD simulations with NPs (see Appendix C, Figures C3-C6).

SMD simulations assist in accelerating the penetration process and also mimic the situation where the NPs are pulled by external or biological forces towards the interior of the cell membrane. In each SMD the system was prepared by first placing the NP above the membrane so that the center of mass (COM) distance between the NP and the membrane was 8 nm. Initial orientation of the NP was chosen in a way such that the axes of its siRNAs were almost perpendicular to the membrane surface. Then, upon solvation with TIP3P [33] water and 150 mM KCL, the system was equilibrated for 6 ns with a harmonic restraint of $10 \text{ kcal mol}^{-1} \text{ \AA}^{-2}$ exerted on the non-H atoms of the NP. The equilibrated membrane-NP system was used next for the SMD simulation, where the COM of the NP was attached to a dummy atom via a virtual spring and the spring was pulled

with a constant velocity along the z direction perpendicular to the membrane surface. The pulling speed $v = 5 \text{ \AA ns}^{-1}$ and spring constant $k = 5 \text{ kcal mol}^{-1} \text{ \AA}^{-2}$ were used. In the literature, pulling speeds in the range of 0.1 to 100 \AA ns^{-1} have been reported for SMD simulations, while lower values of pulling speed have been used to determine the potential of mean force [39]–[45]. Previously[23], we explored the effect of pulling speed and showed that $v = 5 \text{ \AA ns}^{-1}$ was suitable for studying membrane penetration of NPs. Each SMD simulation took 34 ns for the NP to travel a total distance of 170 \AA . In Table 5.1, PEI NP-POPC, PEI NP-DPPC and PEI NP-DLPC are respectively the SMD simulations for the PEI NP crossing POPC, DPPC and DLPC bilayers. The corresponding SMD simulations for the PEI-LA NP are PEI-LA NP-POPC, PEI-LA NP-DPPC and PEI-LA NP-DLPC.

At last, the final configurations from the SMD simulation were used to investigate pore closure by MD simulations without restraints. Specifically, the NP in each system was removed and the deformed membrane was solvated again with TIP3P[33] water and 150 mM KCL. Water molecules were placed at above and below of the membrane. Each of the six membrane systems was then subjected to 64 ns MD. These systems are labeled in Table 5.1 as POPC (PEI NP), DPPC (PEI NP), DLPC (PEI NP), POPC (PEI-LA NP), DPPC (PEI-LA NP) and DLPC (PEI-LA NP).

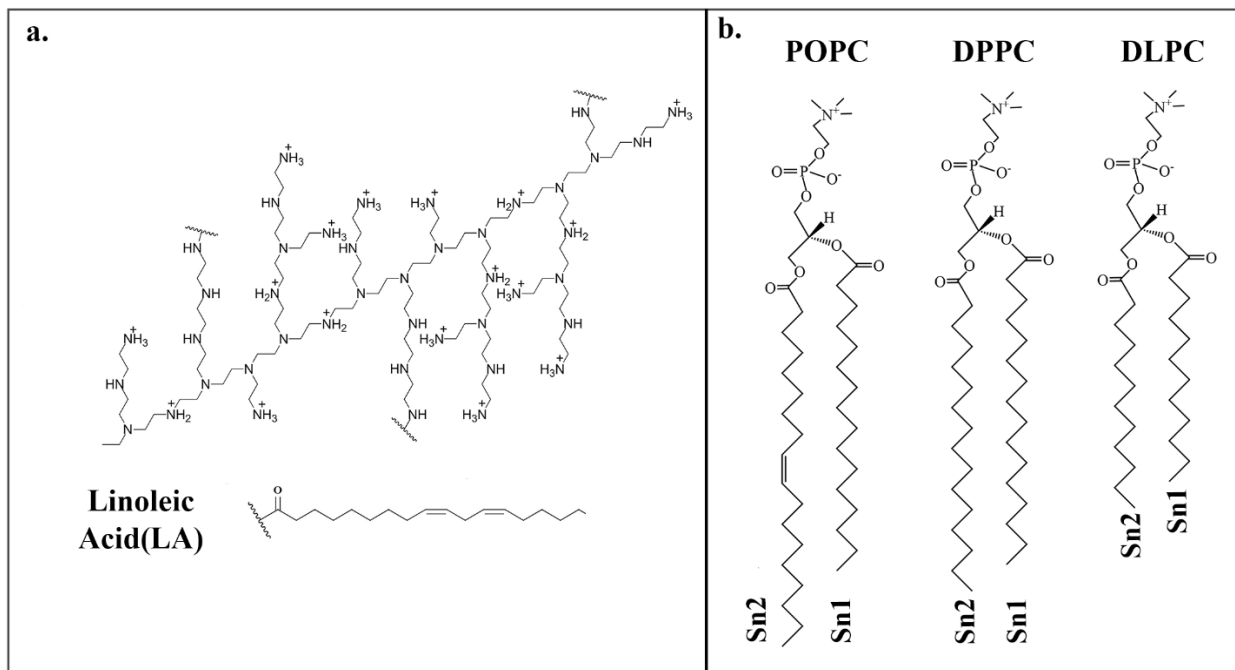


Figure 5.1. Molecular structure of the simulated molecules.

(a) Molecular structure, protonation sites and lipid substitution sites of the simulated PEIs, (b) structures of POPC, DPPC, and DLPC molecules.

Table 5.1. Detailed information of the simulated systems.

System	Number of atoms	Size of the simulation box (\AA^3)	Lipid no./type on each PEI	Charge ratio PEI/siRNA	Simulation time (ns)
PEI NP	85640	90×100×100	None	1.5	40
PEI-LA NP	93691	100×90×100	3 LA	1.27	40
PEI NP-POPC	990451	160 ×180×340	None	1.5	34
PEI NP-DPPC	1018962	160×200×340	None	1.5	34
PEI NP-DLPC	1015417	180×170×340	None	1.5	34
POPC (PEI NP)	658088	160×180×230	-	-	64
DPPC (PEI NP)	632815	160×200×320	-	-	64
DLPC (PEI NP)	633654	180×170×220	-	-	64
PEI-LA NP-POPC	990473	160 ×180×340	3 LA	1.27	34
PEI-LA NP-DPPC	1019002	160×200×340	3 LA	1.27	34
PEI-LA NP-DLPC	1015459	180×170×340	3 LA	1.27	34
POPC (PEI-LA NP)	572647	160×180×200	-	-	64
DPPC (PEI-LA NP)	606802	160×200×310	-	-	64
DLPC (PEI-LA NP)	605079	180×170×220	-	-	64

5.2.2. Simulation details

Force field parameters for the PEI molecules were adopted from a previous study [46] by our group, which were generated according to CHARMM General Force Field and validated with *ab initio* calculations. A CHARMM 36 [47], [48] Force Field was used for other molecules. All simulations were performed using NAMD [49] molecular dynamic package and in NPT ensemble. Time steps of 2 fs and periodic boundary conditions (PBC) in *x*, *y*, and *z* directions were applied. Particle Mesh Ewald [50] (PME) method was employed to calculate long-ranged electrostatic

interactions. The cut off distance was set to 12 Å for van der Waals and short-range electrostatic interactions. The SHAKE [51] algorithm was used for constraining bonds involving H atoms. To maintain the temperature (323K), Langevin dynamics thermostat was used. The pressure was maintained using a semi-isotropic pressure control that decouples the direction normal to the bilayer and the plane of the bilayer. Nose-Hoover Langevin barostat was applied to achieve 1 bar pressure, with a damping time scale of 100 fs and a Langevin piston oscillation period of 200 fs [52], [53]. For visualization and analysis of simulation trajectories, VMD [54] was used.

5.3. Results

5.3.1. Membrane deformations during penetration of PEI NP

Penetration of the PEI NP induced membrane deformation during its entry. To measure the deformation, the positions of all P atoms are shown in Figure 5.2 at different timeframes. All membranes experienced a disruption in their integrity as the NP penetrated. At 10 ns, the disturbance started first in the upper leaflet while the lower leaflet maintained its integrity. At 20 ns, the membranes bent and both leaflets underwent deformation. At 34 ns, the deformation of the membranes was severe, and the P atoms no longer maintained a continuous network as in the earlier timeframes, suggesting the formation of a pore in each membrane. The disruption of the upper leaflet was larger than the lower leaflet, evidenced by the more significant deviation of the P atoms from their initial positions in the upper leaflet. While all membranes showed a similar trend, the level of disruption varied for different membranes. At 34 ns, the P atoms in the POPC bilayer could be found further from their initial positions compared with DPPC and DLPC bilayers, indicating more severe disintegration of the POPC membrane. DLPC displayed lower deviation of the P atoms from their initial positions than the other two membranes, which can be attributed to

its lower resistance against pore formation due to its shorter thickness (Appendix C, Figure C4) and weaker hydrophobic-hydrophobic interactions among its lipid tails.

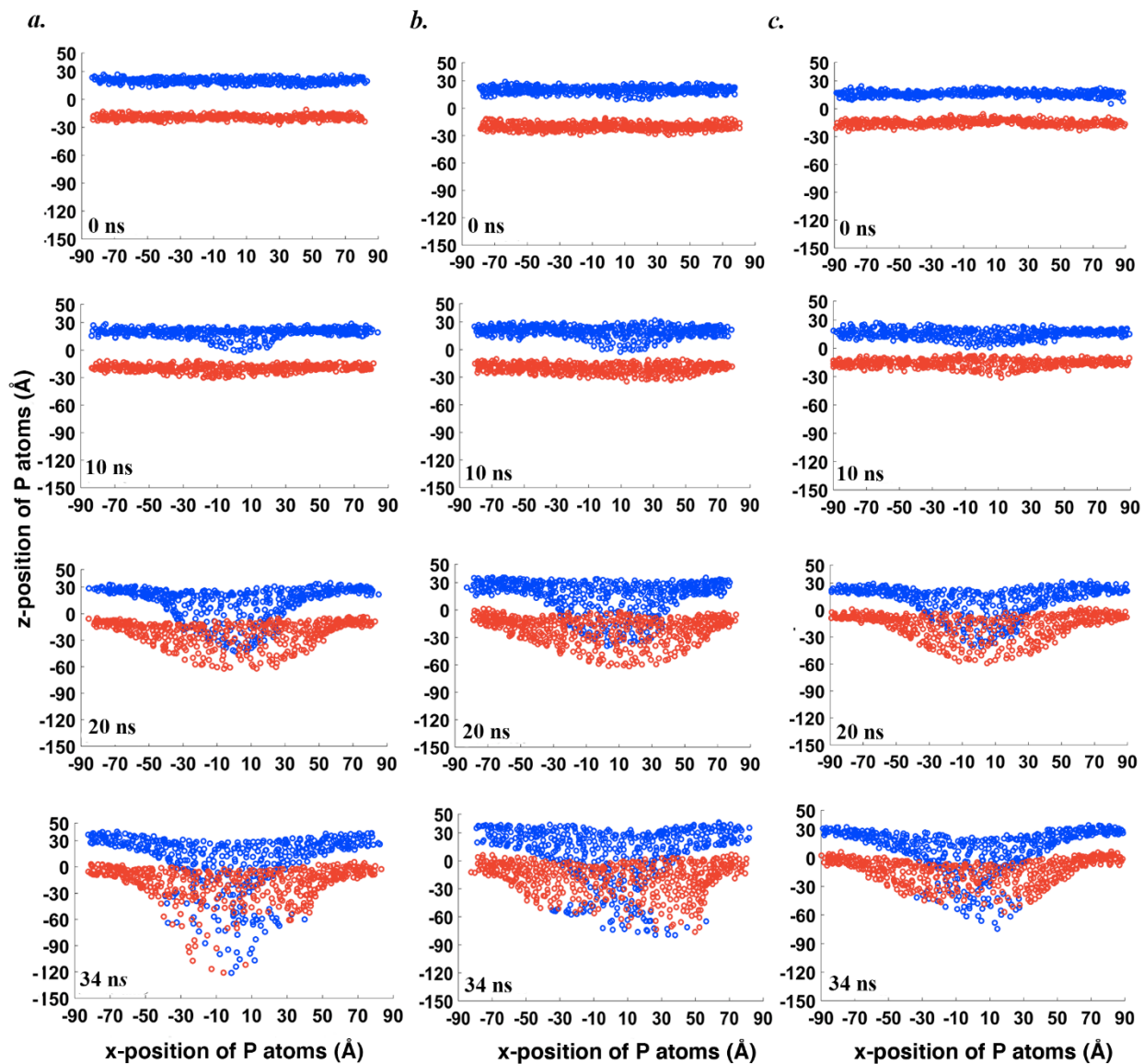


Figure 5.2. Positions of P atoms in the (blue) upper and (red) lower leaflets of membranes (a) POPC (b) DPPC and (c) DLPC membranes during penetration of the PEI NP.

5.3.2. Pore formation caused by PEI NP penetration

Penetration of the PEI NP induced a pore within each membrane. To quantify the size of the formed pore, the positions of P atoms were first projected onto the x - y plane which was parallel to the membrane surface. The same projection was done for the COM of the PEI NP. Then the in-plane distribution of the P atoms around the COM, in terms of areal density (number of P atoms per unit area), was calculated and shown in Figure 5.4 (see Appendix C, Figure C7 for calculation details). For each membrane, Figure 5.3 shows the distribution at three stages: when the membrane was initially undisturbed, when the pore was well established, and at the end of the pulling process in SMD. It is worth noting that the time for a well-established pore, determined from visual observation of the pore transitioning from increasing to decreasing trends, was different for each membrane: 30, 27, and 24 ns, respectively for POPC, DPPC, and DLPC membranes. For undisturbed membranes (blue curves), as the distance from the COM of NP increased, the distribution remained relatively constant. When the pores were well established (red curves), the distribution was zero near the COM of the NP while showing two peaks at larger distances. The first peak (location denoted by r_1) corresponded to the edge of the formed pore where the lipids accumulated, representative of the pore size. The second peak (location denoted by r_2) corresponded to the region where membrane was significantly bent downwards so that the projection of the P atoms onto the x - y plane showed a high local areal density. r_1 was found to be ~ 26 , ~ 30 and ~ 33 Å for POPC, DPPC and DLPC membranes, respectively. This shows that the pore size was largest for the DLPC membrane, which agrees with experimental studies where pore formation was found easier in lipidic membranes with shorter hydrocarbon tails [55]. Values of r_2 were ~ 52 , ~ 57 and ~ 58 Å for POPC, DPPC and DLPC, respectively. The largest r_2 for DLPC was consistent with its largest pore size, i.e. r_1 , among the three membranes. Compared with

DPPC, POPC showed smaller values for both r_1 and r_2 , while the difference in r_2 was more significant. Consulting Figure 5.2, POPC underwent more significant bending deformation during pore formation, which allowed membrane rupture to occur at a shorter distance from the NP. In contrast, DPPC experienced a more gradual deformation that was less localized than POPC and covered a larger area of the membrane. At the end of the pulling process (green curves), the first peak underwent a decrease in height and a shift to the left for the POPC and DPPC membranes, and the changes were more profound for the latter. For the DLPC membrane, the first peak disappeared completely. In addition, the height of the second peak showed a decrease for POPC and DLPC membranes.

This suggests that within our simulation time (34 ns), resealing of the pore started almost immediately after the NP began to detach from the membrane. The recovery was highest for the DLPC membrane and lowest for POPC. Although DLPC had the largest pore size, as can be seen from Fig. 2 its deformation was the least among the three membranes. The thinnest bilayer provided the least resistance to NP entry, and a large pore was able to form without creating significant displacement of the lipids. Consequently, the less lipid displacement facilitated recovery during pore resealing. The opposite is true for POPC, which exhibited the most severe disintegration and largest lipid displacement that are hardest to recover.

Along with the difference in pore size, the three membranes also showed difference in the order and orientation of the acyl chains. To quantify the order in the lipid tails, the probability distribution (PD) of the angle formed between Sn1 and Sn2 acyl chains was monitored. To this end, an angle (θ) was defined between two vectors each associated with one acyl chain (see Figure C8 for details). $\theta = 0^\circ$ corresponds to parallel orientation between Sn1 and Sn2 chains, whereas $\theta = 90^\circ$ represents perpendicular orientation between them. Figure 5.4 shows the PD of θ at 0, 20,

and 34 ns. For all membranes, as time increased and NP penetration progressed, the PD became wider and there was a decline in the peak value, suggesting a reduction in the order of the membrane. At 0 ns, the most probable angle between the two lipid tails was respectively $\sim 27^\circ$, $\sim 22^\circ$ and $\sim 28^\circ$ for POPC, DPPC and DLPC membranes. POPC and DLPC had a wider PD than DPPC, indicating that POPC and DLPC were less aligned and more dynamic. For POPC this originates from the presence of unsaturated Cs on its Sn2 chain which can induce a change in orientation of the chain and cause the POPC membrane to have a lower thickness (as shown in Figure C4). For DLPC, on the other hand, the short acyl chains are the source of the smaller degree of order. The alignment of DPPC lipids increased the intermolecular interaction among them, causing the membrane to be more rigid. Also, the larger angle between two lipid tails in POPC and DLPC has led to a slightly higher free volume within the bilayers than in the DPPC membrane (See Appendix C, section C5), which may impact the configurational changes of the NP during its entry.

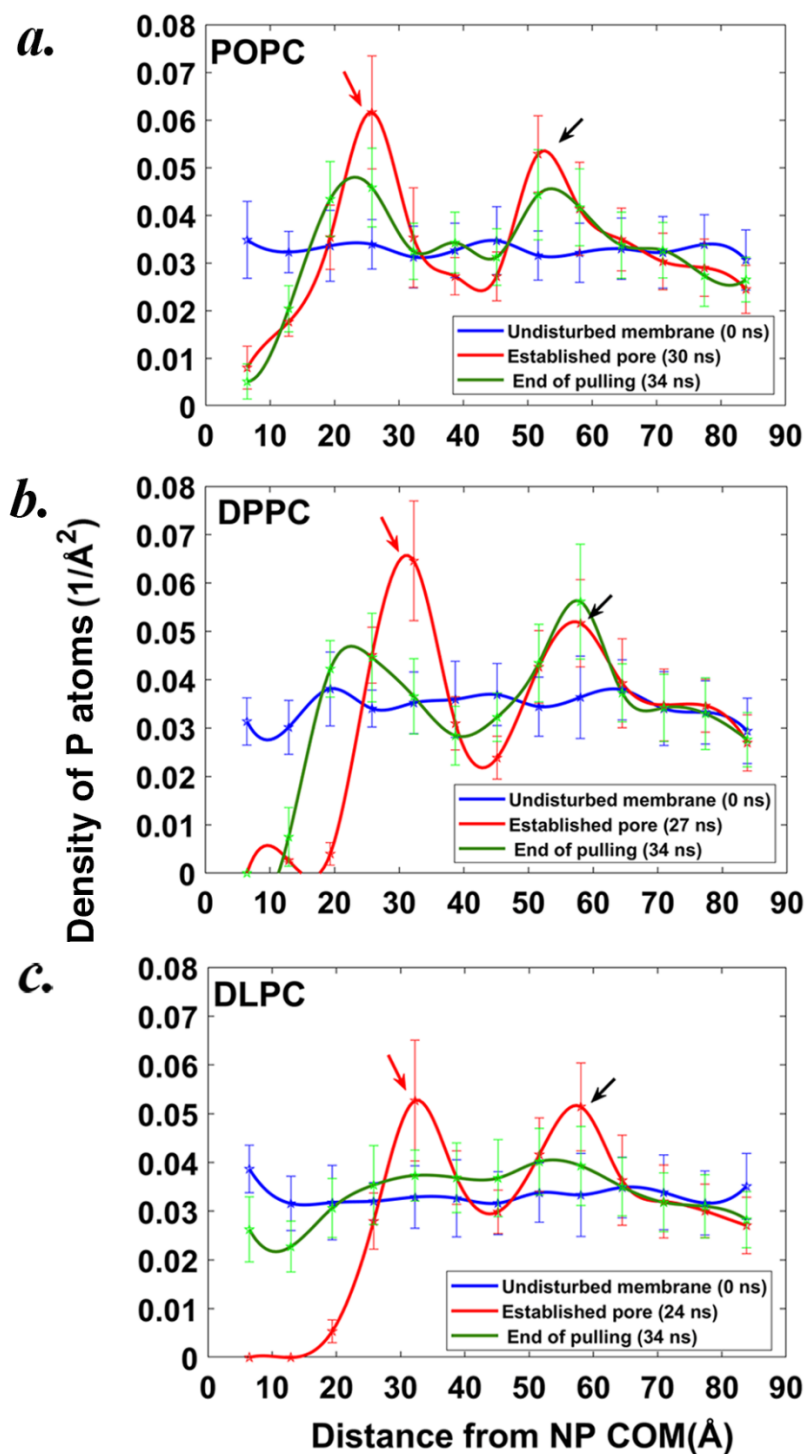


Figure 5.3. Distribution of P atoms around the COM of PEI NP, within the x-y plane, for (a) POPC, (b) DPPC, and (c) DLPC membranes (see Appendix C Figure C.4 for calculation details). Red and black arrows in each subfigure point to the locations of the first and second peaks respectively, for the established pore.

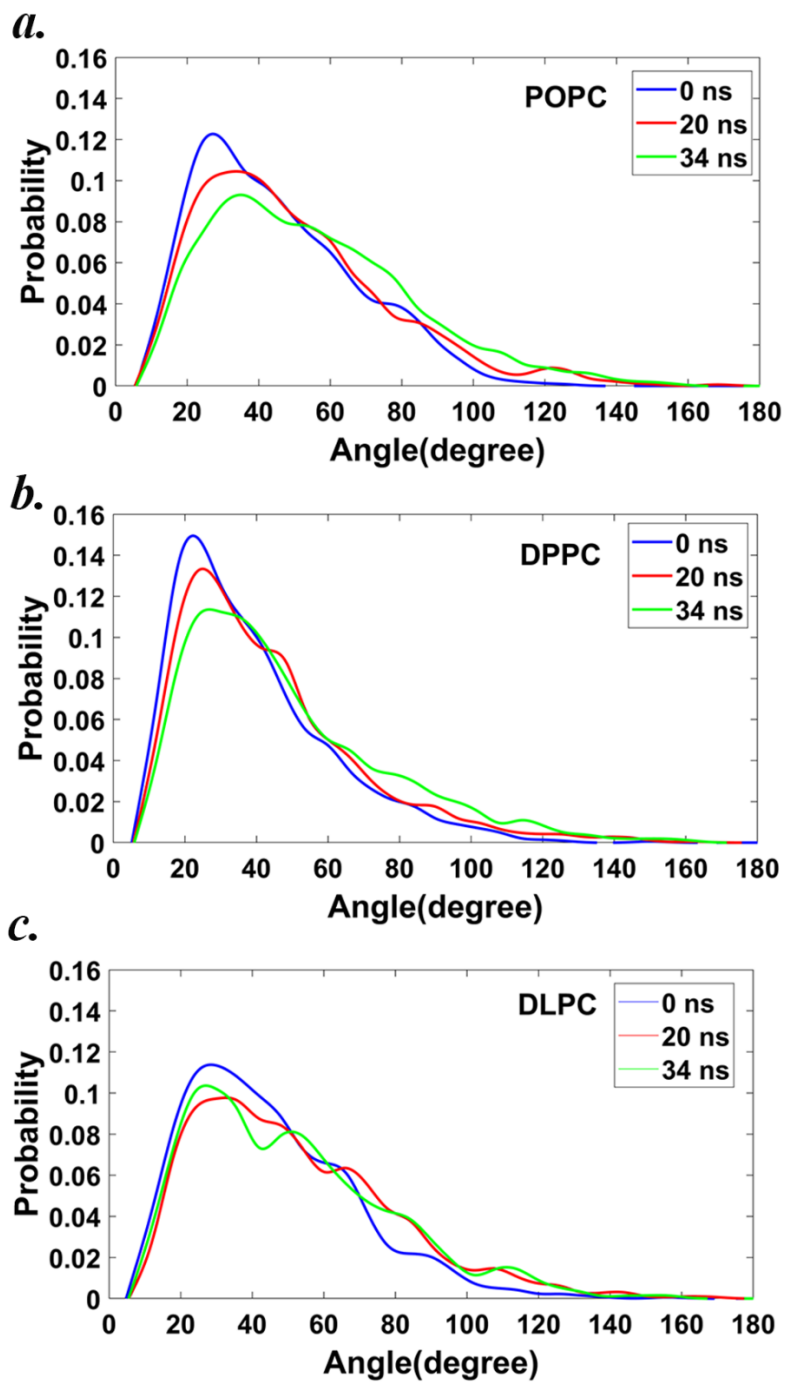


Figure 5.4. Probability distribution of the angle between Sn1 and Sn2 for (a) POPC, (b) DPPC and (c) DLPC membranes.

5.3.3. Interaction between membrane and PEI NP

To evaluate the interplay between PEI NP and the membranes, pulling force and structural parameters of the NP during SMD were monitored. Figure 5.5a shows the pulling force on the PEI NP, plotted against the COM position of the NP. Side-view snapshots of the NP and the membrane at different time during the penetration are shown in SI (Figure C9). All systems followed a similar trend. The force was relatively constant when the NP was approaching the membrane, followed by an increase up to a maximum value. The increase in force originated from the resistance of membrane to deformation and disintegration. Finally, the force decreased as the NP detached from the membrane, although it did not return to the value measured before penetration began because at the end of each simulation some membrane lipids were still attached to the NP (Figure C9). Despite these similarities, the force profiles displayed certain quantitative differences. The maximum force was about 2900, 2880 and 2410 pN respectively for POPC, DPPC and DLPC membranes. This indicates that the resistance to the passage of the NP was higher in POPC and DPPC membranes than the DLPC membrane. This is not surprising, as the POPC and DPPC bilayers had larger thickness (Figure C4) and hence larger bending stiffness. The bending modulus, which is a macroscopic constant that represents the ability of a material to oppose bending [56], was reported to be 25.7 ± 2.1 , 27.5 ± 3.4 , and 20.4 ± 1 kT , respectively for POPC, DPPC and DLPC vesicles [57], where k is the Boltzmann constant and T is temperature. The bending modulus reported in previous MD simulations [58] was 25.3 ± 0.6 , 34.1 ± 0.9 , and 25.8 ± 0.6 kT , respectively for the POPC, DPPC, and DLPC membranes. The difference from the experimental values might be caused by the different temperature, salt concentration, and number of lipid molecules used in the MD simulations. The force profiles for POPC and DPPC membranes almost overlapped except during detachment of the NP (z-position of COM 50-90 Å), where the force was higher for POPC.

Considering that POPC and DPPC have a similar bending modulus, the increase in the force was caused by the higher degree of deformation in POPC membrane during NP detachment of NP as shown in Figure 5.2.

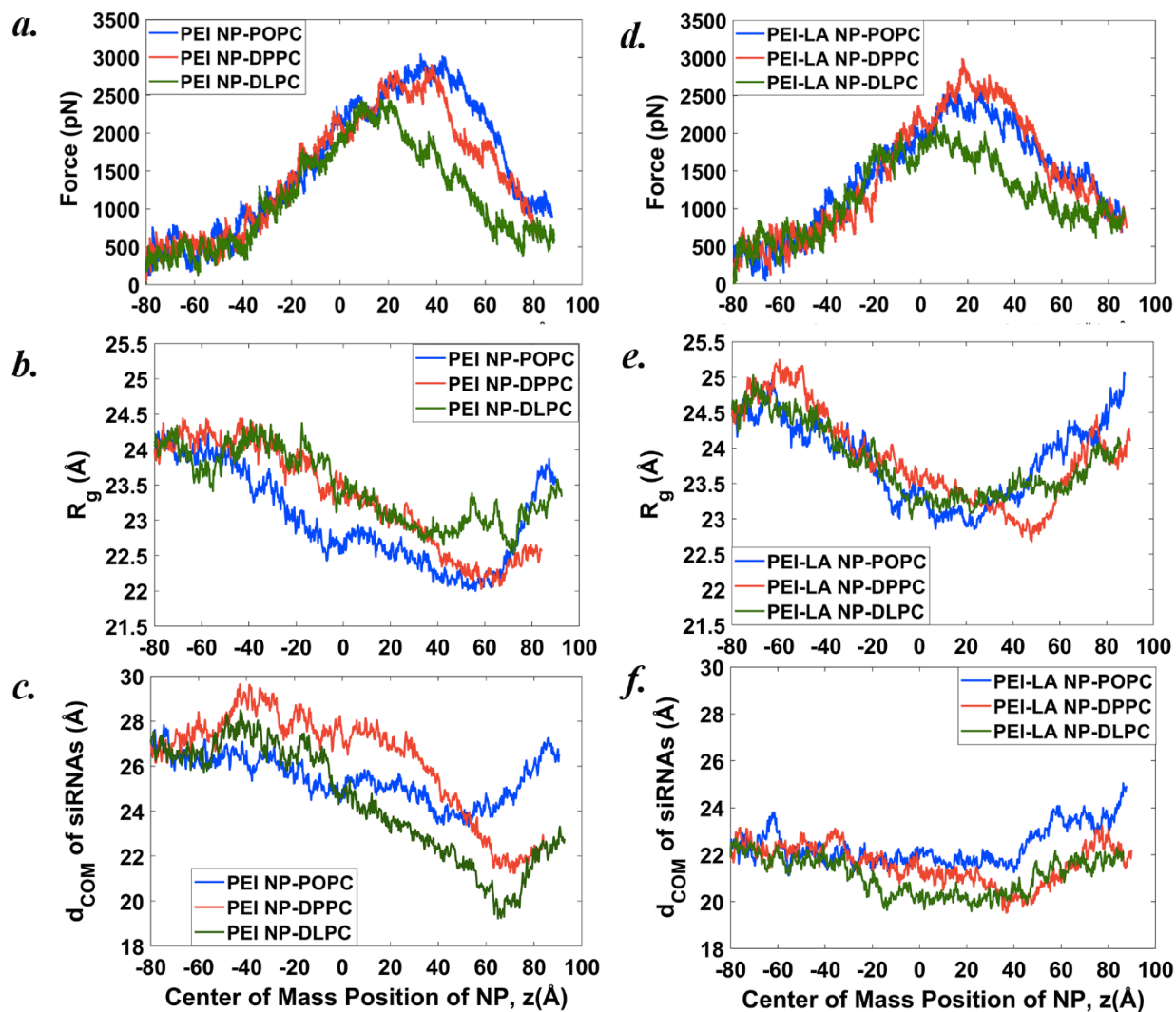


Figure 5.5. Structural changes of NPs during the SMD simulation.

(a,d) Force profile, (b,e) gyration radii and (c,f) d_{COM} distance between the two siRNAs, as functions of COM position of the NP.

The smaller degree of alignment, i.e. order, of POPC and DLPC lipids is expected to affect the NP penetration. Specifically, these two membranes provide a slightly higher free volume within the bilayers for possible configurational changes of the NP as discussed in Figure 5.4. To monitor the configurational changes, R_g of the NP and COM distance between the two siRNAs (d_{COM}) were assessed as a measure of NP compactness (Figure 5.5b and 5.5c). Additionally, the shape anisotropy of the NP, relative orientation of the two siRNAs, and orientation of each siRNAs relative to the z-axis were also measured and discussed (Appendix C, section C7). For all membranes, both R_g and d_{COM} showed an initial decreasing trend, indicating some degree of compaction for the NP. Since the short siRNAs were relatively rigid, the NP compaction could occur through compaction of the constituent PEIs, and/or reduction in d_{COM} . The relative reduction in R_g was $\sim 8.20\%$, $\sim 8.21\%$, and $\sim 5.8\%$, while the relative reduction in d_{COM} was $\sim 13.1\%$, $\sim 20.66\%$, and $\sim 28.78\%$, respectively for POPC, DPPC and DLPC membranes. This suggests that for POPC, both mechanisms played similar roles in compacting the NP, while for DPPC and DLPC the majority of the compaction was caused by a reduction in d_{COM} . POPC and DPPC have a similar length in their acyl chains, but highly aligned tails of the latter membrane necessitated the larger magnitude of reduction in d_{COM} to minimize membrane disruption. Interestingly, the minimum value of R_g showed a positive correlation with the size of the established pore (Figure 5.3). $(R_g)_{min}$ was the same for POPC and DPPC, which was lower than $(R_g)_{min}$ for DLPC. Meanwhile, the pore size was largest for DLPC, while being the same for POPC and DPPC. For DLPC where pore formation was easier (Figure 5.5a), the size of the established pore was larger, and $(R_g)_{min}$ of NP was larger. After reaching the minimum of R_g and d_{COM} , the NP behaved differently for the three membranes. For POPC, both R_g and d_{COM} displayed full recovery to their original values during NP exit. For DPPC, NP showed little recovery from its compacted configuration. For DLPC, R_g

was fully recovered, while d_{COM} showed only partial recovery. The high alignment between the lipids of DPPC (as shown in Figure 5.4) caused the NP to retain its compressed configuration, while the less alignment of the Sn1 and Sn2 chains in POPC allowed more space for the NP to relax and recover during membrane crossing.

5.3.4. Membrane recovery and pore closure

Visual examination of the simulation trajectories revealed that depending on the membrane type, two types of pores, namely asymmetric and symmetric, were formed. In the former case (Figure 5.6a), one side of the bilayer deformed more and moved along with the NP as it exited; while in the latter case (Figure 5.6b), the deformation of the membrane was symmetric around the NP. The overall deformation and disruption of the membrane were therefore larger if the pore was asymmetric. Among the three membranes, POPC (Figure 5.6c) exhibited asymmetric pore formation, while DPPC (Figure 5.6d) and DLPC (Figure 5.6e) showed symmetric pore formation. A quantitative measure of pore symmetry at the end of pulling process (34 ns) is provided in SI, section S8.

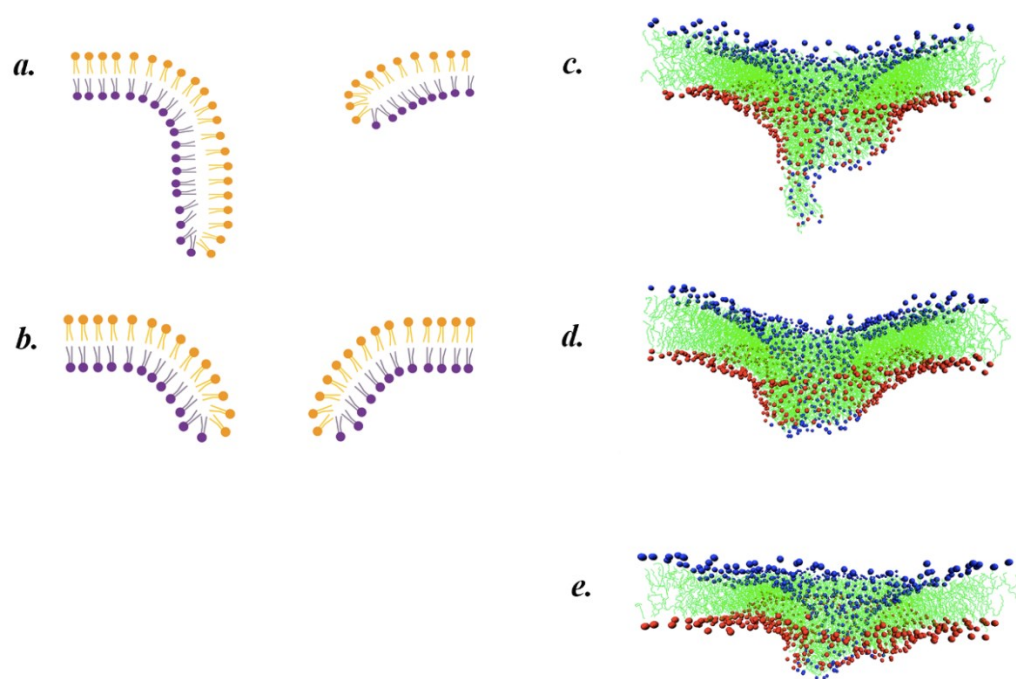


Figure 5.6. Schematic of two types of pores:

(a) asymmetric, (b) symmetric, and side-view snapshots at 34 ns for (c) POPC, (d) DPPC and (e) DLPC membranes. P atoms of upper and lower leaflets are shown in blue and red, respectively. The lipid tails are shown in green.

To measure membranes' recovery from its deformed configurations, MD simulations were performed by removing the NP and allowing the pore to close. Figure 5.7 shows the position of P atoms at different times. All membranes started recovery towards their undeformed flat configuration immediately after NP removal. However, the degree of recovery was different at the end of the 64 ns simulation: both DPPC and DLPC fully regained their flat configuration, while POPC seemed to require more time for a complete recovery. During the recovery, the number density of lipids at the lower leaflet increased for all membranes as lipids from the upper leaflet joined the lower leaflet (blue circles on the lower leaflet in Figure 5.7). This imbalance increased the probability of lipid flip-flops between the leaflets. By 64 ns, lipid translocation from the lower

leaflet to the upper leaflet had occurred to a small degree for POPC (3 lipids) and to a higher degree for DLPC (19 lipids), while DPPC displayed no lipid translocation from the lower to the upper leaflets. The high degree of flip-flops in the DLPC membrane originated from its short acyl chain length which allowed the lipids to be more dynamic. The smaller thickness of the DLPC membrane is also expected to pose a lower energy barrier, compared with the other two membranes, for the exchange of lipids between the two leaflets.

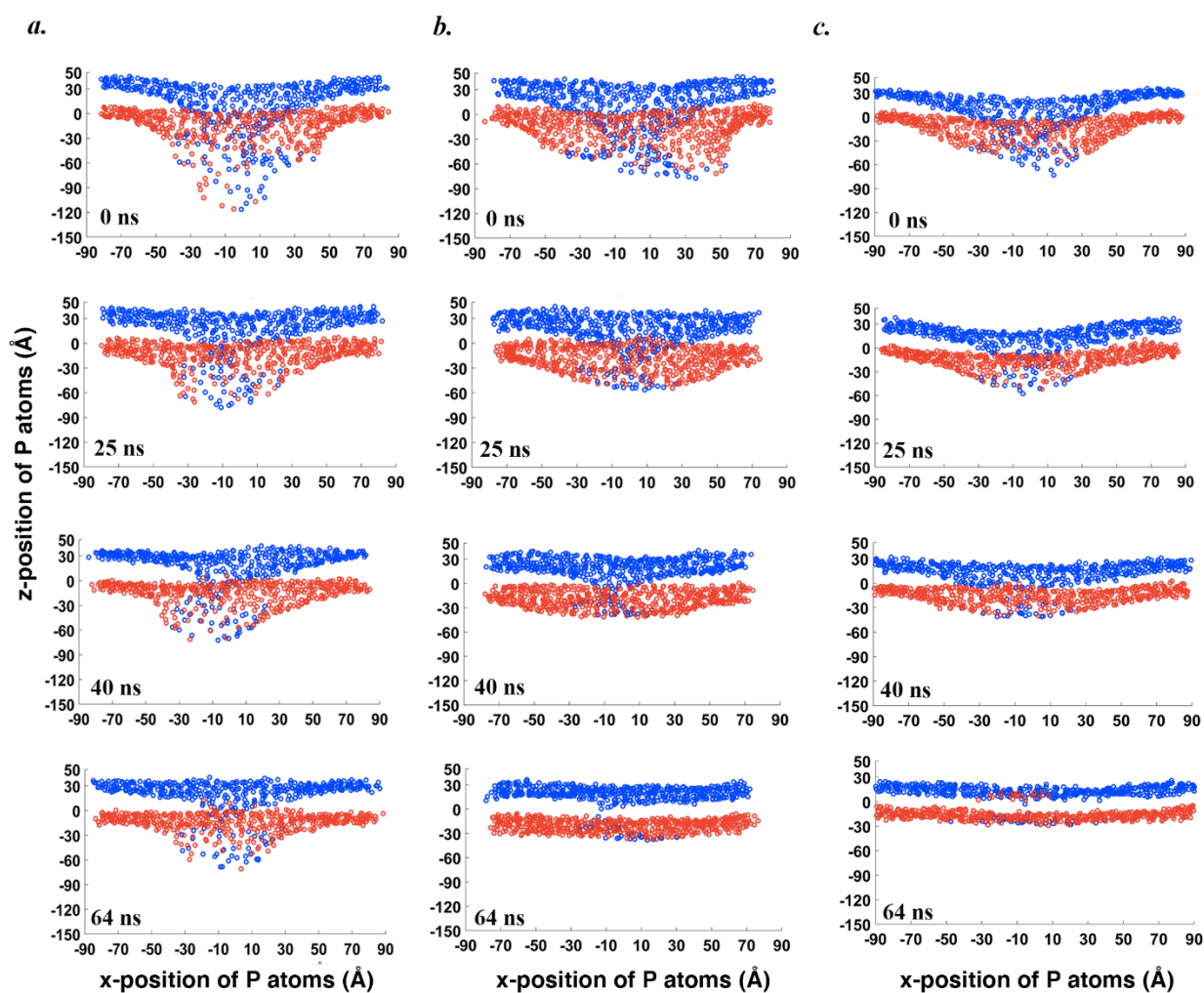


Figure 5.7. Position of P atoms in the (blue) upper and (red) lower leaflets of membrane (a) POPC (b) DPPC and (c) DLPC membranes during pore recovery.

Depending on the types of the formed pore (symmetric or asymmetric), the process of resealing differed. Figure 5.8 shows a simplified schematic of pore resealing process. For an asymmetric pore (Figure 5.8a), the lipids in the vicinity of the pore first moved toward each other to reduce their exposure to water. When the pore size was sufficiently reduced and the lipids initially surrounding the pore started making contact, lateral diffusion of the lipids began to reduce the curvature of the membrane. Due to the asymmetric feature of the pore, the lower leaflet on one side of the pore could readily contact the upper leaflet on the other side (see step 2 in Figure 5.8a). As such, some lipids from the lower leaflet was able to diffuse into the upper leaflet, leading to flip-flop, which continued until the pore was completely sealed.

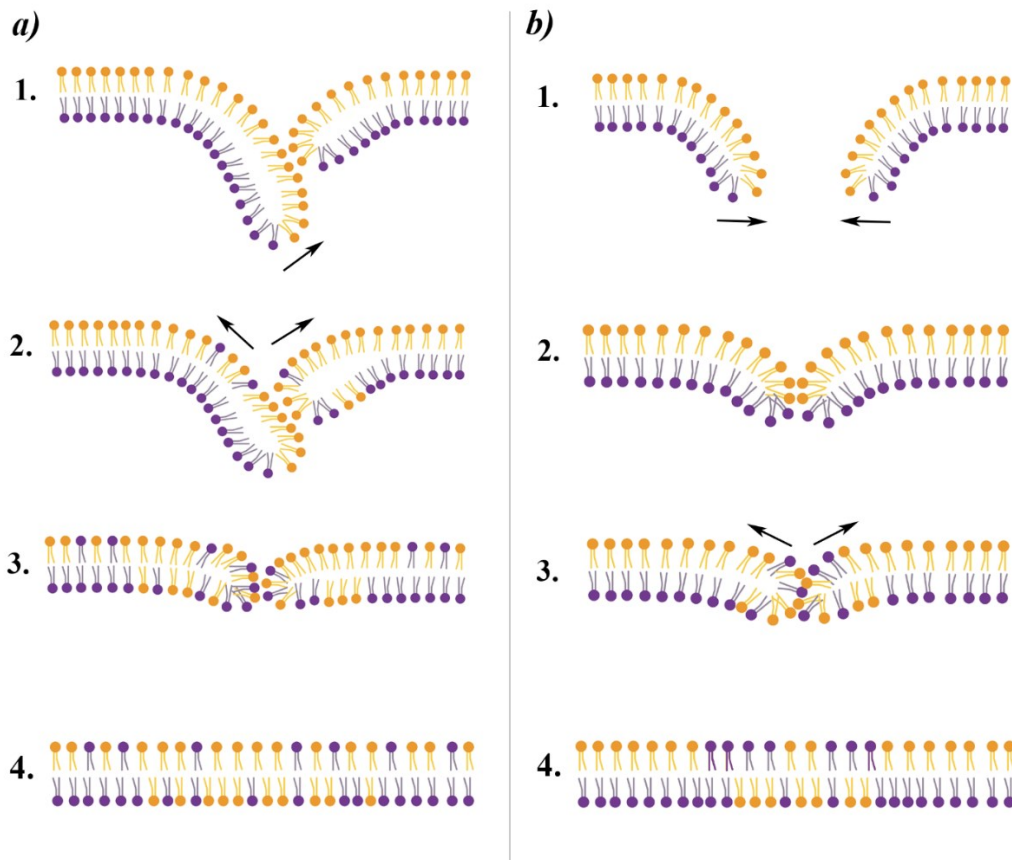


Figure 5.8. Process of pore resealing

for (a) an asymmetric pore, and (b) a symmetric pore.

For the symmetric pore (Figure 5.8b), the resealing process was similar at the beginning. However, the symmetric nature of the pore did not facilitate the contact between the lower leaflet of one side with the upper leaflet of the other side. Consequently, the diffusion of the lipids from the lower leaflet to the upper leaflet did not occur until much later in the resealing process (see step 3 in Figure 5.8b). In addition, the resealing of a symmetric pore was faster than an asymmetric pore due to the overall smaller disruption of the membrane during the pore formation. As a result, the lipids that underwent flip-flop were more concentrated at the pore site rather than migrating further from the pore location. Table C3 in the Appendix C shows that the flip-flops occurred as early as 40 ns in the POPC membrane which contained an asymmetric pore, while flip-flops in the DLPC membrane, with a symmetric pore, did not occur until the end of simulation.

5.3.5. Effect of PEI-LA NP on membranes

The effect of PEI-LA NP penetration on membrane integrity was qualitatively similar to PEI NP, with some slight quantitative differences. Selected results are presented here while others can be found in the Appendix C (Figures C16-C17). For POPC and DLPC, the force required to pull the PEI-LA NP through the membrane was lower than the PEI NP, while the force was similar for the two NPs in the case of DPPC (Figure 5.5d). Figure 5.9 shows both the PEI-LA NP and the hydrophobic tails of the membrane during each penetration process (hydrophilic part of the membrane not included for the simplicity of visualization). Examination of the figure shows that the hydrophobic LA substitutions (purple color) were exposed to the interiors of the POPC and DLPC bilayers during the early stages of the process. On the contrary, the LA substitutions conformed well to the NP and did not insert themselves into the DPPC bilayer until the very end. The interaction of LA substitutions with the hydrophobic part of the lipid bilayer facilitated NP

entry and reduced the force for pore formation. For POPC and DLPC, such hydrophobic-hydrophobic interaction at early stages was facilitated by less alignment of the lipid tails (Figure 5.4) as compared to DPPC.

Results for R_g and d_{COM} of the PEI-LA NP followed a similar trend as the PEI NP (Figure 5.5e and 5.5f), where both NP compaction and relaxation from its compacted configurations were observed in all membranes. The relative reduction in R_g was $\sim 5.93\%$, $\sim 6.62\%$, and $\sim 5.48\%$, while the relative reduction in d_{COM} was $\sim 1.55\%$, $\sim 10.5\%$, and $\sim 10.04\%$, respectively for POPC, DPPC and DLPC membranes. This suggests that NP compaction in POPC was mainly attributed to compaction of the PEIs (with little reduction in d_{COM} , Figure 5.5e), while compaction in DPPC and DLPC membranes occurred mostly through the reduction in d_{COM} . The minimum R_g was about the same for all membranes, consistent with the similar pore size of the membranes (Figure C17). For all membranes, the reduction in d_{COM} was much lower for PEI-LA NP than PEI NP, indicating that PEI-LA NP was more rigid than the PEI NP.

For the PEI-LA NP, POPC displayed symmetric pore formation while DPPC and DLPC exhibited asymmetric pore formation (Figure 5.10a, b, c). As shown earlier, when the PEI NP penetrated the bilayers, the pore formation was symmetric for DPPC and DLPC, while asymmetric for POPC. Therefore, the type of NP affected the deformation and the extent of disturbance in the membranes. MD simulations for pore resealing (Figure 5.10d, e, f) showed that for the same simulation time (64 ns), no full recovery to the flat configuration was observed for the POPC and DLPC membranes. The recovery of DPPC was stronger, but still not as much as what was observed in Figure 5.7 for the PEI NP. The number of lipid flip-flops from the bottom leaflet to the top leaflet in each system is shown in Table C3. Lipid flip-flops from the lower leaflet to the upper leaflet occurred for DPPC and DLPC membranes, but not for POPC membrane. Considering that lipid

flip-flops did not occur for PEI NP-DPPC system, this shows that LA substitutions facilitated lipid flip-flops in the DPPC. Also, for DLPC, the lipids that underwent flip-flop were spotted at further distance from the initial pore location as compared to DPPC. This was caused by the more asymmetric nature of the pore in DLPC (see Appendix C, section C8) as well as its shorter lipid, which enabled the diffusion of the lipids from the lower leaflet to the upper leaflet to occur earlier in the pore resealing process.

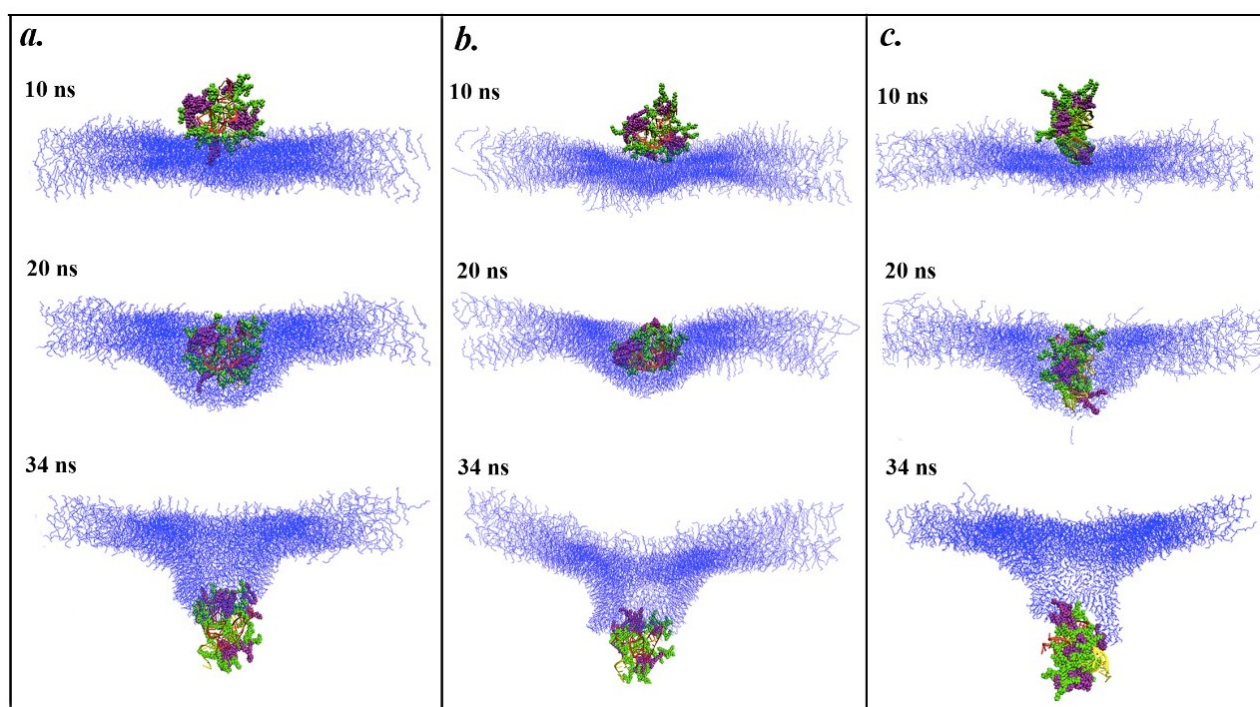


Figure 5.9. Side-view snapshots of PEI-LA NP crossing the membranes

(a) POPC, (b) DPPC and (c) DLPC membranes at different times of the SMD simulations. For simplicity of visualization, water, ions, and hydrophilic parts of the membranes were removed and only the hydrophobic acyl chains of the membranes are shown. siRNA molecules are shown in yellow and red. PEI molecules are shown in green, while its hydrophobic LA substitutions are shown in purple.

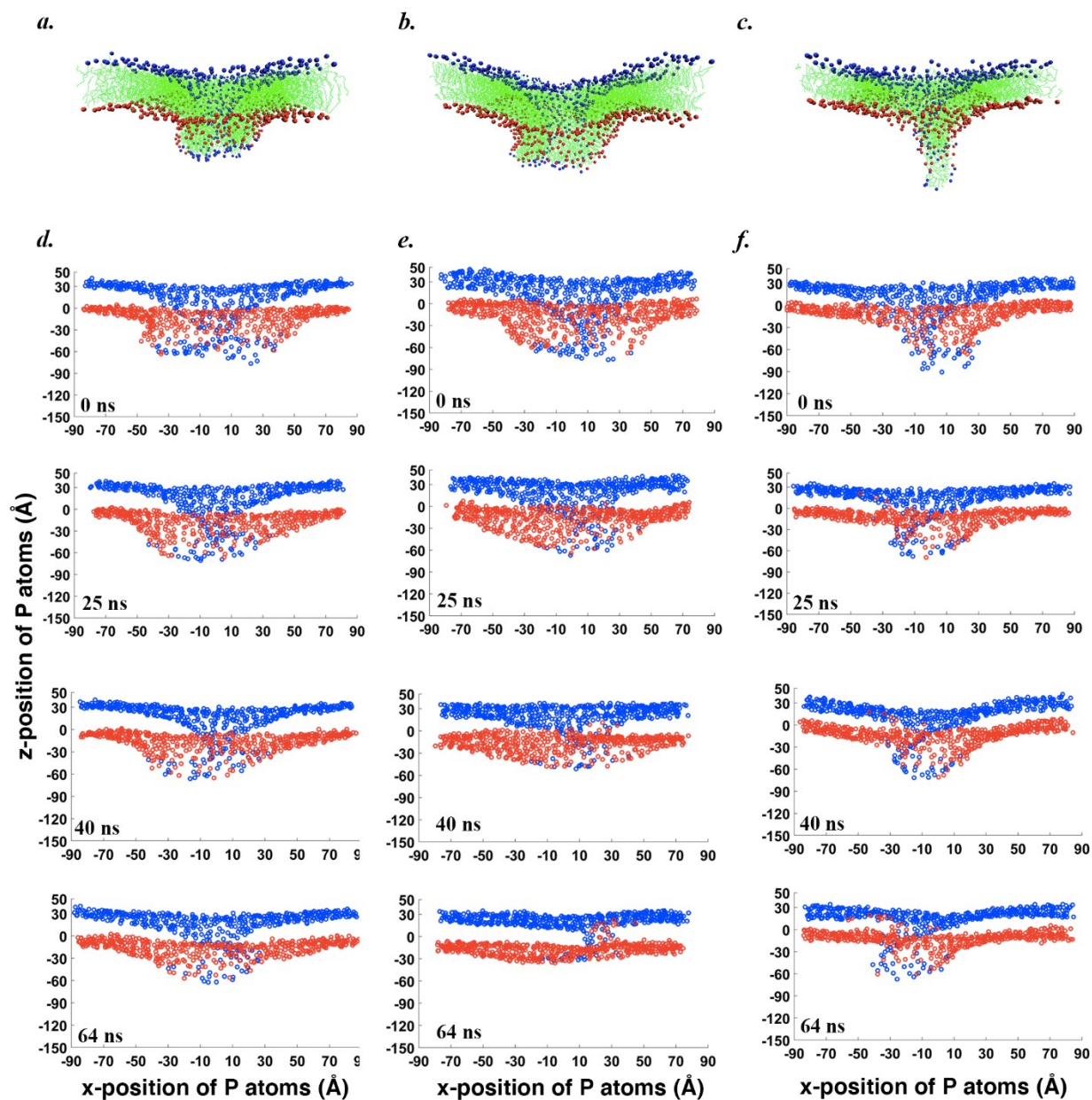


Figure 5.10. Side view snapshots at 34 ns of the SMD

for (a) POPC, (b) DPPC and (c) DLPC membranes. P atoms of upper and lower leaflets are shown in blue and red, respectively. The lipid tails are shown in green. Positions of P atoms in (d) POPC (e) DPPC and (f) DLPC membranes during pore resealing.

5.4. Discussion

5.4.1. Implications

During PEI mediated delivery of siRNA, the PEI/siRNA NPs interact with cell membrane that is composed of lipids with different properties [5]. This study investigated membrane response upon interaction with a PEI/siRNA NP using MD and SMD simulations. Three representative zwitterionic membrane models built from POPC, DPPC and DLPC lipids were employed, along with both native and lipid-modified PEI/siRNA NPs. The presence of a double bond on the Sn2 chain of POPC induced a change in the lipid chain's orientation, leading to less alignment between the Sn1 and Sn2 chains. This allowed POPC to have a smaller membrane thickness compared with DPPC, which had similar numbers of Cs on its tails but was completely saturated. The order of membranes can be quantified in both simulations and experiments through the measurement of deuterium order parameter. Several MD simulations and experiments showed that the deuterium order parameters of both Sn1 and Sn2 chains decreased in lipids with unsaturated Cs and the effect was more pronounced in Sn2 chains [7], [59]. In addition, among saturated membranes, long-tail lipids had larger deuterium order parameter than short-tail lipids, suggesting that the chains were more aligned in long-tail lipids [60]. Our results are in agreement with these previous reports, where the probability distribution for the angle between Sn1 and Sn2 chains was found to be narrower in DPPC (long-tail, saturated) than in POPC (long-tail, unsaturated) and DLPC (short-tail, saturated). Our results also showed that the order of the membranes decreased during NP penetration, resulting in a broader probability distribution and an increase in the most probable angle. This agrees with experiments and previous MD simulations on single polycation interaction with membranes, where polycation was shown to induce disorder of acyl chains in the bilayer organization and reduce packing of the membrane [15].

Less alignment of lipid tails in the bilayer may promote insertion of hydrophobic cationic carriers through hydrophobic interactions, thereby facilitating their entry into the cell. It has been found experimentally that low molecular weight PEI's gene delivery efficacy was improved significantly with the substitution of hydrophobic moieties including aliphatic lipids such as caprylic (8C), myristic (14C), palmitic (16C), stearic (18C), and LA [2], [61]. Our group previously observed that gene delivery performance of 2 kDa modified PEI was increased enormously compared to its unmodified counterpart. Here, we found that hydrophobic LA substitutions on the PEI-LA NP were exposed to the interiors of the POPC and DLPC bilayers, while they could not be inserted into the DPPC bilayers. Because of this, the force required for NP penetration was different depending on the types of NP and membrane. Compared with PEI NP, PEI-LA NP required less force to cross the POPC and DLPC membranes, while the force to cross the DPPC membrane was insensitive to the NP type. It has been suggested that hydrophilic polymers with substituted hydrophobic side chains can insert their hydrophobic part into the membrane, and thereby induce pore formation through the "barrel-stove" or "carpet" mechanisms, the latter relying a large change of the membrane's curvature [62], [63]. Due to the complexity of polymers in terms of their structure, conformation and phase-separation abilities, it is difficult to predict their exact conformations within a lipid bilayer [62]. However, our results suggest that hydrophobic modifications are more likely to interact with the internal hydrophobic regions of membranes that have less alignment of lipid tails, via a higher content of unsaturated lipids or saturated but short-tail lipids.

Our simulation trajectories revealed that, as a NP was crossing a membrane, the lipids near the contact zone reoriented themselves to minimize the unfavorable interaction between hydrophilic NP and hydrophobic tails. This caused a hydrophilic pore to be formed in each

membrane. *Wikosz et al.*[64] observed that polycation embedded into the POPC membrane led to the reorientation of lipid molecules near the polycation, causing the internalization of several lipid headgroups into the hydrophobic core of the membrane and flux of water into the vicinity of the polycation. Here, depending on the natures of membrane lipid composition and NP, we observed two types of pore formations, symmetric and asymmetric. The PEI NP-POPC, PEI-LA NP-DPPC and PEI-LA NP-DLPC systems displayed asymmetric pore formation, while the PEI-LA NP-POPC, PEI NP-DPPC and PEI NP-DLPC systems showed symmetric pore formation. Additionally, the membranes were ranked according to their degree of symmetry as PEI NP-DPPC > PEI-LA NP-POPC > PEI NP-DLPC > PEI NP-POPC > PEI-LA NP-DPPC > PEI-LA NP-DLPC. While a more extensive study is required to determine the exact conditions for the formation of asymmetric vs. symmetric pores, some insight could be drawn from our results. Compared with a symmetric pore, the formation of an asymmetric pore could be associated with certain instability in the membrane during NP penetration. POPC was comparable to DPPC in thickness, however, the unsaturated Cs created misalignment in the lipid tails, increasing the probability of having an instability. Similarly, the short and more dynamic lipid tails in DLPC were also potential source of instability. Interestingly, the presence of hydrophobic LA substitutions changed the pore type from asymmetric to symmetric for POPC, while changing it from symmetric to asymmetric for DLPC and DPPC. It is possible that the easier penetration brought by the interaction of LA with POPC lipids was able to provide extra stabilization for the membrane. On the other hand, the DLPC bilayer was considerably thinner than POPC and easier for the NP to cross. The additional ease brought by the LA substitutions might have made the system too dynamic to be stable. The precise mechanisms behind the interesting observations on pore formation require further investigations.

For both types of NPs and all three membranes, the upper leaflet underwent more profound deformation than the lower leaflet during pore formation. This caused an imbalance in the concentration of lipids in the two leaflets during pore resealing. Additionally, the type of pore formed affected its resealing, where the closure of an asymmetric pore took a longer time than a symmetric pore. During pore resealing and in most of the simulated systems, some lipids from the lower leaflet underwent flip-flops and translocated to the upper leaflet. The degree of lipid flip-flops was higher in asymmetric pores than in symmetric pores with the exception of DLPC systems, where the number of lipid flip-flops was comparable for both pore types (Table C3). Under normal conditions, flip-flop is considered to be an extremely slow process with time scale on the order of seconds, because it requires disruption of the lipid bilayer structure and removal of polar headgroups from the water interface [65]. Experimentally, flip-flops can be measured using chemical probes. *Wimley et al.*[66] measured the rate of lipid flips in DPPC membranes, and suggested the occurrence of flip-flops through transient defects. *Gurtovenko et al.*[67] using MD simulations explored pore mediated flip-flop of membrane lipids. The pore was induced by a transmembrane ion density gradient. The authors proposed the mechanism of flip-flop, where the appearance of a transient pore in the membrane led to diffusive translocation of lipids through the pore. The rate-limiting step in the process of flip-flop was argued to be the formation of water pores [67]. Under equilibrium conditions, pores can be formed but the probability is low due to the significant free energy cost associated with it [68]. *Bennet et al.* [68] using umbrella sampling MD simulations calculated the free energy associated with pore formation across DLPC, DMPC and DPPC bilayers. The reaction coordinate in the umbrellas sampling simulations was the position of the phosphate of a single lipid with respect to the center of mass of the bilayer. The free energy increased as bilayer thickness increased, being ~ 17 , ~ 45 and ~ 78 kJ/mol respectively

for DLPC, DMPC and DPPC lipid bilayers. *Sapay et al.*[69] using MD simulations measured the potential of mean force (PMF) for moving a single lipid molecule from water to the center of a lipid bilayer. They found the PMF to be 89, 80 and 16 kJ/mol, respectively for POPC, DPPC and DLPC bilayers. Pore formation can be expedited by non-equilibrium conditions, including electroporation, mechanical stress, shock wave, surface active molecules, small cationic peptides, and cationic polymers [23]. In the present study, pore formation was accelerated through SMD simulations that induced substantial out-of-plane membrane bending and eventually water pore formation, thereby causing the occurrence of flip-flops during a short time span. The simulations of *Sapay et al.*[69] showed that shorter lipids formed pores more easily than longer lipids, and the corresponding pore size was larger. This agrees with our observations where DLPC underwent the most significant lipid flip-flops from the lower leaflet, due to its short and hence more dynamic lipid tails.

5.5. Conclusion

Membrane deformation, pore formation and resealing during the penetration of PEI and PEI-LA NPs were studied by a series of SMD and MD simulations. Three membrane models based on POPC, DPPC and DLPC lipids were utilized. We found that acyl chains of POPC and DLPC were less aligned than DPPC. Long-tailed LA substitutions could insert themselves into hydrophobic part of the membranes with less aligned tails, thereby reducing the force for NP penetration. Depending on the nature of NPs and membrane models, different types of pores were formed. During pore resealing, membrane lipids were observed to undergo different levels of pore-mediated flip-flops. POPC and DPPC membranes showed lower level of lipid flip-flops due to their long acyl chains, while DLPC membrane showed the largest number of lipid flip-flops due to its short and highly dynamic acyl chains. These mechanistic observations provide valuable

insight into membranes deformation and pore evolution caused by the PEI/siRNA NPs, and could facilitate the design of more efficient gene delivery systems.

5.6. Acknowledgments

Compute Canada and Westgrid are gratefully acknowledged for providing the computing resources and technical support. This work was funded by the Natural Sciences and Engineering Research Council of Canada (NSERC), Canadian Institutes of Health Research (CIHR) and Alberta Innovates Technology Futures (AITF).

5.7. References

- [1] D. Meneksedag-Erol, T. Tang, and H. Uludağ, “Molecular modeling of polynucleotide complexes,” *Biomaterials*, vol. 35, no. 25, pp. 7068–7076, Aug. 2014, doi: 10.1016/j.biomaterials.2014.04.103.
- [2] D. Meneksedag-Erol, R. B. KC, T. Tang, and H. Uludağ, “A Delicate Balance When Substituting a Small Hydrophobe onto Low Molecular Weight Polyethylenimine to Improve Its Nucleic Acid Delivery Efficiency,” *ACS Appl. Mater. Interfaces*, vol. 7, no. 44, pp. 24822–24832, Nov. 2015, doi: 10.1021/acsami.5b07929.
- [3] H. M. Aliabadi *et al.*, “A systematic comparison of lipopolymers for siRNA delivery to multiple breast cancer cell lines: In vitro studies,” *Acta Biomater.*, vol. 102, pp. 351–366, 2020.
- [4] D. Meneksedag-Erol, T. Tang, and H. Uludağ, “Mechanistic insights into the role of glycosaminoglycans in delivery of polymeric nucleic acid nanoparticles by molecular dynamics simulations,” *Biomaterials*, vol. 156, pp. 107–120, Feb. 2018, doi: 10.1016/j.biomaterials.2017.11.037.
- [5] S. J. Marrink, V. Corradi, P. C. T. Souza, H. I. Ingólfsson, D. P. Tieleman, and M. S. P. Sansom, “Computational Modeling of Realistic Cell Membranes,” *Chem. Rev.*, vol. 119, no. 9, pp. 6184–6226, May 2019, doi: 10.1021/acs.chemrev.8b00460.
- [6] P. A. Janmey and P. K. J. Kinnunen, “Biophysical properties of lipids and dynamic membranes,” *Trends Cell Biol.*, vol. 16, no. 10, pp. 538–546, 2006.
- [7] M. T. Hyvönen and P. T. Kovanen, “Molecular dynamics simulations of unsaturated lipid bilayers: effects of varying the numbers of double bonds,” *Eur. Biophys. J.*, vol. 34, no. 4, pp. 294–305, Jun. 2005, doi: 10.1007/s00249-004-0455-7.

- [8] Z. Xu, L. Gao, P. Chen, and L.-T. Yan, “Diffusive transport of nanoscale objects through cell membranes: a computational perspective,” *Soft Matter*, vol. 16, no. 16, pp. 3869–3881, 2020.
- [9] Z. Shen, W. Baker, H. Ye, and Y. Li, “pH-Dependent aggregation and pH-independent cell membrane adhesion of monolayer-protected mixed charged gold nanoparticles,” *Nanoscale*, vol. 11, no. 15, pp. 7371–7385, 2019.
- [10] P. Chen *et al.*, “Transport of a graphene nanosheet sandwiched inside cell membranes,” *Sci. Adv.*, vol. 5, no. 6, p. eaaw3192, 2019.
- [11] L. Zhang, Z. Zhang, M. Negahban, and A. Jérusalem, “Molecular dynamics simulation of cell membrane pore sealing,” *Extrem. Mech. Lett.*, vol. 27, pp. 83–93, Feb. 2019, doi: 10.1016/j.eml.2019.01.008.
- [12] H. Leontiadou, A. E. Mark, and S. J. Marrink, “Molecular Dynamics Simulations of Hydrophilic Pores in Lipid Bilayers,” *Biophys. J.*, vol. 86, no. 4, pp. 2156–2164, Apr. 2004, doi: 10.1016/S0006-3495(04)74275-7.
- [13] U. Kwolek, D. Jamr??z, M. Janiczek, M. Nowakowska, P. Wydro, and M. Kepczynski, “Interactions of Polyethylenimines with Zwitterionic and Anionic Lipid Membranes,” *Langmuir*, vol. 32, no. 19, pp. 5004–5018, May 2016, doi: 10.1021/acs.langmuir.6b00490.
- [14] C. Zhang, F.-G. Wu, P. Hu, and Z. Chen, “Interaction of polyethylenimine with model cell membranes studied by linear and nonlinear spectroscopic techniques,” *J. Phys. Chem. C*, vol. 118, no. 23, pp. 12195–12205, 2014.
- [15] N. Awasthi *et al.*, “Molecular Mechanism of Polycation-Induced Pore Formation in Biomembranes,” *ACS Biomater. Sci. Eng.*, vol. 5, no. 2, pp. 780–794, Feb. 2019, doi: 10.1021/acsbomaterials.8b01495.
- [16] D. P. Tieleman, “The molecular basis of electroporation,” *BMC Biochem.*, vol. 5, no. 1, p. 10, 2004.
- [17] A. A. Gurtovenko and A. S. Lyulina, “Electroporation of asymmetric phospholipid membranes,” *J. Phys. Chem. B*, vol. 118, no. 33, pp. 9909–9918, 2014.
- [18] R. Reigada, “Electroporation of heterogeneous lipid membranes,” *Biochim. Biophys. Acta (BBA)-Biomembranes*, vol. 1838, no. 3, pp. 814–821, 2014.
- [19] S. A. Kirsch and R. A. Böckmann, “Membrane pore formation in atomistic and coarse-grained simulations,” *Biochim. Biophys. Acta (BBA)-Biomembranes*, vol. 1858, no. 10, pp. 2266–2277, 2016.
- [20] M. L. Fernández, G. Marshall, F. Sagués, and R. Reigada, “Structural and kinetic molecular dynamics study of electroporation in cholesterol-containing bilayers,” *J. Phys. Chem. B*, vol.

114, no. 20, pp. 6855–6865, 2010.

- [21] M. J. Ziegler and P. T. Vernier, “Interface water dynamics and porating electric fields for phospholipid bilayers,” *J. Phys. Chem. B*, vol. 112, no. 43, pp. 13588–13596, 2008.
- [22] X. Zhuang, E. M. Dávila-Contreras, A. H. Beaven, W. Im, and J. B. Klauda, “An extensive simulation study of lipid bilayer properties with different head groups, acyl chain lengths, and chain saturations,” *Biochim. Biophys. Acta - Biomembr.*, vol. 1858, no. 12, pp. 3093–3104, Dec. 2016, doi: 10.1016/j.bbamem.2016.09.016.
- [23] Y. Nademi, T. Tang, and H. Uludağ, “Steered molecular dynamics simulations reveal a self-protecting configuration of nanoparticles during membrane penetration,” *Nanoscale*, vol. 10, no. 37, pp. 17671–17682, 2018, doi: 10.1039/C8NR04287J.
- [24] Y. Nademi, T. Tang, and H. Uludağ, “Membrane lipids destabilize short interfering ribonucleic acid (siRNA)/polyethylenimine nanoparticles,” *Nanoscale*, vol. 12, no. 2, pp. 1032–1045, 2020, doi: 10.1039/C9NR08128C.
- [25] H. M. Aliabadi, B. Landry, P. Mahdipoor, C. Y. M. Hsu, and H. Uludağ, “Effective down-regulation of Breast Cancer Resistance Protein (BCRP) by siRNA delivery using lipid-substituted aliphatic polymers,” *Eur. J. Pharm. Biopharm.*, vol. 81, no. 1, pp. 33–42, May 2012, doi: 10.1016/j.ejpb.2012.01.011.
- [26] H. Montazeri Aliabadi, B. Landry, P. Mahdipoor, and H. Uludağ, “Induction of Apoptosis by Survivin Silencing through siRNA Delivery in a Human Breast Cancer Cell Line,” *Mol. Pharm.*, vol. 8, no. 5, pp. 1821–1830, Oct. 2011, doi: 10.1021/mp200176v.
- [27] M. Abbasi *et al.*, “siRNA-Mediated Down-Regulation of P-glycoprotein in a Xenograft Tumor Model in NOD-SCID Mice,” *Pharm. Res.*, vol. 28, no. 10, pp. 2516–2529, Oct. 2011, doi: 10.1007/s11095-011-0480-z.
- [28] K. Utsuno and H. Uludağ, “Thermodynamics of Polyethylenimine-DNA Binding and DNA Condensation,” *Biophys. J.*, vol. 99, no. 1, pp. 201–207, Jul. 2010, doi: 10.1016/j.bpj.2010.04.016.
- [29] J. Suh, H. Paik, and B. K. Hwang, “Ionization of Poly (ethylenimine) and Poly (allylamine) at Various pH's,” *Bioorg. Chem.*, vol. 22, no. 3, pp. 318–327, 1994.
- [30] J. Nagaya, M. Homma, A. Tanioka, and A. Minakata, “Relationship between protonation and ion condensation for branched poly (ethylenimine),” *Biophys. Chem.*, vol. 60, no. 1–2, pp. 45–51, 1996.
- [31] G. J. M. Koper, R. C. van Duijvenbode, D. D. P. W. Stam, U. Steuerle, and M. Borkovec, “Synthesis and protonation behavior of comblike poly (ethyleneimine),” *Macromolecules*, vol. 36, no. 7, pp. 2500–2507, 2003.

- [32] H. M. Aliabadi, B. Landry, C. Sun, T. Tang, and H. Uludağ, “Supramolecular assemblies in functional siRNA delivery: where do we stand?,” *Biomaterials*, vol. 33, no. 8, pp. 2546–2569, 2012.
- [33] W. L. Jorgensen, “Quantum and statistical mechanical studies of liquids. 10. Transferable intermolecular potential functions for water, alcohols, and ethers. Application to liquid water,” *J. Am. Chem. Soc.*, vol. 103, no. 2, pp. 335–340, Jan. 1981, doi: 10.1021/ja00392a016.
- [34] E. L. Wu *et al.*, “CHARMM-GUI membrane builder toward realistic biological membrane simulations,” *J. Comput. Chem.*, vol. 35, no. 27, pp. 1997–2004, 2014.
- [35] B. R. Brooks *et al.*, “CHARMM: the biomolecular simulation program,” *J. Comput. Chem.*, vol. 30, no. 10, pp. 1545–1614, 2009.
- [36] S. Jo, T. Kim, V. G. Iyer, and W. Im, “CHARMM-GUI: a web-based graphical user interface for CHARMM,” *J. Comput. Chem.*, vol. 29, no. 11, pp. 1859–1865, 2008.
- [37] N. Kučerka, Y. Liu, N. Chu, H. I. Petrache, S. Tristram-Nagle, and J. F. Nagle, “Structure of Fully Hydrated Fluid Phase DMPC and DLPC Lipid Bilayers Using X-Ray Scattering from Oriented Multilamellar Arrays and from Unilamellar Vesicles,” *Biophys. J.*, vol. 88, no. 4, pp. 2626–2637, Apr. 2005, doi: 10.1529/biophysj.104.056606.
- [38] J. Lee *et al.*, “CHARMM-GUI input generator for NAMD, GROMACS, AMBER, OpenMM, and CHARMM/OpenMM simulations using the CHARMM36 additive force field,” *J. Chem. Theory Comput.*, vol. 12, no. 1, pp. 405–413, 2015.
- [39] S. Park, F. Khalili-Araghi, E. Tajkhorshid, and K. Schulten, “Free energy calculation from steered molecular dynamics simulations using Jarzynski’s equality,” *J. Chem. Phys.*, vol. 119, no. 6, pp. 3559–3566, Aug. 2003, doi: 10.1063/1.1590311.
- [40] Q. Wei, W. Zhao, Y. Yang, B. Cui, Z. Xu, and X. Yang, “Method Evaluations for Adsorption Free Energy Calculations at the Solid/Water Interface through Metadynamics, Umbrella Sampling, and Jarzynski’s Equality,” *ChemPhysChem*, vol. 210009, pp. 1–14, Feb. 2018, doi: 10.1002/cphc.201701241.
- [41] H. Nguyen, N. Do, T. Phan, and T. Pham, “Steered Molecular Dynamics for Investigating the Interactions Between Insulin Receptor Tyrosine Kinase (IRK) and Variants of Protein Tyrosine Phosphatase 1B (PTP1B),” *Appl. Biochem. Biotechnol.*, vol. 184, no. 2, pp. 401–413, Feb. 2018, doi: 10.1007/s12010-017-2549-6.
- [42] Y. Xu *et al.*, “How does huperzine A enter and leave the binding gorge of acetylcholinesterase? Steered molecular dynamics simulations,” *J. Am. Chem. Soc.*, vol. 125, no. 37, pp. 11340–11349, 2003.
- [43] D. J. Brockwell *et al.*, “Pulling geometry defines the mechanical resistance of a β -sheet

- protein,” *Nat. Struct. Mol. Biol.*, vol. 10, no. 9, p. 731, 2003.
- [44] S. Azadi, M. Tafazzoli-Shadpour, and R. Omidvar, “Steered Molecular Dynamics Simulation Study of Quantified Effects of Point Mutation Induced by Breast Cancer on Mechanical Behavior of E-Cadherin,” *Mol. Biol.*, vol. 52, no. 5, pp. 723–731, 2018.
- [45] H. Lu and K. Schulten, “Steered molecular dynamics simulations of force-induced protein domain unfolding,” *Proteins Struct. Funct. Bioinforma.*, vol. 35, no. 4, pp. 453–463, 1999.
- [46] C. Sun, T. Tang, and H. Uludag, “A molecular dynamics simulation study on the effect of lipid substitution on polyethylenimine mediated siRNA complexation,” *Biomaterials*, vol. 34, no. 11, pp. 2822–2833, Apr. 2013, doi: 10.1016/j.biomaterials.2013.01.011.
- [47] E. J. Denning, U. D. Priyakumar, L. Nilsson, and A. D. Mackerell, “Impact of 2'-hydroxyl sampling on the conformational properties of RNA: Update of the CHARMM all-atom additive force field for RNA,” *J. Comput. Chem.*, vol. 32, no. 9, pp. 1929–1943, Jul. 2011, doi: 10.1002/jcc.21777.
- [48] J. B. Klauda *et al.*, “Update of the CHARMM all-atom additive force field for lipids: validation on six lipid types,” *J. Phys. Chem. B*, vol. 114, no. 23, pp. 7830–7843, Jun. 2010, doi: 10.1021/jp101759q.
- [49] J. C. Phillips *et al.*, “Scalable molecular dynamics with NAMD,” *J. Comput. Chem.*, vol. 26, no. 16, pp. 1781–1802, Dec. 2005, doi: 10.1002/jcc.20289.
- [50] T. Darden, D. York, and L. Pedersen, “Particle mesh Ewald: An $N \cdot \log(N)$ method for Ewald sums in large systems,” *J. Chem. Phys.*, vol. 98, no. 12, pp. 10089–10092, Jun. 1993, doi: 10.1063/1.464397.
- [51] J.-P. Ryckaert, G. Ciccotti, and H. J. . Berendsen, “Numerical integration of the cartesian equations of motion of a system with constraints: molecular dynamics of n-alkanes,” *J. Comput. Phys.*, vol. 23, no. 3, pp. 327–341, Mar. 1977, doi: 10.1016/0021-9991(77)90098-5.
- [52] G. J. Martyna, D. J. Tobias, and M. L. Klein, “Constant pressure molecular dynamics algorithms,” *J. Chem. Phys.*, vol. 101, no. 5, pp. 4177–4189, 1994.
- [53] S. E. Feller, Y. Zhang, R. W. Pastor, and B. R. Brooks, “Constant pressure molecular dynamics simulation: the Langevin piston method,” *J. Chem. Phys.*, vol. 103, no. 11, pp. 4613–4621, 1995.
- [54] W. Humphrey, A. Dalke, and K. Schulten, “VMD: Visual molecular dynamics,” *J. Mol. Graph.*, vol. 14, no. 1, pp. 33–38, Feb. 1996, doi: 10.1016/0263-7855(96)00018-5.
- [55] S. Garcia-Manyes, L. Redondo-Morata, G. Oncins, and F. Sanz, “Nanomechanics of Lipid Bilayers: Heads or Tails?,” *J. Am. Chem. Soc.*, vol. 132, no. 37, pp. 12874–12886, Sep. 2010,

doi: 10.1021/ja1002185.

- [56] D. Bochicchio and L. Monticelli, “The Membrane Bending Modulus in Experiments and Simulations: A Puzzling Picture,” in *Advances in Biomembranes and Lipid Self-Assembly*, 1st ed., vol. 23, Elsevier Inc., 2016, pp. 117–143.
- [57] J. F. Nagle, “Experimentally determined tilt and bending moduli of single-component lipid bilayers,” *Chem. Phys. Lipids*, vol. 205, pp. 18–24, Jun. 2017, doi: 10.1016/j.chemphyslip.2017.04.006.
- [58] M. Doktorova, D. Harries, and G. Khelashvili, “Determination of bending rigidity and tilt modulus of lipid membranes from real-space fluctuation analysis of molecular dynamics simulations,” *Phys. Chem. Chem. Phys.*, vol. 19, no. 25, pp. 16806–16818, 2017.
- [59] L. L. Holte, S. A. Peter, T. M. Sinnwell, and K. Gawrisch, “²H nuclear magnetic resonance order parameter profiles suggest a change of molecular shape for phosphatidylcholines containing a polyunsaturated acyl chain,” *Biophys. J.*, vol. 68, no. 6, pp. 2396–2403, 1995.
- [60] J. P. M. Jämbeck and A. P. Lyubartsev, “Derivation and systematic validation of a refined all-atom force field for phosphatidylcholine lipids,” *J. Phys. Chem. B*, vol. 116, no. 10, pp. 3164–3179, 2012.
- [61] A. Neamark, O. Suwantong, R. B. K. C., C. Y. M. Hsu, P. Supaphol, and H. Uludağ, “Aliphatic Lipid Substitution on 2 kDa Polyethylenimine Improves Plasmid Delivery and Transgene Expression,” *Mol. Pharm.*, vol. 6, no. 6, pp. 1798–1815, Dec. 2009, doi: 10.1021/mp900074d.
- [62] W. H. Binder, “Polymer-Induced Transient Pores in Lipid Membranes,” *Angew. Chemie Int. Ed.*, vol. 47, no. 17, pp. 3092–3095, 2008.
- [63] Y. Shai, “Mechanism of the binding, insertion and destabilization of phospholipid bilayer membranes by α -helical antimicrobial and cell non-selective membrane-lytic peptides,” *Biochim. Biophys. Acta (BBA)-Biomembranes*, vol. 1462, no. 1–2, pp. 55–70, 1999.
- [64] N. Wilkosz *et al.*, “Effect of polycation structure on interaction with lipid membranes,” *J. Phys. Chem. B*, vol. 121, no. 30, pp. 7318–7326, 2017.
- [65] F. Y. Jiang, Y. Bouret, and J. T. Kindt, “Molecular Dynamics Simulations of the Lipid Bilayer Edge,” *Biophys. J.*, vol. 87, no. 1, pp. 182–192, Jul. 2004, doi: 10.1529/biophysj.103.031054.
- [66] W. C. Wimley and T. E. Thompson, “Transbilayer and interbilayer phospholipid exchange in dimyristoylphosphatidylcholine/dimyristoylphosphatidylethanolamine large unilamellar vesicles,” *Biochemistry*, vol. 30, no. 6, pp. 1702–1709, 1991.

- [67] A. A. Gurtovenko and I. Vattulainen, “Molecular mechanism for lipid flip-flops,” *J. Phys. Chem. B*, vol. 111, no. 48, pp. 13554–13559, 2007.
- [68] W. F. D. Bennett, N. Sapay, and D. P. Tieleman, “Atomistic Simulations of Pore Formation and Closure in Lipid Bilayers,” *Biophys. J.*, vol. 106, no. 1, pp. 210–219, Jan. 2014, doi: 10.1016/j.bpj.2013.11.4486.
- [69] N. Sapay, W. F. D. Bennett, and D. P. Tieleman, “Thermodynamics of flip-flop and desorption for a systematic series of phosphatidylcholine lipids,” *Soft Matter*, vol. 5, no. 17, p. 3295, 2009, doi: 10.1039/b902376c.
- [70] G. Van Meer, D. R. Voelker, and G. W. Feigenson, “Membrane lipids: Where they are and how they behave,” *Nat. Rev. Mol. Cell Biol.*, vol. 9, no. 2, pp. 112–124, 2008, doi: 10.1038/nrm2330.
- [71] P. A. Leventis and S. Grinstein, “The Distribution and Function of Phosphatidylserine in Cellular Membranes,” *Annu. Rev. Biophys.*, vol. 39, pp. 407–427, 2010, doi: 10.1146/annurev.biophys.093008.131234.
- [72] F.-X. Contreras, L. Sánchez-Magraner, A. Alonso, and F. M. Goñi, “Transbilayer (flip-flop) lipid motion and lipid scrambling in membranes,” *FEBS Lett.*, vol. 584, no. 9, pp. 1779–1786, May 2010, doi: 10.1016/j.febslet.2009.12.049.
- [73] R. A. Schlegel and P. Williamson, “Phosphatidylserine, a death knell,” *Cell Death Differ.*, vol. 8, no. 6, pp. 551–563, 2001.
- [74] J. Razzokov, M. Yusupov, S. Vanuytsel, E. C. Neyts, and A. Bogaerts, “Phosphatidylserine flip-flop induced by oxidation of the plasma membrane: a better insight by atomic scale modeling,” *Plasma Process. Polym.*, vol. 14, no. 10, pp. 1–6, 2017, doi: 10.1002/ppap.201700013.
- [75] C. Neale, W. F. D. Bennett, D. P. Tieleman, and R. Pomes, “Statistical convergence of equilibrium properties in simulations of molecular solutes embedded in lipid bilayers,” *J. Chem. Theory Comput.*, vol. 7, no. 12, pp. 4175–4188, 2011.
- [76] A. A. Gurtovenko, J. Anwar, and I. Vattulainen, “Defect-mediated trafficking across cell membranes: insights from in silico modeling,” *Chem. Rev.*, vol. 110, no. 10, pp. 6077–6103, 2010.

**6. Modeling Uptake of Polyethylenimine/siRNA Nanoparticles in breast Cancer Cells:
using machine learning**

6.1. Introduction

Gene silencing using polynucleotides aims to silence unwanted genes by blocking the translation of target messenger ribonucleic acids (mRNAs) [1]. Without a carrier, the anionic polynucleotides cannot cross anionic lipid bilayers of cell membranes to induce the gene silencing. Both viral and non-viral carriers can be used to deliver polynucleotides into the cells. Among non-viral carriers, cationic polymers have the advantage of being easily modified with other functional groups, making it feasible to tailor their properties for different applications [2]. Polyethylenimine (PEI) is the most promising and extensively investigated cationic polymer for polynucleotide delivery [3]. The efficacy of PEI was found to increase with its molecular weight [4]. However, high molecular weight (HMW) PEIs (~25 kDa) exhibited significant toxicity [4]. Low molecular weight (LMW) PEIs (< 2 kDa) had an acceptable level of toxicity, but efficacy of its gene delivery was low [5]. Modification of LMW PEIs with hydrophobic substitutions significantly increased its cellular uptake [6], [7]. Various hydrophobic substitutions were used to enhance efficacy of LMW PEIs including cholesterol, phospholipids, hydrophilic alkyl groups such as ethyl octyl, and aliphatic lipids including caprylic, stearic, and linoleic acids [8]–[10]. As a representative example, *Neamark et al.*[10] studied the delivery and transfection efficiency of 2 kDa PEI modified with different hydrophobic substitutions. They observed that these modifications significantly increased cellular uptake compared with unmodified native PEI [10]. The beneficial effect of the hydrophobic modification was shown to depend on both the type and level of the substitution [7].

A number of studies attempted to address the role of lipids in the delivery efficiency of hydrophobically modified PEIs [2], [4], [11], [12]. *Meneksedag-Erol et al.* [4] using molecular dynamics (MD) and experimental tools studied LMW PEI modified with short propionic acid

(PrA), focusing on the role of level of substitutions. They observed the highest surface hydrophobicity and surface charge density of the PEI/siRNA nanoparticle (NP) at an intermediate substitution ratio; substitution level beyond this optimal value induced migration of PrA towards the NP center and had a deleterious effect on both uptake and silencing. Experimental study of *Neammark et.al.*[10] showed that at a similar substitution level, PEI modified with linoleic acid (LA) had a higher transfection efficiency than PEI modified with caprylic acid (CA). These two hydrophobes differ in their length, i.e., number of hydrophobic carbons. These studies highlighted the dependence of PEI's delivery performance on the properties of grafted lipids. However, exhaustive parametric study, experimentally or numerically, on all PEIs and their derivatives is time-consuming and impractical. Additionally, significant amount of experimental data already exists in the literature on modified PEIs but have not been critically analyzed to explore universal relationships between the physicochemical features of the carriers and their efficiency in delivering polynucleotides.

Machine learning methods can help determine complex relationships between participating factors and desired targets, providing a means to predict the outcome without the need to perform extensive testing. In recent years, chemoinformatics methods including quantitative structure activity/property relationship (QSAR/QSPR) have been utilized to predict the activities/properties of a given compound as functions of its molecular substituents [13]. The core assumption in these methods is that variation in the biological activities of a compound is correlated with changes in its molecular structure. To date, there have been only two studies that utilized QSAR method to correlate molecular properties with cellular uptake of NPs. Both studies examined the cellular uptake data of cross-linked iron oxide (CLIO) NPs from *Weissleder et al.* [14]. *Fourches et al.*[15] developed a QSAR model to predict the uptake of CLIO NPs, with a variety of small organic

molecules decorating their surface, by human pancreatic cancer cells (PaCa2). The authors used 150 two-dimensional descriptors for 109 organic compounds, which included surface area, physicochemical properties (such as the net charge and hydrophilicity), Kier & Hall connectivity indices, kappa shape indices, atom and bond counts, adjacency and distance matrix descriptors, molecular charges, and pharmacophore feature descriptors. A 5-fold cross validation k nearest neighbors (kNN) regression was used as the prediction algorithm. The performance of their model under optimum condition resulted in R^2 value of 0.77. It was proposed that higher cellular uptake was associated with higher lipophilicity of the organic molecules bound to the CLIO NP. Using the same dataset, *Winkler et al.*[16] predicted the cellular uptake of CLIO NPs into PaCa2 and human umbilical vein endothelial cells (HUVEC) based on machine learning methods. The dataset, containing 108 data points, was separated into training set (87 data points) and test set (21 data points). Two-dimensional DRAGON descriptors were employed for the decorated CLIO NPs. Using these descriptors, a linear and nonlinear nano-QSAR model was developed. Eleven DRAGON descriptors were utilized for the uptake of NP into HUVEC cells, and the R^2 values for the best fits were 0.63 and 0.66 respectively for the linear and nonlinear models. For the uptake of NPs into PaCa2 cell, 19 DRAGON descriptors were used, which resulted in R^2 of 0.79 and 0.54, respectively for the linear and non-linear models. Different molecular descriptors were used to predict cellular uptake in different cell lines, which was related to different uptake mechanisms. As these two studies used dataset that only involved CLIO NPs, the predictive cellular uptake models can not be applied to more complex systems such as polymeric-nucleotide NPs.

In this chapter, we applied machine learning methods to predict the cellular uptake of PEI/siRNA NPs into breast cancer cell lines for the first time. The dataset for this study originated from published studies in our lab since 2011 that utilized different types of breast cancer cells and

an evolving pattern of hydrophobically modified LMW PEIs. We selected molecular descriptors that are easy to interpret by chemists, thereby providing informative guidance for the design of effective PEI carriers in gene delivery applications.

6.2. Methods

6.2.1. Dataset

The experimental cellular uptake data of PEI/siRNA NPs into various breast cancer cell lines including MDA MB231, MCF7, AU565, MDA 468, MDA 435, MDA 231 were collected from previous publications by our group [17]–[23]. A critical strength of the dataset analyzed here is that all NPs were tested under similar culture conditions in the same laboratory, thereby enabling direct comparisons across NP formulations. The basic methodology remained the same, where a scrambled FAM-labeled siRNA was formulated with PEI carriers and the uptake determined after 24 hours using flow cytometry methodology. The dataset was formed from 197 datapoints where PEI in its native form was the base polymer which was modified with 9 different hydrophobic substitutions including LA, alpha-linoleic acid (α LA), thioester linkage linoleic acid (tLA), CA, oleic acid (OA), palmitic acid (PA), lauric acid (Lau), stearic acid (StA), and cholesterol (Chol). Molecular structures of aforementioned hydrophobic substitutions are shown in Figure 6.1. All these structures except Chol, differ mostly in terms of their length, type of carbon bonds (saturated vs. unsaturated), number of unsaturated carbon bonds, and presence of thioester bonds.

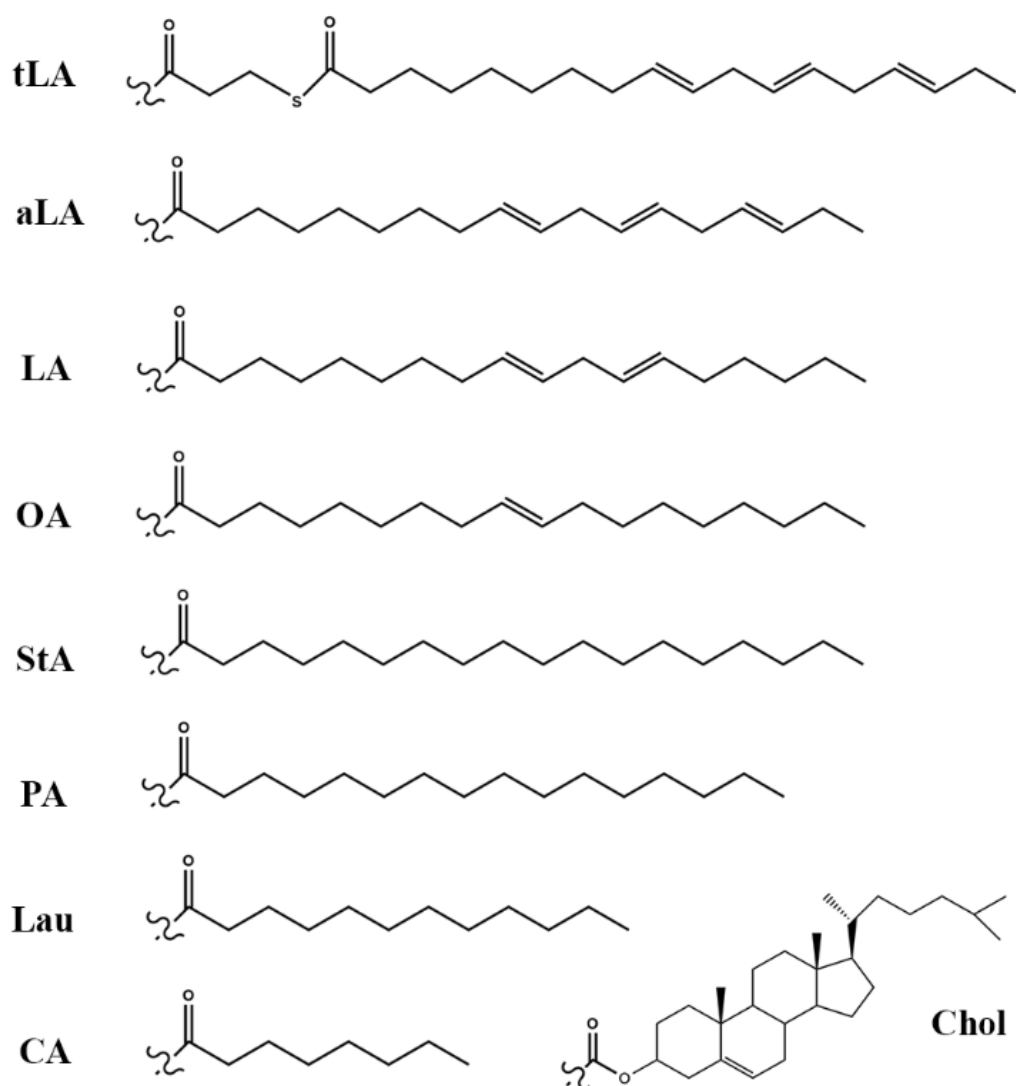


Figure 6.1. Molecular structure of hydrophobic substitutions used in this chapter.

6.2.2. Descriptors

Molecular descriptors were selected to capture the key parameters in the preparation of PEI/siRNA NPs while ensuring easy interpretation by chemists. Considered descriptors and their symbolic notations are shown in Table 6.1. Three descriptors namely N_c , N_{uns} and N_{thio} were generated by multiplying two other descriptors as shown in Table 6.1. The purpose of such an

approach was to add complexity and non-linearity to the descriptors before modeling. The output was logarithmic value of the cellular uptake of PEI/siRNA NPs, hereafter referred to as y ($y = \log(\text{cellular uptake})$).

Table 6.1. Descriptors used to model cellular uptake of PEI/siRNA NPs.

Descriptor	Definition	Range
M_w	MW of PEI (kDa).	0.6-2
r	PEI to siRNA weight ratio; determines the net charge of NP and the amount of bound siRNA.	2-10
BC_{50}	PEI to siRNA weight ratio required for 50% binding of a given siRNA amount; siRNA solution without PEI is taken as 0% binding.	0.1-1.5
n_{sub}	Number of amine groups per PEI modified with hydrophobic substitutions.	0-6.9
n_c	Number of C on each substitution; represents length of the hydrophobic substitution.	0-18
N_c	Total number of C on the substitutions in each PEI ($n_c \times n_{sub}$); related to NP hydrophobicity.	0-110
n_{uns}	Number of unsaturated C (C=C bonds) on each substitution.	0-3
N_{uns}	Total number of unsaturated C on the substitutions in each PEI ($n_{uns} \times n_{sub}$).	0-13
n_{thio}	Number of thioester groups (R-S-C(O)-R) on each substitution.	0-1
N_{thio}	Total number of thioester groups on the substitutions in each PEI ($n_{thio} \times n_{sub}$).	0-7
S	Type of hydrophobic substitution; none (native PEI) or one of the 9 types in Figure 6.1.	-
C_L	Type of breast cancer cell line; one of the 6 types described earlier.	-

6.2.3. Modeling

The dataset was divided into training data (147 data points), and test data (50 data point). Training data was employed at the modeling stage while the test data was used to evaluate model performance. Three different regression models were used, namely random forest (RF), multi-layer perceptron (MLP) and linear regression (LR). RF is an ensemble of large number of individual decision trees, where the predicted output is the average of predicted values from each decision tree. The MLP model was constructed using one input layer, one hidden layer, and one

output layer (see Appendix D, section D1). The activation function for the hidden layer was the ‘ReLU’ function, while the activation function for the output layer was the identity function [24]. The nodes in each layer were connected to the nodes in the next layer by weights, which were interactively adjusted during the training in order to minimize the network error. The network error was calculated from $\frac{1}{2} \|y(\text{predict}) - y(\text{actual})\|_2^2 + \frac{\alpha}{2} \|w\|_2^2$, where the subscript 2 represents l_2 norm, α is a non-negative hyperparameter that penalize large weights ($\alpha = 0.0001$ used in this work), and w is the weight. LR fits a linear model between y and the independent descriptors in order to minimize the model error as calculated by $\|y(\text{predict}) - y(\text{actual})\|_2^2$.

Three approaches were employed for the modeling, using different number of descriptors. In Model type 1, all descriptors in Table 6.1 were directly used, where the two categorical descriptors, S and C_L, were transformed using a dummy encoding scheme. This created a binary column for each category (see Appendix D, section D2). Using this approach, these two categorical descriptors were translated into 16 descriptors, 10 for S and 6 for C_L. Adding the 10 numerical descriptors in Table 1, the total number of descriptors under Model type 1 was 26. In Model type 2, the total number of descriptors was reduced using a binary encoder, where S and C_L were encoded by 4-digit and 3-digit binary numbers, respectively (see Appendix D, section D3). The 4-digit binary number for S translated into 4 index descriptors denoted as I_{sub}-1, I_{sub}-2, I_{sub}-3 and I_{sub}-4. Similarly, the 3-digit binary number for C_L translated into 3 index descriptors denoted as I_{cell}-1, I_{cell}-2 and I_{cell}-3. The total number of descriptors under Model type 2 was 10+4+3 = 17. Although the smaller number of descriptors lacked the ability to independently describe each type of hydrophobic substitution or cell line, this approach reduced overfitting and potential dimensionality problems. When dimensionality increases, the volume of the descriptor space increases, causing the data points to become sparse, which can be problematic for any models. Using Model type 2, the most

informative descriptors were identified as the ones showing more than 10% correlation with cellular uptake, and they were selected for modeling. In Model type 3, the number of descriptors were further reduced from Model type 2 using backward elimination. In this method, independent descriptors were entered into stepwise multilinear regression, followed by trial deletion of each descriptor using a chosen model fit. The descriptor (if any) whose removal gave statistically the most insignificant deterioration of the model fit was deleted, and this was repeated until no further descriptors could be eliminated without a statistically significant loss of fit. Afterwards, the remaining descriptors were used for modeling.

6.2.4. Metrics of model performance

Among various statistical measures for the performance of regression models, we used two criteria for both the training and test data: squared correlation coefficient usually denoted as R^2 , and root mean square error (RMSE). Additionally, accuracy of the model was evaluated using an acceptable difference between the predicted and actual values of y . The overall model Accuracy was calculated by dividing the total number of accurate predictions (within 25% of the actual values) by the total number of predictions.

6.3. Results and discussion

6.3.1. Significant descriptors

Model type 2 had a reduced number of descriptors (17) compared with Model type 1 (26 descriptors). Correlation between these 17 descriptors and cellular uptake was calculated using Pearson correlation coefficient (Table 6.2). The results show that 11 descriptors (highlighted red

in Table 6.2) had correlation of more than 10 % with the cellular uptake. The other 6 descriptors had negligible correlation and hence were removed from further modeling using Model type 2. In Model type 3 where backward elimination was utilized to further remove insignificant descriptors, a significance level of 5% was selected that corresponded to p-value of 0.05. LR regressor was fitted using the 11 descriptors identified from Model type 2, and the descriptor with the highest p-value was examined. If its p-value was greater than the defined significance level of 0.05, the descriptor was removed and LR was implemented again using the remaining descriptors. The process continued until the highest p-value from all the remaining descriptors was less than 0.05. The number of descriptors reduced to 6 after backward elimination, which were r , $I_{\text{sub-1}}$, $I_{\text{sub-2}}$, N_c , N_{uns} , and N_{thio} .

Table 6.2. Correlation of cellular uptake with descriptors used in model type 2.

Descriptor	Correlation with cellular uptake (%)
M_w	7
r	23
$I_{\text{sub-1}}$	27
$I_{\text{sub-2}}$	27
$I_{\text{sub-3}}$	0
$I_{\text{sub-4}}$	1
BC_{50}	24
n_{sub}	33
n_c	57
N_c	44
N_{uns}	37
n_{uns}	31
n_{thio}	13
N_{thio}	12
$I_{\text{cell-1}}$	2
$I_{\text{cell-2}}$	4
$I_{\text{cell-3}}$	8

With the final numbers of descriptors (26 in Model type 1, 11 in Model type 2, 6 in Model type 3), the regression models were trained and their performances were summarized in Table 6.3. Better model performance corresponds to higher values of Accuracy and R^2 , as well as lower values of RMSE. For all model types, non-linear models of RF and MLP had a better performance than the linear model of LR. The model with best performance was RF using Model type 2. However, RF with Model type 3 also showed comparable accuracy while having much fewer descriptors. Our results therefore suggest that the most significant descriptors were those in Model type 3, i.e., r , $I_{\text{sub-1}}$, $I_{\text{sub-2}}$, N_c , N_{uns} , and N_{thio} .

Table 6.3. Performance of different regression models.

Method	no. descriptors	Model type	Accurac y (train)	Accurac y (test)	R^2 (train)	R^2 (test)	RMSE (train)	RMSE (test)
RF	26	1	0.63	0.59	0.70	0.41	0.56	0.77
RF	11	2	0.58	0.47	0.71	0.50	0.56	0.70
RF	6	3	0.60	0.47	0.69	0.46	0.57	0.73
MLP	26	1	0.58	0.57	0.65	0.41	0.61	0.77
MLP	11	2	0.52	0.55	0.51	0.43	0.72	0.75
MLP	6	3	0.50	0.51	0.45	0.42	0.77	0.78
LR	26	1	0.54	0.45	0.54	0.34	0.70	0.81
LR	11	2	0.47	0.53	0.41	0.35	0.79	0.80
LR	6	3	0.45	0.53	0.41	0.39	0.80	0.78

6.3.2. Effect of most significant descriptors

The descriptor r , PEI-to-siRNA weight ratio, usually ranges between 2 and 10 in experiments. Higher r leads to higher positive charge on the PEI/siRNA NPs, causing stronger interaction with cell membranes. Additionally, higher r increases the presence of free PEIs that are not bound to

siRNAs, which might destabilize membrane structure, thereby contributing to the uptake of PEI/nucleic acid NPs [25]. *Boeckle et al.* [25] attributed the increase in gene expression observed with free PEIs to their ability to facilitate proton sponge effect. They proposed that free PEIs could be internalized into endosomes, which could then merge with vesicles containing PEI/DNA NPs. These free PEIs subsequently assisted in the buffering of vesicular pH and accumulation of Cl^- in the endosome leading to its rupture.

Unlike the r , the two index descriptors $I_{\text{sub-1}}$ and $I_{\text{sub-2}}$ by themselves do not have direct physical meaning. They are compacted form of the type of hydrophobic substitution, suggesting that type of hydrophobic substitution plays a significant role in the delivery of siRNA into breast cancer cells. As a supporting evidence, *Aliabadi et al.*[26] explored LMW PEIs substituted by different lipids, as carriers for siRNA-mediated BCRP down-regulation. BCRP is an efflux protein whose activity has been connected to multidrug resistance in breast cancer treatment. It was shown that efficacy of siRNA delivery increased significantly with hydrophobic lipid substitutions ranging from C8 to C18, and that LA- and CA-substituted PEIs were the most effective in both cellular uptake and BCRP down regulation.

$N_c (= n_c \times n_{\text{sub}})$ is a measure of hydrophobicity introduced to the PEI molecules. Same level of hydrophobicity can be obtained experimentally by adjusting either the level of substitutions per PEI (n_{sub}) or the number of C on each substitution (n_c). It is worth noting that backward elimination in Model type 3 eliminated the descriptor of n_c . This indicates that given N_c , n_c itself does not play an important role in cellular uptake. Figure 6.2a shows the relation between y and the two parameters of N_c and n_c , based on experimental data. Reading the plot horizontally at a fixed value of N_c , the variation in y was small suggesting its insensitivity to n_c . Reading the plot vertically, y

exhibited an overall increasing trend with N_c for n_c of 8 and 12, while no specific trend was observed for n_c of 16 and 18.

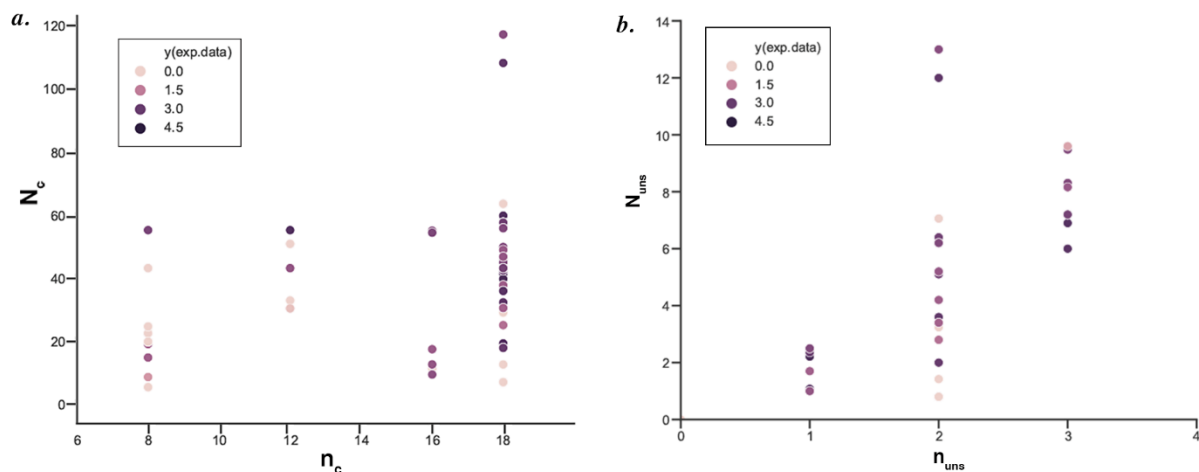


Figure 6.2. Visualization of dataset.

(a) Experimental data (training and test data) for y as a function of N_c and n_c . n_c values correspond to caprylic acid (8), lauric acid (12), palmitic acid (16) and linoleic acid (C18). (b) experimental data for y as a function of N_{uns} and n_{uns} . n_{uns} values correspond to oleic acid (1), linoleic acid (2), and α -linoleic acid (3).

The descriptor N_{uns} was found to be significant to the prediction of cellular uptake, which is a measure of unsaturation level in the lipid substitutions. To further evaluate the role of N_{uns} , the value of y as a function of N_{uns} and n_{uns} is shown in Figure 6.2b. The results suggested that for $n_{uns} = 2$, between 2 and 3 substitutions per PEI ($N_{uns} = (2-3) \times n_{uns} = 4-6$) resulted in higher y value, and substitution level higher than 3 or lower than 2 caused a decrease in y . Because n_{uns} was eliminated in backward elimination, the optimal N_{uns} was expected to be in the same range for other n_{uns} . This cannot be seen directly from Figure 6.2b due to the lack of data points to cover wider range of n_{uns} and N_{uns} , especially since some data points were not considered during training.

Finally, N_{thio} is another important descriptor which represents the total number of thioester groups on hydrophobically modified PEIs. This functional group can increase the sensitivity of

NPs to dissociation due its labile nature under aqueous conditions. Strong electrostatic interaction between cationic polymers and nucleic acids has been shown to benefit the formation of a stable NP to deliver nucleic acids across cell membranes [27]; however, it was also proposed to limit the efficacy of polymers due to insufficient unpacking of NPs in the cytoplasm [28]. *K.C. et al.*[29] showed that introducing electronegativity (with the addition of thioester groups) along with hydrophobic tail decreased the binding strength between lipid-grafted PEI and plasmid DNA (pDNA). Additionally, it was shown that PEI-tLA polymers were easier to dissociate from pDNA than PEI-LA polymers, which resulted in better delivery performance of PEI-tLA polymers.

6.3.3. Closed-form predictions

Although the LR method exhibited poorer performance than the RF and MLP methods, a strength of the LR method is that it can provide predictions in closed form. This can be useful in practical settings where initial screening of the descriptors is done efficiently with relatively low but acceptable accuracy. Here, closed-form predictions of y generated from LR regressor are presented for each model type. The coefficient of each descriptor is shown in Table 4, and absolute value of the coefficient represents significance of the descriptor. For Model type 1 (26 descriptors in total, notations defined in Appendix D, section D2), 6 descriptors had a coefficient whose absolute value was greater than 0.5. For Model types 2 (11 descriptors in total), 6 descriptors had a coefficient with absolute value greater than 0.13. For model type 3 (6 descriptors in total), 3 descriptors had a coefficient with absolute value greater than 0.13. These coefficients are colored red in Table 6.4. All model types suggested that N_{uns} and N_{thio} were significant descriptors. This indicates that that tLA is an important hydrophobic substitution, being the only substitution that carries thioester group on its structure. Also, for both Model type 2 and Model type 3, $I_{\text{sub-1}}$, and

$I_{\text{sub-2}}$ were found to be significant. Although these two descriptors cannot directly distinguish different types of hydrophobic substitutions, some information can be obtained from them. Examining the binary encoding (Table D3 in Appendix D), 7 substitutions had $I_{\text{sub-1}}=1$ or $I_{\text{sub-2}}=1$ including tLA, PA, StA, LA, α LA, Chol, and OA, suggesting long lipids are better hydrophobic modification than short tail lipids (CA, Lau). Among the 6 cell lines, I_{AU565} and $I_{\text{MDA 468}}$ had the smallest coefficient (in magnitude) generated by Model type 1, suggesting insensitivity of y with respect to these two cell lines.

The closed-form LR prediction of y using Model type 3 is given below:

$$y = 0.10 \mathbf{r} + 1.24 \mathbf{I}_{\text{sub-1}} + 0.82 \mathbf{I}_{\text{sub-2}} + 0.02 \mathbf{N}_{\text{c}} - 0.05 \mathbf{N}_{\text{uns}} - 0.20 \mathbf{N}_{\text{thio}}$$

This equation predicts that y increases with \mathbf{r} , $\mathbf{I}_{\text{sub-1}}$, $\mathbf{I}_{\text{sub-2}}$, and \mathbf{N}_{c} , while decreasing with \mathbf{N}_{uns} and \mathbf{N}_{thio} . The coefficient in front of \mathbf{N}_{thio} was negative, which might seem contradictory to the aforementioned beneficiary effect of thioester group on cellular uptake. However, it should be pointed out that the descriptors are interconnected; an increase in \mathbf{N}_{uns} can also be associated with an increase in $\mathbf{I}_{\text{sub-1}}$ or $\mathbf{I}_{\text{sub-2}}$ which are accompanied by positive coefficients. Figure 6.3 shows representative model prediction for y by varying \mathbf{N}_{c} , \mathbf{N}_{uns} and \mathbf{N}_{thio} . In these plots, \mathbf{r} was set to 5, based on its most frequent value in the dataset. Index indicators of $\mathbf{I}_{\text{sub-1}}$ and $\mathbf{I}_{\text{sub-2}}$ were assigned 1 and 0, because no hydrophobic substitutions in the dataset had value of 1 for both two indices (Table D4). Figure 6.3 showed that given \mathbf{N}_{thio} , low \mathbf{N}_{uns} and high \mathbf{N}_{c} resulted in higher y (uptake) into breast cancer cell lines. Such parametric study will help better design more potent PEI carriers for gene delivery applications.

Table 6.4. Coefficients generated from LR using the three model types.

Descriptor	Coefficient (Model type 1)	Coefficient (Model type 2)	Coefficient (Model type 3)
M _w	0.39	-	-
r	0.09	0.10	0.10
I _{sub-1}	-	0.99	1.24
I _{sub-2}	-	0.58	0.82
BC ₅₀	0.52	0.14	-
n _{sub}	0.03	-0.02	-
n _c	0.05	0.01	-
N _c	0.01	0.02	0.02
N _{uns}	-0.11	-0.10	-0.05
n _{uns}	0.79	0.16	-
n _{thio}	0.05	0.37	-
N _{thio}	-0.10	-0.22	-0.20
I _{None}	0.20	-	-
I _{CA}	-0.37	-	-
I _{Lau}	-0.12	-	-
I _{PA}	0.33	-	-
I _{StA}	0.57	-	-
I _{LA}	-1.15	-	-
I _{alA}	-1.20	-	-
I _{Chol}	-0.10	-	-
I _{OA}	-0.68	-	-
I _{tLA}	0.047	-	-
IMDA MB231	0.32	-	-
IMCF7	-0.50	-	-
IAU565	-0.001	-	-
IMDA 468	-0.02	-	-
IMDA 435	0.33	-	-
IMDA 231	-0.13	-	-

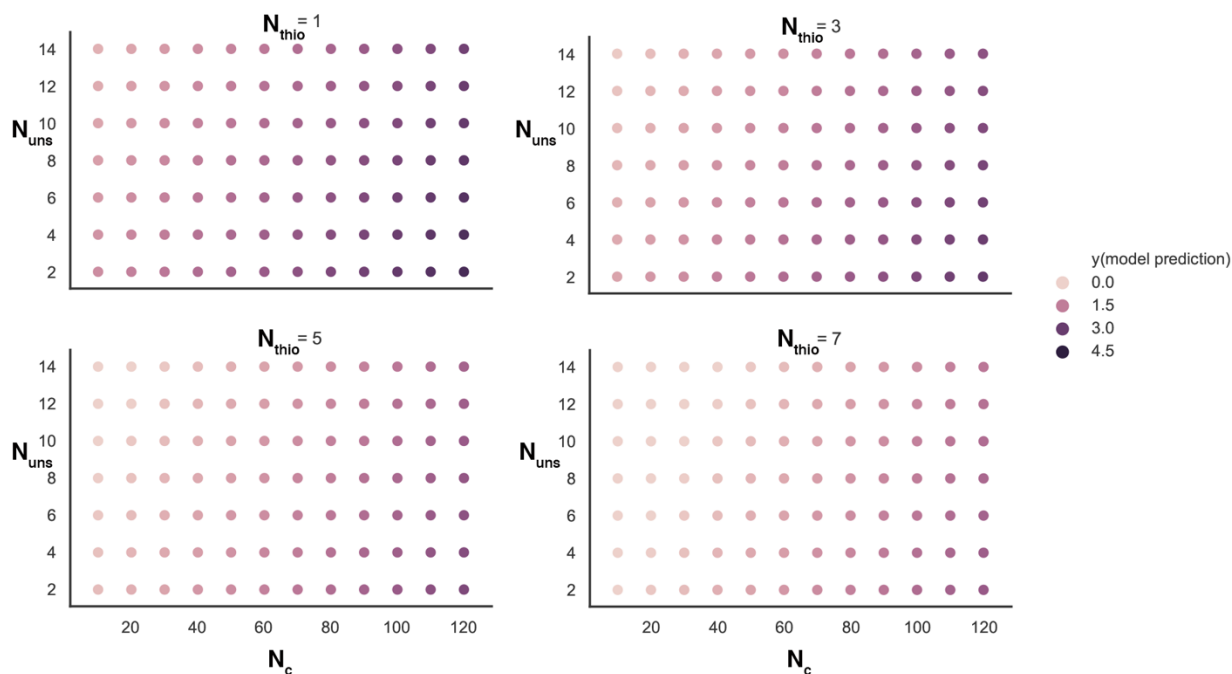


Figure 6.3. Model prediction for y as a function of N_{uns} , N_c , and N_{thio} .

6.4. Limitation and future perspective

A common problem in the modeling of biological effects is the limited number of data points and high number of descriptors. This might lead to overfitting, where the model performs well on the training data but poorly on the test data. Many experimental studies are also typically performed under different conditions including cell medium, baseline polymer, polymer concentration, NP size and charge, number of cells, and instrument used to measure cellular uptake, to name a few. This issue can be addressed by performing systematic experimental studies to generate a large dataset, and normalizing the data into unitless quantities to minimize differences in measurements. The problem of large number of descriptors can be tackled by proper descriptor selection for model construction as used in our study through Model type 3.

The models generated here could be used to predict the cellular uptake of PEI/siRNA NPs where the parameters of hydrophobic substitutions are new and untested. Reliable predictions can

be made within the ranges of the utilized descriptors. To strengthen the model predictions, new experimental data especially on the types of hydrophobic substitutions with low number of data points in current dataset should be added (i.e. wider range of unsaturated lipids with various level of substitutions (Figure 6.2b)), and then the models need to be retrained. Additionally, our model suggested that cellular uptake of PEI/siRNA NPs is insensitive to AU565 and MDA 468 cell lines which needs to be verified with experiments. Another approach is to find more informative descriptors that provide additional information regarding uptake of PEI/siRNA NPs into cancer cell lines. An example of such descriptors could be the toxicity level PEI/siRNA NPs. As new descriptors are added to the models, backward elimination should be employed to test whether the new descriptors are statistically significant.

Computational methods that give better model predictions are usually in some form of artificial neural networks, or other non-linear methods such as the RF used in our study. Selection of methods must take into consideration factors such as the complexity of NPs, number of descriptors affecting cellular uptake, and complexity of the relation between descriptors and cellular uptake. The advantage of non-linear methods is that they can find more complex relation between descriptors and the target (here, cellular uptake), thereby providing better prediction. However, the disadvantage is that such methods cannot separately describe the contribution of individual descriptors and can only be used as a black box algorithm. The simpler LR can provide direct information on the contribution of each descriptor, at the cost of losing accuracy. To improve the performance of linear methods, more complex descriptors can be generated by imposing non-linearity. For example, through multiplication of two descriptors as utilized in our study (N_c , N_{uns} and N_{thio}).

6.5. Conclusions

Machine learning algorithms were employed to model the uptake of PEI/siRNA NPs into breast cancer cells. A large dataset was compiled composed of experimental values for the uptake of LMW PEI/siRNA NPs into six breast cancer cell lines, where the PEIs were modified with different hydrophobic substitutions. Three different regression models namely RF, MLP and LR, as well as various descriptors were used to construct the models. RF and MLP regression methods were found to have a better performance, suggesting that non-linear models were better estimators than the linear model to predict the cellular uptake of PEI/siRNA NPs. Descriptors that had major contribution to uptake included PEI-to-siRNA weight ratio, type of hydrophobic substitution, as well as the total number of C, thioester groups and unsaturated C on the substitutions in each PEI. Our study was the first report of quantitative modeling and prediction of cellular uptake of PEI/siRNA NPs, using chemically interpretable descriptors, which will facilitate the design of more efficient gene delivery systems.

6.6. Acknowledgements

Compute Canada and Westgrid were gratefully acknowledged for providing the computing resources and technical support. This work is funded by Natural Sciences and Engineering Research Council of Canada (NSERC), Canadian Institutes of Health Research (CIHR) and Alberta Innovates-Technology Futures (AITF).

6.7. References

- [1] H. Uludag, A. Ubeda, and A. Ansari, “At the intersection of biomaterials and gene therapy: Progress in non-viral delivery of nucleic acids,” *Front. Bioeng. Biotechnol.*, vol. 7, p. 131, 2019.
- [2] C. Sun, T. Tang, and H. Uludağ, “Probing the Effects of Lipid Substitution on Polycation Mediated DNA Aggregation: A Molecular Dynamics Simulations Study,”

- Biomacromolecules*, vol. 13, no. 9, pp. 2982–2988, Sep. 2012, doi: 10.1021/bm301045b.
- [3] A. P. Pandey and K. K. Sawant, “Polyethylenimine: A versatile, multifunctional non-viral vector for nucleic acid delivery,” *Mater. Sci. Eng. C*, vol. 68, pp. 904–918, Nov. 2016, doi: 10.1016/j.msec.2016.07.066.
- [4] D. Meneksedag-Erol, R. B. KC, T. Tang, and H. Uludağ, “A Delicate Balance When Substituting a Small Hydrophobe onto Low Molecular Weight Polyethylenimine to Improve Its Nucleic Acid Delivery Efficiency,” *ACS Appl. Mater. Interfaces*, vol. 7, no. 44, pp. 24822–24832, Nov. 2015, doi: 10.1021/acsami.5b07929.
- [5] Y. Nademi, T. Tang, and H. Uludağ, “Steered molecular dynamics simulations reveal a self-protecting configuration of nanoparticles during membrane penetration,” *Nanoscale*, vol. 10, no. 37, pp. 17671–17682, 2018, doi: 10.1039/C8NR04287J.
- [6] V. Incani, A. Lavasanifar, and H. Uludağ, “Lipid and hydrophobic modification of cationic carriers on route to superior gene vectors,” *Soft Matter*, vol. 6, no. 10, p. 2124, 2010, doi: 10.1039/b916362j.
- [7] H. M. Aliabadi, B. Landry, C. Sun, T. Tang, and H. Uludağ, “Supramolecular assemblies in functional siRNA delivery: where do we stand?,” *Biomaterials*, vol. 33, no. 8, pp. 2546–2569, 2012.
- [8] D. Wang *et al.*, “Novel Branched Poly(Ethylenimine)–Cholesterol Water-Soluble Lipopolymers for Gene Delivery,” *Biomacromolecules*, vol. 3, no. 6, pp. 1197–1207, Nov. 2002, doi: 10.1021/bm025563c.
- [9] P. Y. Teo *et al.*, “Hydrophobic modification of low molecular weight polyethylenimine for improved gene transfection,” *Biomaterials*, vol. 34, no. 32, pp. 7971–7979, Oct. 2013, doi: 10.1016/j.biomaterials.2013.07.005.
- [10] A. Neamark, O. Suwantong, R. B. K. C., C. Y. M. Hsu, P. Supaphol, and H. Uludağ, “Aliphatic Lipid Substitution on 2 kDa Polyethylenimine Improves Plasmid Delivery and Transgene Expression,” *Mol. Pharm.*, vol. 6, no. 6, pp. 1798–1815, Dec. 2009, doi: 10.1021/mp900074d.
- [11] C. Sun, T. Tang, and H. Uludag, “A molecular dynamics simulation study on the effect of lipid substitution on polyethylenimine mediated siRNA complexation,” *Biomaterials*, vol. 34, no. 11, pp. 2822–2833, Apr. 2013, doi: 10.1016/j.biomaterials.2013.01.011.
- [12] C. Sun, T. Tang, and H. Uludağ, “Molecular Dynamics Simulations for Complexation of

- DNA with 2 kDa PEI Reveal Profound Effect of PEI Architecture on Complexation,” *J. Phys. Chem. B*, vol. 116, no. 8, pp. 2405–2413, Mar. 2012, doi: 10.1021/jp211716v.
- [13] R. Perkins, H. Fang, W. Tong, and W. J. Welsh, “Quantitative structure-activity relationship methods: Perspectives on drug discovery and toxicology,” *Environ. Toxicol. Chem. An Int. J.*, vol. 22, no. 8, pp. 1666–1679, 2003.
- [14] R. Weissleder, K. Kelly, E. Y. Sun, T. Shtatland, and L. Josephson, “Cell-specific targeting of nanoparticles by multivalent attachment of small molecules,” *Nat. Biotechnol.*, vol. 23, no. 11, pp. 1418–1423, 2005.
- [15] D. Fourches *et al.*, “Quantitative nanostructure– activity relationship modeling,” *ACS Nano*, vol. 4, no. 10, pp. 5703–5712, 2010.
- [16] D. A. Winkler *et al.*, “Modelling and predicting the biological effects of nanomaterials,” *SAR QSAR Environ. Res.*, vol. 25, no. 2, pp. 161–172, 2014.
- [17] H. M. Aliabadi *et al.*, “A systematic comparison of lipopolymers for siRNA delivery to multiple breast cancer cell lines: In vitro studies,” *Acta Biomater.*, vol. 102, pp. 351–366, 2020.
- [18] H. Montazeri Aliabadi, B. Landry, P. Mahdipoor, and H. Uludağ, “Induction of Apoptosis by Survivin Silencing through siRNA Delivery in a Human Breast Cancer Cell Line,” *Mol. Pharm.*, vol. 8, no. 5, pp. 1821–1830, Oct. 2011, doi: 10.1021/mp200176v.
- [19] D. N. Meenakshi Sundaram, C. Kucharski, M. B. Parmar, R. B. KC, and H. Uludağ, “Polymeric Delivery of siRNA against Integrin- β 1 (CD29) to Reduce Attachment and Migration of Breast Cancer Cells,” *Macromol. Biosci.*, vol. 17, no. 6, p. 1600430, 2017.
- [20] H. M. Aliabadi, R. Maranchuk, C. Kucharski, P. Mahdipoor, J. Hugh, and H. Uludağ, “Effective response of doxorubicin-sensitive and-resistant breast cancer cells to combinational siRNA therapy,” *J. Control. Release*, vol. 172, no. 1, pp. 219–228, 2013.
- [21] S. Plianwong, B. Thapa, R. B. Kc, C. Kucharski, T. Rojanarata, and H. Uludağ, “Enabling Combinatorial siRNA Delivery against Apoptosis-Related Proteins with Linoleic Acid and α -Linoleic Acid Substituted Low Molecular Weight Polyethylenimines,” *Pharm. Res.*, vol. 37, no. 3, p. 46, 2020.
- [22] S. Xiang *et al.*, “Uptake mechanisms of non-viral gene delivery,” *J. Control. Release*, vol. 158, no. 3, pp. 371–378, Mar. 2012, doi: 10.1016/j.jconrel.2011.09.093.
- [23] B. Thapa, R. Bahadur KC, and H. Uludağ, “Novel targets for sensitizing breast cancer cells

- to TRAIL-induced apoptosis with siRNA delivery,” *Int. J. cancer*, vol. 142, no. 3, pp. 597–606, 2018.
- [24] X. Zhang, Y. Yu, L. Wang, and Q. Gu, “Learning one-hidden-layer relu networks via gradient descent,” in *The 22nd International Conference on Artificial Intelligence and Statistics*, 2019, pp. 1524–1534.
- [25] M. Boeckle, S. , von Gersdorff, K. , van der Piepen, S. , Culmsee, C. , Wagner, E. and Ogris, “Purification of polyethylenimine polyplexes highlights the role of free polycations in gene transfer,” *J. Gene Med.*, vol. 6, pp. 1102–1111, 2004, doi: 10.1002/jgm.598.
- [26] H. M. Aliabadi, B. Landry, P. Mahdipoor, C. Y. M. Hsu, and H. Uludağ, “Effective down-regulation of Breast Cancer Resistance Protein (BCRP) by siRNA delivery using lipid-substituted aliphatic polymers,” *Eur. J. Pharm. Biopharm.*, vol. 81, no. 1, pp. 33–42, May 2012, doi: 10.1016/j.ejpb.2012.01.011.
- [27] D. J. Gary, N. Puri, and Y.-Y. Won, “Polymer-based siRNA delivery: perspectives on the fundamental and phenomenological distinctions from polymer-based DNA delivery,” *J. Control. Release*, vol. 121, no. 1–2, pp. 64–73, 2007.
- [28] A.-L. Bolcato-Bellemin, M.-E. Bonnet, G. Creusat, P. Erbacher, and J.-P. Behr, “Sticky overhangs enhance siRNA-mediated gene silencing,” *Proc. Natl. Acad. Sci.*, vol. 104, no. 41, pp. 16050–16055, 2007.
- [29] R. B. KC, C. Kucharski, and H. Uludağ, “Additive nanocomplexes of cationic lipopolymers for improved non-viral gene delivery to mesenchymal stem cells,” *J. Mater. Chem. B*, vol. 3, no. 19, pp. 3972–3982, 2015.

7. Overall conclusions, General Discussion and Future Perspectives

7.1. Overall conclusions

This dissertation investigated the interaction between polymer/siRNA NPs with the cell membranes through a series of computational studies, along with some experimental studies. I focused specifically on structural changes of NPs during membrane penetration as well as the effect of membrane properties on penetration of NPs. The thesis work started with an in-depth literature review on molecular dynamics simulations studies performed on NPs-membrane interactions presented in **Chapter 2**. Majority of the simulation studies investigated the effect of NP's physical properties on direct penetration using dissipative particle dynamics (DPD) simulations, while very few studies focused on all-atom simulations of direct penetration of NPs. Also, very few studies addressed the dissociation capability of membrane's surface molecules to disassemble polynucleotide NPs. The knowledge gaps discussed in this chapter motivated the studies executed in Chapters 3-5.

Chapter 3 investigated the stability and configurational changes of NPs formed by 6 PEI and 2 siRNA molecules during penetration into the zwitterionic POPC membranes. Three types of PEI molecules, namely unmodified PEI and PEIs modified with hydrophobic substitutions of CA and LA were employed for NP formation. The results showed that HB formation between the PEIs and the membrane did not cause instability of the PEI/siRNA NPs during the internalization process. Instead, the results suggested adoption of a “self-protecting” configuration by the PEI/siRNA NP during membrane penetration, where the NP becomes more compact and siRNAs become aligned leading to more stable configurations while detaching from the membrane. Among types of PEI molecules, the PEI/siRNA NP modified with LA showed the smallest structural change due to its strong intra-particle lipid associations and the resulting rigidity, while NP modified with CA exhibited the largest structural changes.

There exist various types of lipid molecules on the cell membrane surface, which can induce configurational changes of the NP and possibly affect their functional performance. **Chapter 4** focused on understanding the role of cell membranes lipids on integrity and configurational changes of PEI/siRNA NPs using SMD simulations and dissociation experiments. The NPs were derived from two different PEIs, unmodified LMW PEI and LA-substituted PEI, and utilized membranes were anionic POPS and zwitterionic POPC. The experiments showed that POPS liposomes interacted strongly with both types of NPs, which caused partial dissociation of the NPs, while POPC liposomes did not induce any dissociation. Consistent with the experiments, SMD simulations showed a stronger interaction between the NPs and the POPS membranes than between the NPs and the POPC membranes. The presence of LA substitutions on the PEIs enhanced the stability of NPs during membrane crossing; similarly to the results of **Chapter 3**, lipid association between PEIs of LA-bearing NPs as well as aligned orientation of the siRNAs provided protection against their dissociation unlike NPs from unmodified PEI.

Up to this, the role of polymeric structure and its stability upon interactions with lipid membranes were addressed. However, the role of membrane deformations and its pore closure is of great importance in studying NP-membrane interactions. **Chapter 5** focused on the effect of NP penetration on the integrity of various membrane models where the acyl chain lengths and saturation levels were altered. To this end, SMD and MD simulations were employed using three membrane bilayer built from zwitterionic POPC, DPPC, and DLPC membranes. Studied NPs formed by 2 siRNA and 6 PEI molecules, where two types of PEI molecules were exploited—unmodified PEI and PEIs modified with hydrophobic LA substitutions. The results showed that different membrane lipids could lead to differences in pore formation symmetric vs. asymmetric, as well as could undergo different levels of pore-mediated flip-flops during its closure.

Additionally, introduction of LA substitutions onto the PEIs was facilitate pore formation, since the long LA tails could insert themselves into the hydrophobic part of the membrane where the lipid tails were less aligned. Among simulated membranes, POPC and DLPC had more space among their lipids compared with DPPC, which promoted the insertion of LA tails and hence NP entry into the cell. The results reported in this dissertation on several aspects of polymer/siRNA NPs – membrane interactions enhanced our understanding of the key properties of polymer siRNA delivery system , which can help design polymer with better functional performance.

Machine learning methods can help us to extract useful information in terms of identifying the important descriptors, and also to predict the desired outcome without the needs to perform extensive experimental testing. Also, many experimental studies already existed, but what can be learned from generated data is limited due to contribution of various factors on the output target. To this end, chemoinformatics methods including QSAR/QSPR have been utilized in the literature. The core assumption of the QSAR method is that the variation in biological activities of a NP is correlated with changes in its molecular structure. **Chapter 6** investigated the cellular uptake of PEI/siRNA NPs into various breast cancer cell lines, and by using machine learning algorithms a predictive model using easy to interpret descriptors was generated. The most important descriptors were found to be PEI-to-siRNA weight ratio, type of hydrophobic substitution, as well as the total number of C, thioester groups and unsaturated C on the substitutions in each PEI. This chapter was the first report of quantitative modeling on prediction of cellular uptake of PEI/siRNA NPs, which provides valuable insight for the design of improved hydrophobic substituents on cationic PEI polymer.

7.2. Limitation and future direction to study polynucleotide NP-membrane interactions

While past molecular simulations have provided insight into the interaction of polynucleotide NP with cell membrane, much remains to be explored. To start, the correct compositions of lipidic membranes are essential to their better simulation behaviors [1]. Eukaryotic cell membrane consists of as many as 1000 different lipid species, with variations of aliphatic chain lengths, head groups and other structures [2]. The frequently used lipid bilayer structures in molecular simulations are relatively simple and composed of a single or a binary mixture of lipid constituents (e.g., POPC or POPA). The presence of different components can significantly affect cellular uptake pathways, and utilizing more complex membrane models by introducing biologically relevant molecules, such as cholesterol, heparin, and protein receptors will be more realistic. Additionally, lipid compositions can differ considerably between the two leaflets at the cytosolic vs. extracellular interfaces [3]. For example, plasma membrane have an asymmetric lipid distribution, where phosphatidylcholine (PC) and sphingomyelin (SM) are mainly localized in the extracellular leaflet, whereas phosphatidylethanolamine (PE) and phosphatidylserine (PS) are exclusively present in the cytoplasmic leaflet [4]. The resulting asymmetry affects the curvature of the membrane, and can impose a transmembrane electrostatic potential difference [5]. In addition to asymmetry in composition, the solvent facing the two leaflets are different in terms of pH, ionic strength, and electric potential [6]. MD simulations that probe such heterogeneous membrane structures and environment will better shed light on the integrity of membranes and the flip-flop process during NP penetration. The effect of lipid flip-flop is expected be more significant in mixed lipid membranes, where the anionic lipids might undergo translocation from the lower leaflet to the upper leaflet. An example of such lipids is PS that is normally located in the inner

leaflet of the plasma membrane. If PS undergoes flip-flop from the inner leaflet to the outer leaflet, it can act as an apoptotic signal for lymphocytic cells [7] [8].

Protein corona adsorbed on the NPs can substantially influence the NP-membrane interaction. Along with experiments, molecular simulations can help us address whether the protein adsorption is beneficial or detrimental for the uptake. For example, the nature of proteins in the corona can first be identified experimentally based on the biological fluids the NPs come in contact with (e.g., Albumin, HAS). Simulations starts providing insight on NP-membrane interaction in presence of the protein adsorption. However, simulations are at the early stage with focus only on CG simulations and one type of protein corona. Various types of protein corona exist that can adsorb on NP surface and affect NP-membrane interactions. Atomistic insights on such interactions will guide us to design efficient NPs with promoted or inhibited protein adsorption.

One of the general limitations with any all-atom MD simulation is the length and time scales that make it highly challenging to investigate the dynamics of real-size supramolecular assemblies. Because of this, computing resources do not allow us to investigate the full-scale dynamics of complex biological systems. For example, the largest size of our simulated NPs is ~3 nm, while the size of polymeric NPs for nucleic acid delivery is reported to be in the 100-200 nm range [9]. Therefore, direct quantitative comparisons cannot be made between the simulation results and the experimental observations. Some significant efforts have been made for the development of algorithms to overcome aforementioned limitation. These methods include replica exchange MD [10], SMD [11], simulated annealing [12], or CG [13] to name a few. An example of CG approaches is DPD. In the DPD method, a cluster of atoms is treated as one soft spherical bead, whose motion is governed by the interactions among beads and certain collision rules, thus decreasing the degrees of freedom and enabling larger time steps. However, CG

methods cause loss of atomistic detail of the simulated systems. To better reveal the complete picture of complex processes such as cellular uptake is usage of advanced MD approaches in conjunction with all-atom MD simulations. For example, in **Chapter 5**, we were able to determine the role of membrane deformations provide insight into pore mediated lipid flip-flops using combination of SMD and MD simulations.

Current molecular simulations usually study small numbers of factors at a time. In recent years, with the increase in computational power and available data, machine learning is starting to be applied in materials design. By studying a large amount of data, this method can provide consolidated information on what are the dominating factors for NP uptake, and how these factors mutually influence each other. There is room for integrating machine learning with molecular simulations to expedite our design of polynucleotide NP-membrane interaction. In **Chapter 6**, we were able to generate a predictive model for cellular uptake of PEI/siRNA NP into breast cancer cell lines. The next step in model development is expansion of dataset through addition of descriptors and data points in order to provide more accurate cellular uptake prediction. Also, new output targets can be added into the dataset, and model can be developed to provide more complex scientific questions. As a representative example, the purpose of PEI/siRNA NPs delivery is down regulate specific messenger RNAs (mRNAs) involved in signaling, thereby effectively reducing the intracellular levels of desired proteins [14]. By altering the nucleotide sequence of siRNA molecules, one can silence a broad range of mRNAs to restore the normal physiology. In case of breast cancer cell lines, a wide range of targets was identified to silence breast cancer cells including Src kinase in MDA-MB-231, anti-apoptosis Mcl-1 in the MDA-MB-435 to name a few [14]. The efficacy of siRNA molecules depends on an effective delivery system that can transport siRNA into cells and release it into cytoplasm to exert its effect. A new

dataset can be built using our current descriptors with the addition of cellular uptake as a new descriptor. The new target for model prediction is the silencing efficiency of PEI/siRNA NPs. Such a model can provide valuable information in terms of polymer modification with the purpose of better delivery vector for silencing the target proteins.

7.3. References

- [1] D. P. Tieleman, H. Leontiadou, A. E. Mark, and S.-J. Marrink, "Simulation of Pore Formation in Lipid Bilayers by Mechanical Stress and Electric Fields," *J. Am. Chem. Soc.*, vol. 125, no. 21, pp. 6382–6383, May 2003, doi: 10.1021/ja029504i.
- [2] M. Sud *et al.*, "LMSD: LIPID MAPS structure database," *Nucleic Acids Res.*, vol. 35, no. suppl_1, pp. D527–D532, Nov. 2006, doi: 10.1093/nar/gkl838.
- [3] P. A. Leventis and S. Grinstein, "The Distribution and Function of Phosphatidylserine in Cellular Membranes," *Annu. Rev. Biophys.*, vol. 39, pp. 407–427, 2010, doi: 10.1146/annurev.biophys.093008.131234.
- [4] F.-X. Contreras, L. Sánchez-Magraner, A. Alonso, and F. M. Goñi, "Transbilayer (flip-flop) lipid motion and lipid scrambling in membranes," *FEBS Lett.*, vol. 584, no. 9, pp. 1779–1786, May 2010, doi: 10.1016/j.febslet.2009.12.049.
- [5] G. Van Meer, D. R. Voelker, and G. W. Feigenson, "Membrane lipids: Where they are and how they behave," *Nat. Rev. Mol. Cell Biol.*, vol. 9, no. 2, pp. 112–124, 2008, doi: 10.1038/nrm2330.
- [6] S. J. Marrink, V. Corradi, P. C. T. Souza, H. I. Ingólfsson, D. P. Tieleman, and M. S. P. Sansom, "Computational Modeling of Realistic Cell Membranes," *Chem. Rev.*, vol. 119, no. 9, pp. 6184–6226, May 2019, doi: 10.1021/acs.chemrev.8b00460.
- [7] R. A. Schlegel and P. Williamson, "Phosphatidylserine, a death knell," *Cell Death Differ.*, vol. 8, no. 6, pp. 551–563, 2001.
- [8] J. Razzokov, M. Yusupov, S. Vanuytsel, E. C. Neyts, and A. Bogaerts, "Phosphatidylserine flip-flop induced by oxidation of the plasma membrane: a better insight by atomic scale modeling," *Plasma Process. Polym.*, vol. 14, no. 10, pp. 1–6, 2017, doi: 10.1002/ppap.201700013.
- [9] H. M. Aliabadi, B. Landry, C. Sun, T. Tang, and H. Uludağ, "Supramolecular assemblies in functional siRNA delivery: where do we stand?," *Biomaterials*, vol. 33, no. 8, pp. 2546–2569, 2012.
- [10] Y. Sugita and Y. Okamoto, "Replica-exchange molecular dynamics method for protein folding," *Chem. Phys. Lett.*, vol. 314, no. 1–2, pp. 141–151, 1999.
- [11] S. Park, F. Khalili-Araghi, E. Tajkhorshid, and K. Schulten, "Free energy calculation from

steered molecular dynamics simulations using Jarzynski's equality," *J. Chem. Phys.*, vol. 119, no. 6, pp. 3559–3566, Aug. 2003, doi: 10.1063/1.1590311.

[12] C. Tsallis and D. A. Stariolo, "Generalized simulated annealing," *Phys. A Stat. Mech. its Appl.*, vol. 233, no. 1–2, pp. 395–406, 1996.

[13] M. Levitt, "A simplified representation of protein conformations for rapid simulation of protein folding," *J. Mol. Biol.*, vol. 104, no. 1, pp. 59–107, 1976.

[14] H. M. Aliabadi *et al.*, "A systematic comparison of lipopolymers for siRNA delivery to multiple breast cancer cell lines: In vitro studies," *Acta Biomater.*, vol. 102, pp. 351–366, 2020.

Unified Bibliography

- [1.1] H. M. Aliabadi, B. Landry, C. Sun, T. Tang, and H. Uludağ, “Supramolecular assemblies in functional siRNA delivery: where do we stand?,” *Biomaterials*, vol. 33, no. 8, pp. 2546–2569, 2012.
- [2.1] H. Ding and Y. Ma, “Theoretical and Computational Investigations of Nanoparticle-Biomembrane Interactions in Cellular Delivery,” *Small*, vol. 11, no. 9–10, pp. 1055–1071, Mar. 2015, doi: 10.1002/sml.201401943.
- [2.2] A. A. Gurtovenko, J. Anwar, and I. Vattulainen, “Defect-mediated trafficking across cell membranes: insights from in silico modeling,” *Chem. Rev.*, vol. 110, no. 10, pp. 6077–6103, 2010.
- [2.3] H. Nakamura and S. Watano, “Direct Permeation of Nanoparticles across Cell Membrane: A Review,” *KONA Powder Part. J.*, vol. 35, no. 35, pp. 49–65, 2018, doi: 10.14356/kona.2018011.
- [2.4] I. a Khalil, K. Kogure, H. Akita, and H. Harashima, “Uptake pathways and subsequent intracellular trafficking in nonviral gene delivery.,” *Pharmacol. Rev.*, vol. 58, no. 1, pp. 32–45, Mar. 2006, doi: 10.1124/pr.58.1.8.
- [2.5] S. Zhang, H. Gao, and G. Bao, “Physical Principles of Nanoparticle Cellular Endocytosis,” *ACS Nano*, vol. 9, no. 9, pp. 8655–8671, Sep. 2015, doi: 10.1021/acs.nano.5b03184.
- [2.6] G. Sahay, D. Y. Alakhova, and A. V. Kabanov, “Endocytosis of nanomedicines,” *J. Control. Release*, vol. 145, no. 3, pp. 182–195, Aug. 2010, doi: 10.1016/j.jconrel.2010.01.036.
- [2.7] L. Kou, J. Sun, Y. Zhai, and Z. He, “The endocytosis and intracellular fate of nanomedicines: Implication for rational design,” *Asian J. Pharm. Sci.*, vol. 8, no. 1, pp. 1–8, 2013, doi: 10.1016/j.ajps.2013.07.001.
- [2.8] A. Aderem and D. M. Underhill, “MECHANISMS OF PHAGOCYTOSIS IN MACROPHAGES,” *Annu. Rev. Immunol.*, vol. 17, no. 1, pp. 593–623, Apr. 1999, doi: 10.1146/annurev.immunol.17.1.593.
- [2.9] S. Xiang *et al.*, “Uptake mechanisms of non-viral gene delivery,” *J. Control. Release*, vol. 158, no. 3, pp. 371–378, Mar. 2012, doi: 10.1016/j.jconrel.2011.09.093.
- [2.10] J. P. Lim and P. A. Gleeson, “Macropinocytosis: an endocytic pathway for internalising large gulps,” *Immunol. Cell Biol.*, vol. 89, no. 8, pp. 836–843, Nov. 2011, doi: 10.1038/icb.2011.20.
- [2.11] S. Falcone, E. Cocucci, P. Podini, T. Kirchhausen, E. Clementi, and J. Meldolesi, “Macropinocytosis: regulated coordination of endocytic and exocytic membrane traffic events,” *J. Cell Sci.*, vol. 119, no. 22, pp. 4758–4769, 2006, doi: 10.1242/jcs.03238.

- [2.12] M. Hamasaki, N. Araki, and T. Hatae, “Association of early endosomal autoantigen 1 with macropinocytosis in EGF-stimulated a431 cells,” *Anat. Rec.*, vol. 277A, no. 2, pp. 298–306, Apr. 2004, doi: 10.1002/ar.a.20027.
- [2.13] S. D. Conner and S. L. Schmid, “Regulated portals of entry into the cell,” *Nature*, vol. 422, no. 6927, pp. 37–44, Mar. 2003, doi: 10.1038/nature01451.
- [2.14] J. Z. Rappoport, “Focusing on clathrin-mediated endocytosis,” *Biochem. J.*, vol. 412, no. 3, pp. 415–423, Jun. 2008, doi: 10.1042/BJ20080474.
- [2.15] J. REJMAN, V. OBERLE, I. S. ZUHORN, and D. HOEKSTRA, “Size-dependent internalization of particles via the pathways of clathrin- and caveolae-mediated endocytosis,” *Biochem. J.*, vol. 377, no. 1, pp. 159–169, Jan. 2004, doi: 10.1042/bj20031253.
- [2.16] H. Hillaireau and P. Couvreur, “Nanocarriers’ entry into the cell: relevance to drug delivery,” *Cell. Mol. Life Sci.*, vol. 66, no. 17, pp. 2873–2896, Sep. 2009, doi: 10.1007/s00018-009-0053-z.
- [2.17] L. BAREFORD and P. SWAAN, “Endocytic mechanisms for targeted drug delivery☆,” *Adv. Drug Deliv. Rev.*, vol. 59, no. 8, pp. 748–758, Aug. 2007, doi: 10.1016/j.addr.2007.06.008.
- [2.18] G. J. Doherty and H. T. McMahon, “Mechanisms of Endocytosis,” *Annu. Rev. Biochem.*, vol. 78, no. 1, pp. 857–902, Jun. 2009, doi: 10.1146/annurev.biochem.78.081307.110540.
- [2.19] S. Y. Wong, J. M. Pelet, and D. Putnam, “Polymer systems for gene delivery—Past, present, and future,” *Prog. Polym. Sci.*, vol. 32, no. 8–9, pp. 799–837, Aug. 2007, doi: 10.1016/j.progpolymsci.2007.05.007.
- [2.20] C. Pichon, L. Billiet, and P. Midoux, “Chemical vectors for gene delivery: uptake and intracellular trafficking,” *Curr. Opin. Biotechnol.*, vol. 21, no. 5, pp. 640–645, Oct. 2010, doi: 10.1016/j.copbio.2010.07.003.
- [2.21] I. Kopatz, J.-S. Remy, and J.-P. Behr, “A model for non-viral gene delivery: through syndecan adhesion molecules and powered by actin,” *J. Gene Med.*, vol. 6, no. 7, pp. 769–776, Jul. 2004, doi: 10.1002/jgm.558.
- [2.22] J. L. Dreyfuss, C. V. Regatieri, T. R. Jarrouge, R. P. Cavalheiro, L. O. Sampaio, and H. B. Nader, “Heparan sulfate proteoglycans: structure, protein interactions and cell signaling,” *An. Acad. Bras. Cienc.*, vol. 81, no. 3, pp. 409–429, Sep. 2009, doi: 10.1590/S0001-37652009000300007.
- [2.23] D. Frenkel, B. Smit, and M. A. Ratner, “Understanding Molecular Simulation: From Algorithms to Applications,” *Phys. Today*, vol. 50, no. 7, pp. 66–66, Jul. 1997, doi: 10.1063/1.881812.
- [2.24] F. Tian, T. Yue, Y. Li, and X. Zhang, “Computer simulation studies on the interactions between nanoparticles and cell membrane,” *Sci. China Chem.*, vol. 57, no. 12, pp. 1662–1671, Dec. 2014, doi: 10.1007/s11426-014-5231-7.

- [2.25] G. Rossi and L. Monticelli, “Simulating the interaction of lipid membranes with polymer and ligand-coated nanoparticles,” *Adv. Phys. X*, vol. 1, no. 2, pp. 276–296, Mar. 2016, doi: 10.1080/23746149.2016.1177468.
- [2.26] C. M. Beddoes, C. P. Case, and W. H. Briscoe, “Understanding nanoparticle cellular entry: A physicochemical perspective,” *Adv. Colloid Interface Sci.*, vol. 218, pp. 48–68, Apr. 2015, doi: 10.1016/j.cis.2015.01.007.
- [2.27] D. Meneksedag-Erol, T. Tang, and H. Uludağ, “Molecular modeling of polynucleotide complexes,” *Biomaterials*, vol. 35, no. 25, pp. 7068–7076, Aug. 2014, doi: 10.1016/j.biomaterials.2014.04.103.
- [2.28] S. J. Marrink, A. H. de Vries, and D. P. Tieleman, “Lipids on the move: Simulations of membrane pores, domains, stalks and curves,” *Biochim. Biophys. Acta - Biomembr.*, vol. 1788, no. 1, pp. 149–168, Jan. 2009, doi: 10.1016/j.bbamem.2008.10.006.
- [2.29] S. J. Marrink, H. J. Risselada, S. Yefimov, D. P. Tieleman, and A. H. De Vries, “The MARTINI force field: coarse grained model for biomolecular simulations,” *J. Phys. Chem. B*, vol. 111, no. 27, pp. 7812–7824, 2007.
- [2.30] P. J. Hoogerbrugge and J. M. V. A. Koelman, “Simulating Microscopic Hydrodynamic Phenomena with Dissipative Particle Dynamics,” *Europhys. Lett.*, vol. 19, no. 3, pp. 155–160, Jun. 1992, doi: 10.1209/0295-5075/19/3/001.
- [2.31] R. D. Groot and P. B. Warren, “Dissipative particle dynamics: Bridging the gap between atomistic and mesoscopic simulation,” *J. Chem. Phys.*, vol. 107, no. 11, pp. 4423–4435, Sep. 1997, doi: 10.1063/1.474784.
- [2.32] P. L. Yeagle, *The structure of biological membranes*. CRC press, 2011.
- [2.33] K. Simons and E. Ikonen, “Functional rafts in cell membranes,” *Nature*, vol. 387, no. 6633, p. 569, 1997.
- [2.34] K. Simons and W. L. C. Vaz, “Model systems, lipid rafts, and cell membranes,” *Annu. Rev. Biophys. Biomol. Struct.*, vol. 33, pp. 269–295, 2004.
- [2.35] E. Sezgin, I. Levental, S. Mayor, and C. Eggeling, “The mystery of membrane organization: composition, regulation and roles of lipid rafts,” *Nat. Rev. Mol. Cell Biol.*, vol. 18, no. 6, pp. 361–374, Mar. 2017, doi: 10.1038/nrm.2017.16.
- [2.36] E. Rascol, J.-M. Devoisselle, and J. Chopineau, “The relevance of membrane models to understand nanoparticles–cell membrane interactions,” *Nanoscale*, vol. 8, no. 9, pp. 4780–4798, 2016, doi: 10.1039/C5NR07954C.
- [2.37] M. VENTUROLI, M. MADDALENASPEROTTO, M. KRANENBURG, and B. SMIT, “Mesoscopic models of biological membranes,” *Phys. Rep.*, vol. 437, no. 1–2, pp. 1–54, Dec. 2006, doi: 10.1016/j.physrep.2006.07.006.
- [2.38] G. Van Meer, D. R. Voelker, and G. W. Feigenson, “Membrane lipids: Where they are and how they behave,” *Nat. Rev. Mol. Cell Biol.*, vol. 9, no. 2, pp. 112–124, 2008, doi:

10.1038/nrm2330.

- [2.39] J. A. McCammon and Y. Wang, “Lipid Bilayers: Structure, Dynamics, and Interactions with Antimicrobial Peptides,” in *Molecular Modeling at the Atomic Scale*, CRC Press, 2014, pp. 210–233.
- [2.40] I. Chandrasekhar *et al.*, “A consistent potential energy parameter set for lipids: dipalmitoylphosphatidylcholine as a benchmark of the GROMOS96 45A3 force field,” *Eur. Biophys. J.*, vol. 32, no. 1, pp. 67–77, 2003.
- [2.41] L. D. Schuler, X. Daura, and W. F. Van Gunsteren, “An improved GROMOS96 force field for aliphatic hydrocarbons in the condensed phase,” *J. Comput. Chem.*, vol. 22, no. 11, pp. 1205–1218, 2001.
- [2.42] J. B. Klauda *et al.*, “Update of the CHARMM all-atom additive force field for lipids: validation on six lipid types,” *J. Phys. Chem. B*, vol. 114, no. 23, pp. 7830–7843, Jun. 2010, doi: 10.1021/jp101759q.
- [2.43] S. J. Marrink, A. H. De Vries, and A. E. Mark, “Coarse grained model for semiquantitative lipid simulations,” *J. Phys. Chem. B*, vol. 108, no. 2, pp. 750–760, 2004.
- [2.44] I. R. Cooke, K. Kremer, and M. Deserno, “Tunable generic model for fluid bilayer membranes,” *Phys. Rev. E*, vol. 72, no. 1, p. 11506, 2005.
- [2.45] A. E. Nel *et al.*, “Understanding biophysicochemical interactions at the nano–bio interface,” *Nat. Mater.*, vol. 8, no. 7, pp. 543–557, Jul. 2009, doi: 10.1038/nmat2442.
- [2.46] M. Deserno and T. Bickel, “Wrapping of a spherical colloid by a fluid membrane,” *Europhys. Lett.*, vol. 62, no. 5, pp. 767–774, Jun. 2003, doi: 10.1209/epl/i2003-00438-4.
- [2.47] M. Deserno, “Elastic deformation of a fluid membrane upon colloid binding,” *Phys. Rev. E*, vol. 69, no. 3, pp. 1–14, 2004, doi: 10.1103/PhysRevE.69.031903.
- [2.48] B. J. Reynwar, G. Illya, V. A. Harmandaris, M. M. Müller, K. Kremer, and M. Deserno, “Aggregation and vesiculation of membrane proteins by curvature-mediated interactions,” *Nature*, vol. 447, no. 7143, pp. 461–464, May 2007, doi: 10.1038/nature05840.
- [2.49] W. Helfrich, J. Charvolin, J. F. Joanny, and J. Zinn-Justin, “Liquids at interfaces,” *Les Houches Sess. XLVIII*, 1990.
- [2.50] W. Helfrich, “Elastic properties of lipid membranes: theory and possible experiments,” *Zeitschrift für Naturforsch. C*, vol. 28, p. 693703, 1973.
- [2.51] A. H. Bahrami, R. Lipowsky, and T. R. Weikl, “The role of membrane curvature for the wrapping of nanoparticles,” *Soft Matter*, vol. 12, no. 2, pp. 581–587, 2016, doi: 10.1039/C5SM01793A.
- [2.52] R. Vácha, F. J. Martinez-Veracoechea, and D. Frenkel, “Receptor-Mediated Endocytosis of Nanoparticles of Various Shapes,” *Nano Lett.*, vol. 11, no. 12, pp. 5391–5395, Dec. 2011, doi: 10.1021/nl2030213.

- [2.53] T. Yue and X. Zhang, “Molecular understanding of receptor-mediated membrane responses to ligand-coated nanoparticles,” *Soft Matter*, vol. 7, no. 19, p. 9104, 2011, doi: 10.1039/c1sm05398a.
- [2.54] H. Ding, W. Tian, and Y. Ma, “Designing Nanoparticle Translocation through Membranes by Computer Simulations,” *ACS Nano*, vol. 6, no. 2, pp. 1230–1238, Feb. 2012, doi: 10.1021/nn2038862.
- [2.55] T. Yue, X. Zhang, and F. Huang, “Molecular modeling of membrane responses to the adsorption of rotating nanoparticles: promoted cell uptake and mechanical membrane rupture,” *Soft Matter*, vol. 11, no. 3, pp. 456–465, 2015, doi: 10.1039/C4SM01760A.
- [2.56] X. Lin, Y. Li, and N. Gu, “Nanoparticle’s Size Effect on Its Translocation Across a Lipid Bilayer: A Molecular Dynamics Simulation,” *J. Comput. Theor. Nanosci.*, vol. 7, no. 1, pp. 269–276, Jan. 2010, doi: 10.1166/jctn.2010.1358.
- [2.57] E. M. Curtis, A. H. Bahrami, T. R. Weigl, and C. K. Hall, “Modeling nanoparticle wrapping or translocation in bilayer membranes,” *Nanoscale*, vol. 7, no. 34, pp. 14505–14514, 2015, doi: 10.1039/C5NR02255J.
- [2.58] X. Chen, F. Tian, X. Zhang, and W. Wang, “Internalization pathways of nanoparticles and their interaction with a vesicle,” *Soft Matter*, vol. 9, no. 31, p. 7592, 2013, doi: 10.1039/c3sm50931a.
- [2.59] E. Zhang, M. F. Kircher, M. Koch, L. Eliasson, S. N. Goldberg, and E. Renström, “Dynamic Magnetic Fields Remote-Control Apoptosis via Nanoparticle Rotation,” *ACS Nano*, vol. 8, no. 4, pp. 3192–3201, Apr. 2014, doi: 10.1021/nn406302j.
- [2.60] K. Yang and Y.-Q. Ma, “Computer simulation of the translocation of nanoparticles with different shapes across a lipid bilayer,” *Nat. Nanotechnol.*, vol. 5, no. 8, pp. 579–583, Aug. 2010, doi: 10.1038/nnano.2010.141.
- [2.61] H. Ding and Y. Ma, “Interactions between Janus particles and membranes,” *Nanoscale*, vol. 4, no. 4, pp. 1116–1122, 2012, doi: 10.1039/C1NR11425E.
- [2.62] H. Gao, W. Shi, and L. B. Freund, “Mechanics of receptor-mediated endocytosis,” *Proc. Natl. Acad. Sci.*, vol. 102, no. 27, pp. 9469–9474, Jul. 2005, doi: 10.1073/pnas.0503879102.
- [2.63] V. B. Shenoy and L. B. Freund, “Growth and shape stability of a biological membrane adhesion complex in the diffusion-mediated regime,” *Proc. Natl. Acad. Sci.*, vol. 102, no. 9, pp. 3213–3218, Mar. 2005, doi: 10.1073/pnas.0500368102.
- [2.64] S. Tzlil, M. Deserno, W. M. Gelbart, and A. Ben-Shaul, “A Statistical-Thermodynamic Model of Viral Budding,” *Biophys. J.*, vol. 86, no. 4, pp. 2037–2048, Apr. 2004, doi: 10.1016/S0006-3495(04)74265-4.
- [2.65] A. Albanese, P. S. Tang, and W. C. W. Chan, “The Effect of Nanoparticle Size, Shape, and Surface Chemistry on Biological Systems,” *Annu. Rev. Biomed. Eng.*, vol. 14, no. 1, pp. 1–16, Aug. 2012, doi: 10.1146/annurev-bioeng-071811-150124.

- [2.66] S. E. A. Gratton *et al.*, “The effect of particle design on cellular internalization pathways,” *Proc. Natl. Acad. Sci.*, vol. 105, no. 33, pp. 11613–11618, Aug. 2008, doi: 10.1073/pnas.0801763105.
- [2.67] B. D. Chithrani, A. A. Ghazani, and W. C. W. Chan, “Determining the Size and Shape Dependence of Gold Nanoparticle Uptake into Mammalian Cells,” *Nano Lett.*, vol. 6, no. 4, pp. 662–668, Apr. 2006, doi: 10.1021/nl052396o.
- [2.68] Y. Liu, B. Peng, S. Sohrabi, and Y. Liu, “The Configuration of Copolymer Ligands on Nanoparticles Affects Adhesion and Uptake,” *Langmuir*, vol. 32, no. 39, pp. 10136–10143, Oct. 2016, doi: 10.1021/acs.langmuir.6b02371.
- [2.69] V. Schubertová, F. J. Martinez-Veracoechea, and R. Vácha, “Influence of ligand distribution on uptake efficiency,” *Soft Matter*, vol. 11, no. 14, pp. 2726–2730, 2015, doi: 10.1039/C4SM02815E.
- [2.70] S. Nangia and R. Sureshkumar, “Effects of Nanoparticle Charge and Shape Anisotropy on Translocation through Cell Membranes,” *Langmuir*, vol. 28, no. 51, pp. 17666–17671, Dec. 2012, doi: 10.1021/la303449d.
- [2.71] K. Yang and Y. Ma, “Wrapping and Internalization of Nanoparticles by Lipid Bilayers: a Computer Simulation Study,” *Aust. J. Chem.*, vol. 64, no. 7, p. 894, 2011, doi: 10.1071/CH11053.
- [2.72] Y. Li, T. Yue, K. Yang, and X. Zhang, “Molecular modeling of the relationship between nanoparticle shape anisotropy and endocytosis kinetics,” *Biomaterials*, vol. 33, no. 19, pp. 4965–4973, Jun. 2012, doi: 10.1016/j.biomaterials.2012.03.044.
- [2.73] J. Li *et al.*, “Why synthetic virus-like nanoparticles can achieve higher cellular uptake efficiency?,” *Nanoscale*, vol. 12, no. 27, pp. 14911–14918, 2020.
- [2.74] C. Huang, Y. Zhang, H. Yuan, H. Gao, and S. Zhang, “Role of Nanoparticle Geometry in Endocytosis: Laying Down to Stand Up,” *Nano Lett.*, vol. 13, no. 9, pp. 4546–4550, Sep. 2013, doi: 10.1021/nl402628n.
- [2.75] L. Zhang, Y. Zhao, and X. Wang, “Nanoparticle-mediated mechanical destruction of cell membranes: A coarse-grained molecular dynamics study,” *ACS Appl. Mater. Interfaces*, vol. 9, no. 32, pp. 26665–26673, 2017.
- [2.76] Y. Li, X. Chen, and N. Gu, “Computational Investigation of Interaction between Nanoparticles and Membranes: Hydrophobic/Hydrophilic Effect,” *J. Phys. Chem. B*, vol. 112, no. 51, pp. 16647–16653, Dec. 2008, doi: 10.1021/jp8051906.
- [2.77] A. Verma and F. Stellacci, “Effect of Surface Properties on Nanoparticle Cell Interactions,” *Small*, vol. 6, no. 1, pp. 12–21, Jan. 2010, doi: 10.1002/sml.200901158.
- [2.78] M. Werner, J.-U. U. Sommer, and V. A. Baulin, “Homo-polymers with balanced hydrophobicity translocate through lipid bilayers and enhance local solvent permeability,” *Soft Matter*, vol. 8, no. 46, p. 11714, 2012, doi: 10.1039/c2sm26008e.

- [2.79] Y. Li, X. Li, Z. Li, and H. Gao, “Surface-structure-regulated penetration of nanoparticles across a cell membrane,” *Nanoscale*, vol. 4, no. 12, pp. 3768–3775, 2012, doi: 10.1039/c2nr30379e.
- [2.80] S. Wang, H. Guo, Y. Li, and X. Li, “Penetration of nanoparticles across a lipid bilayer: effects of particle stiffness and surface hydrophobicity,” *Nanoscale*, vol. 11, no. 9, pp. 4025–4034, 2019.
- [2.81] N. Arai, K. Yasuoka, and X. C. Zeng, “A vesicle cell under collision with a Janus or homogeneous nanoparticle: translocation dynamics and late-stage morphology,” *Nanoscale*, vol. 5, no. 19, pp. 9089–9100, 2013.
- [2.82] A. C. Balazs, O. Kuksenok, and A. Alexeev, “Modeling the Interactions between Membranes and Inclusions: Designing Self-Cleaning Films and Resealing Pores,” *Macromol. Theory Simulations*, vol. 18, no. 1, pp. 11–24, 2009.
- [2.83] A. Alexeev, W. E. Uspal, and A. C. Balazs, “Harnessing Janus nanoparticles to create controllable pores in membranes,” *ACS Nano*, vol. 2, no. 6, pp. 1117–1122, 2008.
- [2.84] L. Zhang, M. Becton, and X. Wang, “Designing Nanoparticle Translocation through Cell Membranes by Varying Amphiphilic Polymer Coatings,” *J. Phys. Chem. B*, vol. 119, no. 9, pp. 3786–3794, Mar. 2015, doi: 10.1021/acs.jpcc.5b00825.
- [2.85] Y. Liu *et al.*, “Design of small nanoparticles decorated with amphiphilic ligands: self-preservation effect and translocation into a plasma membrane,” *ACS Appl. Mater. Interfaces*, vol. 11, no. 27, pp. 23822–23831, 2019.
- [2.86] H. Ding and Y. Ma, “Controlling Cellular Uptake of Nanoparticles with pH-Sensitive Polymers,” *Sci. Rep.*, vol. 3, no. 1, p. 2804, Dec. 2013, doi: 10.1038/srep02804.
- [2.87] H. Ding and Y. Ma, “Role of physicochemical properties of coating ligands in receptor-mediated endocytosis of nanoparticles,” *Biomaterials*, vol. 33, no. 23, pp. 5798–5802, Aug. 2012, doi: 10.1016/j.biomaterials.2012.04.055.
- [2.88] H. Yuan and S. Zhang, “Effects of particle size and ligand density on the kinetics of receptor-mediated endocytosis of nanoparticles,” *Appl. Phys. Lett.*, vol. 96, no. 3, p. 033704, Jan. 2010, doi: 10.1063/1.3293303.
- [2.89] Q. Xia, H. Ding, and Y. Ma, “Can dual-ligand targeting enhance cellular uptake of nanoparticles?,” *Nanoscale*, vol. 9, no. 26, pp. 8982–8989, 2017, doi: 10.1039/C7NR01020F.
- [2.90] J. Xue, Z. Guan, J. Lin, C. Cai, W. Zhang, and X. Jiang, “Cellular Internalization of Rod-Like Nanoparticles with Various Surface Patterns: Novel Entry Pathway and Controllable Uptake Capacity,” *small*, vol. 13, no. 24, p. 1604214, 2017.
- [2.91] Z. Shen, H. Ye, and Y. Li, “Understanding receptor-mediated endocytosis of elastic nanoparticles through coarse grained molecular dynamic simulation,” *Phys. Chem. Chem. Phys.*, vol. 20, no. 24, pp. 16372–16385, 2018.

- [2.92] D. F. Hayes *et al.*, “Circulating tumor cells at each follow-up time point during therapy of metastatic breast cancer patients predict progression-free and overall survival,” *Clin. Cancer Res.*, vol. 12, no. 14, pp. 4218–4224, 2006.
- [2.93] L. Huang, Y. Yu, X. Lu, H. Ding, and Y. Ma, “Designing a nanoparticle-containing polymeric substrate for detecting cancer cells by computer simulations,” *Nanoscale*, vol. 11, no. 5, pp. 2170–2178, 2019.
- [2.94] Q. Xia, T. Zhu, Z. Jiang, H. Ding, and Y. Ma, “Enhancing the targeting ability of nanoparticles via protected copolymers,” *Nanoscale*, vol. 12, no. 14, pp. 7804–7813, 2020.
- [2.95] B. Kharazian, N. L. Hadipour, and M. R. Ejtehad, “Understanding the nanoparticle–protein corona complexes using computational and experimental methods,” *Int. J. Biochem. Cell Biol.*, vol. 75, pp. 162–174, Jun. 2016, doi: 10.1016/j.biocel.2016.02.008.
- [2.96] C. C. Fleischer and C. K. Payne, “Nanoparticle–Cell Interactions: Molecular Structure of the Protein Corona and Cellular Outcomes,” *Acc. Chem. Res.*, vol. 47, no. 8, pp. 2651–2659, Aug. 2014, doi: 10.1021/ar500190q.
- [2.97] S.-T. Yang, Y. Liu, Y.-W. Wang, and A. Cao, “Biosafety and Bioapplication of Nanomaterials by Designing Protein-Nanoparticle Interactions,” *Small*, vol. 9, no. 9–10, pp. 1635–1653, May 2013, doi: 10.1002/smll.201201492.
- [2.98] S. Behzadi *et al.*, “Protein corona change the drug release profile of nanocarriers: The ‘overlooked’ factor at the nanobio interface,” *Colloids Surfaces B Biointerfaces*, vol. 123, pp. 143–149, Nov. 2014, doi: 10.1016/j.colsurfb.2014.09.009.
- [2.99] M. Mahmoudi *et al.*, “Temperature: The ‘Ignored’ Factor at the NanoBio Interface,” *ACS Nano*, vol. 7, no. 8, pp. 6555–6562, Aug. 2013, doi: 10.1021/nm305337c.
- [2.100] A. Lesniak, F. Fenaroli, M. P. Monopoli, C. Åberg, K. A. Dawson, and A. Salvati, “Effects of the Presence or Absence of a Protein Corona on Silica Nanoparticle Uptake and Impact on Cells,” *ACS Nano*, vol. 6, no. 7, pp. 5845–5857, Jul. 2012, doi: 10.1021/nm300223w.
- [2.101] H. Ding and Y. Ma, “Design strategy of surface decoration for efficient delivery of nanoparticles by computer simulation,” *Sci. Rep.*, vol. 6, no. May, p. 26783, May 2016, doi: 10.1038/srep26783.
- [2.102] H. Ding and Y. Ma, “Computer simulation of the role of protein corona in cellular delivery of nanoparticles,” *Biomaterials*, vol. 35, no. 30, pp. 8703–8710, Oct. 2014, doi: 10.1016/j.biomaterials.2014.06.033.
- [2.103] T. Yue and X. Zhang, “Cooperative Effect in Receptor-Mediated Endocytosis of Multiple Nanoparticles,” *ACS Nano*, vol. 6, no. 4, pp. 3196–3205, Apr. 2012, doi: 10.1021/nm205125e.
- [2.104] T. Yue, X. Wang, F. Huang, and X. Zhang, “An unusual pathway for the membrane wrapping of rodlike nanoparticles and the orientation- and membrane wrapping-dependent nanoparticle interaction,” *Nanoscale*, vol. 5, no. 20, p. 9888, 2013, doi: 10.1039/c3nr02683c.

- [2.105]K. Xiong, J. Zhao, D. Yang, Q. Cheng, J. Wang, and H. Ji, “Cooperative wrapping of nanoparticles of various sizes and shapes by lipid membranes,” *Soft Matter*, vol. 13, no. 26, pp. 4644–4652, 2017, doi: 10.1039/C7SM00345E.
- [2.106]A. H. Bahrami, R. Lipowsky, and T. R. Weikl, “Tubulation and Aggregation of Spherical Nanoparticles Adsorbed on Vesicles,” *Phys. Rev. Lett.*, vol. 109, no. 18, p. 188102, Oct. 2012, doi: 10.1103/PhysRevLett.109.188102.
- [2.107]Z. Yan, Z. Wu, S. Li, X. Zhang, X. Yi, and T. Yue, “Curvature-mediated cooperative wrapping of multiple nanoparticles at the same and opposite membrane sides,” *Nanoscale*, vol. 11, no. 42, pp. 19751–19762, 2019.
- [2.108]S. Ni, Y. Yin, X. Li, H. Ding, and Y. Ma, “Controlling the Interaction of Nanoparticles with Cell Membranes by the Polymeric Tether,” *Langmuir*, vol. 35, no. 39, pp. 12851–12857, 2019.
- [2.109]K. A. Smith, D. Jasnow, and A. C. Balazs, “Designing synthetic vesicles that engulf nanoscopic particles,” *J. Chem. Phys.*, vol. 127, no. 8, p. 084703, Aug. 2007, doi: 10.1063/1.2766953.
- [2.110]S. L. Veatch and S. L. Keller, “Separation of Liquid Phases in Giant Vesicles of Ternary Mixtures of Phospholipids and Cholesterol,” *Biophys. J.*, vol. 85, no. 5, pp. 3074–3083, Nov. 2003, doi: 10.1016/S0006-3495(03)74726-2.
- [2.111]X. Lin, X. Lin, and N. Gu, “Optimization of hydrophobic nanoparticles to better target lipid rafts with molecular dynamics simulations,” *Nanoscale*, vol. 12, no. 6, pp. 4101–4109, 2020.
- [2.112]K. Yang *et al.*, “Partitioning of nanoscale particles on a heterogeneous multicomponent lipid bilayer,” *Phys. Chem. Chem. Phys.*, vol. 20, no. 44, pp. 28241–28248, 2018.
- [2.113]D. Allan Butterfield, “Amyloid β -peptide (1-42)-induced oxidative stress and neurotoxicity: implications for neurodegeneration in Alzheimer’s disease brain. A review,” *Free Radic. Res.*, vol. 36, no. 12, pp. 1307–1313, 2002.
- [2.114]C.-F. Su, H. Merlitz, F. Thalmann, C. Marques, and J.-U. Sommer, “Coarse-Grained Model of Oxidized Membranes and Their Interactions with Nanoparticles of Various Degrees of Hydrophobicity,” *J. Phys. Chem. C*, vol. 123, no. 11, pp. 6839–6848, 2019.
- [2.115]H. Aceves-Luna, D. Glossman-Mitnik, and N. Flores-Holguín, “Oxidation degree of a cell membrane model and its response to structural changes, a coarse-grained molecular dynamics approach,” *J. Biomol. Struct. Dyn.*, vol. 0, no. 0, pp. 1–12, 2020, doi: 10.1080/07391102.2020.1833759.
- [2.116]J. Zimmerberg and M. M. Kozlov, “How proteins produce cellular membrane curvature,” *Nat. Rev. Mol. Cell Biol.*, vol. 7, no. 1, pp. 9–19, Jan. 2006, doi: 10.1038/nrm1784.
- [2.117]Y. Nademi, T. Tang, and H. Uludağ, “Steered molecular dynamics simulations reveal a self-protecting configuration of nanoparticles during membrane penetration,” *Nanoscale*, vol. 10, no. 37, pp. 17671–17682, 2018, doi: 10.1039/C8NR04287J.

- [2.118] C. K. Choudhury, A. Kumar, and S. Roy, "Characterization of Conformation and Interaction of Gene Delivery Vector Polyethylenimine with Phospholipid Bilayer at Different Protonation State," *Biomacromolecules*, vol. 14, no. 10, pp. 3759–3768, Oct. 2013, doi: 10.1021/bm4011408.
- [2.119] U. Kwolek, D. Jamroz, M. Janiczek, M. Nowakowska, P. Wydro, and M. Kepczynski, "Interactions of Polyethylenimines with Zwitterionic and Anionic Lipid Membranes," *Langmuir*, vol. 32, no. 19, pp. 5004–5018, May 2016, doi: 10.1021/acs.langmuir.6b00490.
- [2.120] A. Y. Antipina and A. A. Gurtovenko, "Molecular-level insight into the interactions of DNA with phospholipid bilayers: barriers and triggers," *RSC Adv.*, vol. 6, no. 43, pp. 36425–36432, 2016, doi: 10.1039/C6RA05607E.
- [2.121] C. Sun, T. Tang, H. Uludağ, and J. E. Cuervo, "Molecular dynamics simulations of DNA/PEI complexes: Effect of PEI branching and protonation state," *Biophys. J.*, vol. 100, no. 11, pp. 2754–2763, 2011, doi: 10.1016/j.bpj.2011.04.045.
- [2.122] C. Sun, T. Tang, and H. Uludağ, "Molecular Dynamics Simulations for Complexation of DNA with 2 kDa PEI Reveal Profound Effect of PEI Architecture on Complexation," *J. Phys. Chem. B*, vol. 116, no. 8, pp. 2405–2413, Mar. 2012, doi: 10.1021/jp211716v.
- [2.123] D. Meneksedag-Erol, R. B. KC, T. Tang, and H. Uludağ, "A Delicate Balance When Substituting a Small Hydrophobe onto Low Molecular Weight Polyethylenimine to Improve Its Nucleic Acid Delivery Efficiency," *ACS Appl. Mater. Interfaces*, vol. 7, no. 44, pp. 24822–24832, Nov. 2015, doi: 10.1021/acsami.5b07929.
- [2.124] C. Sun, T. Tang, and H. Uludağ, "A molecular dynamics simulation study on the effect of lipid substitution on polyethylenimine mediated siRNA complexation," *Biomaterials*, vol. 34, no. 11, pp. 2822–2833, Apr. 2013, doi: 10.1016/j.biomaterials.2013.01.011.
- [2.125] D. Meneksedag-Erol, T. Tang, and H. Uludağ, "Mechanistic insights into the role of glycosaminoglycans in delivery of polymeric nucleic acid nanoparticles by molecular dynamics simulations," *Biomaterials*, vol. 156, pp. 107–120, Feb. 2018, doi: 10.1016/j.biomaterials.2017.11.037.
- [2.126] D. P. Tieleman, H. Leontiadou, A. E. Mark, and S.-J. Marrink, "Simulation of Pore Formation in Lipid Bilayers by Mechanical Stress and Electric Fields," *J. Am. Chem. Soc.*, vol. 125, no. 21, pp. 6382–6383, May 2003, doi: 10.1021/ja029504i.
- [2.127] M. Sud *et al.*, "LMSD: LIPID MAPS structure database," *Nucleic Acids Res.*, vol. 35, no. suppl_1, pp. D527–D532, Nov. 2006, doi: 10.1093/nar/gkl838.
- [2.128] D. A. Winkler *et al.*, "Modelling and predicting the biological effects of nanomaterials," *SAR QSAR Environ. Res.*, vol. 25, no. 2, pp. 161–172, 2014.
- [3.1] S. M. Elbashir, J. Harborth, W. Lendeckel, A. Yalcin, K. Weber, and T. Tuschl, "Duplexes of 21-nucleotide RNAs mediate RNA interference in cultured mammalian cells," *Nature*, vol. 411, no. 6836, p. 494, 2001.

- [3.2] D. Castanotto and J. J. Rossi, “The promises and pitfalls of RNA-interference-based therapeutics,” *Nature*, vol. 457, no. 7228, p. 426, 2009.
- [3.3] M. Zheng *et al.*, “Targeting the Blind Spot of Polycationic Nanocarrier-Based siRNA Delivery,” *ACS Nano*, vol. 6, no. 11, pp. 9447–9454, Nov. 2012, doi: 10.1021/nn301966r.
- [3.4] A. S. Ansari, P. J. Santerre, and H. Uludağ, “Biomaterials for polynucleotide delivery to anchorage-independent cells,” *J. Mater. Chem. B*, vol. 5, no. 35, pp. 7238–7261, 2017, doi: 10.1039/C7TB01833A.
- [3.5] D. Meneksedag-Erol, T. Tang, and H. Uludağ, “Mechanistic insights into the role of glycosaminoglycans in delivery of polymeric nucleic acid nanoparticles by molecular dynamics simulations,” *Biomaterials*, vol. 156, pp. 107–120, Feb. 2018, doi: 10.1016/j.biomaterials.2017.11.037.
- [3.6] D. Meneksedag-Erol, R. B. KC, T. Tang, and H. Uludağ, “A Delicate Balance When Substituting a Small Hydrophobe onto Low Molecular Weight Polyethylenimine to Improve Its Nucleic Acid Delivery Efficiency,” *ACS Appl. Mater. Interfaces*, vol. 7, no. 44, pp. 24822–24832, Nov. 2015, doi: 10.1021/acsami.5b07929.
- [3.7] D. Fischer, Y. Li, B. Ahlemeyer, J. Krieglstein, and T. Kissel, “In vitro cytotoxicity testing of polycations: influence of polymer structure on cell viability and hemolysis,” *Biomaterials*, vol. 24, pp. 1121–31, 2003, doi: S0142961202004453 [pii].
- [3.8] V. Incani, A. Lavasanifar, and H. Uludağ, “Lipid and hydrophobic modification of cationic carriers on route to superior gene vectors,” *Soft Matter*, vol. 6, no. 10, p. 2124, 2010, doi: 10.1039/b916362j.
- [3.9] H. M. Aliabadi, B. Landry, R. K. Bahadur, A. Neamark, O. Suwantong, and H. Uludağ, “Impact of Lipid Substitution on Assembly and Delivery of siRNA by Cationic Polymers,” *Macromol. Biosci.*, vol. 11, no. 5, pp. 662–672, May 2011, doi: 10.1002/mabi.201000402.
- [3.10] H. Ding and Y. Ma, “Theoretical and Computational Investigations of Nanoparticle-Biomembrane Interactions in Cellular Delivery,” *Small*, vol. 11, no. 9–10, pp. 1055–1071, Mar. 2015, doi: 10.1002/sml.201401943.
- [3.11] S. Zhang, H. Gao, and G. Bao, “Physical Principles of Nanoparticle Cellular Endocytosis,” *ACS Nano*, vol. 9, no. 9, pp. 8655–8671, Sep. 2015, doi: 10.1021/acs.nano.5b03184.
- [3.12] J.-U. Sommer, M. Werner, and V. A. Baulin, “Critical adsorption controls translocation of polymer chains through lipid bilayers and permeation of solvent,” *EPL (Europhysics Lett.)*, vol. 98, no. 1, p. 18003, Apr. 2012, doi: 10.1209/0295-5075/98/18003.
- [3.13] M. Werner, J.-U. U. Sommer, and V. A. Baulin, “Homo-polymers with balanced hydrophobicity translocate through lipid bilayers and enhance local solvent permeability,” *Soft Matter*, vol. 8, no. 46, p. 11714, 2012, doi: 10.1039/c2sm26008e.
- [3.14] A. A. Gurtovenko, J. Anwar, and I. Vattulainen, “Defect-mediated trafficking across cell membranes: insights from in silico modeling,” *Chem. Rev.*, vol. 110, no. 10, pp. 6077–6103, 2010.

- [3.15] D. P. Tieleman, “The molecular basis of electroporation,” *BMC Biochem.*, vol. 5, no. 1, p. 10, 2004.
- [3.16] T. Kodama, A. G. Doukas, and M. R. Hamblin, “Shock wave-mediated molecular delivery into cells,” *Biochim. Biophys. Acta (BBA)-Molecular Cell Res.*, vol. 1542, no. 1–3, pp. 186–194, 2002.
- [3.17] K. Koshiyama, T. Kodama, T. Yano, and S. Fujikawa, “Structural change in lipid bilayers and water penetration induced by shock waves: molecular dynamics simulations,” *Biophys. J.*, vol. 91, no. 6, pp. 2198–2205, 2006.
- [3.18] A. A. Gurtovenko and J. Anwar, “Modulating the structure and properties of cell membranes: the molecular mechanism of action of dimethyl sulfoxide,” *J. Phys. Chem. B*, vol. 111, no. 35, pp. 10453–10460, 2007.
- [3.19] H. Leontiadou, A. E. Mark, and S. J. Marrink, “Antimicrobial peptides in action,” *J. Am. Chem. Soc.*, vol. 128, no. 37, pp. 12156–12161, 2006.
- [3.20] H. Lee and R. G. Larson, “Molecular dynamics simulations of PAMAM dendrimer-induced pore formation in DPPC bilayers with a coarse-grained model,” *J. Phys. Chem. B*, vol. 110, no. 37, pp. 18204–18211, 2006.
- [3.21] H. Nakamura and S. Watano, “Direct Permeation of Nanoparticles across Cell Membrane: A Review,” *KONA Powder Part. J.*, vol. 35, no. 35, pp. 49–65, 2018, doi: 10.14356/kona.2018011.
- [3.22] C. Sun, T. Tang, and H. Uludag, “A molecular dynamics simulation study on the effect of lipid substitution on polyethylenimine mediated siRNA complexation,” *Biomaterials*, vol. 34, no. 11, pp. 2822–2833, Apr. 2013, doi: 10.1016/j.biomaterials.2013.01.011.
- [3.23] C. Sun, T. Tang, and H. Uludağ, “Molecular Dynamics Simulations for Complexation of DNA with 2 kDa PEI Reveal Profound Effect of PEI Architecture on Complexation,” *J. Phys. Chem. B*, vol. 116, no. 8, pp. 2405–2413, Mar. 2012, doi: 10.1021/jp211716v.
- [3.24] C. Sun, T. Tang, and H. Uludağ, “Probing the Effects of Lipid Substitution on Polycation Mediated DNA Aggregation: A Molecular Dynamics Simulations Study,” *Biomacromolecules*, vol. 13, no. 9, pp. 2982–2988, Sep. 2012, doi: 10.1021/bm301045b.
- [3.25] Y. Li, X. Li, Z. Li, and H. Gao, “Surface-structure-regulated penetration of nanoparticles across a cell membrane,” *Nanoscale*, vol. 4, no. 12, pp. 3768–3775, 2012, doi: 10.1039/c2nr30379e.
- [3.26] Q. Xia, H. Ding, and Y. Ma, “Can dual-ligand targeting enhance cellular uptake of nanoparticles?,” *Nanoscale*, vol. 9, no. 26, pp. 8982–8989, 2017, doi: 10.1039/C7NR01020F.
- [3.27] T. Yue, X. Wang, F. Huang, and X. Zhang, “An unusual pathway for the membrane wrapping of rodlike nanoparticles and the orientation- and membrane wrapping-dependent nanoparticle interaction,” *Nanoscale*, vol. 5, no. 20, p. 9888, 2013, doi: 10.1039/c3nr02683c.

- [3.28] X. Chen, D. P. Tieleman, and Q. Liang, “Modulating interactions between ligand-coated nanoparticles and phase-separated lipid bilayers by varying the ligand density and the surface charge,” *Nanoscale*, vol. 10, no. 5, pp. 2481–2491, 2018, doi: 10.1039/C7NR06494B.
- [3.29] K. Shimizu, H. Nakamura, and S. Watano, “MD simulation study of direct permeation of a nanoparticle across the cell membrane under an external electric field,” *Nanoscale*, vol. 8, no. 23, pp. 11897–11906, 2016, doi: 10.1039/C6NR02051H.
- [3.30] U. Kwolek, D. Jamr??z, M. Janiczek, M. Nowakowska, P. Wydro, and M. Kepczynski, “Interactions of Polyethylenimines with Zwitterionic and Anionic Lipid Membranes,” *Langmuir*, vol. 32, no. 19, pp. 5004–5018, May 2016, doi: 10.1021/acs.langmuir.6b00490.
- [3.31] A. Y. Antipina and A. A. Gurtovenko, “Molecular-level insight into the interactions of DNA with phospholipid bilayers: barriers and triggers,” *RSC Adv.*, vol. 6, no. 43, pp. 36425–36432, 2016, doi: 10.1039/C6RA05607E.
- [3.32] C. K. Choudhury, A. Kumar, and S. Roy, “Characterization of Conformation and Interaction of Gene Delivery Vector Polyethylenimine with Phospholipid Bilayer at Different Protonation State,” *Biomacromolecules*, vol. 14, no. 10, pp. 3759–3768, Oct. 2013, doi: 10.1021/bm4011408.
- [3.33] M. Abbasi *et al.*, “siRNA-Mediated Down-Regulation of P-glycoprotein in a Xenograft Tumor Model in NOD-SCID Mice,” *Pharm. Res.*, vol. 28, no. 10, pp. 2516–2529, Oct. 2011, doi: 10.1007/s11095-011-0480-z.
- [3.34] M. Abbasi, A. Lavasanifar, L. G. Berthiaume, M. Weinfeld, and H. Uludağ, “Cationic polymer-mediated small interfering RNA delivery for P-glycoprotein down-regulation in tumor cells,” *Cancer*, vol. 116, no. 23, pp. 5544–5554, Dec. 2010, doi: 10.1002/ncr.25321.
- [3.35] K. Utsuno and H. Uludağ, “Thermodynamics of Polyethylenimine-DNA Binding and DNA Condensation,” *Biophys. J.*, vol. 99, no. 1, pp. 201–207, Jul. 2010, doi: 10.1016/j.bpj.2010.04.016.
- [3.36] L. E. Gerweck, “Tumor pH controls the in vivo efficacy of weak acid and base chemotherapeutics,” *Mol. Cancer Ther.*, vol. 5, no. 5, pp. 1275–1279, 2006, doi: 10.1158/1535-7163.MCT-06-0024.
- [3.37] Y. Kato *et al.*, “Acidic extracellular microenvironment and cancer,” *Cancer Cell Int.*, vol. 13, no. 1, p. 89, 2013, doi: 10.1186/1475-2867-13-89.
- [3.38] W. L. Jorgensen, “Quantum and statistical mechanical studies of liquids. 10. Transferable intermolecular potential functions for water, alcohols, and ethers. Application to liquid water,” *J. Am. Chem. Soc.*, vol. 103, no. 2, pp. 335–340, Jan. 1981, doi: 10.1021/ja00392a016.
- [3.39] J. C. Phillips *et al.*, “Scalable molecular dynamics with NAMD,” *J. Comput. Chem.*, vol. 26, no. 16, pp. 1781–1802, Dec. 2005, doi: 10.1002/jcc.20289.
- [3.40] W. Humphrey, A. Dalke, and K. Schulten, “VMD: Visual molecular dynamics,” *J. Mol.*

- Graph.*, vol. 14, no. 1, pp. 33–38, Feb. 1996, doi: 10.1016/0263-7855(96)00018-5.
- [3.41] R. D. Hills and N. McGlinchey, “Model parameters for simulation of physiological lipids,” *J. Comput. Chem.*, vol. 37, no. 12, pp. 1112–1118, May 2016, doi: 10.1002/jcc.24324.
- [3.42] N. Kučerka, S. Tristram-Nagle, and J. F. Nagle, “Structure of Fully Hydrated Fluid Phase Lipid Bilayers with Monounsaturated Chains,” *J. Membr. Biol.*, vol. 208, no. 3, pp. 193–202, Jan. 2006, doi: 10.1007/s00232-005-7006-8.
- [3.43] J. M. Smaby, M. M. Momsen, H. L. Brockman, and R. E. Brown, “Phosphatidylcholine acyl unsaturation modulates the decrease in interfacial elasticity induced by cholesterol,” *Biophys. J.*, vol. 73, no. 3, pp. 1492–1505, 1997, doi: 10.1016/S0006-3495(97)78181-5.
- [3.44] B. Isralewitz, J. Baudry, J. Gullingsrud, D. Kosztin, and K. Schulten, “Steered molecular dynamics investigations of protein function,” *J. Mol. Graph. Model.*, vol. 19, no. 1, pp. 13–25, 2001.
- [3.45] S. Z. Mousavi, S. Amjad-Iranagh, Y. Nademi, and H. Modarress, “Carbon Nanotube-Encapsulated Drug Penetration Through the Cell Membrane: An Investigation Based on Steered Molecular Dynamics Simulation,” *J. Membr. Biol.*, vol. 246, no. 9, pp. 697–704, Sep. 2013, doi: 10.1007/s00232-013-9587-y.
- [3.46] Q. Wei, W. Zhao, Y. Yang, B. Cui, Z. Xu, and X. Yang, “Method Evaluations for Adsorption Free Energy Calculations at the Solid/Water Interface through Metadynamics, Umbrella Sampling, and Jarzynski’s Equality,” *ChemPhysChem*, vol. 210009, pp. 1–14, Feb. 2018, doi: 10.1002/cphc.201701241.
- [3.47] S. Park, F. Khalili-Araghi, E. Tajkhorshid, and K. Schulten, “Free energy calculation from steered molecular dynamics simulations using Jarzynski’s equality,” *J. Chem. Phys.*, vol. 119, no. 6, pp. 3559–3566, Aug. 2003, doi: 10.1063/1.1590311.
- [3.48] H. Nguyen, N. Do, T. Phan, and T. Pham, “Steered Molecular Dynamics for Investigating the Interactions Between Insulin Receptor Tyrosine Kinase (IRK) and Variants of Protein Tyrosine Phosphatase 1B (PTP1B),” *Appl. Biochem. Biotechnol.*, vol. 184, no. 2, pp. 401–413, Feb. 2018, doi: 10.1007/s12010-017-2549-6.
- [3.49] E. J. Denning, U. D. Priyakumar, L. Nilsson, and A. D. Mackerell, “Impact of 2’-hydroxyl sampling on the conformational properties of RNA: Update of the CHARMM all-atom additive force field for RNA,” *J. Comput. Chem.*, vol. 32, no. 9, pp. 1929–1943, Jul. 2011, doi: 10.1002/jcc.21777.
- [3.50] J. B. Klauda *et al.*, “Update of the CHARMM all-atom additive force field for lipids: validation on six lipid types,” *J. Phys. Chem. B*, vol. 114, no. 23, pp. 7830–7843, Jun. 2010, doi: 10.1021/jp101759q.
- [3.51] T. Darden, D. York, and L. Pedersen, “Particle mesh Ewald: An $N \cdot \log(N)$ method for Ewald sums in large systems,” *J. Chem. Phys.*, vol. 98, no. 12, pp. 10089–10092, Jun. 1993, doi: 10.1063/1.464397.
- [3.52] J.-P. Ryckaert, G. Ciccotti, and H. J. Berendsen, “Numerical integration of the cartesian

- equations of motion of a system with constraints: molecular dynamics of n-alkanes,” *J. Comput. Phys.*, vol. 23, no. 3, pp. 327–341, Mar. 1977, doi: 10.1016/0021-9991(77)90098-5.
- [3.53] G. J. Martyna, D. J. Tobias, and M. L. Klein, “Constant pressure molecular dynamics algorithms,” *J. Chem. Phys.*, vol. 101, no. 5, pp. 4177–4189, 1994.
- [3.54] S. E. Feller, Y. Zhang, R. W. Pastor, and B. R. Brooks, “Constant pressure molecular dynamics simulation: the Langevin piston method,” *J. Chem. Phys.*, vol. 103, no. 11, pp. 4613–4621, 1995.
- [3.55] S. Bagai, C. Sun, and T. Tang, “Lipid-modified polyethylenimine-mediated DNA attraction evaluated by molecular dynamics simulations,” *J. Phys. Chem. B*, vol. 118, no. 25, pp. 7070–7076, 2014, doi: 10.1021/jp503381r.
- [3.56] X. Yi, X. Shi, and H. Gao, “Cellular Uptake of Elastic Nanoparticles,” *Phys. Rev. Lett.*, vol. 107, no. 9, p. 098101, Aug. 2011, doi: 10.1103/PhysRevLett.107.098101.
- [3.57] R. Vácha, F. J. Martinez-Veracoechea, and D. Frenkel, “Receptor-Mediated Endocytosis of Nanoparticles of Various Shapes,” *Nano Lett.*, vol. 11, no. 12, pp. 5391–5395, Dec. 2011, doi: 10.1021/nl2030213.
- [3.58] Y. Liu, B. Peng, S. Sohrabi, and Y. Liu, “The Configuration of Copolymer Ligands on Nanoparticles Affects Adhesion and Uptake,” *Langmuir*, vol. 32, no. 39, pp. 10136–10143, Oct. 2016, doi: 10.1021/acs.langmuir.6b02371.
- [3.59] K. Yang and Y.-Q. Ma, “Computer simulation of the translocation of nanoparticles with different shapes across a lipid bilayer,” *Nat. Nanotechnol.*, vol. 5, no. 8, pp. 579–583, Aug. 2010, doi: 10.1038/nnano.2010.141.
- [3.60] K. Yang and Y. Ma, “Wrapping and Internalization of Nanoparticles by Lipid Bilayers: a Computer Simulation Study,” *Aust. J. Chem.*, vol. 64, no. 7, p. 894, 2011, doi: 10.1071/CH11053.
- [3.61] Y. Li, T. Yue, K. Yang, and X. Zhang, “Molecular modeling of the relationship between nanoparticle shape anisotropy and endocytosis kinetics,” *Biomaterials*, vol. 33, no. 19, pp. 4965–4973, Jun. 2012, doi: 10.1016/j.biomaterials.2012.03.044.
- [3.62] C. Huang, Y. Zhang, H. Yuan, H. Gao, and S. Zhang, “Role of Nanoparticle Geometry in Endocytosis: Laying Down to Stand Up,” *Nano Lett.*, vol. 13, no. 9, pp. 4546–4550, Sep. 2013, doi: 10.1021/nl402628n.
- [3.63] H. M. Aliabadi, B. Landry, P. Mahdipoor, C. Y. M. Hsu, and H. Uludağ, “Effective down-regulation of Breast Cancer Resistance Protein (BCRP) by siRNA delivery using lipid-substituted aliphatic polymers,” *Eur. J. Pharm. Biopharm.*, vol. 81, no. 1, pp. 33–42, May 2012, doi: 10.1016/j.ejpb.2012.01.011.
- [3.64] H. Montazeri Aliabadi, B. Landry, P. Mahdipoor, and H. Uludağ, “Induction of Apoptosis by Survivin Silencing through siRNA Delivery in a Human Breast Cancer Cell Line,” *Mol. Pharm.*, vol. 8, no. 5, pp. 1821–1830, Oct. 2011, doi: 10.1021/mp200176v.

- [3.65] A. Neamark, O. Suwanton, R. B. K. C., C. Y. M. Hsu, P. Supaphol, and H. Uludağ, “Aliphatic Lipid Substitution on 2 kDa Polyethylenimine Improves Plasmid Delivery and Transgene Expression,” *Mol. Pharm.*, vol. 6, no. 6, pp. 1798–1815, Dec. 2009, doi: 10.1021/mp900074d.
- [3.66] S. Pogodin, M. Werner, J.-U. Sommer, and V. A. Baulin, “Nanoparticle-induced permeability of lipid membranes,” *ACS Nano*, vol. 6, no. 12, pp. 10555–10561, 2012.
- [3.67] S. Park and K. Schulten, “Calculating potentials of mean force from steered molecular dynamics simulations,” *J. Chem. Phys.*, vol. 120, no. 13, pp. 5946–5961, Apr. 2004, doi: 10.1063/1.1651473.
- [3.68] E. Schöll-Paschinger and C. Dellago, “A proof of Jarzynski’s nonequilibrium work theorem for dynamical systems that conserve the canonical distribution,” *J. Chem. Phys.*, vol. 125, no. 5, p. 054105, Aug. 2006, doi: 10.1063/1.2227025.
- [4.1] D. Pezzoli, E. K. Tsekoura, K. C. R. Bahadur, G. Candiani, D. Mantovani, and H. Uludağ, “Hydrophobe-substituted bPEI derivatives: boosting transfection on primary vascular cells,” *Sci. China Mater.*, vol. 60, no. 6, pp. 529–542, 2017.
- [4.2] S. K. Samal *et al.*, “Cationic polymers and their therapeutic potential,” *Chem. Soc. Rev.*, vol. 41, no. 21, pp. 7147–7194, 2012.
- [4.3] J. Sabín, C. Vázquez-Vázquez, G. Prieto, F. Bordi, and F. Sarmiento, “Double charge inversion in polyethylenimine-decorated liposomes,” *Langmuir*, vol. 28, no. 28, pp. 10534–10542, 2012.
- [4.4] K. Utsuno, H. Kono, E. Tanaka, N. Jouna, Y. Kojima, and H. Uludağ, “Low molecular weight branched PEI binding to linear DNA,” *Chem. Pharm. Bull.*, vol. 64, no. 10, pp. 1484–1491, 2016.
- [4.5] D. Meneksedag-Erol, T. Tang, and H. Uludağ, “Mechanistic insights into the role of glycosaminoglycans in delivery of polymeric nucleic acid nanoparticles by molecular dynamics simulations,” *Biomaterials*, vol. 156, pp. 107–120, Feb. 2018, doi: 10.1016/j.biomaterials.2017.11.037.
- [4.6] M. Laurencin, T. Georgelin, B. Malezieux, J.-M. Siaugue, and C. Ménager, “Interactions between giant unilamellar vesicles and charged core–shell magnetic nanoparticles,” *Langmuir*, vol. 26, no. 20, pp. 16025–16030, 2010.
- [4.7] M. Boeckle, S. von Gersdorff, K. van der Piepen, S. Culmsee, C. Wagner, E. and Ogris, “Purification of polyethylenimine polyplexes highlights the role of free polycations in gene transfer,” *J. Gene Med.*, vol. 6, pp. 1102–1111, 2004, doi: 10.1002/jgm.598.
- [4.8] C. Zhang, F.-G. Wu, P. Hu, and Z. Chen, “Interaction of polyethylenimine with model cell membranes studied by linear and nonlinear spectroscopic techniques,” *J. Phys. Chem. C*, vol. 118, no. 23, pp. 12195–12205, 2014.
- [4.9] K. Yasuhara, M. Tsukamoto, Y. Tsuji, and J. Kikuchi, “Unique concentration dependence on the fusion of anionic liposomes induced by polyethyleneimine,” *Colloids Surfaces A*

- Physicochem. Eng. Asp.*, vol. 415, pp. 461–467, 2012, doi: <https://doi.org/10.1016/j.colsurfa.2012.01.024>.
- [4.10] R. Jahn, T. Lang, and T. C. Südhof, “Membrane fusion,” *Cell*, vol. 112, no. 4, pp. 519–533, 2003.
- [4.11] S. R. Clark *et al.*, “Determining the effects of PEI adsorption on the permeability of 1,2-dipalmitoylphosphatidylcholine/bis(monoacylglycero)phosphate membranes under osmotic stress,” *Acta Biomater.*, vol. 65, pp. 317–326, 2018, doi: <https://doi.org/10.1016/j.actbio.2017.10.027>.
- [4.12] S. Hong *et al.*, “Interaction of Polycationic Polymers with Supported Lipid Bilayers and Cells: Nanoscale Hole Formation and Enhanced Membrane Permeability,” *Bioconjug. Chem.*, vol. 17, no. 3, pp. 728–734, May 2006, doi: 10.1021/bc060077y.
- [4.13] U. Kwolek, D. Jamroz, M. Janiczek, M. Nowakowska, P. Wydro, and M. Kepczynski, “Interactions of Polyethylenimines with Zwitterionic and Anionic Lipid Membranes,” *Langmuir*, vol. 32, no. 19, pp. 5004–5018, May 2016, doi: 10.1021/acs.langmuir.6b00490.
- [4.14] C. K. Choudhury, A. Kumar, and S. Roy, “Characterization of Conformation and Interaction of Gene Delivery Vector Polyethylenimine with Phospholipid Bilayer at Different Protonation State,” *Biomacromolecules*, vol. 14, no. 10, pp. 3759–3768, Oct. 2013, doi: 10.1021/bm4011408.
- [4.15] L. Kjellen and U. Lindahl, “Proteoglycans: structures and interactions,” *Annu. Rev. Biochem.*, vol. 60, no. 1, pp. 443–475, 1991.
- [4.16] T. Miller, M. C. Goude, T. C. McDevitt, and J. S. Temenoff, “Molecular engineering of glycosaminoglycan chemistry for biomolecule delivery,” *Acta Biomater.*, vol. 10, no. 4, pp. 1705–1719, 2014.
- [4.17] I. Moret *et al.*, “Stability of PEI–DNA and DOTAP–DNA complexes: effect of alkaline pH, heparin and serum,” *J. Control. Release*, vol. 76, no. 1–2, pp. 169–181, 2001.
- [4.18] A. Kwok and S. L. Hart, “Comparative structural and functional studies of nanoparticle formulations for DNA and siRNA delivery,” *Nanomedicine Nanotechnology, Biol. Med.*, vol. 7, no. 2, pp. 210–219, 2011.
- [4.19] N. Ernst *et al.*, “Interaction of liposomal and polycationic transfection complexes with pulmonary surfactant,” *J. Gene Med. A cross-disciplinary J. Res. Sci. gene Transf. its Clin. Appl.*, vol. 1, no. 5, pp. 331–340, 1999.
- [4.20] A. A. Gurtovenko, “Molecular-Level Insight into the Interactions of DNA-Polycation Complexes with Model Cell Membranes,” *J. Phys. Chem. B*, vol. 123, no. 30, pp. 6505–6514, 2019, doi: <https://doi.org/10.1021/acs.jpcc.9b05110>.
- [4.21] P. Chen *et al.*, “Diffusion and directionality of charged nanoparticles on lipid bilayer membrane,” *ACS Nano*, vol. 10, no. 12, pp. 11541–11547, 2016.
- [4.22] G. Zhu, Z. Huang, Z. Xu, and L.-T. Yan, “Tailoring interfacial nanoparticle organization

- through entropy,” *Acc. Chem. Res.*, vol. 51, no. 4, pp. 900–909, 2018.
- [4.23] P. Chen *et al.*, “Transport of a graphene nanosheet sandwiched inside cell membranes,” *Sci. Adv.*, vol. 5, no. 6, p. eaaw3192, 2019.
- [4.24] H. M. Aliabadi, B. Landry, R. K. Bahadur, A. Neamark, O. Suwantong, and H. Uludağ, “Impact of Lipid Substitution on Assembly and Delivery of siRNA by Cationic Polymers,” *Macromol. Biosci.*, vol. 11, no. 5, pp. 662–672, May 2011, doi: 10.1002/mabi.201000402.
- [4.25] C. Sun, T. Tang, and H. Uludag, “A molecular dynamics simulation study on the effect of lipid substitution on polyethylenimine mediated siRNA complexation,” *Biomaterials*, vol. 34, no. 11, pp. 2822–2833, Apr. 2013, doi: 10.1016/j.biomaterials.2013.01.011.
- [4.26] A. Neamark, O. Suwantong, R. B. K. C., C. Y. M. Hsu, P. Supaphol, and H. Uludağ, “Aliphatic Lipid Substitution on 2 kDa Polyethylenimine Improves Plasmid Delivery and Transgene Expression,” *Mol. Pharm.*, vol. 6, no. 6, pp. 1798–1815, Dec. 2009, doi: 10.1021/mp900074d.
- [4.27] M. Abbasi *et al.*, “siRNA-Mediated Down-Regulation of P-glycoprotein in a Xenograft Tumor Model in NOD-SCID Mice,” *Pharm. Res.*, vol. 28, no. 10, pp. 2516–2529, Oct. 2011, doi: 10.1007/s11095-011-0480-z.
- [4.28] K. Utsuno and H. Uludağ, “Thermodynamics of Polyethylenimine-DNA Binding and DNA Condensation,” *Biophys. J.*, vol. 99, no. 1, pp. 201–207, Jul. 2010, doi: 10.1016/j.bpj.2010.04.016.
- [4.29] A. von Harpe, H. Petersen, Y. Li, and T. Kissel, “Characterization of commercially available and synthesized polyethylenimines for gene delivery,” *J. Control. Release*, vol. 69, no. 2, pp. 309–322, 2000.
- [4.30] J. Suh, H. Paik, and B. K. Hwang, “Ionization of Poly (ethylenimine) and Poly (allylamine) at Various pH’ s,” *Bioorg. Chem.*, vol. 22, no. 3, pp. 318–327, 1994.
- [4.31] J. Nagaya, M. Homma, A. Tanioka, and A. Minakata, “Relationship between protonation and ion condensation for branched poly (ethylenimine),” *Biophys. Chem.*, vol. 60, no. 1–2, pp. 45–51, 1996.
- [4.32] G. J. M. Koper, R. C. van Duijvenbode, D. D. P. W. Stam, U. Steuerle, and M. Borkovec, “Synthesis and protonation behavior of comblike poly (ethyleneimine),” *Macromolecules*, vol. 36, no. 7, pp. 2500–2507, 2003.
- [4.33] Y. Nademi, T. Tang, and H. Uludağ, “Steered molecular dynamics simulations reveal a self-protecting configuration of nanoparticles during membrane penetration,” *Nanoscale*, vol. 10, no. 37, pp. 17671–17682, 2018, doi: 10.1039/C8NR04287J.
- [4.34] E. L. Wu *et al.*, “CHARMM-GUI membrane builder toward realistic biological membrane simulations,” *J. Comput. Chem.*, vol. 35, no. 27, pp. 1997–2004, 2014.
- [4.35] B. R. Brooks *et al.*, “CHARMM: the biomolecular simulation program,” *J. Comput. Chem.*, vol. 30, no. 10, pp. 1545–1614, 2009.

- [4.36] S. Jo, T. Kim, V. G. Iyer, and W. Im, “CHARMM-GUI: a web-based graphical user interface for CHARMM,” *J. Comput. Chem.*, vol. 29, no. 11, pp. 1859–1865, 2008.
- [4.37] W. L. Jorgensen, “Quantum and statistical mechanical studies of liquids. 10. Transferable intermolecular potential functions for water, alcohols, and ethers. Application to liquid water,” *J. Am. Chem. Soc.*, vol. 103, no. 2, pp. 335–340, Jan. 1981, doi: 10.1021/ja00392a016.
- [4.38] J. Lee *et al.*, “CHARMM-GUI input generator for NAMD, GROMACS, AMBER, OpenMM, and CHARMM/OpenMM simulations using the CHARMM36 additive force field,” *J. Chem. Theory Comput.*, vol. 12, no. 1, pp. 405–413, 2015.
- [4.39] S. Park, F. Khalili-Araghi, E. Tajkhorshid, and K. Schulten, “Free energy calculation from steered molecular dynamics simulations using Jarzynski’s equality,” *J. Chem. Phys.*, vol. 119, no. 6, pp. 3559–3566, Aug. 2003, doi: 10.1063/1.1590311.
- [4.40] Q. Wei, W. Zhao, Y. Yang, B. Cui, Z. Xu, and X. Yang, “Method Evaluations for Adsorption Free Energy Calculations at the Solid/Water Interface through Metadynamics, Umbrella Sampling, and Jarzynski’s Equality,” *ChemPhysChem*, vol. 210009, pp. 1–14, Feb. 2018, doi: 10.1002/cphc.201701241.
- [4.41] H. Nguyen, N. Do, T. Phan, and T. Pham, “Steered Molecular Dynamics for Investigating the Interactions Between Insulin Receptor Tyrosine Kinase (IRK) and Variants of Protein Tyrosine Phosphatase 1B (PTP1B),” *Appl. Biochem. Biotechnol.*, vol. 184, no. 2, pp. 401–413, Feb. 2018, doi: 10.1007/s12010-017-2549-6.
- [4.42] Y. Xu *et al.*, “How does huperzine A enter and leave the binding gorge of acetylcholinesterase? Steered molecular dynamics simulations,” *J. Am. Chem. Soc.*, vol. 125, no. 37, pp. 11340–11349, 2003.
- [4.43] D. J. Brockwell *et al.*, “Pulling geometry defines the mechanical resistance of a β -sheet protein,” *Nat. Struct. Mol. Biol.*, vol. 10, no. 9, p. 731, 2003.
- [4.44] S. Azadi, M. Tafazzoli-Shadpour, and R. Omidvar, “Steered Molecular Dynamics Simulation Study of Quantified Effects of Point Mutation Induced by Breast Cancer on Mechanical Behavior of E-Cadherin,” *Mol. Biol.*, vol. 52, no. 5, pp. 723–731, 2018.
- [4.45] H. Lu and K. Schulten, “Steered molecular dynamics simulations of force-induced protein domain unfolding,” *Proteins Struct. Funct. Bioinforma.*, vol. 35, no. 4, pp. 453–463, 1999.
- [4.46] E. J. Denning, U. D. Priyakumar, L. Nilsson, and A. D. Mackerell, “Impact of 2'-hydroxyl sampling on the conformational properties of RNA: Update of the CHARMM all-atom additive force field for RNA,” *J. Comput. Chem.*, vol. 32, no. 9, pp. 1929–1943, Jul. 2011, doi: 10.1002/jcc.21777.
- [4.47] J. B. Klauda *et al.*, “Update of the CHARMM all-atom additive force field for lipids: validation on six lipid types,” *J. Phys. Chem. B*, vol. 114, no. 23, pp. 7830–7843, Jun. 2010, doi: 10.1021/jp101759q.
- [4.48] J. C. Phillips *et al.*, “Scalable molecular dynamics with NAMD,” *J. Comput. Chem.*, vol.

- 26, no. 16, pp. 1781–1802, Dec. 2005, doi: 10.1002/jcc.20289.
- [4.49] T. Darden, D. York, and L. Pedersen, “Particle mesh Ewald: An $N \cdot \log(N)$ method for Ewald sums in large systems,” *J. Chem. Phys.*, vol. 98, no. 12, pp. 10089–10092, Jun. 1993, doi: 10.1063/1.464397.
- [4.50] J.-P. Ryckaert, G. Ciccotti, and H. J. Berendsen, “Numerical integration of the cartesian equations of motion of a system with constraints: molecular dynamics of n-alkanes,” *J. Comput. Phys.*, vol. 23, no. 3, pp. 327–341, Mar. 1977, doi: 10.1016/0021-9991(77)90098-5.
- [4.51] G. J. Martyna, D. J. Tobias, and M. L. Klein, “Constant pressure molecular dynamics algorithms,” *J. Chem. Phys.*, vol. 101, no. 5, pp. 4177–4189, 1994.
- [4.52] S. E. Feller, Y. Zhang, R. W. Pastor, and B. R. Brooks, “Constant pressure molecular dynamics simulation: the Langevin piston method,” *J. Chem. Phys.*, vol. 103, no. 11, pp. 4613–4621, 1995.
- [4.53] W. Humphrey, A. Dalke, and K. Schulten, “VMD: Visual molecular dynamics,” *J. Mol. Graph.*, vol. 14, no. 1, pp. 33–38, Feb. 1996, doi: 10.1016/0263-7855(96)00018-5.
- [4.54] D. Meneksedag-Erol, T. Tang, and H. Uludağ, “Probing the effect of miRNA on siRNA–PEI polyplexes,” *J. Phys. Chem. B*, vol. 119, no. 17, pp. 5475–5486, 2015.
- [4.55] J. Ziebarth and Y. Wang, “Molecular dynamics simulations of DNA-polycation complex formation,” *Biophys. J.*, vol. 97, no. 7, pp. 1971–1983, 2009.
- [4.56] C. Sun, T. Tang, H. Uludağ, and J. E. Cuervo, “Molecular dynamics simulations of DNA/PEI complexes: Effect of PEI branching and protonation state,” *Biophys. J.*, vol. 100, no. 11, pp. 2754–2763, 2011, doi: 10.1016/j.bpj.2011.04.045.
- [4.57] H. M. Aliabadi, B. Landry, C. Sun, T. Tang, and H. Uludağ, “Supramolecular assemblies in functional siRNA delivery: where do we stand?,” *Biomaterials*, vol. 33, no. 8, pp. 2546–2569, 2012.
- [4.58] M. Sud *et al.*, “LMSD: LIPID MAPS structure database,” *Nucleic Acids Res.*, vol. 35, no. suppl_1, pp. D527–D532, Nov. 2006, doi: 10.1093/nar/gkl838.
- [4.59] G. Caracciolo and H. Amenitsch, “Cationic liposome/DNA complexes: from structure to interactions with cellular membranes,” *Eur. Biophys. J.*, vol. 41, no. 10, pp. 815–829, 2012.
- [4.60] R. Dias, M. Rosa, A. C. Pais, M. Miguel, and B. Lindman, “DNA-Surfactant Interactions. Compaction, Condensation, Decompaction and Phase Separation,” *J. Chinese Chem. Soc.*, vol. 51, no. 3, pp. 447–469, 2004.
- [4.61] G. Caracciolo, D. Pozzi, H. Amenitsch, and R. Caminiti, “Interaction of lipoplexes with anionic lipids resulting in DNA release is a two-stage process,” *Langmuir*, vol. 23, no. 17, pp. 8713–8717, 2007.
- [4.62] Y. Xu and F. C. Szoka, “Mechanism of DNA release from cationic liposome/DNA

- complexes used in cell transfection,” *Biochemistry*, vol. 35, no. 18, pp. 5616–5623, 1996.
- [4.63] G. Caracciolo *et al.*, “On the correlation between phase evolution of lipoplexes/anionic lipid mixtures and DNA release,” *Appl. Phys. Lett.*, vol. 91, no. 14, p. 143903, 2007.
- [4.64] G. Caracciolo *et al.*, “Structural stability against disintegration by anionic lipids rationalizes the efficiency of cationic liposome/DNA complexes,” *Langmuir*, vol. 23, no. 8, pp. 4498–4508, 2007.
- [4.65] M. Langner and K. Kubica, “The electrostatics of lipid surfaces,” *Chem. Phys. Lipids*, vol. 101, no. 1, pp. 3–35, 1999.
- [4.66] D. Bach, E. Wachtel, N. Borochoy, G. Senisterra, and R. M. Epand, “Phase behaviour of heteroacid phosphatidylserines and cholesterol,” *Chem. Phys. Lipids*, vol. 63, no. 1–2, pp. 105–113, 1992.
- [4.67] K. L. Koster, M. S. Webb, G. Bryant, and D. V Lynch, “Interactions between soluble sugars and POPC (1-palmitoyl-2-oleoylphosphatidylcholine) during dehydration: vitrification of sugars alters the phase behavior of the phospholipid,” *Biochim. Biophys. Acta (BBA)-Biomembranes*, vol. 1193, no. 1, pp. 143–150, 1994.
- [4.68] D. Meneksedag-Erol, T. Tang, and H. Uludağ, “Molecular modeling of polynucleotide complexes,” *Biomaterials*, vol. 35, no. 25, pp. 7068–7076, Aug. 2014, doi: 10.1016/j.biomaterials.2014.04.103.
- [4.69] S. Zhang, H. Gao, and G. Bao, “Physical Principles of Nanoparticle Cellular Endocytosis,” *ACS Nano*, vol. 9, no. 9, pp. 8655–8671, Sep. 2015, doi: 10.1021/acs.nano.5b03184.
- [4.70] B. Czech and G. J. Hannon, “Small RNA sorting: matchmaking for Argonautes,” *Nat. Rev. Genet.*, vol. 12, no. 1, p. 19, 2011.
- [4.71] P. A. Leventis and S. Grinstein, “The Distribution and Function of Phosphatidylserine in Cellular Membranes,” *Annu. Rev. Biophys.*, vol. 39, pp. 407–427, 2010, doi: 10.1146/annurev.biophys.093008.131234.
- [4.72] M. Sikor *et al.*, “Interaction of a charged polymer with zwitterionic lipid vesicles,” *Langmuir*, vol. 26, no. 6, pp. 4095–4102, 2010.
- [4.73] N. Wilkosz *et al.*, “Effect of polycation structure on interaction with lipid membranes,” *J. Phys. Chem. B*, vol. 121, no. 30, pp. 7318–7326, 2017.
- [4.74] L. Wang and N. Malmstadt, “Interactions between charged nanoparticles and giant vesicles fabricated from inverted-headgroup lipids,” *J. Phys. D: Appl. Phys.*, vol. 50, no. 41, p. 415402, 2017.
- [5.1] D. Meneksedag-Erol, T. Tang, and H. Uludağ, “Molecular modeling of polynucleotide complexes,” *Biomaterials*, vol. 35, no. 25, pp. 7068–7076, Aug. 2014, doi: 10.1016/j.biomaterials.2014.04.103.
- [5.2] D. Meneksedag-Erol, R. B. KC, T. Tang, and H. Uludağ, “A Delicate Balance When

Substituting a Small Hydrophobe onto Low Molecular Weight Polyethylenimine to Improve Its Nucleic Acid Delivery Efficiency,” *ACS Appl. Mater. Interfaces*, vol. 7, no. 44, pp. 24822–24832, Nov. 2015, doi: 10.1021/acsami.5b07929.

- [5.3] H. M. Aliabadi *et al.*, “A systematic comparison of lipopolymers for siRNA delivery to multiple breast cancer cell lines: In vitro studies,” *Acta Biomater.*, vol. 102, pp. 351–366, 2020.
- [5.4] D. Meneksedag-Erol, T. Tang, and H. Uludağ, “Mechanistic insights into the role of glycosaminoglycans in delivery of polymeric nucleic acid nanoparticles by molecular dynamics simulations,” *Biomaterials*, vol. 156, pp. 107–120, Feb. 2018, doi: 10.1016/j.biomaterials.2017.11.037.
- [5.5] S. J. Marrink, V. Corradi, P. C. T. Souza, H. I. Ingólfsson, D. P. Tieleman, and M. S. P. Sansom, “Computational Modeling of Realistic Cell Membranes,” *Chem. Rev.*, vol. 119, no. 9, pp. 6184–6226, May 2019, doi: 10.1021/acs.chemrev.8b00460.
- [5.6] P. A. Janmey and P. K. J. Kinnunen, “Biophysical properties of lipids and dynamic membranes,” *Trends Cell Biol.*, vol. 16, no. 10, pp. 538–546, 2006.
- [5.7] M. T. Hyvönen and P. T. Kovanen, “Molecular dynamics simulations of unsaturated lipid bilayers: effects of varying the numbers of double bonds,” *Eur. Biophys. J.*, vol. 34, no. 4, pp. 294–305, Jun. 2005, doi: 10.1007/s00249-004-0455-7.
- [5.8] Z. Xu, L. Gao, P. Chen, and L.-T. Yan, “Diffusive transport of nanoscale objects through cell membranes: a computational perspective,” *Soft Matter*, vol. 16, no. 16, pp. 3869–3881, 2020.
- [5.9] Z. Shen, W. Baker, H. Ye, and Y. Li, “pH-Dependent aggregation and pH-independent cell membrane adhesion of monolayer-protected mixed charged gold nanoparticles,” *Nanoscale*, vol. 11, no. 15, pp. 7371–7385, 2019.
- [5.10] P. Chen *et al.*, “Transport of a graphene nanosheet sandwiched inside cell membranes,” *Sci. Adv.*, vol. 5, no. 6, p. eaaw3192, 2019.
- [5.11] L. Zhang, Z. Zhang, M. Negahban, and A. Jérusalem, “Molecular dynamics simulation of cell membrane pore sealing,” *Extrem. Mech. Lett.*, vol. 27, pp. 83–93, Feb. 2019, doi: 10.1016/j.eml.2019.01.008.
- [5.12] H. Leontiadou, A. E. Mark, and S. J. Marrink, “Molecular Dynamics Simulations of Hydrophilic Pores in Lipid Bilayers,” *Biophys. J.*, vol. 86, no. 4, pp. 2156–2164, Apr. 2004, doi: 10.1016/S0006-3495(04)74275-7.
- [5.13] U. Kwolek, D. Jamr??z, M. Janiczek, M. Nowakowska, P. Wydro, and M. Kepczynski, “Interactions of Polyethylenimines with Zwitterionic and Anionic Lipid Membranes,” *Langmuir*, vol. 32, no. 19, pp. 5004–5018, May 2016, doi: 10.1021/acs.langmuir.6b00490.

- [5.14] C. Zhang, F.-G. Wu, P. Hu, and Z. Chen, “Interaction of polyethylenimine with model cell membranes studied by linear and nonlinear spectroscopic techniques,” *J. Phys. Chem. C*, vol. 118, no. 23, pp. 12195–12205, 2014.
- [5.15] N. Awasthi *et al.*, “Molecular Mechanism of Polycation-Induced Pore Formation in Biomembranes,” *ACS Biomater. Sci. Eng.*, vol. 5, no. 2, pp. 780–794, Feb. 2019, doi: 10.1021/acsbiomaterials.8b01495.
- [5.16] D. P. Tieleman, “The molecular basis of electroporation,” *BMC Biochem.*, vol. 5, no. 1, p. 10, 2004.
- [5.17] A. A. Gurtovenko and A. S. Lyulina, “Electroporation of asymmetric phospholipid membranes,” *J. Phys. Chem. B*, vol. 118, no. 33, pp. 9909–9918, 2014.
- [5.18] R. Reigada, “Electroporation of heterogeneous lipid membranes,” *Biochim. Biophys. Acta (BBA)-Biomembranes*, vol. 1838, no. 3, pp. 814–821, 2014.
- [5.19] S. A. Kirsch and R. A. Böckmann, “Membrane pore formation in atomistic and coarse-grained simulations,” *Biochim. Biophys. Acta (BBA)-Biomembranes*, vol. 1858, no. 10, pp. 2266–2277, 2016.
- [5.20] M. L. Fernández, G. Marshall, F. Sagués, and R. Reigada, “Structural and kinetic molecular dynamics study of electroporation in cholesterol-containing bilayers,” *J. Phys. Chem. B*, vol. 114, no. 20, pp. 6855–6865, 2010.
- [5.21] M. J. Ziegler and P. T. Vernier, “Interface water dynamics and porating electric fields for phospholipid bilayers,” *J. Phys. Chem. B*, vol. 112, no. 43, pp. 13588–13596, 2008.
- [5.22] X. Zhuang, E. M. Dávila-Contreras, A. H. Beaven, W. Im, and J. B. Klauda, “An extensive simulation study of lipid bilayer properties with different head groups, acyl chain lengths, and chain saturations,” *Biochim. Biophys. Acta - Biomembr.*, vol. 1858, no. 12, pp. 3093–3104, Dec. 2016, doi: 10.1016/j.bbamem.2016.09.016.
- [5.23] Y. Nademi, T. Tang, and H. Uludağ, “Steered molecular dynamics simulations reveal a self-protecting configuration of nanoparticles during membrane penetration,” *Nanoscale*, vol. 10, no. 37, pp. 17671–17682, 2018, doi: 10.1039/C8NR04287J.
- [5.24] Y. Nademi, T. Tang, and H. Uludağ, “Membrane lipids destabilize short interfering ribonucleic acid (siRNA)/polyethylenimine nanoparticles,” *Nanoscale*, vol. 12, no. 2, pp. 1032–1045, 2020, doi: 10.1039/C9NR08128C.
- [5.25] H. M. Aliabadi, B. Landry, P. Mahdipoor, C. Y. M. Hsu, and H. Uludağ, “Effective down-regulation of Breast Cancer Resistance Protein (BCRP) by siRNA delivery using lipid-substituted aliphatic polymers,” *Eur. J. Pharm. Biopharm.*, vol. 81, no. 1, pp. 33–42, May 2012, doi: 10.1016/j.ejpb.2012.01.011.

- [5.26] H. Montazeri Aliabadi, B. Landry, P. Mahdipoor, and H. Uludağ, “Induction of Apoptosis by Survivin Silencing through siRNA Delivery in a Human Breast Cancer Cell Line,” *Mol. Pharm.*, vol. 8, no. 5, pp. 1821–1830, Oct. 2011, doi: 10.1021/mp200176v.
- [5.27] M. Abbasi *et al.*, “siRNA-Mediated Down-Regulation of P-glycoprotein in a Xenograft Tumor Model in NOD-SCID Mice,” *Pharm. Res.*, vol. 28, no. 10, pp. 2516–2529, Oct. 2011, doi: 10.1007/s11095-011-0480-z.
- [5.28] K. Utsuno and H. Uludağ, “Thermodynamics of Polyethylenimine-DNA Binding and DNA Condensation,” *Biophys. J.*, vol. 99, no. 1, pp. 201–207, Jul. 2010, doi: 10.1016/j.bpj.2010.04.016.
- [5.29] J. Suh, H. Paik, and B. K. Hwang, “Ionization of Poly (ethylenimine) and Poly (allylamine) at Various pH's,” *Bioorg. Chem.*, vol. 22, no. 3, pp. 318–327, 1994.
- [5.30] J. Nagaya, M. Homma, A. Tanioka, and A. Minakata, “Relationship between protonation and ion condensation for branched poly (ethylenimine),” *Biophys. Chem.*, vol. 60, no. 1–2, pp. 45–51, 1996.
- [5.31] G. J. M. Koper, R. C. van Duijvenbode, D. D. P. W. Stam, U. Steuerle, and M. Borkovec, “Synthesis and protonation behavior of comblike poly (ethyleneimine),” *Macromolecules*, vol. 36, no. 7, pp. 2500–2507, 2003.
- [5.32] H. M. Aliabadi, B. Landry, C. Sun, T. Tang, and H. Uludağ, “Supramolecular assemblies in functional siRNA delivery: where do we stand?,” *Biomaterials*, vol. 33, no. 8, pp. 2546–2569, 2012.
- [5.33] W. L. Jorgensen, “Quantum and statistical mechanical studies of liquids. 10. Transferable intermolecular potential functions for water, alcohols, and ethers. Application to liquid water,” *J. Am. Chem. Soc.*, vol. 103, no. 2, pp. 335–340, Jan. 1981, doi: 10.1021/ja00392a016.
- [5.34] E. L. Wu *et al.*, “CHARMM-GUI membrane builder toward realistic biological membrane simulations,” *J. Comput. Chem.*, vol. 35, no. 27, pp. 1997–2004, 2014.
- [5.35] B. R. Brooks *et al.*, “CHARMM: the biomolecular simulation program,” *J. Comput. Chem.*, vol. 30, no. 10, pp. 1545–1614, 2009.
- [5.36] S. Jo, T. Kim, V. G. Iyer, and W. Im, “CHARMM-GUI: a web-based graphical user interface for CHARMM,” *J. Comput. Chem.*, vol. 29, no. 11, pp. 1859–1865, 2008.
- [5.37] N. Kučerka, Y. Liu, N. Chu, H. I. Petrache, S. Tristram-Nagle, and J. F. Nagle, “Structure of Fully Hydrated Fluid Phase DMPC and DLPC Lipid Bilayers Using X-Ray Scattering from Oriented Multilamellar Arrays and from Unilamellar Vesicles,” *Biophys. J.*, vol. 88, no. 4, pp. 2626–2637, Apr. 2005, doi: 10.1529/biophysj.104.056606.

- [5.38] J. Lee *et al.*, “CHARMM-GUI input generator for NAMD, GROMACS, AMBER, OpenMM, and CHARMM/OpenMM simulations using the CHARMM36 additive force field,” *J. Chem. Theory Comput.*, vol. 12, no. 1, pp. 405–413, 2015.
- [5.39] S. Park, F. Khalili-Araghi, E. Tajkhorshid, and K. Schulten, “Free energy calculation from steered molecular dynamics simulations using Jarzynski’s equality,” *J. Chem. Phys.*, vol. 119, no. 6, pp. 3559–3566, Aug. 2003, doi: 10.1063/1.1590311.
- [5.40] Q. Wei, W. Zhao, Y. Yang, B. Cui, Z. Xu, and X. Yang, “Method Evaluations for Adsorption Free Energy Calculations at the Solid/Water Interface through Metadynamics, Umbrella Sampling, and Jarzynski’s Equality,” *ChemPhysChem*, vol. 210009, pp. 1–14, Feb. 2018, doi: 10.1002/cphc.201701241.
- [5.41] H. Nguyen, N. Do, T. Phan, and T. Pham, “Steered Molecular Dynamics for Investigating the Interactions Between Insulin Receptor Tyrosine Kinase (IRK) and Variants of Protein Tyrosine Phosphatase 1B (PTP1B),” *Appl. Biochem. Biotechnol.*, vol. 184, no. 2, pp. 401–413, Feb. 2018, doi: 10.1007/s12010-017-2549-6.
- [5.42] Y. Xu *et al.*, “How does huperzine A enter and leave the binding gorge of acetylcholinesterase? Steered molecular dynamics simulations,” *J. Am. Chem. Soc.*, vol. 125, no. 37, pp. 11340–11349, 2003.
- [5.43] D. J. Brockwell *et al.*, “Pulling geometry defines the mechanical resistance of a β -sheet protein,” *Nat. Struct. Mol. Biol.*, vol. 10, no. 9, p. 731, 2003.
- [5.44] S. Azadi, M. Tafazzoli-Shadpour, and R. Omidvar, “Steered Molecular Dynamics Simulation Study of Quantified Effects of Point Mutation Induced by Breast Cancer on Mechanical Behavior of E-Cadherin,” *Mol. Biol.*, vol. 52, no. 5, pp. 723–731, 2018.
- [5.45] H. Lu and K. Schulten, “Steered molecular dynamics simulations of force-induced protein domain unfolding,” *Proteins Struct. Funct. Bioinforma.*, vol. 35, no. 4, pp. 453–463, 1999.
- [5.46] C. Sun, T. Tang, and H. Uludag, “A molecular dynamics simulation study on the effect of lipid substitution on polyethylenimine mediated siRNA complexation,” *Biomaterials*, vol. 34, no. 11, pp. 2822–2833, Apr. 2013, doi: 10.1016/j.biomaterials.2013.01.011.
- [5.47] E. J. Denning, U. D. Priyakumar, L. Nilsson, and A. D. Mackerell, “Impact of 2'-hydroxyl sampling on the conformational properties of RNA: Update of the CHARMM all-atom additive force field for RNA,” *J. Comput. Chem.*, vol. 32, no. 9, pp. 1929–1943, Jul. 2011, doi: 10.1002/jcc.21777.
- [5.48] J. B. Klauda *et al.*, “Update of the CHARMM all-atom additive force field for lipids: validation on six lipid types,” *J. Phys. Chem. B*, vol. 114, no. 23, pp. 7830–7843, Jun. 2010, doi: 10.1021/jp101759q.

- [5.49] J. C. Phillips *et al.*, “Scalable molecular dynamics with NAMD,” *J. Comput. Chem.*, vol. 26, no. 16, pp. 1781–1802, Dec. 2005, doi: 10.1002/jcc.20289.
- [5.50] T. Darden, D. York, and L. Pedersen, “Particle mesh Ewald: An $N \cdot \log(N)$ method for Ewald sums in large systems,” *J. Chem. Phys.*, vol. 98, no. 12, pp. 10089–10092, Jun. 1993, doi: 10.1063/1.464397.
- [5.51] J.-P. Ryckaert, G. Ciccotti, and H. J. Berendsen, “Numerical integration of the cartesian equations of motion of a system with constraints: molecular dynamics of n-alkanes,” *J. Comput. Phys.*, vol. 23, no. 3, pp. 327–341, Mar. 1977, doi: 10.1016/0021-9991(77)90098-5.
- [5.52] G. J. Martyna, D. J. Tobias, and M. L. Klein, “Constant pressure molecular dynamics algorithms,” *J. Chem. Phys.*, vol. 101, no. 5, pp. 4177–4189, 1994.
- [5.53] S. E. Feller, Y. Zhang, R. W. Pastor, and B. R. Brooks, “Constant pressure molecular dynamics simulation: the Langevin piston method,” *J. Chem. Phys.*, vol. 103, no. 11, pp. 4613–4621, 1995.
- [5.54] W. Humphrey, A. Dalke, and K. Schulten, “VMD: Visual molecular dynamics,” *J. Mol. Graph.*, vol. 14, no. 1, pp. 33–38, Feb. 1996, doi: 10.1016/0263-7855(96)00018-5.
- [5.55] S. Garcia-Manyes, L. Redondo-Morata, G. Oncins, and F. Sanz, “Nanomechanics of Lipid Bilayers: Heads or Tails?,” *J. Am. Chem. Soc.*, vol. 132, no. 37, pp. 12874–12886, Sep. 2010, doi: 10.1021/ja1002185.
- [5.56] D. Bochicchio and L. Monticelli, “The Membrane Bending Modulus in Experiments and Simulations: A Puzzling Picture,” in *Advances in Biomembranes and Lipid Self-Assembly*, 1st ed., vol. 23, Elsevier Inc., 2016, pp. 117–143.
- [5.57] J. F. Nagle, “Experimentally determined tilt and bending moduli of single-component lipid bilayers,” *Chem. Phys. Lipids*, vol. 205, pp. 18–24, Jun. 2017, doi: 10.1016/j.chemphyslip.2017.04.006.
- [5.58] M. Doktorova, D. Harries, and G. Khelashvili, “Determination of bending rigidity and tilt modulus of lipid membranes from real-space fluctuation analysis of molecular dynamics simulations,” *Phys. Chem. Chem. Phys.*, vol. 19, no. 25, pp. 16806–16818, 2017.
- [5.59] L. L. Holte, S. A. Peter, T. M. Sinnwell, and K. Gawrisch, “ ^2H nuclear magnetic resonance order parameter profiles suggest a change of molecular shape for phosphatidylcholines containing a polyunsaturated acyl chain,” *Biophys. J.*, vol. 68, no. 6, pp. 2396–2403, 1995.
- [5.60] J. P. M. Jämbeck and A. P. Lyubartsev, “Derivation and systematic validation of a refined all-atom force field for phosphatidylcholine lipids,” *J. Phys. Chem. B*, vol. 116, no. 10, pp. 3164–3179, 2012.

- [5.61] A. Neamnark, O. Suwantong, R. B. K. C., C. Y. M. Hsu, P. Supaphol, and H. Uludağ, “Aliphatic Lipid Substitution on 2 kDa Polyethylenimine Improves Plasmid Delivery and Transgene Expression,” *Mol. Pharm.*, vol. 6, no. 6, pp. 1798–1815, Dec. 2009, doi: 10.1021/mp900074d.
- [5.62] W. H. Binder, “Polymer-Induced Transient Pores in Lipid Membranes,” *Angew. Chemie Int. Ed.*, vol. 47, no. 17, pp. 3092–3095, 2008.
- [5.63] Y. Shai, “Mechanism of the binding, insertion and destabilization of phospholipid bilayer membranes by α -helical antimicrobial and cell non-selective membrane-lytic peptides,” *Biochim. Biophys. Acta (BBA)-Biomembranes*, vol. 1462, no. 1–2, pp. 55–70, 1999.
- [5.64] N. Wilkosz *et al.*, “Effect of polycation structure on interaction with lipid membranes,” *J. Phys. Chem. B*, vol. 121, no. 30, pp. 7318–7326, 2017.
- [5.65] F. Y. Jiang, Y. Bouret, and J. T. Kindt, “Molecular Dynamics Simulations of the Lipid Bilayer Edge,” *Biophys. J.*, vol. 87, no. 1, pp. 182–192, Jul. 2004, doi: 10.1529/biophysj.103.031054.
- [5.66] W. C. Wimley and T. E. Thompson, “Transbilayer and interbilayer phospholipid exchange in dimyristoylphosphatidylcholine/dimyristoylphosphatidylethanolamine large unilamellar vesicles,” *Biochemistry*, vol. 30, no. 6, pp. 1702–1709, 1991.
- [5.67] A. A. Gurtovenko and I. Vattulainen, “Molecular mechanism for lipid flip-flops,” *J. Phys. Chem. B*, vol. 111, no. 48, pp. 13554–13559, 2007.
- [5.68] W. F. D. Bennett, N. Sapay, and D. P. Tieleman, “Atomistic Simulations of Pore Formation and Closure in Lipid Bilayers,” *Biophys. J.*, vol. 106, no. 1, pp. 210–219, Jan. 2014, doi: 10.1016/j.bpj.2013.11.4486.
- [5.69] N. Sapay, W. F. D. Bennett, and D. P. Tieleman, “Thermodynamics of flip-flop and desorption for a systematic series of phosphatidylcholine lipids,” *Soft Matter*, vol. 5, no. 17, p. 3295, 2009, doi: 10.1039/b902376c.
- [5.70] G. Van Meer, D. R. Voelker, and G. W. Feigenson, “Membrane lipids: Where they are and how they behave,” *Nat. Rev. Mol. Cell Biol.*, vol. 9, no. 2, pp. 112–124, 2008, doi: 10.1038/nrm2330.
- [5.71] P. A. Leventis and S. Grinstein, “The Distribution and Function of Phosphatidylserine in Cellular Membranes,” *Annu. Rev. Biophys.*, vol. 39, pp. 407–427, 2010, doi: 10.1146/annurev.biophys.093008.131234.
- [5.72] F.-X. Contreras, L. Sánchez-Magraner, A. Alonso, and F. M. Goñi, “Transbilayer (flip-flop) lipid motion and lipid scrambling in membranes,” *FEBS Lett.*, vol. 584, no. 9, pp. 1779–1786, May 2010, doi: 10.1016/j.febslet.2009.12.049.

- [5.73] R. A. Schlegel and P. Williamson, “Phosphatidylserine, a death knell,” *Cell Death Differ.*, vol. 8, no. 6, pp. 551–563, 2001.
- [5.74] J. Razzokov, M. Yusupov, S. Vanuytsel, E. C. Neyts, and A. Bogaerts, “Phosphatidylserine flip-flop induced by oxidation of the plasma membrane: a better insight by atomic scale modeling,” *Plasma Process. Polym.*, vol. 14, no. 10, pp. 1–6, 2017, doi: 10.1002/ppap.201700013.
- [5.75] C. Neale, W. F. D. Bennett, D. P. Tieleman, and R. Pomes, “Statistical convergence of equilibrium properties in simulations of molecular solutes embedded in lipid bilayers,” *J. Chem. Theory Comput.*, vol. 7, no. 12, pp. 4175–4188, 2011.
- [5.76] A. A. Gurtovenko, J. Anwar, and I. Vattulainen, “Defect-mediated trafficking across cell membranes: insights from in silico modeling,” *Chem. Rev.*, vol. 110, no. 10, pp. 6077–6103, 2010.
- [6.1] H. Uludag, A. Ubeda, and A. Ansari, “At the intersection of biomaterials and gene therapy: Progress in non-viral delivery of nucleic acids,” *Front. Bioeng. Biotechnol.*, vol. 7, p. 131, 2019.
- [6.2] C. Sun, T. Tang, and H. Uludağ, “Probing the Effects of Lipid Substitution on Polycation Mediated DNA Aggregation: A Molecular Dynamics Simulations Study,” *Biomacromolecules*, vol. 13, no. 9, pp. 2982–2988, Sep. 2012, doi: 10.1021/bm301045b.
- [6.3] A. P. Pandey and K. K. Sawant, “Polyethylenimine: A versatile, multifunctional non-viral vector for nucleic acid delivery,” *Mater. Sci. Eng. C*, vol. 68, pp. 904–918, Nov. 2016, doi: 10.1016/j.msec.2016.07.066.
- [6.4] D. Meneksedag-Erol, R. B. KC, T. Tang, and H. Uludağ, “A Delicate Balance When Substituting a Small Hydrophobe onto Low Molecular Weight Polyethylenimine to Improve Its Nucleic Acid Delivery Efficiency,” *ACS Appl. Mater. Interfaces*, vol. 7, no. 44, pp. 24822–24832, Nov. 2015, doi: 10.1021/acsami.5b07929.
- [6.5] Y. Nademi, T. Tang, and H. Uludağ, “Steered molecular dynamics simulations reveal a self-protecting configuration of nanoparticles during membrane penetration,” *Nanoscale*, vol. 10, no. 37, pp. 17671–17682, 2018, doi: 10.1039/C8NR04287J.
- [6.6] V. Incani, A. Lavasanifar, and H. Uludağ, “Lipid and hydrophobic modification of cationic carriers on route to superior gene vectors,” *Soft Matter*, vol. 6, no. 10, p. 2124, 2010, doi: 10.1039/b916362j.
- [6.7] H. M. Aliabadi, B. Landry, C. Sun, T. Tang, and H. Uludağ, “Supramolecular assemblies

- in functional siRNA delivery: where do we stand?," *Biomaterials*, vol. 33, no. 8, pp. 2546–2569, 2012.
- [6.8] D. Wang *et al.*, "Novel Branched Poly(Ethylenimine)–Cholesterol Water-Soluble Lipopolymers for Gene Delivery," *Biomacromolecules*, vol. 3, no. 6, pp. 1197–1207, Nov. 2002, doi: 10.1021/bm025563c.
- [6.9] P. Y. Teo *et al.*, "Hydrophobic modification of low molecular weight polyethylenimine for improved gene transfection," *Biomaterials*, vol. 34, no. 32, pp. 7971–7979, Oct. 2013, doi: 10.1016/j.biomaterials.2013.07.005.
- [6.10] A. Neamnark, O. Suwanton, R. B. K. C., C. Y. M. Hsu, P. Supaphol, and H. Uludağ, "Aliphatic Lipid Substitution on 2 kDa Polyethylenimine Improves Plasmid Delivery and Transgene Expression," *Mol. Pharm.*, vol. 6, no. 6, pp. 1798–1815, Dec. 2009, doi: 10.1021/mp900074d.
- [6.11] C. Sun, T. Tang, and H. Uludag, "A molecular dynamics simulation study on the effect of lipid substitution on polyethylenimine mediated siRNA complexation," *Biomaterials*, vol. 34, no. 11, pp. 2822–2833, Apr. 2013, doi: 10.1016/j.biomaterials.2013.01.011.
- [6.12] C. Sun, T. Tang, and H. Uludağ, "Molecular Dynamics Simulations for Complexation of DNA with 2 kDa PEI Reveal Profound Effect of PEI Architecture on Complexation," *J. Phys. Chem. B*, vol. 116, no. 8, pp. 2405–2413, Mar. 2012, doi: 10.1021/jp211716v.
- [6.13] R. Perkins, H. Fang, W. Tong, and W. J. Welsh, "Quantitative structure-activity relationship methods: Perspectives on drug discovery and toxicology," *Environ. Toxicol. Chem. An Int. J.*, vol. 22, no. 8, pp. 1666–1679, 2003.
- [6.14] R. Weissleder, K. Kelly, E. Y. Sun, T. Shtatland, and L. Josephson, "Cell-specific targeting of nanoparticles by multivalent attachment of small molecules," *Nat. Biotechnol.*, vol. 23, no. 11, pp. 1418–1423, 2005.
- [6.15] D. Fourches *et al.*, "Quantitative nanostructure– activity relationship modeling," *ACS Nano*, vol. 4, no. 10, pp. 5703–5712, 2010.
- [6.16] D. A. Winkler *et al.*, "Modelling and predicting the biological effects of nanomaterials," *SAR QSAR Environ. Res.*, vol. 25, no. 2, pp. 161–172, 2014.
- [6.17] H. M. Aliabadi *et al.*, "A systematic comparison of lipopolymers for siRNA delivery to multiple breast cancer cell lines: In vitro studies," *Acta Biomater.*, vol. 102, pp. 351–366, 2020.

- [6.18] H. Montazeri Aliabadi, B. Landry, P. Mahdipoor, and H. Uludağ, “Induction of Apoptosis by Survivin Silencing through siRNA Delivery in a Human Breast Cancer Cell Line,” *Mol. Pharm.*, vol. 8, no. 5, pp. 1821–1830, Oct. 2011, doi: 10.1021/mp200176v.
- [6.19] D. N. Meenakshi Sundaram, C. Kucharski, M. B. Parmar, R. B. KC, and H. Uludağ, “Polymeric Delivery of siRNA against Integrin-β1 (CD29) to Reduce Attachment and Migration of Breast Cancer Cells,” *Macromol. Biosci.*, vol. 17, no. 6, p. 1600430, 2017.
- [6.20] H. M. Aliabadi, R. Maranchuk, C. Kucharski, P. Mahdipoor, J. Hugh, and H. Uludağ, “Effective response of doxorubicin-sensitive and-resistant breast cancer cells to combinational siRNA therapy,” *J. Control. Release*, vol. 172, no. 1, pp. 219–228, 2013.
- [6.21] S. Plianwong, B. Thapa, R. B. Kc, C. Kucharski, T. Rojanarata, and H. Uludağ, “Enabling Combinatorial siRNA Delivery against Apoptosis-Related Proteins with Linoleic Acid and α-Linoleic Acid Substituted Low Molecular Weight Polyethylenimines,” *Pharm. Res.*, vol. 37, no. 3, p. 46, 2020.
- [6.22] S. Xiang *et al.*, “Uptake mechanisms of non-viral gene delivery,” *J. Control. Release*, vol. 158, no. 3, pp. 371–378, Mar. 2012, doi: 10.1016/j.jconrel.2011.09.093.
- [6.23] B. Thapa, R. Bahadur KC, and H. Uludağ, “Novel targets for sensitizing breast cancer cells to TRAIL-induced apoptosis with siRNA delivery,” *Int. J. cancer*, vol. 142, no. 3, pp. 597–606, 2018.
- [6.24] X. Zhang, Y. Yu, L. Wang, and Q. Gu, “Learning one-hidden-layer relu networks via gradient descent,” in *The 22nd International Conference on Artificial Intelligence and Statistics*, 2019, pp. 1524–1534.
- [6.25] M. Boeckle, S. , von Gersdorff, K. , van der Piepen, S. , Culmsee, C. , Wagner, E. and Ogris, “Purification of polyethylenimine polyplexes highlights the role of free polycations in gene transfer,” *J. Gene Med.*, vol. 6, pp. 1102–1111, 2004, doi: 10.1002/jgm.598.
- [6.26] H. M. Aliabadi, B. Landry, P. Mahdipoor, C. Y. M. Hsu, and H. Uludağ, “Effective down-regulation of Breast Cancer Resistance Protein (BCRP) by siRNA delivery using lipid-substituted aliphatic polymers,” *Eur. J. Pharm. Biopharm.*, vol. 81, no. 1, pp. 33–42, May 2012, doi: 10.1016/j.ejpb.2012.01.011.
- [6.27] D. J. Gary, N. Puri, and Y.-Y. Won, “Polymer-based siRNA delivery: perspectives on the fundamental and phenomenological distinctions from polymer-based DNA delivery,” *J. Control. Release*, vol. 121, no. 1–2, pp. 64–73, 2007.

- [6.28] A.-L. Bolcato-Bellemin, M.-E. Bonnet, G. Creusat, P. Erbacher, and J.-P. Behr, “Sticky overhangs enhance siRNA-mediated gene silencing,” *Proc. Natl. Acad. Sci.*, vol. 104, no. 41, pp. 16050–16055, 2007.
- [6.29] R. B. KC, C. Kucharski, and H. Uludağ, “Additive nanocomplexes of cationic lipopolymers for improved non-viral gene delivery to mesenchymal stem cells,” *J. Mater. Chem. B*, vol. 3, no. 19, pp. 3972–3982, 2015.
- [7.1] D. P. Tieleman, H. Leontiadou, A. E. Mark, and S.-J. Marrink, “Simulation of Pore Formation in Lipid Bilayers by Mechanical Stress and Electric Fields,” *J. Am. Chem. Soc.*, vol. 125, no. 21, pp. 6382–6383, May 2003, doi: 10.1021/ja029504i.
- [7.2] M. Sud *et al.*, “LMSD: LIPID MAPS structure database,” *Nucleic Acids Res.*, vol. 35, no. suppl_1, pp. D527–D532, Nov. 2006, doi: 10.1093/nar/gkl838.
- [7.3] P. A. Leventis and S. Grinstein, “The Distribution and Function of Phosphatidylserine in Cellular Membranes,” *Annu. Rev. Biophys.*, vol. 39, pp. 407–427, 2010, doi: 10.1146/annurev.biophys.093008.131234.
- [7.4] F.-X. Contreras, L. Sánchez-Magraner, A. Alonso, and F. M. Goñi, “Transbilayer (flip-flop) lipid motion and lipid scrambling in membranes,” *FEBS Lett.*, vol. 584, no. 9, pp. 1779–1786, May 2010, doi: 10.1016/j.febslet.2009.12.049.
- [7.5] G. Van Meer, D. R. Voelker, and G. W. Feigenson, “Membrane lipids: Where they are and how they behave,” *Nat. Rev. Mol. Cell Biol.*, vol. 9, no. 2, pp. 112–124, 2008, doi: 10.1038/nrm2330.
- [7.6] S. J. Marrink, V. Corradi, P. C. T. Souza, H. I. Ingólfsson, D. P. Tieleman, and M. S. P. Sansom, “Computational Modeling of Realistic Cell Membranes,” *Chem. Rev.*, vol. 119, no. 9, pp. 6184–6226, May 2019, doi: 10.1021/acs.chemrev.8b00460.
- [7.7] R. A. Schlegel and P. Williamson, “Phosphatidylserine, a death knell,” *Cell Death Differ.*, vol. 8, no. 6, pp. 551–563, 2001.
- [7.8] J. Razzokov, M. Yusupov, S. Vanuytsel, E. C. Neyts, and A. Bogaerts, “Phosphatidylserine flip-flop induced by oxidation of the plasma membrane: a better insight by atomic scale modeling,” *Plasma Process. Polym.*, vol. 14, no. 10, pp. 1–6, 2017, doi: 10.1002/ppap.201700013.
- [7.9] H. M. Aliabadi, B. Landry, C. Sun, T. Tang, and H. Uludağ, “Supramolecular assemblies in functional siRNA delivery: where do we stand?,” *Biomaterials*, vol. 33, no. 8, pp. 2546–2569, 2012.
- [7.10] Y. Sugita and Y. Okamoto, “Replica-exchange molecular dynamics method for protein folding,” *Chem. Phys. Lett.*, vol. 314, no. 1–2, pp. 141–151, 1999.
- [7.11] S. Park, F. Khalili-Araghi, E. Tajkhorshid, and K. Schulten, “Free energy calculation from steered molecular dynamics simulations using Jarzynski’s equality,” *J. Chem. Phys.*, vol. 119, no. 6, pp. 3559–3566, Aug. 2003, doi: 10.1063/1.1590311.

- [7.12] C. Tsallis and D. A. Stariolo, “Generalized simulated annealing,” *Phys. A Stat. Mech. its Appl.*, vol. 233, no. 1–2, pp. 395–406, 1996.
- [7.13] M. Levitt, “A simplified representation of protein conformations for rapid simulation of protein folding,” *J. Mol. Biol.*, vol. 104, no. 1, pp. 59–107, 1976.
- [7.14] H. M. Aliabadi *et al.*, “A systematic comparison of lipopolymers for siRNA delivery to multiple breast cancer cell lines: In vitro studies,” *Acta Biomater.*, vol. 102, pp. 351–366, 2020.

APPENDIX A: Supplementary Information for Chapter 3

A.1. Simulation of CA-NP with a Different Initial Configuration

The initial structure of CA-NP discussed in Chapter 3 was generated from a previous study[1] where the original system contained 4 siRNAs and 18 PEI molecules. Two siRNAs and 6 PEIs were selected from the original system (already equilibrated) and the COM distance between the 2 siRNA molecules was 32.5 Å. In Section 3.3.1 of Chapter 3, it was observed that the CA-NP had a much looser structure compared with native NP and LA-NP. To ensure that this is not caused by the specific initial configuration, we conducted a separate simulation with a more compact initial CA-NP structure. This structure also contained 2 siRNAs and 6 PEIs, but the initial COM distance between the siRNAs was much closer (27 Å).

Figure A.1 shows R_g of the CA-NP and COM distance between the 2 siRNAs as a function of simulation time for this new simulation. The horizontal time axis starts at 5 ns since the NP is subjected to restrained simulations with little structural changes during the first 5 ns. It is observed that R_g has an initial increase and decrease during the first 15 ns of the simulation, but ultimately reaches a stable value of 25.45 ± 0.338 Å (data collected from the last 20 ns). The COM distance has a stable value during the first 15 ns of the simulation followed by an increasing trend, indicating siRNA molecules are moving apart compared to their starting configuration. The COM distance averaged over the last 20 ns is 29.33 ± 0.556 Å. The final equilibrium values of R_g and COM distance are close to those given in the main text which resulted from a very different initial configuration. Therefore, it can be concluded that the looser structure of CA-NP, compared with native NP and LA-NP, is not caused by the specific initial configuration but rather due to the steric hindrance of the bridging PEIs.

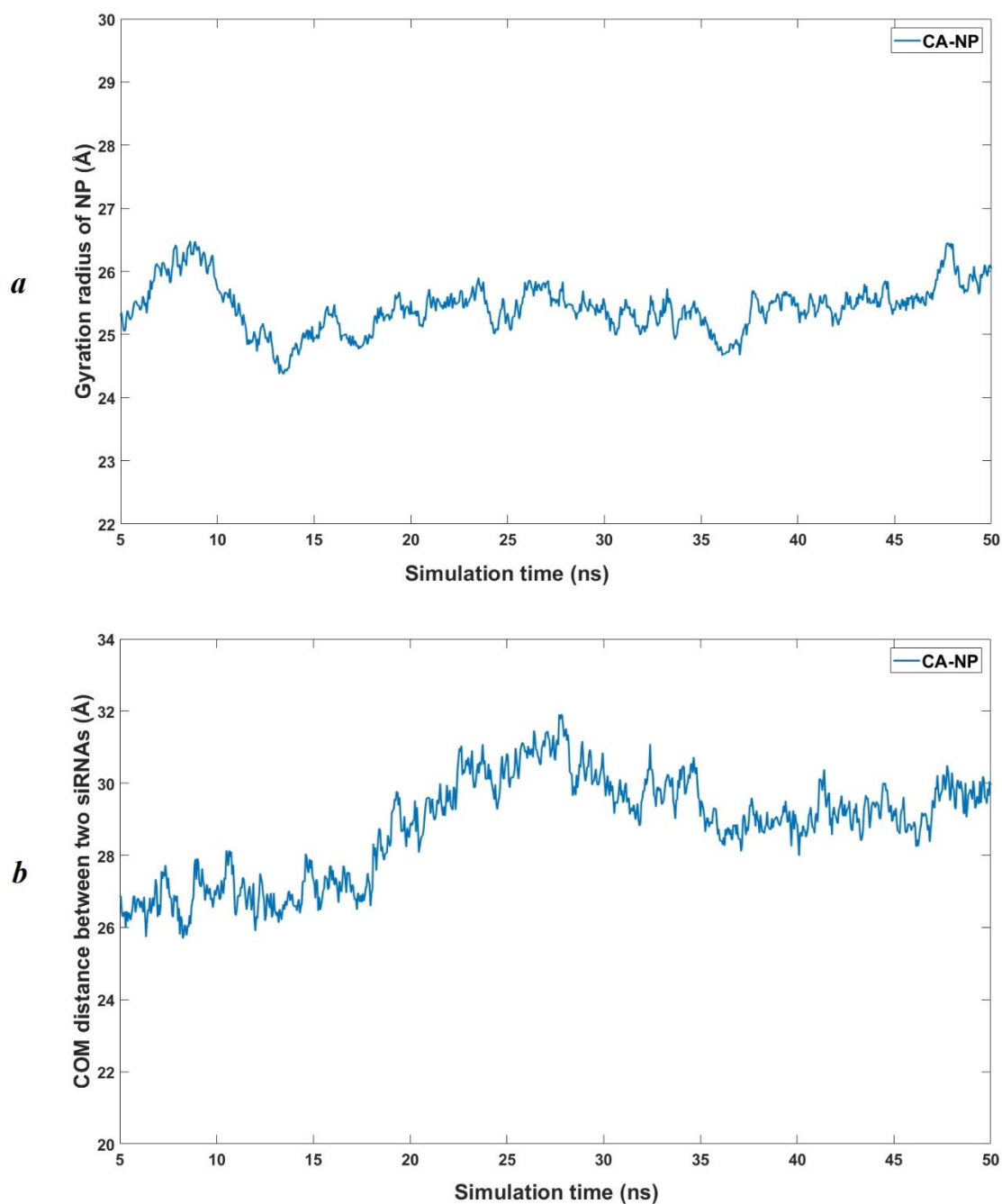


Figure A.1. Time evolution of (a) gyration radius (b) COM distance between the two siRNA molecules in CA-NP with the new initial configuration.

A.2. Number of Water-Membrane HB and Water-NP HB

In Section 3.3.2 of Chapter 3, the number of HB between NPs and membrane have been discussed. Here we show the number of HB between water and the membrane, and between water and the NPs (Figure A.2). Number of HB between the membrane and water has an almost constant value during approach and attachment stages followed by an increase during embedment and detachment stages (Figure A.2a). The increasing trend indicates that initially the membrane surface was not saturated with the water due to the NP above the membrane. As the NP is pulled through the membrane to create a pore, the membrane molecules become more exposed to water, leading to formation of more HB between them.

Number of HB between water and the NP (Figure A.2b) also has an almost constant value during approach stage, followed by a decrease during attachment and embedment stages, and ultimately an increasing trend during detachment stage. The initial constant value is caused by the lack of interaction between the NP and the membrane so that the NP can maintain its interaction with surrounding waters. As the NP interacts with the membrane, increase in HB between the NP and the membrane causes the HB between water and the NP to decrease. During detachment, number of HB between water and the NP increases again, which is consistent with the decrease of HB between the membrane and NP.

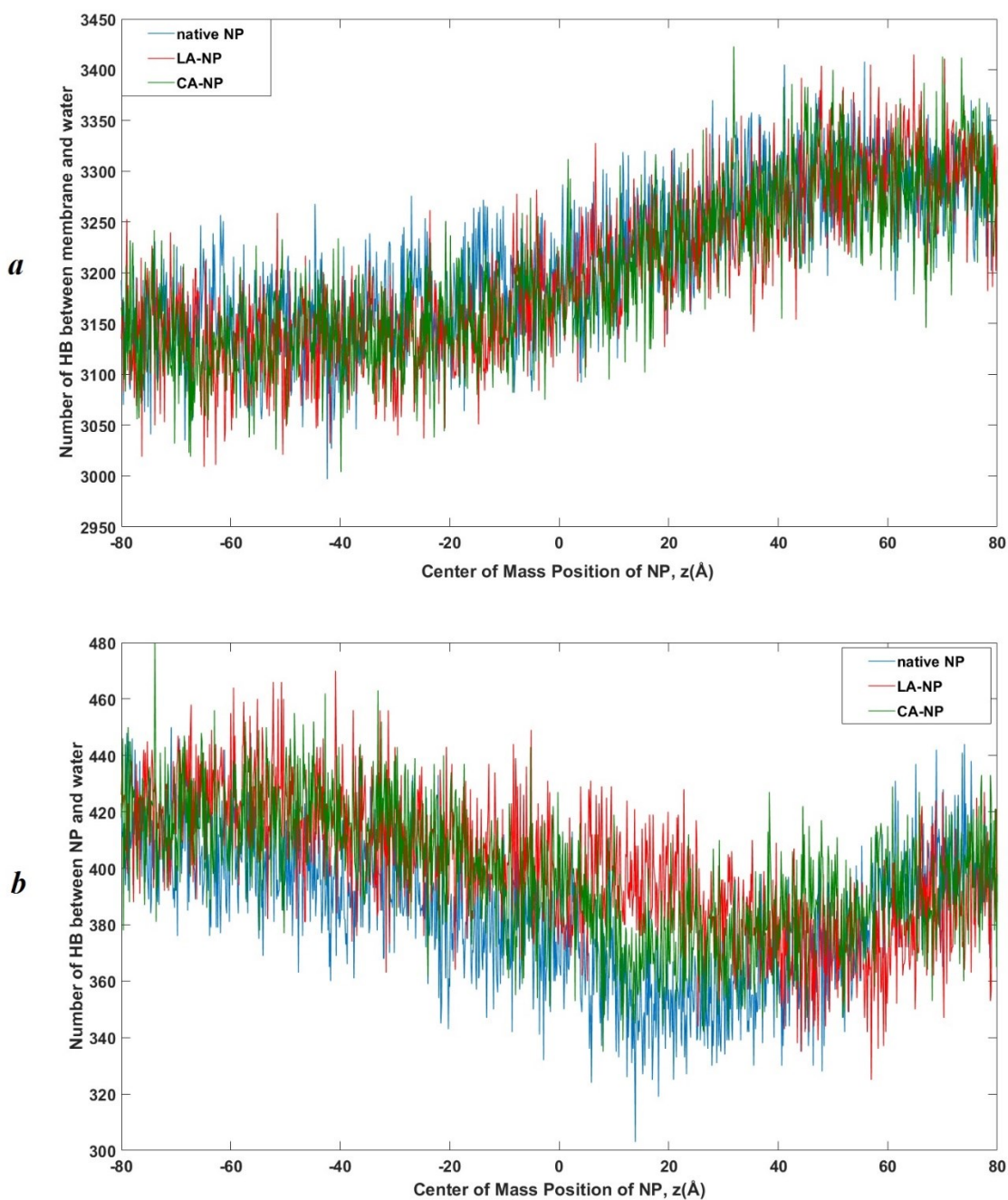


Figure A.2. Number of HB (*a*) between water and the membrane, and (*b*) between water and the NPs as functions of COM position of the NP.

A.3. Membrane Deformation during NP Penetration

Figure A.3 shows the z and x positions of phosphate (P) atoms of the membrane at selected time during the penetration. For clarity the position of other membrane atoms are not shown. Similar trends of membrane deformation are observed for native NP, CA-NP and LA-NP, where the P atoms rearranged themselves to interact with the polar amine groups of the NPs, and this led to pore formation that allowed the NP and water to cross the membrane. At the end of the penetration process (Figure A.3c), the LA-NP has pulled out some lipids which can be seen from the presence of some P atoms at very low locations along the z -axis. This phenomenon is consistent with Figure 3.4b in Chapter 3 where HB counts between NP and the membrane is higher for the LA-NP indicating stronger contact between LA-NP and the membrane.

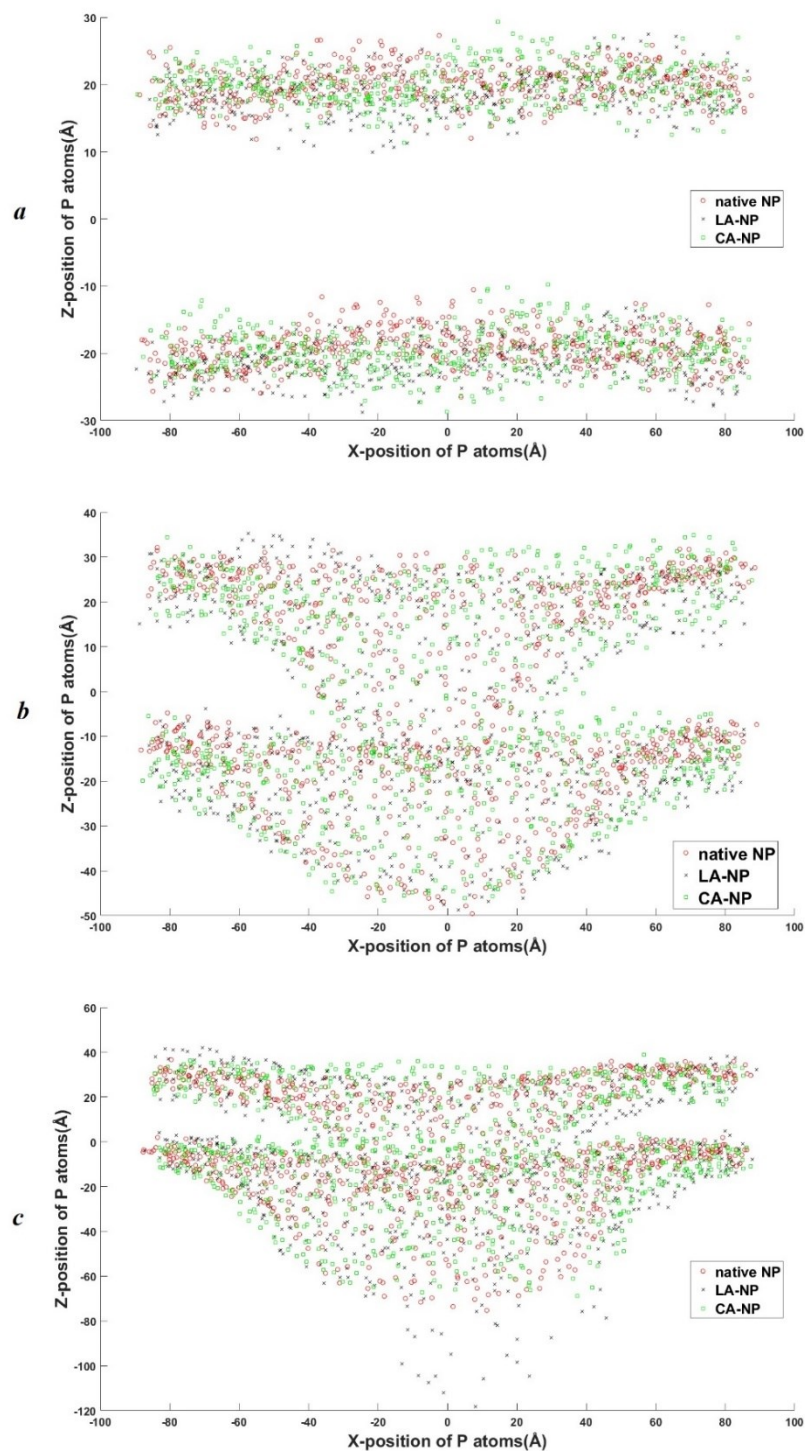


Figure A.3. Position of phosphate (P) atoms of the membrane at selected time of the penetration process: (a) 0 ns, COM of NP at -80\AA , (b) 30 ns, COM of NP at -4\AA , and (c) 64 ns, COM of NP at 80\AA .

A.4. Relative Orientation of siRNAs

In Section 3.3.3 of Chapter 3, the relative orientation of the 2 siRNAs was monitored by measuring the angle (θ) between two vectors each defined in one siRNA. This vector was defined by connecting two atoms at the opposite ends of the siRNA, which are C1' of the 18th residue in each strand. These vectors are schematically shown in Figure A.4. We then measured the angle θ between the two vectors as a function of COM position of the NP.

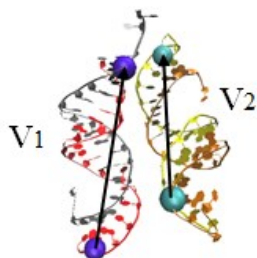


Figure A.4: Schematic representative of defined vectors. Each color represent one strand of siRNA molecules. The spheres are C_1' atoms of the 18th residue in each strand.

A.5. Angle between siRNAs of NPs and Unperturbed Membrane Surface

In Section 3.4.1 of Chapter 3, the angle between each siRNA of the NPs and the unperturbed membrane surface is shown (Figure 3.7) at four locations where snapshots in Figure 3.5 are taken. Here, we show this angle during the entire penetration process (Figure A.5). For all the three systems, we have observed the rotation of each siRNA from its relatively upright initial configuration to a relatively parallel orientation during embedment, and returning to a relatively upright orientation again during detachment. The upright orientation is more evident in native NP and CA-NP than in LA-NP.

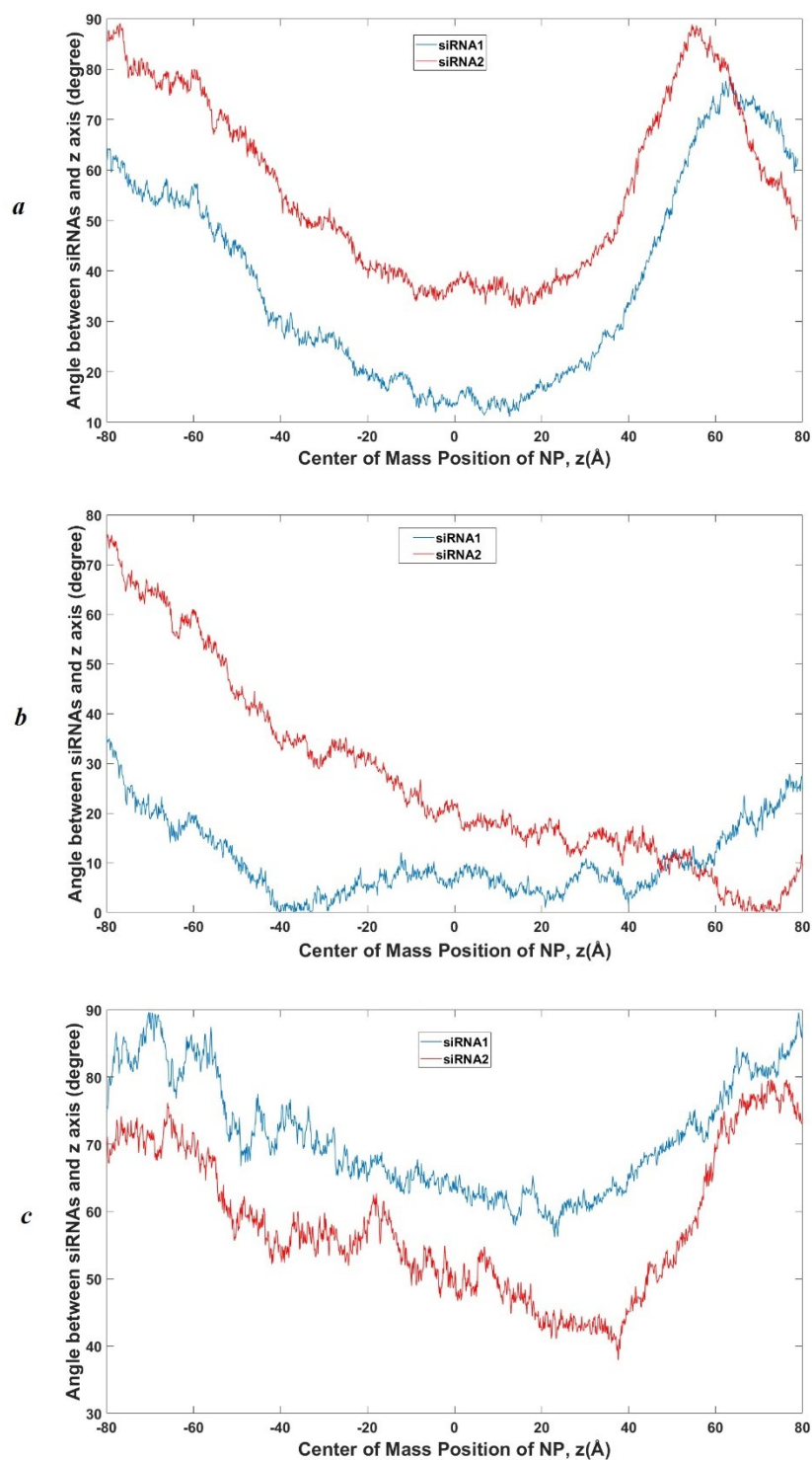


Figure A.5. Angle between each siRNA and the unperturbed membrane surface during the penetration process for (a) native NP, (b) LA-NP and (c) CA-NP.

A.6. Pore Resealing after Restraint Removal

A series of MD simulations were performed in absence of the pulling force on the NPs. In particular, for each NP, two configurations obtained from the SMD simulation were selected: (I) one corresponding to maximum compaction of the NP (minimum R_g) and (II) one from the end of the SMD simulation. Each configuration was used as the initial configuration for a MD simulation in which the restraint on the COM of NP was removed and the system was simulated for 20 ns. The time evolutions of COM position of the NP, R_g of the NP, COM distance between the two siRNA molecules and relative angle between the two siRNA molecules were monitored. Figure A.6 shows the results for initial configuration (I), and Figure A.7 shows the results for initial configuration (II).

For all the three systems, COM position of NP (Figure A.6a) decreases with time, indicating that once the pulling force is removed the NP is repelled from the membrane and hence the induced pore is unstable. During the NP's separation from the membrane, R_g of each NP (Figure A.6b) increases and the increase is more noticeable for LA-NP. For LA-NP and native NP, the COM distance between the siRNAs slightly rises (Figure A.6c), while it decreases for CA-NP. For all three systems, the relative angle between the siRNAs (Figure A.6d) shows an insignificant change. Similar repulsion of NP by the membrane is also observed in Figure A.7 with initial configuration (II). CA-NP has a slight reduction in R_g , while the change is insignificant for LA-NP and Native NP. COM distance between the siRNAs is relatively stable for Native NP, while increases slightly for LA-NP and CA-NP. For all three NPs, the change in relative angle between the siRNAs (Figure A.6d) is insignificant.

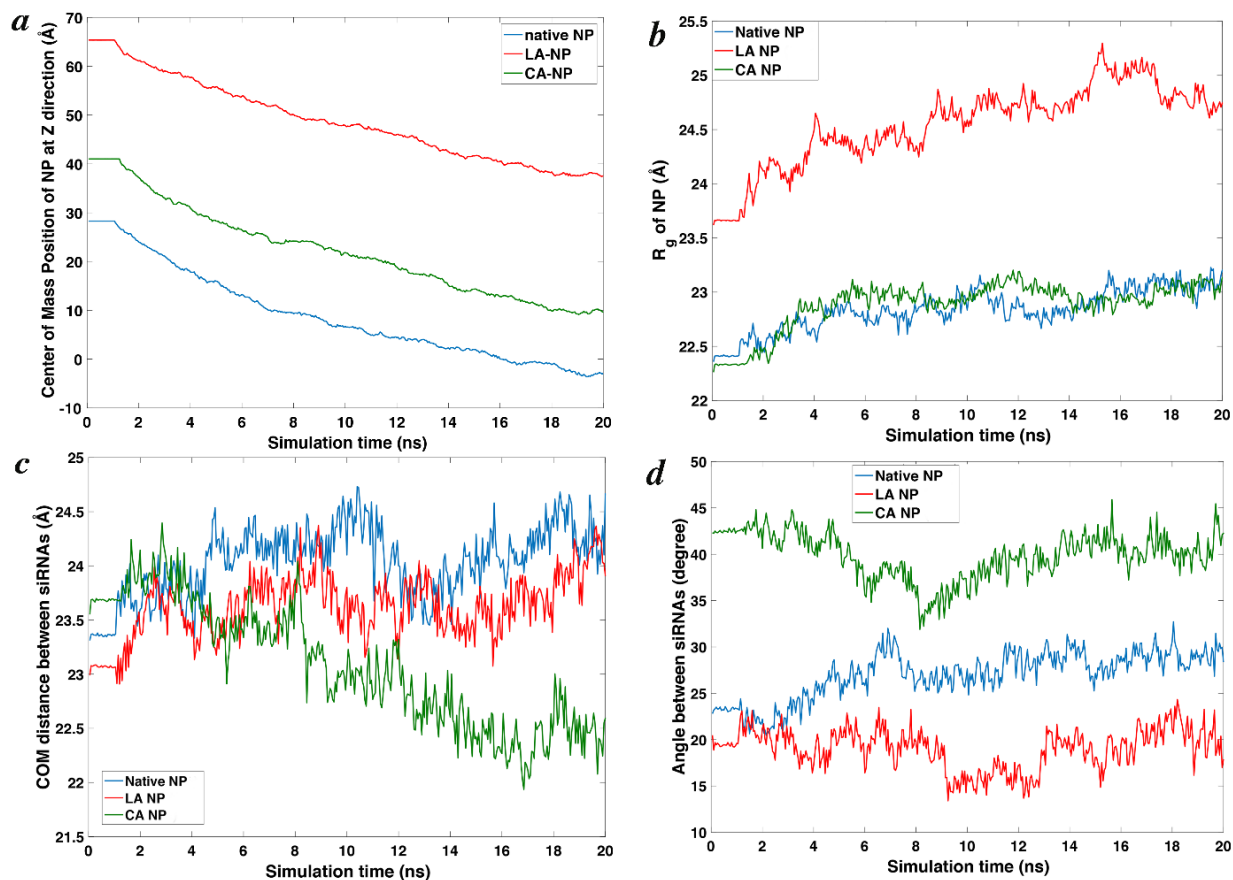


Figure A.6. (a) COM position of NP, (b) Gyration radius of the NP, (c) COM distance between the two siRNA molecules, and (d) Relative angle between the two siRNA molecules, each as a function of simulation time during the standard MD simulation. The initial configurations for these simulation were selected from the SMD simulation at the maximum compaction of the NP.

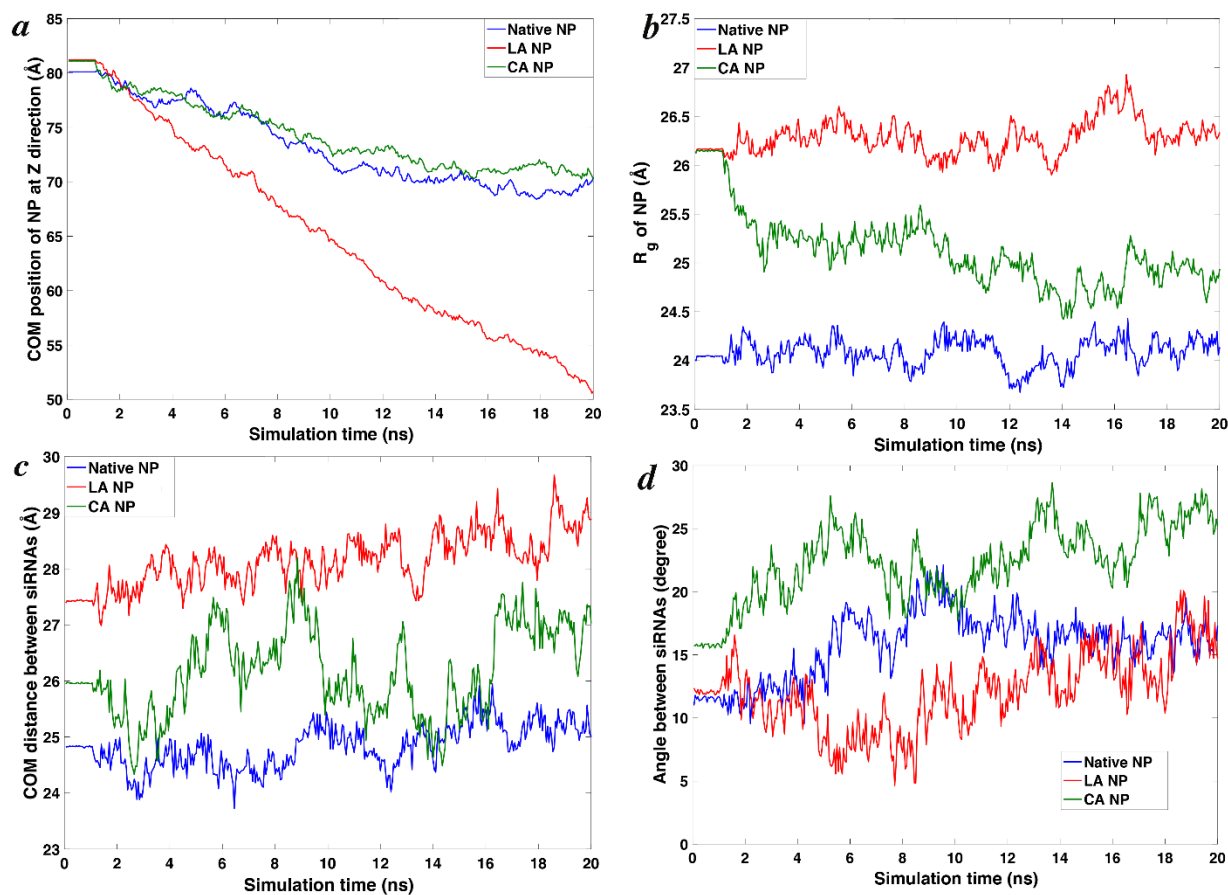


Figure A.7. (a) COM position of NP, (b) Gyration radius of the NP, (c) COM distance between the two siRNA molecules, and (d) Relative angle between the two siRNA molecules, each as a function of simulation time during the standard MD simulation. The initial configurations for these simulations were selected from the end of the SMD simulation.

A.7. Sensitivity of Result to Pulling Speed

To evaluate the sensitivity of our result to the pulling speed, we performed a series of SMD simulations on the CA-NP using two other speeds of 5 Å/ns and 10 Å/ns (usual pulling speed was 2.5 Å/ns). Figure A.8 displays the force profile, R_g , the siRNA separation distance and relative angle between siRNAs as functions of COM position of the CA-NP. The results show that while the magnitude of the force rises upon increase in the pulling speed, the qualitative behavior of the CA-NP is the same irrespective of the pulling speed. Importantly, the same behavior was observed at all pulling speeds for the gyration radius (compaction of CA-NP), siRNA separation distance, and change in the relative angle between the siRNAs (siRNA alignment).

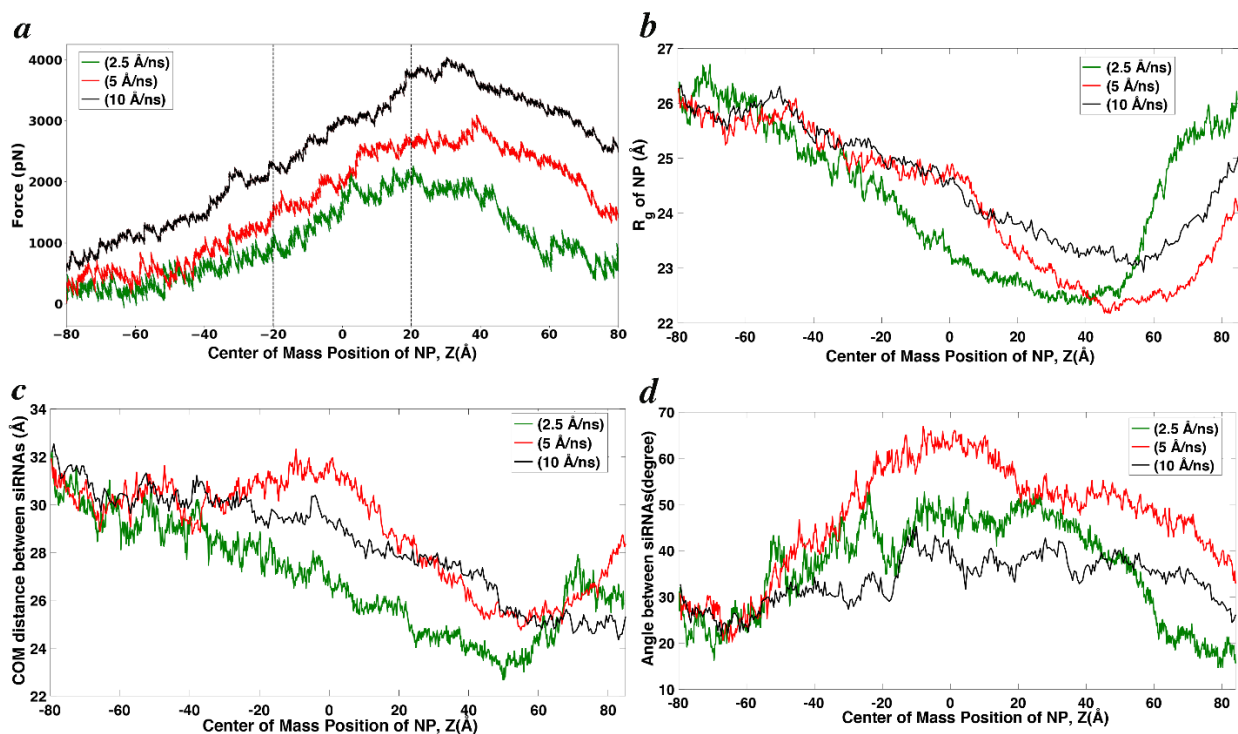


Figure A.8. (a) Force profile (b) Gyration radius (c) COM distance between the two siRNA molecules, and (d) Relative angle between the two siRNA molecules, each as a function of the NP COM. All simulations are for the CA-NP.

A.8. References

- [1] C. Sun, T. Tang, and H. Uludag, “A molecular dynamics simulation study on the effect of lipid substitution on polyethylenimine mediated siRNA complexation,” *Biomaterials*, vol. 34, no. 11, pp. 2822–2833, Apr. 2013, doi: 10.1016/j.biomaterials.2013.01.011.

APPENDIX B: Supplementary Information for Chapter 4

B.1. Structural parameters for the two types of NPs and two membranes.

In Section 4.3.3 of Chapter 4, structural parameters of NPs have been discussed. Here, Table B.1 summarizes the changes in the structural parameters for the two types of NPs and two membranes.

Table B.1. Changes in structural parameters of PEI/siRNA NPs during four stages of membrane crossing process. Key differences between POPS and POPC membranes are shown in red color.

NP	MEMBRANE MODEL	PARAMETER	APPROACH	ATTACHMENT	EMBEDMENT	DETACHMENT
PEI NP	POPS	R_g	Relatively constant	Decrease	Decrease	Increase to 1.5 Å larger than initial value
	POPC		Relatively constant	Decrease	Decrease	Increase to initial value
PEI-LA NP	POPS		Relatively constant	Decrease	Decrease	Increase to initial value
	POPC		Relatively constant	Decrease	Decrease	Increase to 1 Å larger than initial value
PEI NP	POPS	COM distance between siRNAs	Relatively constant	Relatively constant	Relatively constant	Increase to much larger than initial value
	POPC		Relatively constant	Relatively constant	Decrease	Increase to initial value
PEI-LA NP	POPS		Relatively constant	Relatively constant	Relatively constant	Slightly decrease
	POPC		Relatively constant	Relatively constant	Slightly decrease	Relatively constant
PEI NP	POPS	Angle between siRNAs	Relatively constant	Relatively constant	Relatively constant	Increase to 15 degree more than initial value
	POPC		Relatively constant	Slightly increase	Slightly increase	Decrease to initial value
PEI-LA NP	POPS		Relatively constant	Relatively constant	Decrease	Decrease to almost parallel orientation
	POPC		Relatively constant	Slightly decrease	Decrease	Decrease to almost parallel orientation

B.2. Number of hydrogen bonds (HBs) between siRNAs and PEI molecules

In section 4.3.3 of the Chapter 4, the number of PEI N atoms within 4 Å of any N/O atoms of siRNA as a function of COM position of NP have been discussed. Here, Figure B.1 and Figure B.2 show the number of HBs between PEIs and siRNA molecules as a function of COM position of NP for POPS and POPC membranes, respectively. Compared with Figure 4.6 and Figure 4.7 of Chapter 4, the trend of the curves remain the same.

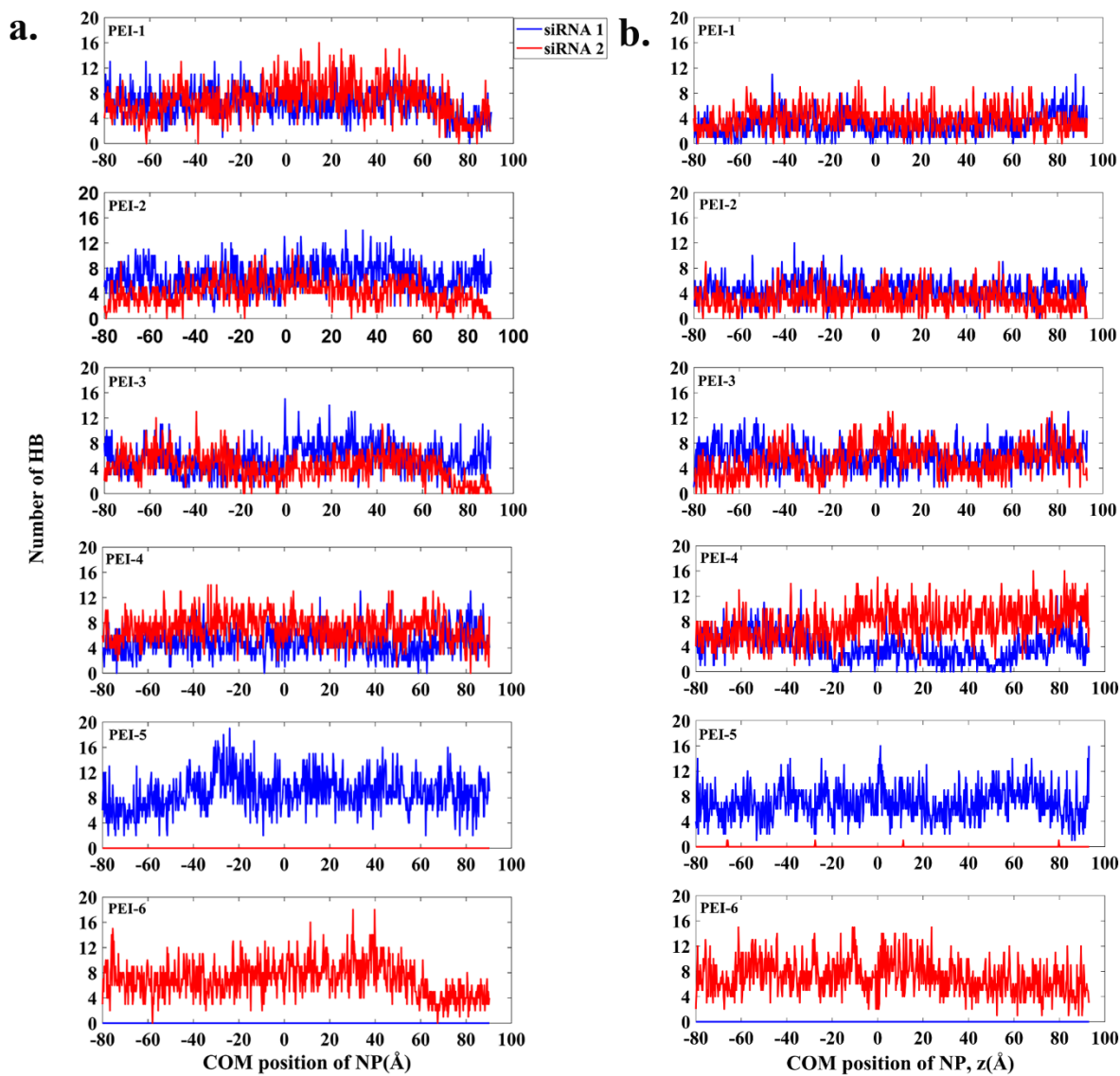


Figure B.1. Number of HBs between PEIs and siRNA molecules as a function of COM position of NP while crossing the POPS membrane, (a) PEI NP and (b) PEI-LA NP.

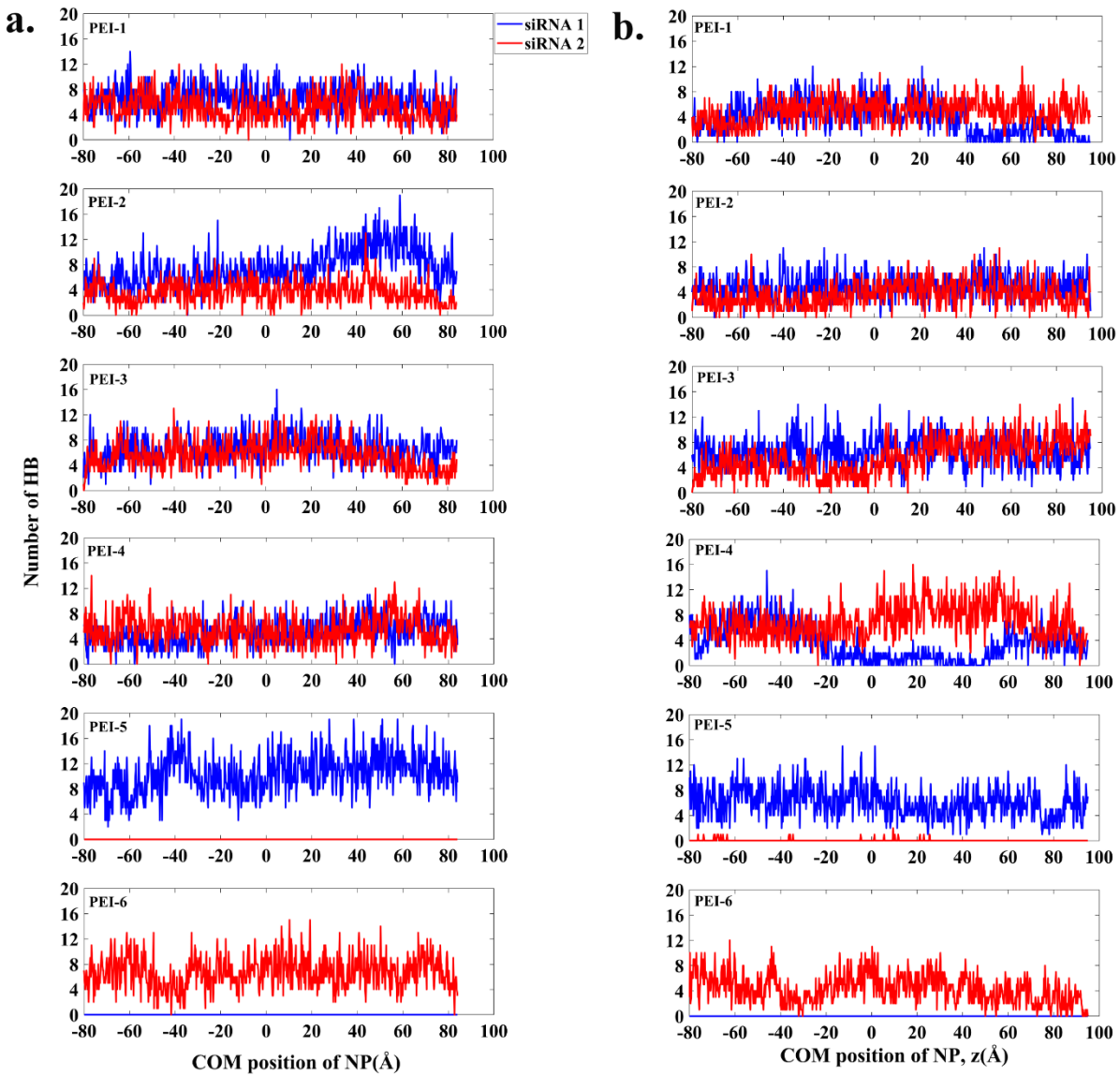


Figure B.2. Number of HBs between PEIs and siRNA molecules as a function of COM position of NP while crossing the POPC membrane, (a) PEI NP and (b) PEI-LA NP.

B.3. Number of membrane-NP hydrogen bonds (HBs)

In Section 4.4 of Chapter 4, correlation between force profiles and HBs between NPs and membranes have been discussed. Here, Figure B.3 shows the number of HBs between each NP and membranes. For both NP and membranes, the number of HBs is zero during the approach stage. During attachment and embedment, the number of HBs between NP and membrane increases, and finally during detachment, the number of HBs display a decreasing trend. For both NPs, number of HBs formed between NP and the POPS membrane is higher than between NP and the POPC membrane, suggesting that interaction between NPs and the POPS is stronger than that of POPC membrane.

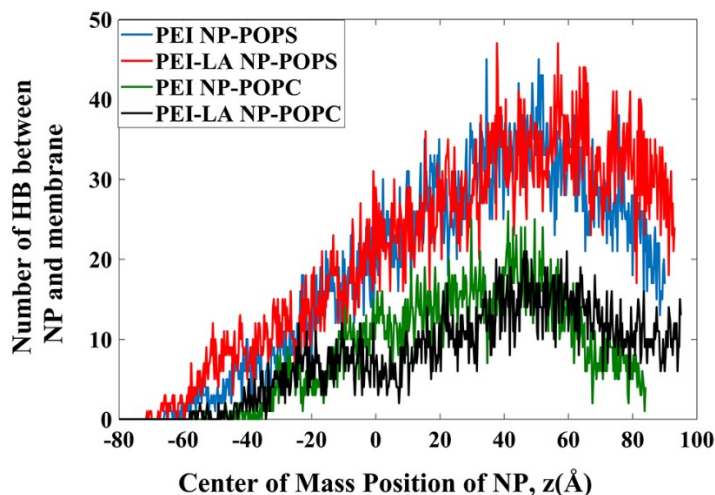


Figure B.3. Number of HBs between NPs and membranes as a function of COM position of the NP.

B.4. Lipid associations between PEIs of PEI-LA NPs

In Section 4.4 of Chapter 4, lipid associations between the PEIs of PEI-LA NP have been discussed. Here, Figure B.4 shows the lipid associations between the PEIs of PEI-LA NP and membranes. Lipid associations is quantified based on the number of pairs of lipid Cs that are closer than 5 Å between each pair of PEIs. The 5 Å limit is based on the closest carbon-carbon distance within which the free energy for the association of two alkane molecules is negative, and therefore, association is energetically favorable[1]. Considering that the LA lipid has 18 carbons and each PEI of PEI-LA NP has 3 substitutions, all possible pairing of carbons between two PEIs would be 2916. During approach and attachment stage, the associations is stable for both membranes, followed by a decreasing trend during detachment, in which associations are completely lost in POPC membrane, while it is strongly weakened in the POPS membrane.

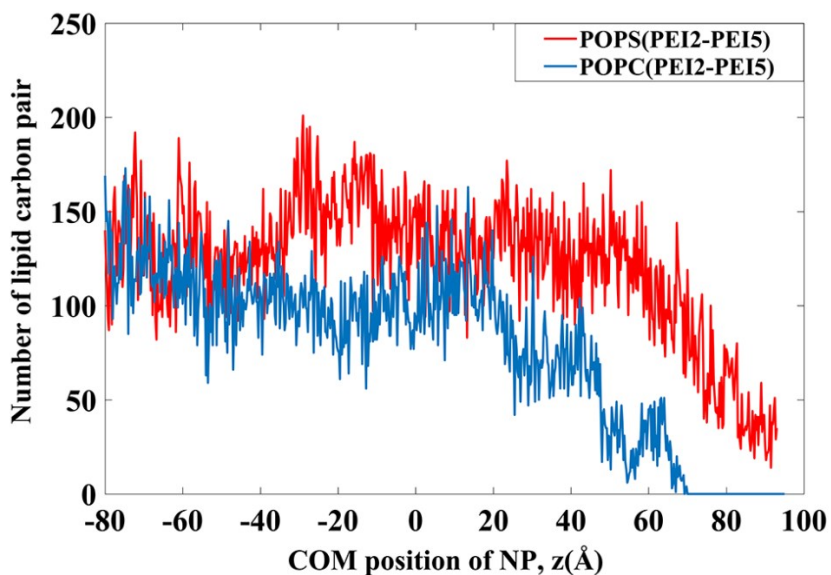


Figure B.4. Number of LA lipid carbon pairs that are closer than 5 Å between PEI-2 and PEI-5 of PEI-LA NP as a function of COM position of NP.

B.5. References

- [1] C. Sun, T. Tang, and H. Uludağ, “Probing the Effects of Lipid Substitution on Polycation Mediated DNA Aggregation: A Molecular Dynamics Simulations Study,” *Biomacromolecules*, vol. 13, no. 9, pp. 2982–2988, Sep. 2012, doi: 10.1021/bm301045b.

APPENDIX C: Supplementary Information for Chapter 5

C1. Equilibration of isolated NPs

NPs were subjected to 40 ns of equilibration at 323K. Figure C1 shows the initial (left) and final (right) equilibrated configurations of PEI and PEI-LA NPs in the absence of the membrane. Time evolution of the gyration radius of the NPs (R_g) and center of mass distance between the siRNAs (d_{COM}) are shown in Figure C.2a and Figure C.2b, respectively. For the PEI NP, R_g was rather constant (~ 24 Å), but d_{COM} increased from 25 Å to ~ 27 Å, indicating that the siRNAs formed a looser configuration at higher temperature. For the PEI-LA NP, R_g displayed a 0.5 Å reduction compared with its starting value (25 Å), while d_{COM} was relatively constant. This indicates that PEI-LA NP became more compacted through its lipid-substituted PEIs. It was shown by *Sun et al.* [1] that lipid-substituted PEIs formed associations among their lipids, which increased the stability of NP. Here, for both NPs, higher temperature increased the dynamics of the PEIs. For PEI-LA NP, lipid associations between PEIs increased. Specifically, lipids from two pairs of PEIs formed association at the end of equilibration, in comparison to 1 pair of PEIs at the start. PEI NP, on the other hand, lacked lipid associations, making it more susceptible to structural loosening at higher temperature.

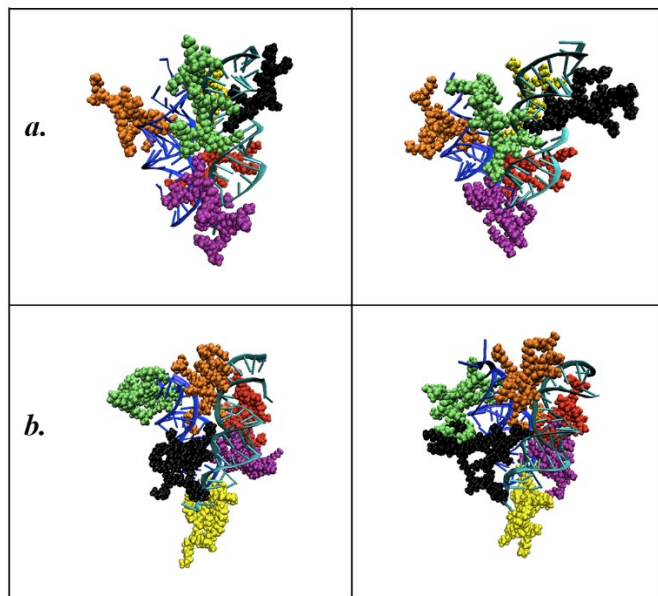


Figure C1. Snapshots of initial (left panel) and final (right panel) configurations of the NPs in the absence of the membrane for (a) PEI NP, and (b) PEI-LA NP. Different PEIs and siRNAs are represented by different colors. For clarity, water and ions are removed.

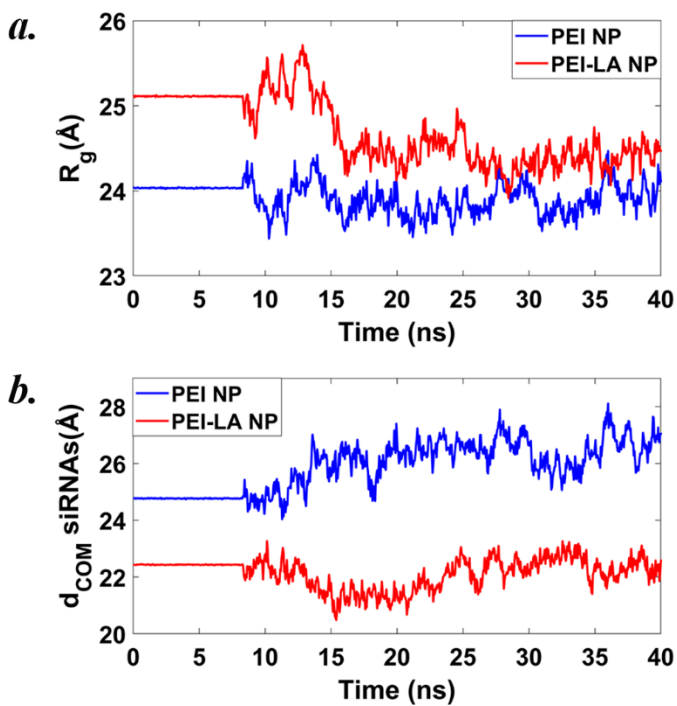


Figure C.2. (a) Gyration radius of NPs and (b) the COM distance between the siRNAs as functions of the simulation time in absence of the membrane.

C2. Equilibration of isolated membranes

Before SMD simulations of NP-membrane interactions, the membranes were subjected to 50 ns MD simulations without restraints. Membrane thickness was calculated by plotting the mass density of P atoms as a function of z coordinate, measured from the center of the bilayer in the direction perpendicular to the membrane surface. The density showed two peaks (Figure C3), and the distance between these two peaks was considered as the membrane thickness. The membrane thicknesses (Figure C4) were relatively constant: 39.25 ± 0.16 Å, 41.00 ± 0.27 Å, and 32.02 ± 0.39 Å (data collected from last 20 ns) respectively for the POPC, DPPC and DLPC bilayers. These thicknesses are in line with reported values in the literature [2], [3]. DLPC had the lowest thickness, consistent with its shortest lipid tails. For the DPPC and POPC membranes, POPC has a longer length on its Sn2 chain, but its thickness was slightly lower than DPPC. This suggests that the presence of unsaturated Cs induced a change in orientation of the lipid tails which led to a more compressed structure than DPPC.

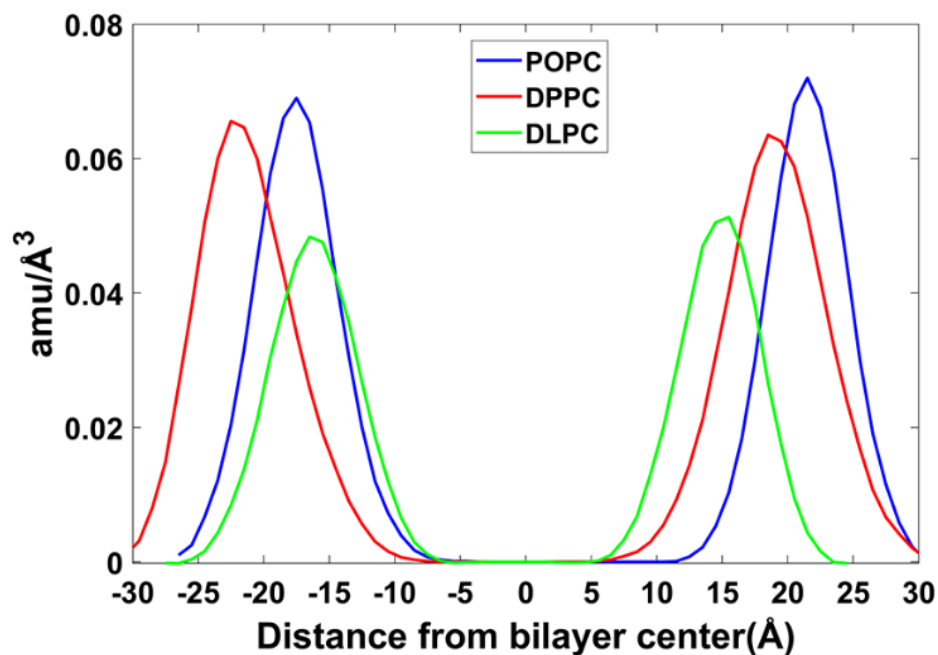


Figure C3. Mass density profile of P atoms as a function of distance form bilayer center.

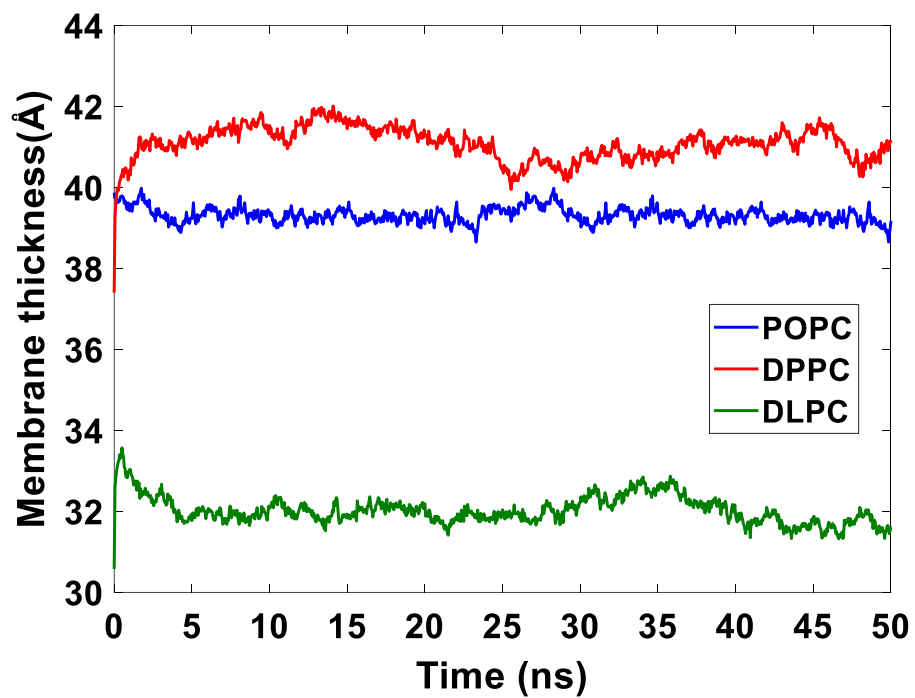


Figure C4. Time evolution of membrane thickness.

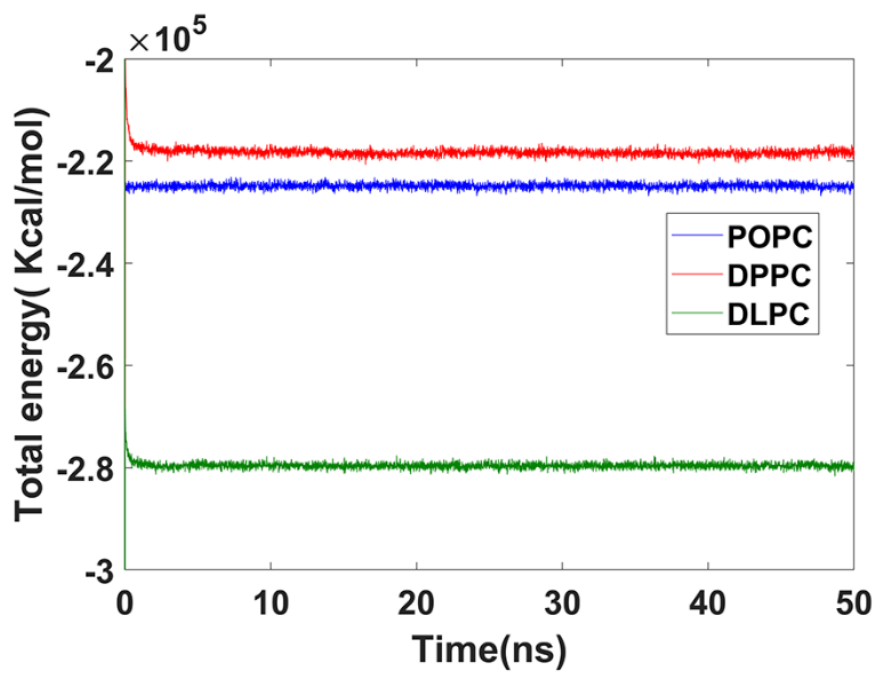


Figure C5. Total energy of the membranes during equilibration.

Figure C5 shows the total energy of the systems as a function of simulation time, which converged over a short period of time and remained stable throughout the simulation. The time evolution of area per lipid for each membrane (Figure C6) also shows convergence and equilibration of the membrane.

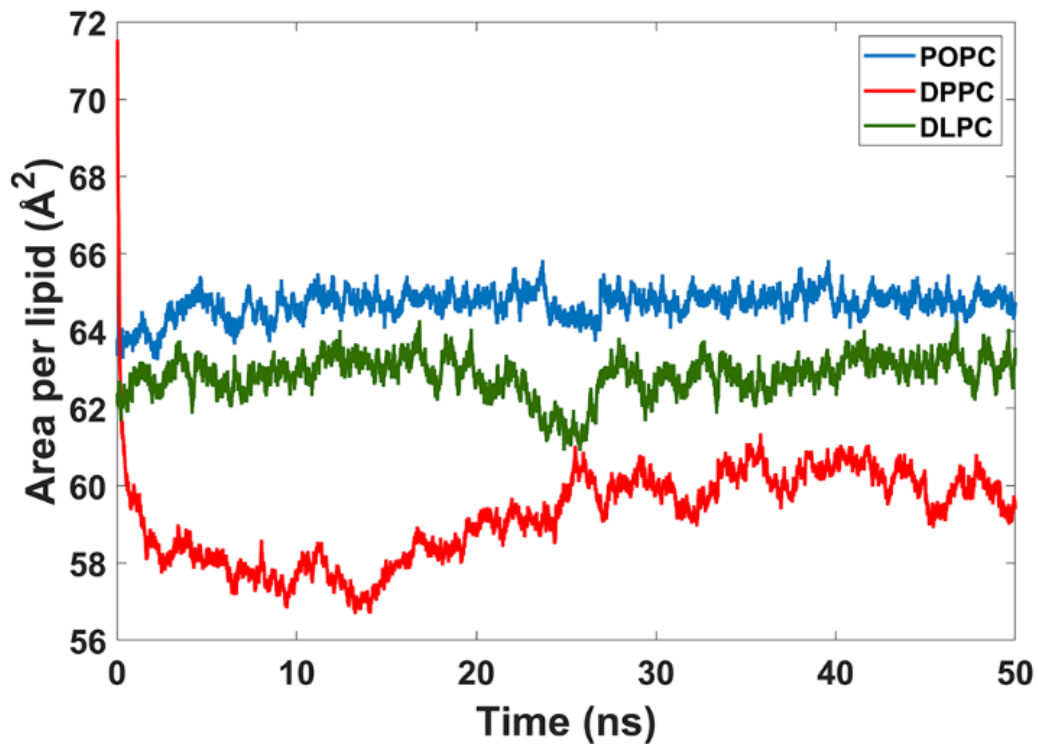


Figure C6. Time evolution of area per lipid for each simulated membrane.

C3. Schematic representation for the calculation of in-plane distribution of P atoms around COM of NP

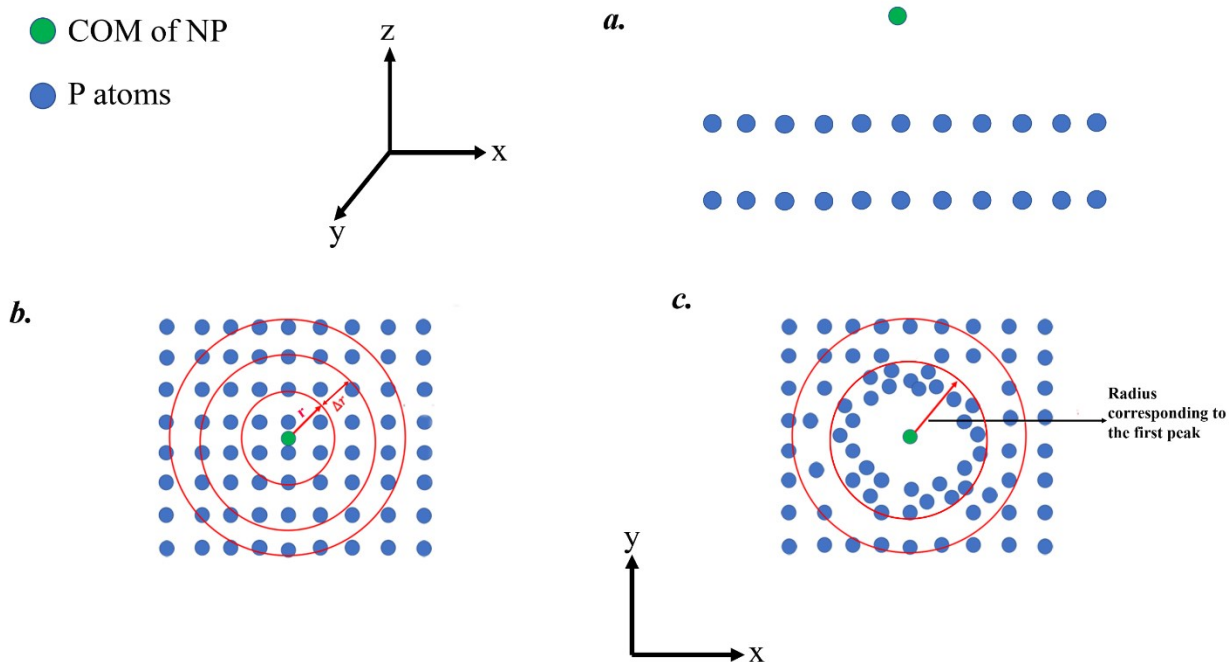


Figure C7. Schematic representation for the calculation of in-plane distribution of P atoms around COM of NP. (a) side view of the membrane and COM position of NP, (b) top view of undisturbed membrane, and (c) top view of formed pore within the membrane. $N(r)$ is the number of P atoms enclosed by the circle in the x-y plane with radius r from the projected location of the NP COM. The in-plane distribution of P atoms around the NP COM is quantified by the local areal density calculated from $\frac{\Delta N}{\Delta A} = \frac{N(r+\Delta r) - N(r)}{2\pi r^* \Delta r}$ where $r^* = r + \Delta r/2$. $\Delta r = 6.45 \text{ \AA}$ was used in the calculations. The density within the first circle was calculated from $\frac{N(r)}{\pi r^2}$.

C4. Angle calculation between lipid tails

In Chapter 5, the probability distribution was shown for the angle between the two tails of the membrane lipid. This angle was measured between two vectors, one attributed to each tail. Each vector was defined by connecting two atoms on the chain as shown in Figure C8.

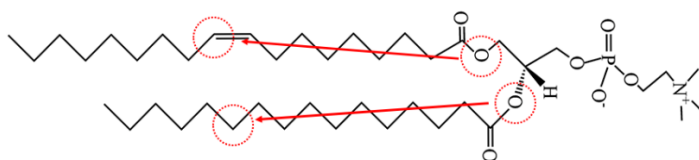


Figure C8. Two vectors defined, one in each tail, for calculating the angle between the two chains.

C5. Free volume of membranes

To measure the free volume inside the membrane, we first filled the empty space of the membranes with water molecules. To this end, no water molecules were added within 1.5 Å of any atoms of the membrane lipids. Afterward, the number density of water molecules within each membrane was measured (Table C1) and multiplied by 0.0299 nm³, which is the volume occupied by each water molecule. The output of this multiplication was considered as percentage of free volume within each membrane (Table C1).

Table S1. Free volume within each membrane.

Membrane	# of water molecules per nm ³ of membrane	Percentage of free volume inside membrane (%)
POPC	4.82	14.4
DPPC	4.58	13.7
DLPC	4.68	14.0

C6. Side view snapshots of the NP and the membrane during SMD

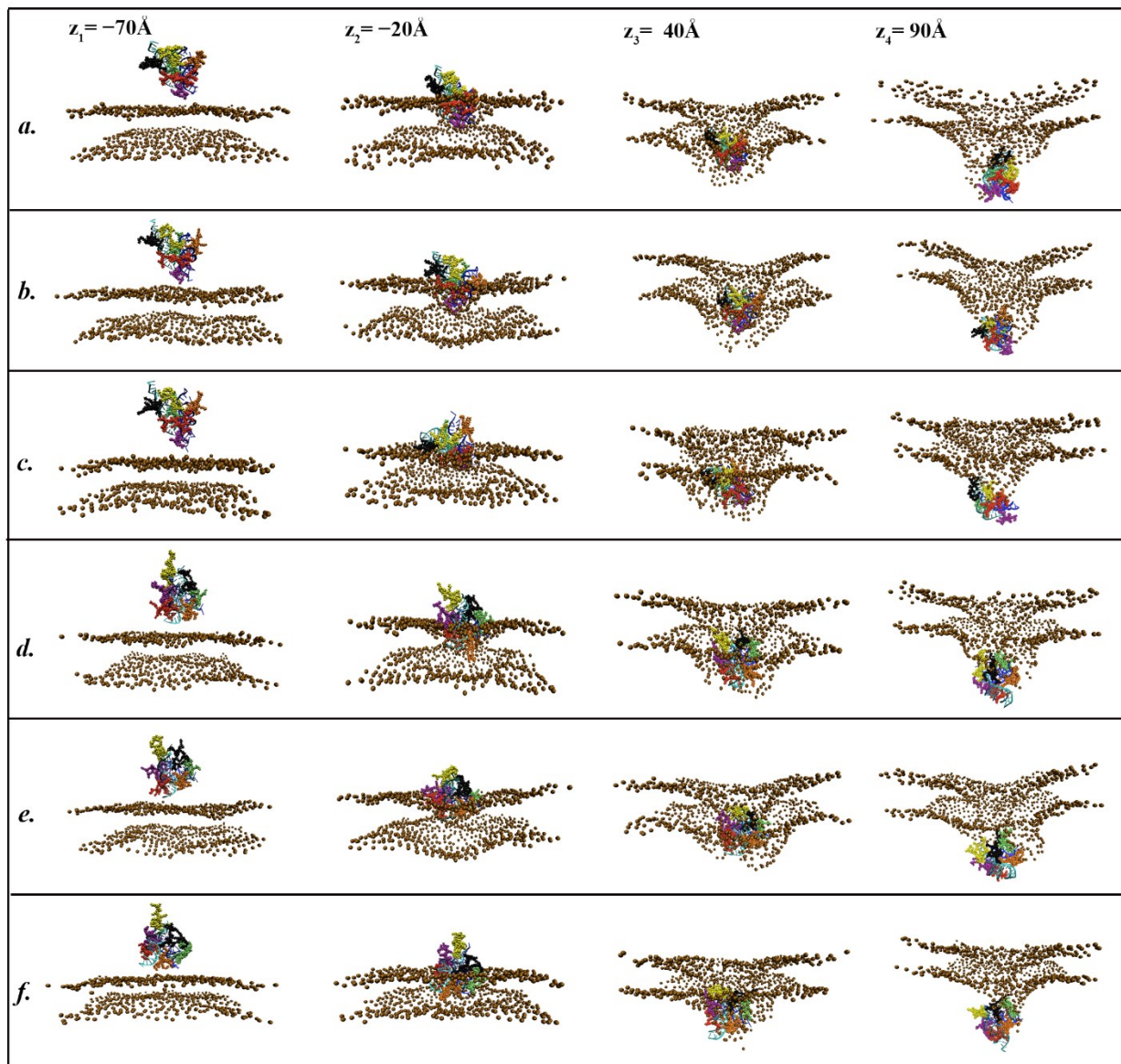


Figure C9. Side-view snapshots of the NP and membranes at different time of the SMD simulations for (a) PEI NP-POPC, (b) PEI NP-DPPC, (c) PEI NP-DLPC, (d) PEI-LA NP-POPC, (e) PEI-LA NP-DPPC, and (f) PEI-LA NP-DLPC. z_1 , z_2 , z_3 and z_4 are the z -positions of the COM of the NP when the snapshots were taken. Different PEIs and siRNAs are represented by different colors. For simplicity of visualization, water and ions are removed and only the P atoms of the membranes are shown (in ochre).

C7. Additional characterization of the NP

C7.1. shape anisotropy of NP

The relative shape anisotropy (κ^2) of the NP was calculated using Equation S1, where $\lambda_1, \lambda_2, \lambda_3$ are the three eigenvalues of the gyration tensor of the NP. The value of κ^2 is limited between 0 and 1. For highly symmetric spherical structure, κ^2 is close to 0, and κ^2 reaches 1 if all atoms lie on a straight line.

$$\kappa^2 = \frac{3\lambda_1^2 + \lambda_2^2 + \lambda_3^2}{2(\lambda_1 + \lambda_2 + \lambda_3)^2} - \frac{1}{2} \quad (\text{S1})$$

Figure C8 shows κ^2 of all the NPs, plotted against their COM position. To facilitate the discussion, we divide the penetration process into two stages: insertion (NP COM from -60 to 60 Å), and detachment (NP COM from 60 to 90 Å). From -80 to -60 Å the NP was approaching the membrane but had limited interaction with it. Consider first the PEI NP. During insertion and for POPC and DPPC membranes, κ^2 followed a similar trend as R_g : it decreased which corresponded to a slightly more isotropic configuration. During detachment and for POPC membrane, κ^2 increased back to its initial value, while it remained low for the DPPC membrane. For the DLPC membrane and during insertion, R_g of the NP showed a decreasing trend, while its κ^2 remained relatively constant. This suggests that the NP underwent compaction with minimal change in its shape anisotropy. During detachment from the DLPC membrane, R_g showed full recovery, while κ^2 slightly decreased. For the PEI-LA NP, κ^2 followed a similar trend as R_g in all three cases. However, during detachment, the increase in κ^2 was higher for POPC membrane than for DPPC and DLPC membranes. This suggests that the NP changed to a more anisotropic structure during detachment from the POPC membrane.

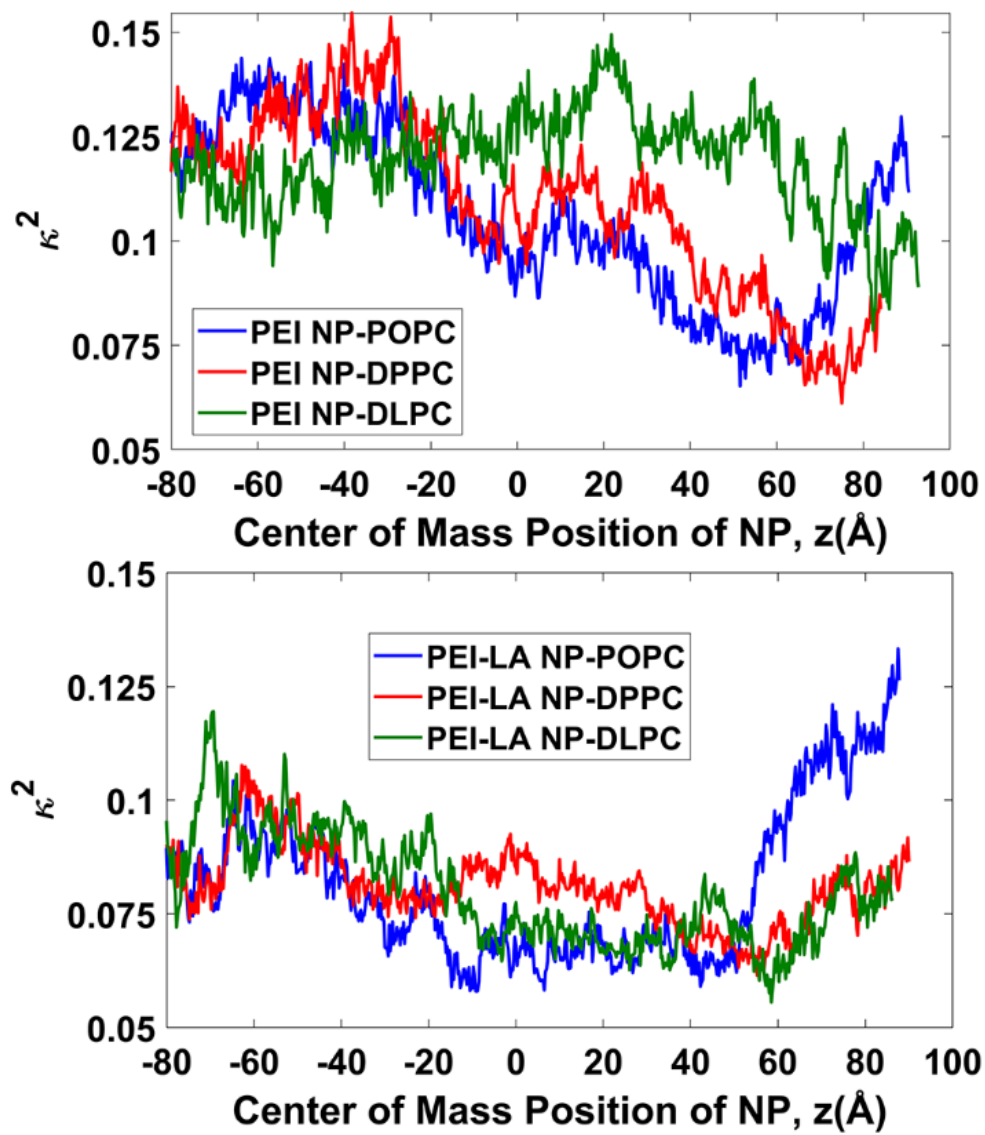


Figure C10. κ^2 of NP as a function of COM position of NP.

C7.2. Relative Orientation of siRNAs

The relative orientation of the 2 siRNAs was monitored by measuring the angle (θ) between two vectors each defined in one siRNA. This vector was defined by connecting two atoms at the opposite ends of the siRNA, which are C1' of the 18th residue in each strand. These vectors are schematically shown in Figure C11. We then measured the angle θ between the two vectors as a function of COM position of the NP. $\theta = 0^\circ$ corresponds to the siRNAs being parallel, whereas $\theta = 90^\circ$ represents two siRNAs perpendicular to each other.

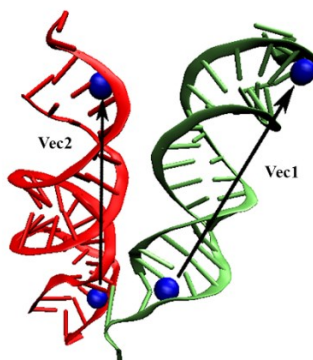


Figure C11: Schematic representative of the vectors defined to measure the relative orientation of the two siRNAs. The spheres are C_1' atoms of the 18th residue in each strand.

Figure C12 shows θ as a function of COM position of the NP. For PEI NP, θ followed a fluctuating trend in all membranes within the range of 30-55°. For PEI-LA NP and POPC membrane, starting from 50° θ followed an increasing trend and during detachment the two siRNAs formed a relatively perpendicular orientation ($\theta \sim 70^\circ$). For DPPC membrane, θ first increased from 50° to $\sim 70^\circ$, but decreased to its initial value during detachment from the membrane. For DLPC, the angle did not deviate significantly from its initial value throughout the penetration process.

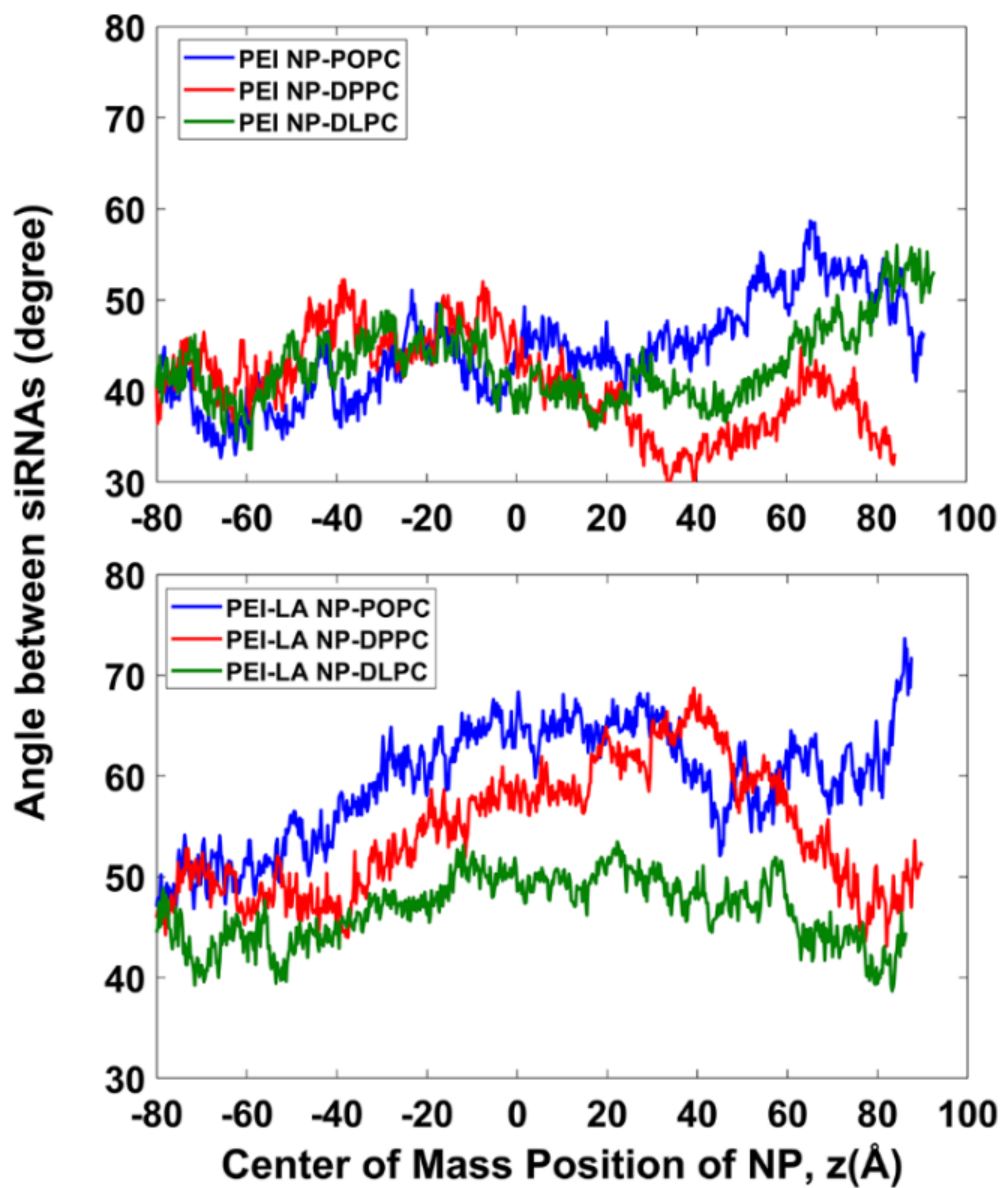


Figure C12. Relative angle between the two siRNAs as a function of COM position of the NP.

C7.3. Angle between each siRNA and z-axis

To measure the rotation of siRNA during the penetration process, the angle between each siRNA of the NP and the z-axis (perpendicular to the membrane surface) was calculated (see Figure C13). Figure C14 shows the angle for the two siRNAs (labeled siRNA1 and siRNA2) as functions of COM position of the NP. For all systems, the siRNAs underwent rotation during detachment and became more parallel with respect to the unperturbed membrane surface.

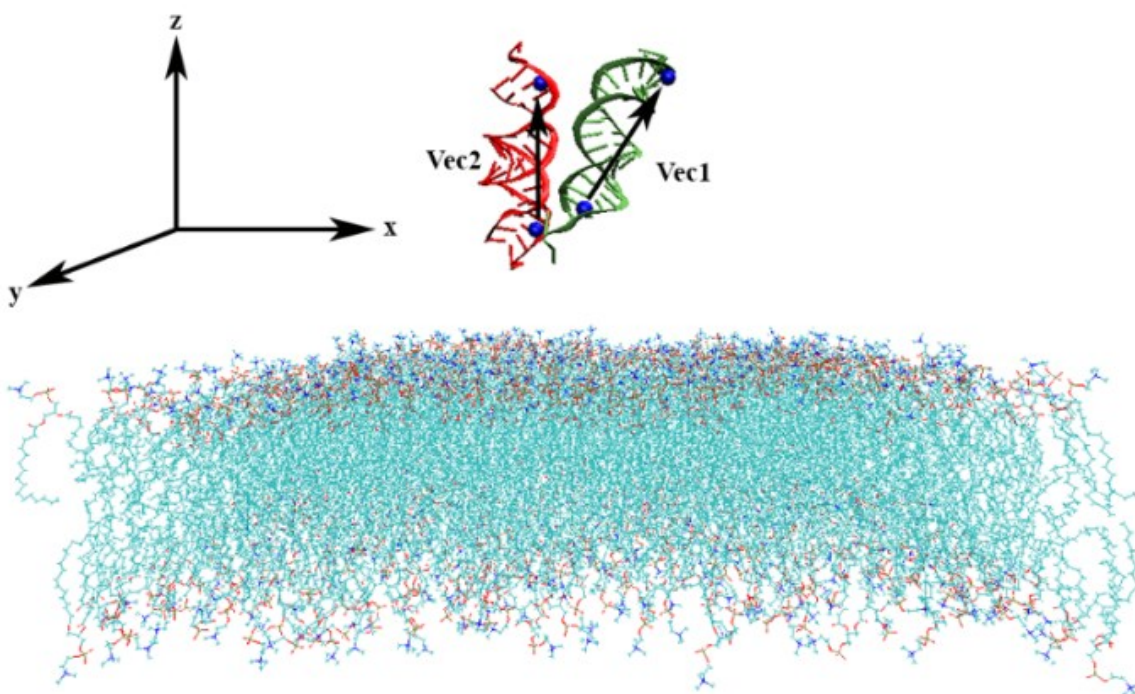


Figure C13. Schematic representative of vectors defined to measure the orientation of each siRNA relative to the membrane. Details for the definition of the vector representing axis of each siRNA are given in Figure C11. The angle between each vector of siRNA and z-axis was measured.

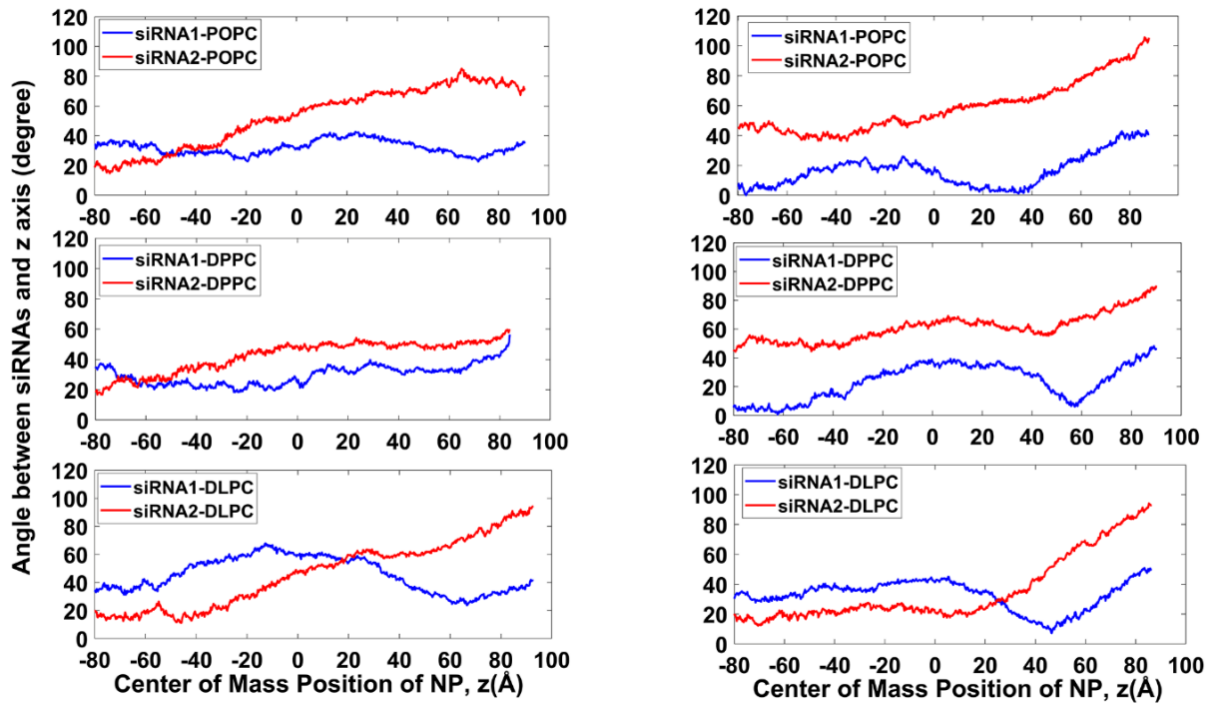


Figure C14. Angle between each siRNA and the z-axis during the penetration process for (left) PEI NP, (right) PEI-LA NP.

C8. Pore symmetry

To provide a quantitative assessment of pore symmetry at the end of NP pulling (34 ns), all P atoms located below $z = -50 \text{ \AA}$ were first projected onto the x-y plane which was parallel to the undisturbed membrane surface. The center of the pore was identified as the center of the circle that best fit the void in the x-y plane due to the absence of P atoms. Then, a new coordinate x' - y' was established in the x-y plane, with the origin located at the center of the pore. All projected P atoms within 4 nm of the pore center were considered, and the number of P atoms in each quadrant of the x' - y' plane was counted for further analysis (Figure C15).

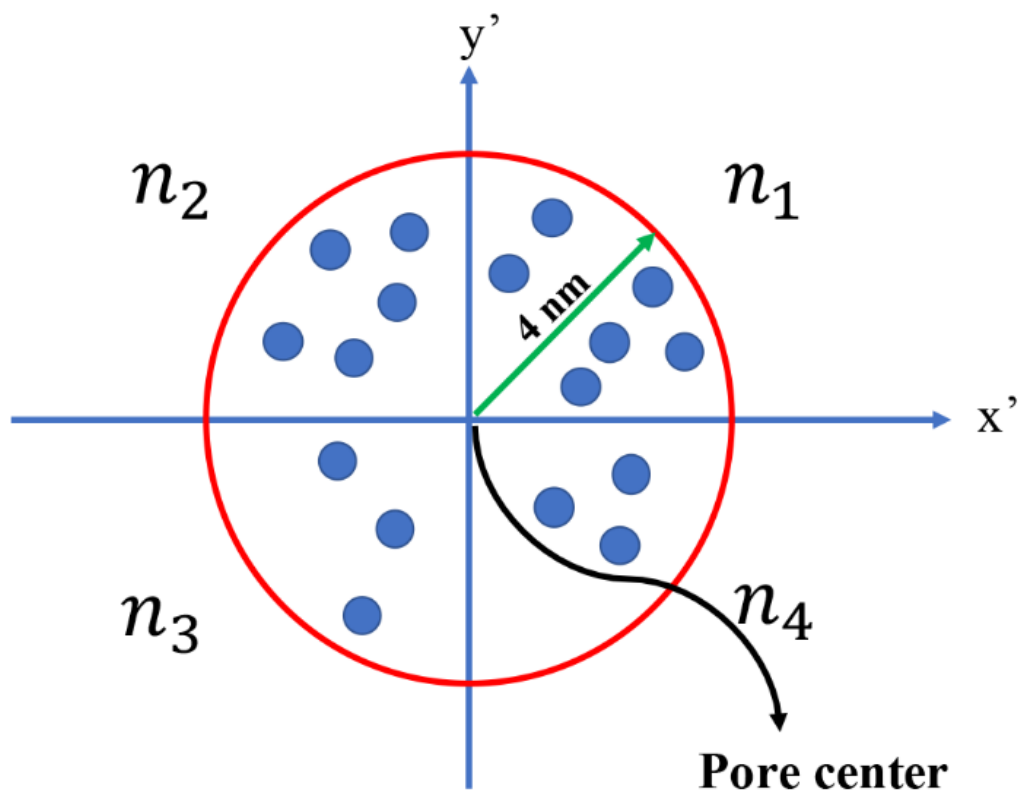


Figure C15. Schematic of P atoms in the four quadrants of the x' - y' coordinates.

Let n_i be the number of P atoms in the i^{th} quadrant, a bi-quadrant symmetry index was introduced

$$\alpha_{ij} = \frac{4n_i n_j}{(n_i + n_j)^2} \quad (i, j = 1, 2, 3, 4; i \neq j).$$

α_{ij} ranges between 0 and 1, and the maximum value of $\alpha_{ij}=1$ is achieved when $n_i = n_j$, i.e., when the P atoms are distributed equally between the i^{th} and j^{th} quadrants. $\alpha_{ij}=0$ corresponds to the case where there are no P atoms in one of the quadrants. Since $\alpha_{ij} = \alpha_{ji}$, the 4 quadrants generated 6 distinct indices: $\alpha_{12}, \alpha_{13}, \alpha_{14}, \alpha_{23}, \alpha_{24}, \alpha_{34}$. Using these α_{ij} values, the sum $\sum \alpha_{ij}$ and product $\prod \alpha_{ij}$ were calculated and summarized in Table C2 for all the simulated systems. The closer $\sum \alpha_{ij}$ is to 6, the more symmetric is the pore. Similarly, larger values of $\prod \alpha_{ij}$ correspond to more symmetric pores, and when $\prod \alpha_{ij} = 0$ at least one quadrant had no P atoms in it, suggesting strong asymmetry. Among the systems, PEI NP-DPPC, and PEI-LA NP-DLPC displayed the highest- and lowest values of $\sum \alpha_{ij}$, respectively. This suggest that PEI NP-DPPC had the highest pore symmetry, while PEI-LA NP-DLPC had the lowest pore symmetry. $\sum \alpha_{ij} = 3$ represent 50% of its maximum attainable value, and was chosen in this work to separate the symmetric pores from the asymmetric ones. Based on this definition, the pores in PEI NP-POPC, PEI-LA NP-DPPC and PEI-LA NP-DLPC were asymmetric, while the ones in PEI NP-DPPC, PEI NP-DLPC and PEI-LA NP-POPC were symmetric. Based on $\sum \alpha_{ij}$, we also ranked the degree of symmetry as: PEI NP-DPPC > PEI-LA NP-POPC > PEI NP-DLPC > PEI NP-POPC > PEI-LA NP-DPPC > PEI-LA NP-DLPC.

Table C2. Pore symmetry evaluation for the simulation systems.

System	$\sum \alpha_{ij}$	$\prod \alpha_{ij}$	Pore type
PEI NP-POPC	2.8017	0	Asymmetric
PEI NP-DPPC	5.7379	0.7603	Symmetric
PEI NP-DLPC	4.1068	0.0719	Symmetric
PEI-LA NP-POPC	5.1795	0.3843	Symmetric
PEI-LA NP-DPPC	2.7867	0	Asymmetric
PEI-LA NP-DLPC	0.9467	0	Asymmetric

C9. Additional results for PEI-LA NP

Deformation of the membranes caused by PEI-LA NP was measured by plotting the position of all P atoms (Figure C16). The results showed that compared with PEI NP in the same membrane, the deviation of P atoms from their initial position was lower in the POPC membrane, while it was higher in the DLPC membrane. This was caused by the type of pore formed (Table C2), which for POPC changed from asymmetric (PEI NP) to symmetric (PEI-LA NP), but for DLPC changed from symmetric (PEI NP) to asymmetric (PEI-LA NP). For the DPPC membrane, the type of pore changed from symmetric (PEI NP) to asymmetric (PEI-LA NP).

For all three membranes, in-plane distribution of P atoms around the NP COM (Figure C17a-c) was similar for PEI-LA NP and PEI NP, where for a well-established pore, two peaks were observed. The first peak was located at ~ 30 , ~ 29 , and ~ 30 Å from the NP COM, while the second peak was located at ~ 59 , ~ 56 , and 54 Å, respectively for POPC, DPPC, and DLPC membranes.

Probability distribution (PD) of the angle between Sn1 and Sn2 acyl chains (Figure C17d-f) followed a similar trend as that of PEI NP. For all membranes, as time increased and NP penetration progressed, there was a decline in the peak value of the PD and the angle distribution became wider, suggesting a reduction in the order of the membrane. The most probable angle between the two lipid tails was respectively $\sim 27^\circ$, $\sim 22^\circ$ and $\sim 28^\circ$ for POPC, DPPC and DLPC membranes at 0 ns.

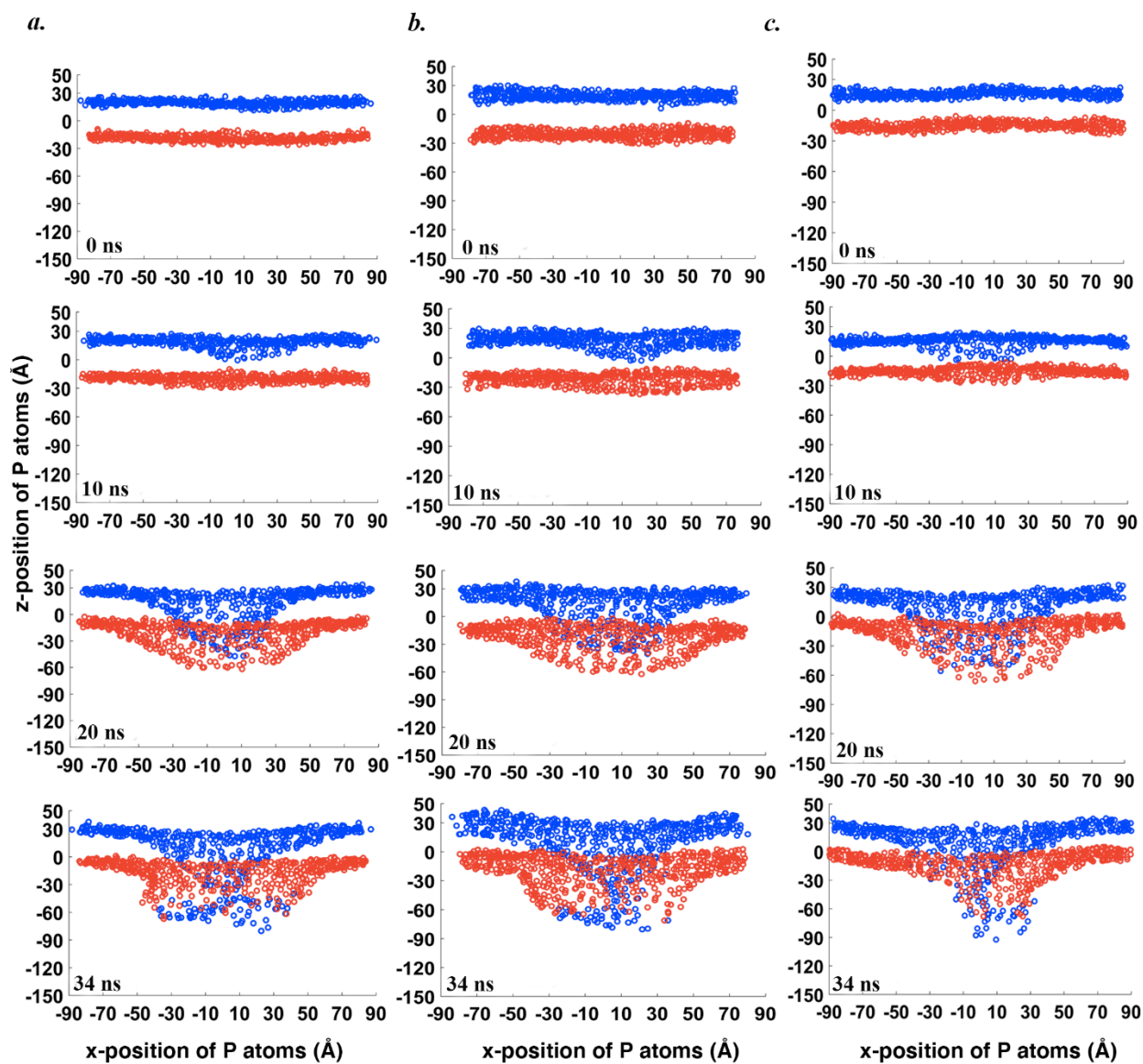


Figure C16. Position of P atoms at the (blue) upper and (red) lower leaflets of (a) POPC (b) DPPC and (c) DLPC membranes during penetration of PEI-LA NP.

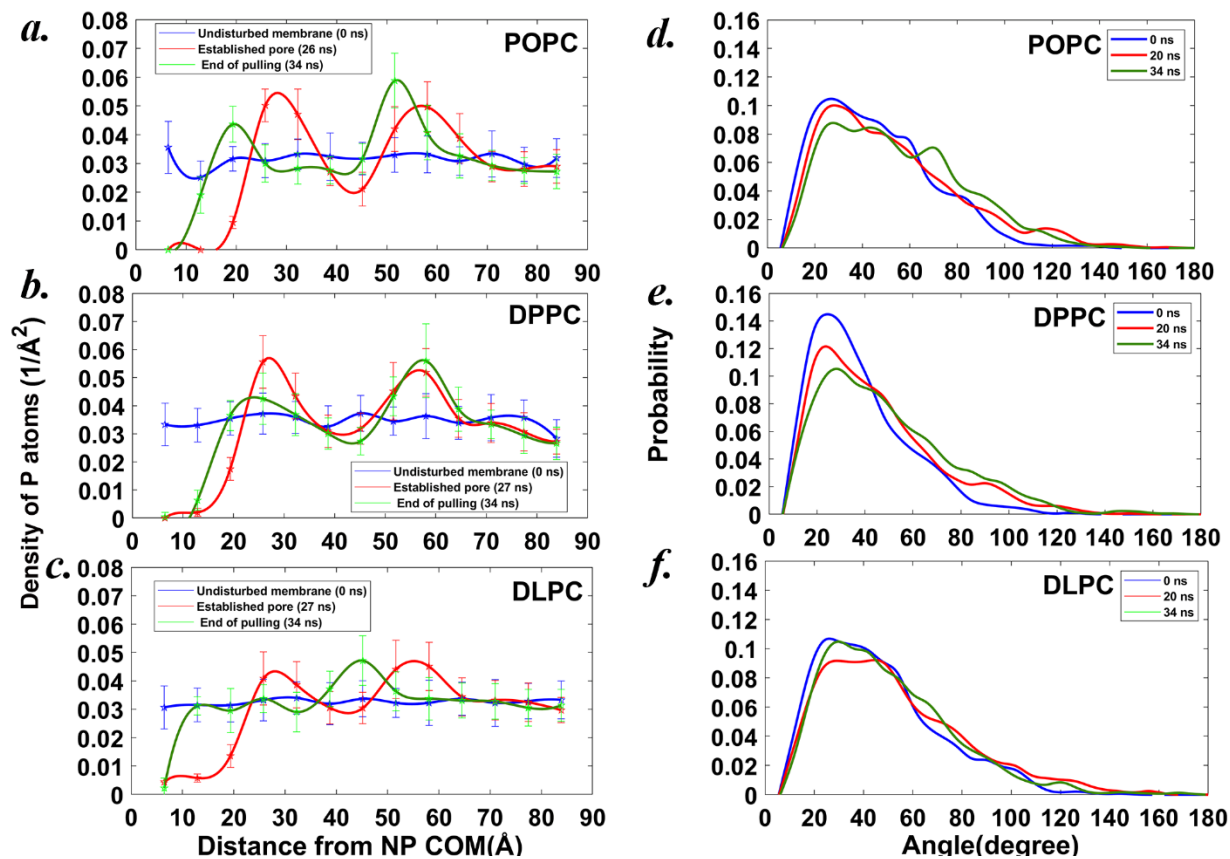


Figure C17. (Left panel) in-plane distribution of P atoms around the COM of the PEI-LA NP for (a) POPC, (b) DPPC and (c) DLPC membranes. (Right panel) probability distribution of the angle between Sn1 and Sn2 chains for (d) POPC, (e) DPPC, and (f) DLPC membranes during penetration of PEI-LA NP.

C10. Number of lipid flip-flops in each system

Table C3. Number of lipid flip-flops from the bottom leaflet to the top leaflet in each system.

System	Pore type	Number of lipid flip-flops (25 ns)	Number of lipid flip-flops (40 ns)	Number of lipid flip-flops (64 ns)	Total number of lipid flip-flops
PEI-NP-POPC	asymmetric	0	2	1	3
PEI-NP-DPPC	symmetric	0	0	0	0
PEI-NP-DLPC	symmetric	0	0	19	19
PEI-LA NP-POPC	symmetric	0	0	0	0
PEI-LA NP-DPPC	symmetric	0	4	7	11
PEI-LA NP-DLPC	asymmetric	3	3	10	16

C11. References

- [1] C. Sun, T. Tang, and H. Uludag, "A molecular dynamics simulation study on the effect of lipid substitution on polyethylenimine mediated siRNA complexation," *Biomaterials*, vol. 34, no. 11, pp. 2822–2833, Apr. 2013, doi: 10.1016/j.biomaterials.2013.01.011.
- [2] M. T. Hyvönen and P. T. Kovanen, "Molecular dynamics simulations of unsaturated lipid bilayers: effects of varying the numbers of double bonds," *Eur. Biophys. J.*, vol. 34, no. 4, pp. 294–305, Jun. 2005, doi: 10.1007/s00249-004-0455-7.
- [3] R. R. Gullapalli, M. C. Demirel, and P. J. Butler, "Molecular dynamics simulations of DiI-C18(3) in a DPPC lipid bilayer," *Phys. Chem. Chem. Phys.*, vol. 10, no. 24, p. 3548, 2008, doi: 10.1039/b716979e.

APPENDIX D: Supplementary Information for Chapter 6

D1. Detail of multi-layer perception (MLP) regression model

A schematic of MLP network, with only one hidden layer, is shown in Figure D1. The input layer consists of a set of nodes $\{x_1, x_2, \dots, x_n\}$ representing the input descriptors. Each node in the hidden layer $\{a_1, a_2, \dots, a_k\}$ results from the previous layer by a weighted linear summation followed by a ReLU activation function (e.g. $a_1 = \max(0, w_{11}x_1 + w_{21}x_2 + w_{31}x_3 + \dots + w_{n1}x_n)$), where w_{ij} is the weight associated with x_i and a_j . Once $\{a_1, a_2, \dots, a_k\}$ are determined, they become the new input representation to learn the output layer. The output layer for linear regression would be a weighted linear combination of nodes in the hidden layer, $f(X) = a_1w'_1 + a_2w'_2 + a_3w'_3 + \dots + a_kw'_k$.

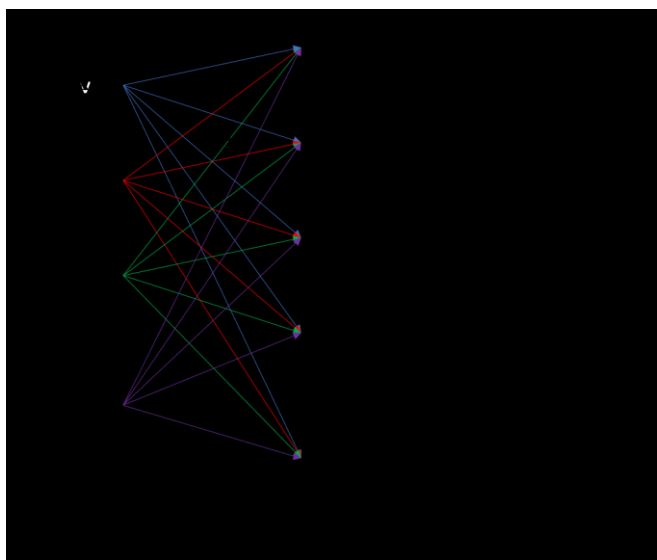


Figure D1. Schematic of MLP with one hidden layer.

D2. Dummy encoding for categorical descriptors

In Model type 1, the two categorical descriptors S and C_L were transformed using a dummy encoding scheme. The type of hydrophobic substitution, S, consisted of 10 categories (9 hydrophobic substitutions and another category “none” representing no modifications). For each category a column was generated as shown in Table D1. As a result, the categorical descriptor of S was converted into 10 new descriptors. For example, if a data point involved the use of Chol as the substitution, then the descriptor I_{Chol} would have the value of 1 while the other 9 descriptors in Table D1 would be 0.

Table D1. The transformation of categorical descriptor S using dummy encoding.

S	I _{None}	I _{CA}	I _{Lau}	I _{PA}	I _{StA}	I _{LA}	I _{αLA}	I _{Chol}	I _{OA}	I _{tLA}
None	1	0	0	0	0	0	0	0	0	0
CA	0	1	0	0	0	0	0	0	0	0
Lau	0	0	1	0	0	0	0	0	0	0
PA	0	0	0	1	0	0	0	0	0	0
StA	0	0	0	0	1	0	0	0	0	0
LA	0	0	0	0	0	1	0	0	0	0
αLA	0	0	0	0	0	0	1	0	0	0
Chol	0	0	0	0	0	0	0	1	0	0
OA	0	0	0	0	0	0	0	0	1	0
tLA	0	0	0	0	0	0	0	0	0	1

Similarly, the categorical descriptor of C_L, type of cell line, was transformed as shown in Table S2 where 6 new descriptors were generated. When a particular cell line was used for a data point, the corresponding description would take the value of 1 while others took the value of 0.

Table D2. The transformation of C_L using dummy encoding.

C _L	I _{MDA MB231}	I _{MCF7}	I _{AU565}	I _{MDA-468}	I _{MDA 435}	I _{MDA 231}
MDA MB231	1	0	0	0	0	0
MCF7	0	1	0	0	0	0
AU565	0	0	1	0	0	0
MDA-468	0	0	0	1	0	0
MDA 435	0	0	0	0	1	0
MDA 231	0	0	0	0	0	1

D3. Binary encoding for categorical descriptors

Binary encoding converts a category into a binary number, and each binary digit creates one descriptor column. The transformations of categorical descriptors S and C_L using binary encoding are shown in Tables D3 and D4, respectively. Take Table D3 for example, each category was first converted into a 4-digit binary number. The left-most digit corresponded to column I_{sub-1} , the second digit from left corresponded to I_{sub-2} , etc. Four descriptors (I_{sub-1} , I_{sub-2} , I_{sub-3} , I_{sub-4}) resulted from this conversion. The same was done for the categorical descriptor of C_L , where only 3 descriptors were needed (I_{cell-1} , I_{cell-2} , I_{cell-3}).

Table D3. The transformation of categorical descriptor S using binary encoding.

S	I_{sub-1}	I_{sub-2}	I_{sub-3}	I_{sub-4}
None	0	0	0	1
CA	0	0	1	0
Lau	0	0	1	1
PA	0	1	0	0
StA	0	1	0	1
LA	0	1	1	0
α LA	0	1	1	1
Chol	1	0	0	0
OA	1	0	0	1
tLA	1	0	1	1

Table D4. The transformation of categorical descriptor C_L using binary encoding.

C_L	I_{cell-1}	I_{cell-2}	I_{cell-3}
MDA MB231	0	0	1
MCF7	0	1	0
AU565	0	1	1
MDA-468	1	0	0
MDA 435	1	0	1
MDA 231	1	1	0